ATOMIC AND PLASMA-MATERIAL INTERACTION DATA FOR FUSION

VOLUME 12

INTERNATIONAL ATOMIC ENERGY AGENCY, VIENNA, 2003

The volumes of ATOMIC AND PLASMA–MATERIAL INTERACTION DATA FOR FUSION are published by the International Atomic Energy normally once a year.

For these volumes, papers, letters and reviews are accepted which deal with the following topics:

- Elementary collision processes in fusion plasmas involving photons, electrons, ions, atoms and molecules;
- Collision processes of plasma particles with surfaces of fusion relevant materials;
- Plasma-material interaction phenomena, including the thermophysical response of materials.

Each submitted contribution should contain fusion relevant data and information in either of the above areas. Original contributions should provide new data, using well established methods. Review articles should give a critical analysis or evaluation of a wider range of data. They are normally prepared on the invitation by the Editor or on prior mutual consent. Each submitted contribution is assessed by two independent referees.

Every manuscript submitted must be accompanied by a *disclaimer* stating that the paper has not been published and is not being considered for publication elsewhere. If no copyright is claimed by the authors, the IAEA automatically owns the copyright of the paper.

Guidelines for the preparation of manuscripts are given on the inside back cover. Manuscripts and correspondence should be addressed to: The Editor, ATOMIC AND PLASMA–MATERIAL INTERACTION DATA FOR FUSION, International Atomic Energy Agency, Wagramer Strasse 5, P.O. Box 100, A-1400 Vienna, Austria.

Publisher: International Atomic Energy Agency, Wagramer Strasse 5, P.O. Box 100, A-1400 Vienna, Austria

Editor: R.E.H. Clark, Atomic and Molecular Data Unit, Division of Physical and Chemical Sciences

---

ATOMIC AND PLASMA–MATERIAL INTERACTION DATA FOR FUSION, VOLUME 12
IAEA, VIENNA, 2003
STI/PUB/023/APID/12
ISBN 92–0–111803–1
ISSN 1018–5577

FOREWORD

In the conditions typical of plasmas found in nuclear fusion machines the temperatures are such that the light elements are completely stripped of their electrons. However, heavier impurity materials retain bound electrons. Such materials may exist in the plasma from contamination from the wall materials or may be introduced in the divertor region to dissipate energy from the plasma. These heavy elements can be very efficient radiators. This can be a problem in maintaining a high temperature in the plasma core. However, this process can be advantageous in the divertor region of the plasma where it is necessary to dissipate energy from the plasma with minimum disruption of the vessel walls. In either case it is important to have an accurate estimate of the total power radiated from heavy elements that are likely to be found in fusion machines. This was the focus of a recent IAEA Co-ordinated Research Project.

The calculation of total radiated power represents one of the more challenging tasks in plasma modelling. It is first necessary to construct a complete atomic database for all ionisation stages of the element under consideration. This includes all energy levels as well as excitation and ionisation processes and their inverse processes. In addition all radiative processes must be calculated. There can be large numbers of energy levels for each ionisation stage. The number of processes will increase roughly as the square of the number of levels. Furthermore, it is necessary to calculate cross sections for each transition over a range of energies for the calculation of rate coefficients, which require integration of cross section over the electron distribution for a range of electron velocities. Once all the atomic physics data have been gathered, it is necessary to solve the rate equations to arrive at a calculation of the total radiated power. These calculations are extremely time consuming and it is difficult to carry them out for heavy elements due to the large number of bound electrons resulting in a proliferation of energy levels.

The present volume of Atomic and Plasma-Material Interaction Data for Fusion represents the result of a co-ordinated effort of leading theoretical groups within the IAEA Co-ordinated Research Project (CRP) on Radiative Cooling Rates of Fusion Plasma Impurities. The contributions of the participants of this CRP, contained in the present volume, significantly enlarge information on radiative processes taking place in different regions of fusion plasmas. This information is an important ingredient in many modelling and diagnostic studies of fusion plasmas.

The IAEA is taking this opportunity to acknowledge the Co-ordinated Research Project participants for their dedicated effort and contribution to this volume.

IN MEMORIUM

It is with great sadness that the editors of the *Atomic and Plasma-Material Interaction Data for Fusion* note the passing away of one of the contributors to this issue. Professor Kan Ashida lost his battle with cancer on August 3, 2000. Professor Kuniaki Watanabe provided the following eulogy for Professor Ashida.

Professor Kan Ashida of the Hydrogen Isotope Research Center of Toyama University passed away on Thursday, August 3, 2000 at the age of forty-six after six months of a severe struggle with lung cancer.

Professor Ashida received a Masters degree in Science from the Graduate School of Toyama University on March 25, 1980. He then started his professional career in research and technological development on April 1, 1980 as a technical staff member at the newly established Tritium Research Center of Toyama University. He was promoted to research assistant in July 1987 and to associate professor in April 1995. He has also been a visiting associate professor at the National Institute for Fusion Science and a lecturer at the Toyama National College of Technology since April 1999. During this period he earned a doctorate in engineering from Nagoya University in March 1992 on the topic of physicochemical interactions between hydrogen isotopes and graphite.

Professor Ashida's distinguished research covered a wide area including R&D of tritium experimental systems, characterization of tritium-getting materials, physicochemical interactions between hydrogen isotopes and graphite, and other areas. His contributions to these areas were highly regarded worldwide. His openness and desire to work on difficult problems led to his being universally well liked. The deep regret for his untimely death was shared by the Japanese communities as well as his international colleagues.

His forty-six years of life was very brief, but it was a life that should be the cause of pride for his endeavours and achievements. On behalf of his family (his wife, two steady sons and a cheerful daughter) as well as the staff of the Hydrogen Isotope Research Center, I heartily appreciate your close collegial and personal friendships with him.

Kuniaki Watanabe

Director,
Hydrogen Isotope Research Center
Toyama University

EDITORIAL NOTE

CONTENTS

PREPARATION AND CHARACTERIZATION OF C-Be AND C-W SAMPLES FOR MIXED PLASMA-FACING MATERIALS RESEARCH AT THE INEEL

R.A. ANDERL, G.R. LONGHURST, R.J. PAWELKO
Idaho National Engineering and Environmental Laboratory,
Idaho Falls, Idaho, United States of America

Abstract

This paper presents a summary description of the preparation and characterization of C-Be and C-W mixed materials. The materials are used in experiments to investigate hydrogen isotope retention in plasma-facing component materials.

1. INTRODUCTION

Mixed-materials research at the Idaho National Engineering and Environmental Laboratory (INEEL) has focused on the C-Be and C-W systems. The primary purpose of this work was to investigate hydrogen isotope retention in these systems. For this purpose, we simulated plasma mixed-material layers by using carbon-coated Be and carbon-coated W specimens that were heat-treated and by using tungsten and tungsten carbide specimens prepared by chemical vapor deposition (CVD). This contribution summarizes the materials preparation and characterization activities. A second contribution to this issue summaries the hydrogen retention measurements. Results of this work on C-Be were published in refs. [1-3]. References [4-6] document the results of our studies on C-W materials.

2. SAMPLE PREPARATION AND CHARACTERIZATION

2.1. C-Be samples

Sample preparation entailed fabrication of carbon-coated Be foils, heating of the composite samples at different temperatures and depth-profile Auger electron spectrometry (AES) analyses for the coated samples. The depth-profile analyses used an Ar ion beam to sputter the sample, and Auger electron signatures corresponding to C, Be and O were monitored throughout. Coated specimens were prepared by exposing Brush Wellman Be foils [type IF-1 (99.8% Be, 150 ppm BeO) and type PF-60 (99.5% Be, 0.6% BeO)] in a vacuum chamber to carbon vapor generated from an arc discharge between high-purity carbon electrodes. Specimens with carbon layers of 10, 50, 100 and 130-nm thickness were prepared. Samples were annealed in a high-vacuum environment at temperatures of 300, 400, and 500°C. After cool-down to room temperature, the samples were retrieved and installed in a separate vacuum system for AES depth-profile analyses. Some of the results of these analyses for samples coated with 130 nm of carbon are shown in Figures 1 and 2. Figure 1 compares the depth-profile analyses of C, Be and O for a C-coated Be sample that was heated at 400°C for 2 hours with an analysis for an unheated sample having a comparable carbon coating. The AES data for the unheated (25°C) sample show a relatively sharp interface between the carbon coating and the Be substrate. This analysis shows the presence of a thin oxide layer at the interface. AES analysis for a coated sample annealed at 300°C revealed no visible difference in

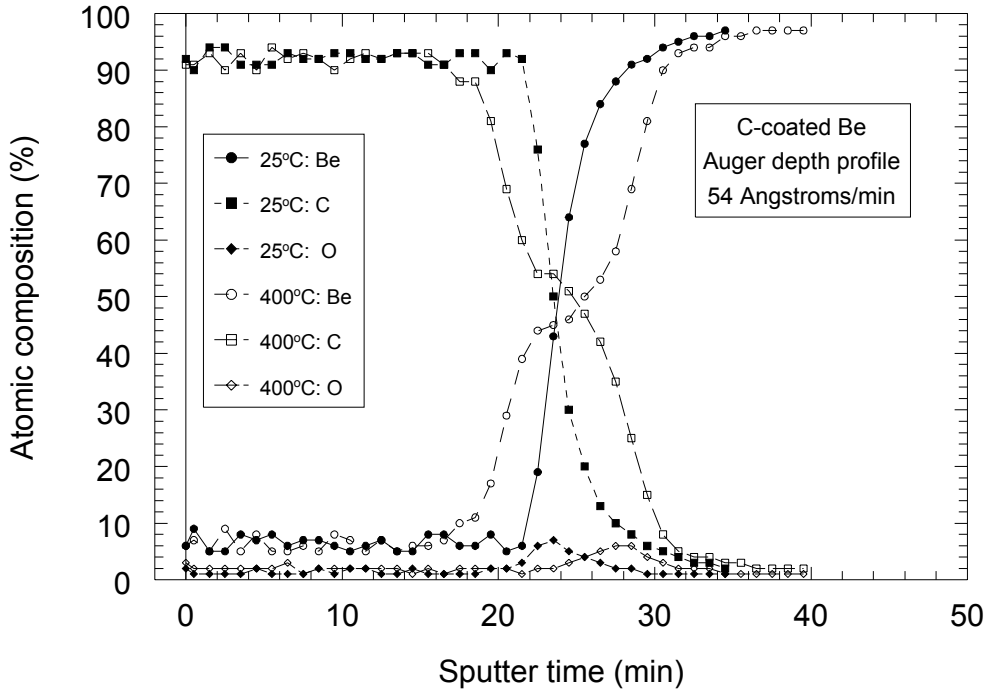

Figure 1: Comparison of the AES depth profiles of C, Be, and O concentrations in two PF-60 Be samples coated with 130 nm of carbon, one sample that was not annealed and one that was annealed at 400℃ for 2 hours.

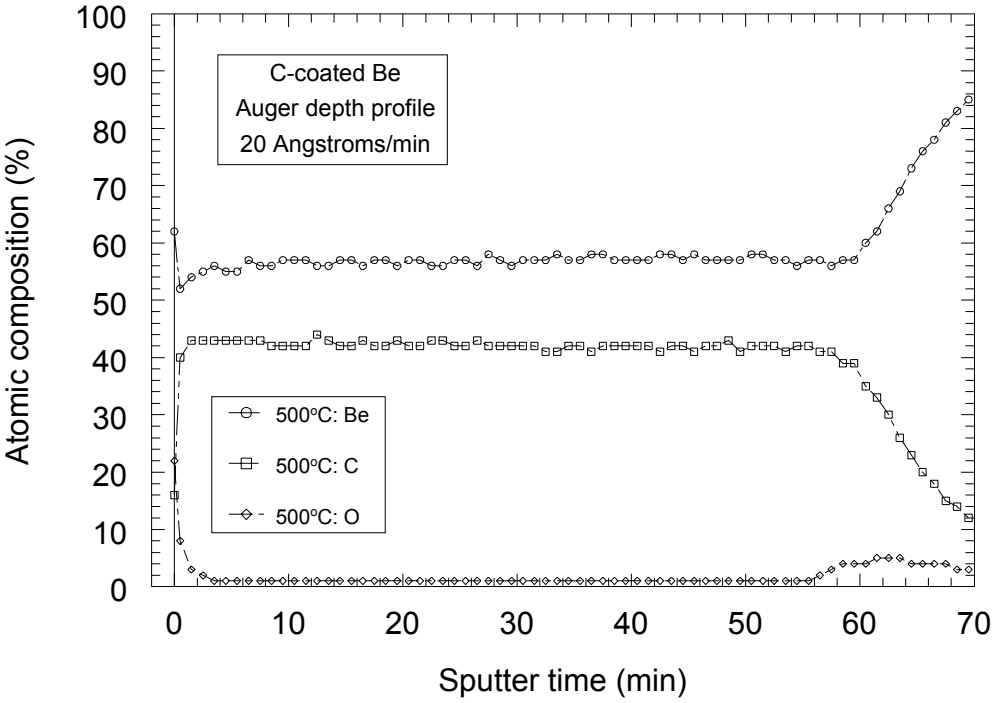

Figure 2: AES depth profile showing C, Be and O concentrations in a PF-60 sample coated with 130 nm of carbon and annealed at 500℃ for 2 hours.

the C, Be and O depth profiles for the 25°C and the 300°C data, indicating that for a temperature of 300°C, no Be/C inter-diffusion was observed during a two-hour annealing. However, as shown in Figure 1, inter-diffusion of Be and C was observed at the interface of the sample annealed at 400°C for 2 hours. A thin oxide layer is still observed at the C-Be interface. Figure 2 shows the AES depth-profile data for a C-coated Be sample that was annealed at 500°C for two hours. These data indicate that Be diffusion into the carbon was quite rapid at this temperature and that Be had migrated through the entire carbon layer. A thin oxide layer was present at the surface layer/Be substrate interface. Based on the relative atomic compositions shown in Figure 2 for C and Be in the coating, we believe that the layer comprises Be_2C and some graphitic phases throughout the mixed layer with a thin BeO layer at the original C-Be interface.

2.2. C-W samples

Two types of C-W mixed material samples were fabricated for the hydrogen retention studies; carbon-coated discs of W1%La and tungsten carbide discs made by CVD. Carbon-coated samples were prepared by exposing polished W1%La discs to carbon vapor generated from an arc between two carbon electrodes in a vacuum system. Nominal coating thickness ranged from 100 to 150 nm. Carbon-coated samples with 100-nm thickness were used in annealing studies to determine inter-diffusion properties of the C-W system. Depth-profile Auger analyses were performed for three different samples annealed at 400°C, 600°C, and 800°C for 3 hours each. Principal results of these analyses are presented in Figures 3 and 4. Figure 3 shows the C and W concentration profiles as a function of depth in the carbon coating and into the W substrate for an un-annealed sample and for a sample annealed at 600°C. The profiles for the un-annealed sample are essentially identical indicating that there was no measurable C-W inter-diffusion for samples annealed at temperatures as high as 600°C. Figure 4 shows the C and W concentration profiles as a function of depth for an un-annealed C-coated W1%La sample and one that was annealed at 800°C for 3 hours. The comparison demonstrates that there was some inter-diffusion of carbon and tungsten in the material interface region.

Tungsten and tungsten carbide samples were made by ULTRAMET using proprietary CVD techniques. These samples were machined from deposits collected on Mo cylindrical mandrels exposed to different CVD atmospheres. CVD-W material was deposited in a single deposition cycle, whereas, multiple cycles were required to achieve the required thickness for tungsten carbide. As a consequence, the tungsten carbide microstructure contained distinct columnar layers and interfaces between the layers. In contrast, the CVD-W had a single layer, columnar microstructure and no indications of porosity or secondary-phase interstitials. As determined by X-ray diffraction analyses, the CVD tungsten carbide was principally W_2C with indications of trace C, most likely at the grain boundaries of the structure. CVD-W_2C had a density of 18.3 g/cm^3 and a microhardness of 2040-2450 VHN, dependent on the sample tested. CVD-W had a density of 19 g/cm^3 and a microhardness of 525 VHN.

This work was performed within an IAEA Co-ordinated Research Project (CRP) on "Plasma-Material Interaction (PMI) Data for Mixed Plasma Facing Materials in Fusion Reactors" and supported by the US Department of Energy, Office of Sciences, under DOE Idaho Operations Contract Number DE-AC07-99ID13727.

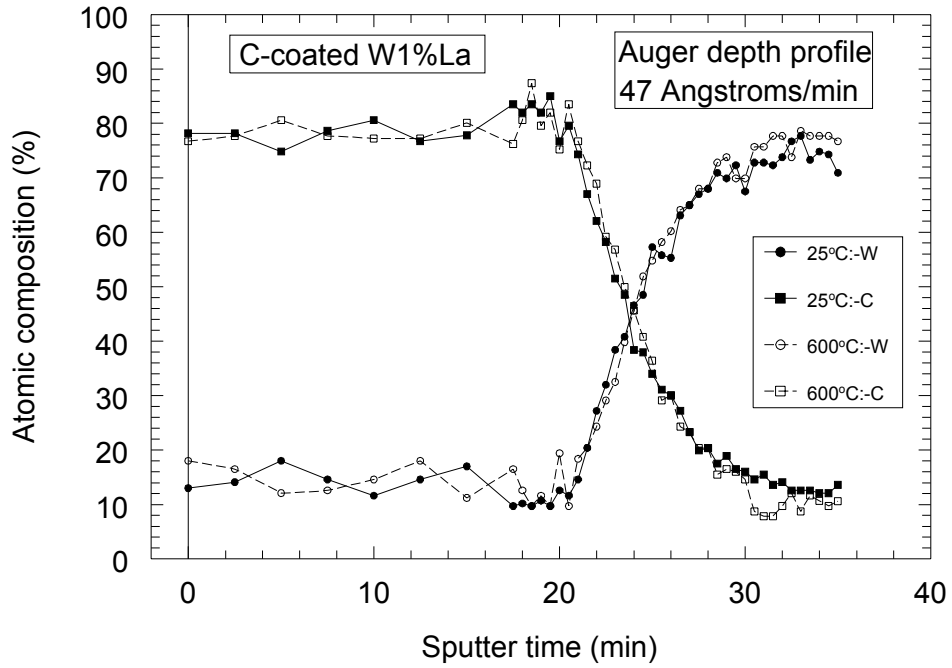

Figure 3: AES depth profile of C and W concentrations in two W1%La samples coated with 100-nm of carbon, one un-annealed and one annealed for 3 hours at 600 ℃.

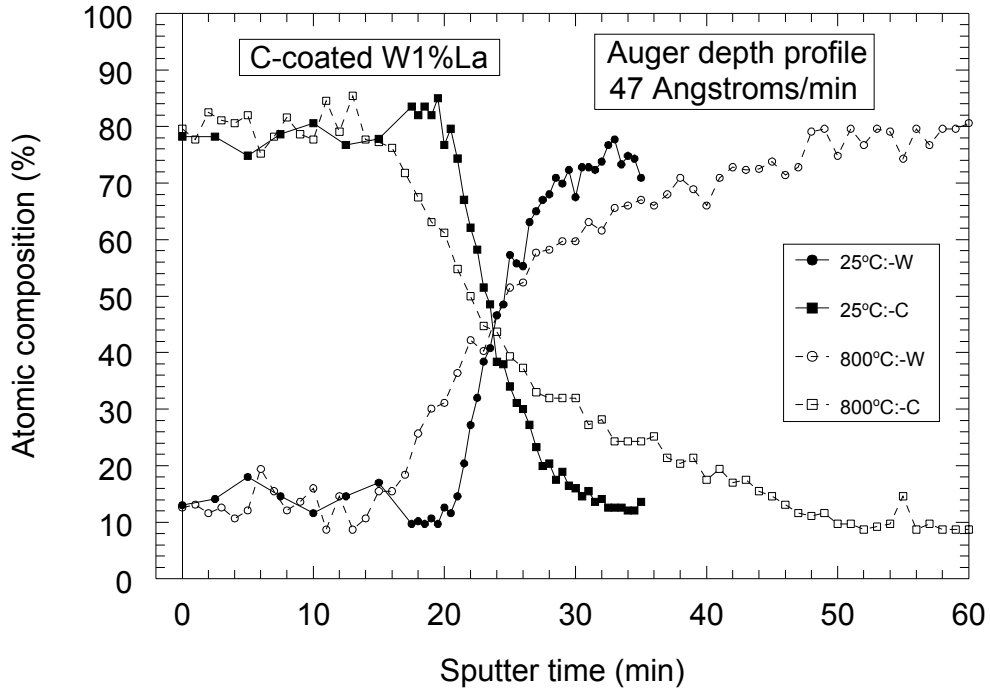

Figure 4: AES depth profile of C and W concentrations in two W1%La samples coated with 100-nm of carbon, one un-annealed and one annealed for 3 hours at 800 ℃.

REFERENCES

[1] ANDERL, R. A., CAUSEY R. A., DAVIS, J. W., DOERNER, R. P., FEDERICI, G., HAASZ, A. A., LONGHURST, G. R., WAMPLER, W. R., WILSON, K. L., J. Nucl. Materials **273** (1999) 1-26.

[2] ANDERL, R. A., LONGHURST, G. R., PAWELKO, R. J., OATES, M. A., J. Fusion Energy **16** (1997) 95-100.

[3] ANDERL, R. A., "Initial Deuterium implantation thermal desorption experiments for Be and C-coated Be," Engineering Design File, EDF No: ITER/US/96/TE/SA-13, August 7, 1996, INEEL, Idaho Falls, ID.

[4] ANDERL, R. A., PAWELKO, R. J., SCHUETZ, S. T., J. Nucl. Materials **290-293** (2001) 38-41.

[5] ANDERL, R. A., PAWELKO, R. J., SCHUETZ, S. T., "Deuterium retention in W foil, CVD-W and CVD-W_2C," INEEL External Report INEEL/EXT-2000-00702, June, 2000.

[6] ANDERL, R. A., "Deuterium implantation and mobilization behavior in carbon-coated tungsten," Engineering Design File, EDF No: ITER/US/98/TE/SA-14, July 17, 1998, INEEL, Idaho Falls, ID.

MIXED-MATERIALS DEVELOPMENT AND CHARACTERIZATION IN PISCES

R.P. DOERNER and the PISCES TEAM
Center for Energy Research, University of California San Diego,
La Jolla, California, United States of America

Abstract

Auger Electron Spectrometer (AES) and an X ray Photoelectron Spectrometer (XPS) are used to investigate carbon-containing mixed-material layer formation during plasma bombardment of beryllium and tungsten samples. The concentration of impurities in the plasma (and therefore the arrival rate of these impurities at the surface) is influential in determining the resultant chemical bonding on the surface. If the arrival rate of carbon at the surface is large, then a surface rich in carbon-carbon bonding develops. If the arrival rate of carbon at the surface is reduced, then the carbon in the surface exhibits preferential carbidic bonding. At low carbon concentration, carbidic bonding is observed in the surface layer regardless of the temperature of the sample during the plasma exposure.

I. Introdcution

The material characteristics of carbon-containing mixed-material layers formed during plasma exposure in PISCES-B have been measured for both tungsten and beryllium samples. PISCES-B is equipped with an in-situ surface analysis station containing both an Auger Electron Spectrometer (AES) and an X ray Photoelectron Spectrometer (XPS). In addition, an accompanying ion beam can be used for depth profiling using either diagnostic.

II. Be/C Surfaces

Experiments using the Be/C system have focused on the following, partial surface coverage region. The surfaces that result from deuterium plasma exposure under the conditions of 0.3% carbon impurity concentration at a sample temperature of 810 K and 100 eV ion bombarding energy. Under these conditions, the surface is well adhered to the substrate, with no flakes or chipped regions on the sample surface visible. During higher impurity concentration plasma bombardment, a surface that is almost entirely carbon forms and covers the substrate material, described as thick, black carbon films in [1]. During higher plasma impurity concentration bombardment (0.8% carbon), the growth rate of carbon on the surface is such that the resultant surfaces are almost entirely composed of deposited carbon and the material then behaves like a bulk carbon material [2].

The XPS and AES systems have been used to investigate the surfaces resulting during 0.3% carbon impurity concentration plasma bombardment. The surface concentration of carbon on these samples is approximately 30%, gradually decreasing to about 10% after ion

beam etching into the surface 0.3 microns. The chemical bonding of this carbon is also much different under these exposure conditions. Figure 1 shows results from XPS analysis of this surface compared to a surface where the deposition rate of carbon from the plasma dominated. During high impurity fraction (0.8%) plasma exposure the resultant film is dominated by carbon-carbon bonds. As the impurity fraction in the plasma is reduced to 0.3%, a significant amount of the carbon in the surface exhibits carbidic bonding (Be_2C). In fact, as the surface is etched away the fraction of carbidic bonding increases.

This trend toward increased formation of Be_2C during plasma exposures with a slower carbon deposition rate is also shown in Figure 2. In the figure this is exhibited as a broadening of the signal toward lower energy as the impurity fraction is decreased. Interestingly, an XPS C1s signal from a sample exposed to a low carbon impurity fraction (≈0.3%) plasma at room temperature also exhibits significant carbide formation as is shown in the figure. Beryllium carbide has been measured to form at temperatures around 770 K during heating of carbon and beryllium samples [3–5] but clearly the carbide bonds are forming at much lower temperature during plasma bombardment. It is speculated that the damage induced in the implantation region due to plasma ion bombardment is allowing the deposited carbon atoms to form carbides at the surface even though the bulk of the material remains at room temperature. Similar formation of carbides at room temperature has been observed in ion beam devices [6].

III. W/C Surfaces

A similar carbidic interlayer has been observed in PISCES with the W/C system. To study the transition from the carbon layer to the tungsten substrate, a depth profile of Auger spectroscopy was taken and is shown in Figure 3. Four sets of XPS data were also taken to study the chemical state of the carbon. The results are depicted in Figure 4, showing the shifting of the binding energies of carbon at the surface (t = 0 min), a mixed layer (t = 22 min), and the interlayer (t = 120 min). The binding energy for the carbon peak (C 1s) in graphite is 284 eV. The shifting of the carbon peak to 283.3 eV in the interlayer seems almost completed at t = 120 min. Compared with the binding energy of the tungsten carbide standard, which shows a carbon peak at 282.6 eV, it is therefore believed that the interlayer contains other forms in the carbon-tungsten system. The AES profile in Figure 3 offers a clue to determine the composition and stochiometry of the interlayer, although not conclusive. At t =

0 min, the fraction of surface tungsten, as shown, is about 28%. Assuming that represents the percentage of area on tungsten which is free of carbon, then the composition of the interlayer can be determined at t = 120 min, which shows 70% tungsten and 22% carbon. Subtracting the initial 28%, the ratio of tungsten to carbon at t = 120 min is 1.9:1, which is very close to the 2:1 ratio for di-tungsten carbide (W_2C). After an additional 20 minutes of ion sputtering, the ratio only increases slightly to 2.2:1 at t = 140 min. The ratio continues to increase as the interlayer is gradually depleted by the ion sputtering process.

IV. B/C Surfaces

The final area of mixed-material surface characterization has been the observation of surface layers on tiles removed from the DIII-D tokamak [7]. After the mixed-material tile surfaces were produced by repeated boronization and operation of DIII-D, the samples were exposed to plasma bombardment in PISCES. Before the PISCES exposure the tiles had a carbon rich surface, presumably from carbon deposition during typical DIII-D shots (Figure 5). After exposure to PISCES plasma bombardment, without any impurity seeding of the plasma, the tiles are observed to have a boron rich surface. The ratio of boron to carbon on the final surface is consistent with a B_4C rich surface layer. One can, therefore, speculate that similar to the Be/C and W/C systems the carbon-carbon bonded surface was quickly removed by the plasma until a region rich in chemically bonded carbide was reached. The carbide rich layer would then inhibit subsequent erosion.

V. Summary

The data presented suggests the importance of the deposition conditions on the resultant mixed-material surfaces. When the carbon impurity deposition rate is high, the depositing material can completely cover and shield the substrate material from plasma bombardment. In this case the resultant plasma-facing surface may be expected to act like a bulk carbon material. In the region between the substrate and the coating layer, a region of chemically interacted material (i.e. carbide) has been observed to form. When the deposition rate is lower, a chemically altered mixed-material surface layer containing a large fraction of carbidic bonding is observed to form. The bonding nature of the surface can then play an important role in determining the plasma-material interaction behavior of the component [8].

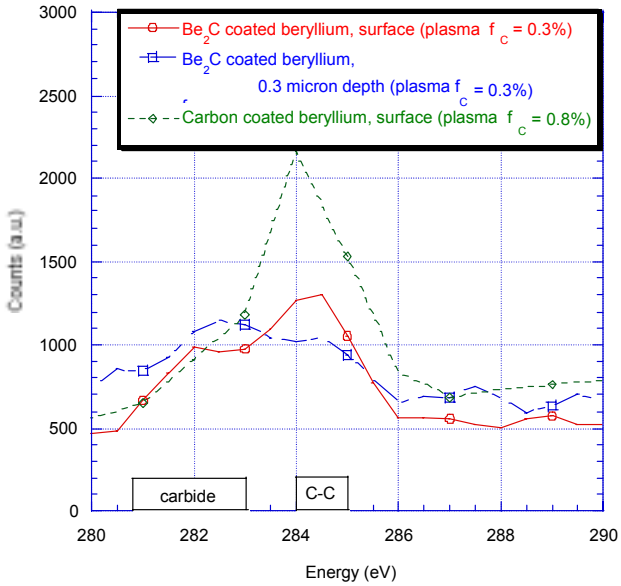

Figure 1 – XPS signals of the C1s line show that under high carbon impurity content plasma bombardment (f_c = 0.8%), the surface carbon exhibits predominantly carbon-carbon bonds. During lower impurity content plasma bombardment (f_c = 0.3%), significant carbide bonding becomes present on the surface and increases further down into the layer. Sample exposure temperature in each case was 770 K.

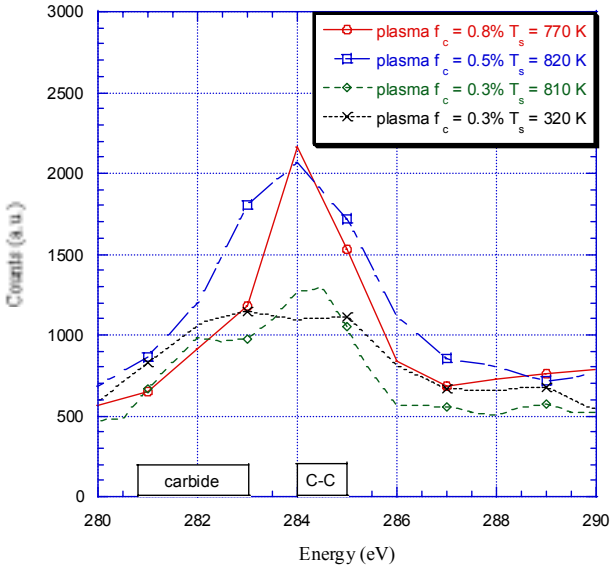

Figure 2 – The amount of carbidic bonding, as seen from an XPS C1s signal, increases as the carbon deposition rate during plasma bombardment decreases. During low carbon deposition rate conditions, even during room temperature exposure, significant carbide bonding is detected.

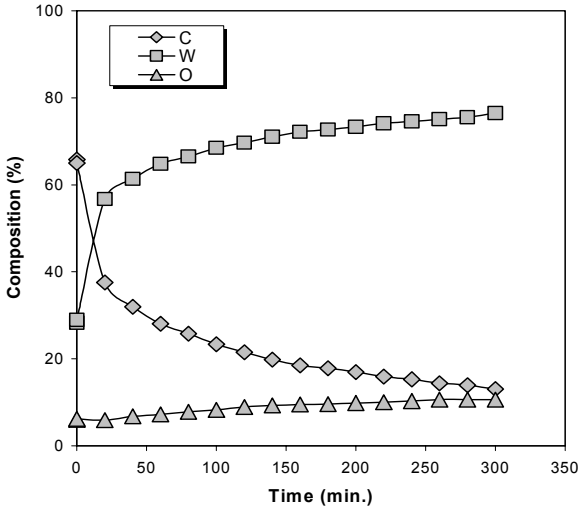

Figure 3 - AES depth profile of the carbon contaminated tungsten surface.

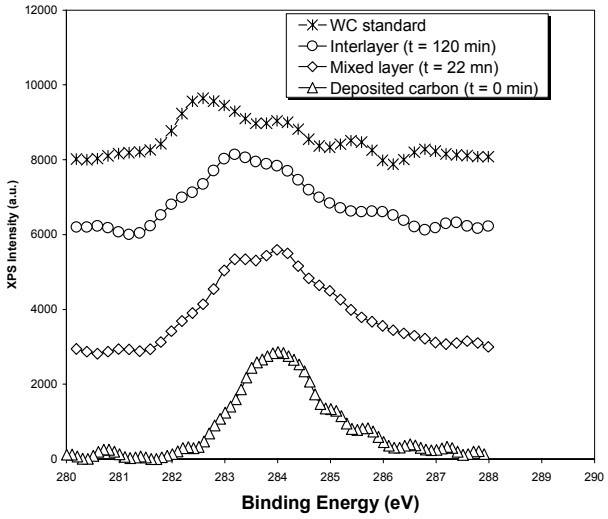

Figure 4 - XPS data showing the shifting of C1s peak in the W/C system. As the layer is etched away, the peak shifts toward lower energy indicating more of the carbon present is chemically bound up as a carbide.

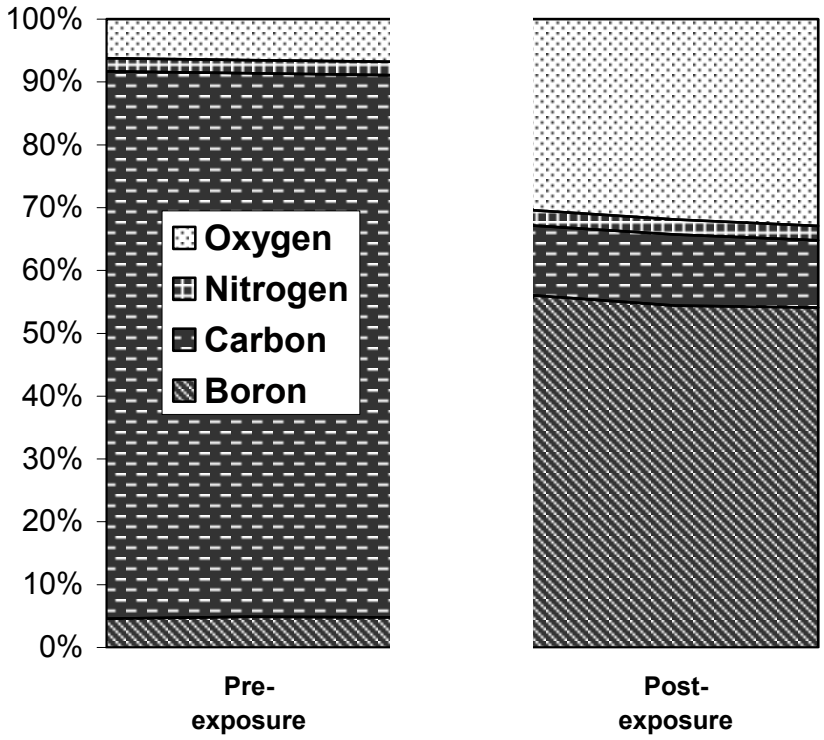

Figure 5 – Repeated boronization and operation of the DIII-D tokamak produced tile surfaces rich in carbon before exposure to PISCES plasma bombardment (pre-expsoure). The PISCES plasma expsoure easily removed this carbon rich surface layer until a surface with a composition consistent with B_4C rich layer was reached (post-exposure).

REFERENCES

[1] J. Won et al., J. Nucl. Mater. 241-243 (1997) 1110.
[2] R.P. Doerner et al., J. Nucl. Mater. 266-269 (1999) 392
[3] Roth, J., Wampler, W. R. and Jacob, W., J. Nucl. Mater. 250 (1997) 23.
[4] Anderl, R. A., Longhurst, G. R., Pawelko, R. J. and Oates, M. A., J. Fusion Energy 16 (1997) 95.
[5] Ashida, K. and Watanabe, K., Fus. Engr. And Design 37 (1997) 307.
[6] J. Roth, this journal.
[7] D.G. Whyte, W.P. West, R. Doerner, N.H. Brooks, R.C. Isler, G.L. Jackson, G. Porter, M.R.Wade, C.P.C. Wong, J. Nucl. Mater. 290-293 (2001) 356.
[8] R. Doerner, "Mixed-Material Erosion Processes in PISCES", this publication.

FORMATION AND CHARACTERIZATION OF CKC DOPED GRAPHITES

A.A. HAASZ, J.W. DAVIS

Abstract
In order to improve graphite's erosion resistance for fusion reactor application, doping with other elements has received extensive attention. Here we report on the fabrication, surface characterization and thermal properties of doped graphites produced by a Canadian company, Ceramics Kingston Ceramique Inc. (CKC). The dopants used include B, Si, Ti, Ni, and W. Surface and bulk dopant concentrations were measured by nuclear reaction analysis for B, and Rutherford backscattering for Si, Ti, Ni, and W. Concentrations ranged from ~2-30 at% in the bulk (>1μm)and from~1-15 at% in the near surface (<1μm). The thermal properties of the specimens were measured using the laser flash technique. In general, the dopants tend to reduce the thermal conductivity, when compared to the undoped 'CKC Reference' material.

1. Doped Graphites Made by CKC

Graphite is being planned for high heat flux areas in the divertor of next-step fusion devices, such as ITER, because of its excellent thermo-mechanical properties. However, graphite's major drawbacks are its erosion and hydrogen retention characteristics. In order to improve graphite's erosion resistance, doping with other elements has received extensive attention. We have studied the effect of doping on chemical erosion, radiation-enhanced sublimation (RES), and hydrogen retention using specially fabricated specimens provided by a Canadian company, Ceramics Kingston Ceramique Inc. (CKC). Our study has also included an assessment of the thermal behaviour of the doped materials. Here we shall provide results on surface composition analysis and thermal diffusivity/conductivity measurements. Erosion and H-retention results are presented elsewhere in this issue.

1.1. Surface and Bulk Analysis of CKC Doped Graphites

Two series of compression molded doped graphites were fabricated by CKC for the purpose of studying their suitability as fusion reactor first wall materials. In the first series of materials, single dopant specimen blocks were manufactured from finely ground pyrolytic graphite (10-45 μm) mixed with an organic binder. Dopants (B, Si, Ti, Ni, W) were added in particulates of pure metal or carbides. Specimen blocks were then prepared with a final heating stage at 2270K [1-3]. Specimens doped with Al were also produced, but after several months in air, this material just disintegrated, obviously unsuitable for reactor use. For the TiB_2-doped materials, the specimen blocks were fabricated from finely ground pyrolytic graphite (μm-size), mixed with μm-size TiB_2 powder and an organic binder [4]. Again, specimen blocks were prepared with final heating at ~ 2270K. For both series of materials, undoped reference specimens were made by the same method as the doped materials, but containing no dopants. A summary of the properties of the doped specimens and the various reference graphites studied is given in Table 1. Surface and bulk dopant concentrations were measured by nuclear reaction analysis for B, and Rutherford backscattering for Si, Ti, Ni, and W.

SEM photographs of the surfaces [2] revealed that the dopant particulates tended to clump together, such that the dopants were less finely distributed than the size of the dopant particulates would indicate. As shown in Table 1, dopant concentrations were found to be lower at cut surfaces than in the bulk, possibly indicating a lack of adhesion between the dopants and the graphite matrix. Heating and irradiation were found to enhance the dopant concentration at the surface [2].

1.2. Thermal Diffusivity and Conductivity of Doped Graphites

The thermal properties of graphites doped with B, Si, Ti, Ni, W and TiB_2 were measured using the laser flash technique. Thermal diffusivities and heat capacities were measured for temperatures between 300 and 1000K, allowing thermal conductivities to be calculated [1]. Comparisons were made with EK98 isotropic graphite.

All of the doped materials in the study showed similar trends for the thermal diffusivity and conductivity dependence on temperature. Representative thermal data for the TiB_2-doped material [4] are shown in Fig. 1. All of the specimens were found to be highly anisotropic vis a vis thermal diffusivity and conductivity. For the high thermal flow direction (see 'edge' in Fig. 1), all materials showed a general trend to lower thermal conductivity with increasing dopant concentration. For dopant concentrations of a few per cent, reductions in thermal conductivity were not generally significant. For the larger dopant concentrations, reductions of a factor of 1.5 - 4 were observed, leading to thermal conductivity values similar to, or lower than, EK98.

In the low thermal flow direction (see 'base' in Fig. 1), the thermal conductivities are a factor of 2 - 10 lower than in the high thermal flow ('edge') direction. When compared to EK98, the thermal conductivities were a factor of 2-4 lower. In general, the dopants tend to reduce the thermal conductivity, when compared to the undoped 'CKC Reference' case, to a larger extent at low temperatures. This leads to the thermal conductivity having reduced temperature dependence as compared to the undoped reference material.

REFERENCES

[1] B.N. Enweani, J.W. Davis, A.A. Haasz, "Thermal diffusivity/conductivity of doped graphites," J. Nucl. Mater. 224 (1995) 245-253.

[2] P. Franzen, A.A. Haasz, J.W. Davis, "Radiation-enhanced sublimation of doped graphites," J. Nucl. Mater. 226 (1995) 15-26.

[3] A.Y.K. Chen, A.A. Haasz, J.W. Davis, "Comparison of chemical erosion yields of doped graphites," J. Nucl. Mater. 227 (1995) 66-75.

[4] A.A. Haasz, J.W. Davis, "Thermal transport in CKC TiB_2-doped graphite," J. Nucl. Mater. 252 (1998) 150-155.

[5] E. P. Roth, R. D. Watson, M. Moss, and W. D. Drotning, "Thermophysical Properties of Advanced Carbon Materials for Tokamak Limiters", Sandia National Laboratories Report No. SAND88-2057, April 1989.

[6] M. W. Chase Jr., et al. JANAF Thermochemical Tables, 3rd ed., 1985. J. Phys. Chem. Ref. Data 14 (Suppl. 1) (1985).

Table 1. Summary of doped CKC specimen characteristics [2,4]. The calculated densities are computed by combining a graphite phase with the theoretical density of carbon (2260 kg/m^3) and a dopant phase. Specimen porosity is represented by $\Delta\rho \equiv (\rho_{calc} - \rho_m)/\rho_{calc}$. All depth profiles of the concentrations are nearly constant for depth > 1000 nm, except tungsten[b].

SPECIMEN DESIGNATION[a]	DOPANT CONCENTRATION		FORM / SIZE OF DOPANTS	DENSITIES / (kg/m^3)		POROSITY / (%)
	Bulk / (at. %) depth > ~ 1 μm	Surface / (at. %) depth < 1 μm for B depth < 0.1 μm for Si and Ti		Measured ρ_m	Calculated ρ_{calc}	
CKC-B2	2.0 ± 0.9	1.2 ± 0.6	Metal/few ❍m	2090	2261	8.9
-B10	9.4 ±1.6	7.9 ± 2.4	Metal/few ❍m	2000	2267	10.9
-B20	20.1 ± 3.6	13.8 ± 2.2	Metal/few ❍m	1970	2274	13.4
CKC-Si3	3.0 ± 0.5	0.7 ± 0.2	Metal/few ❍m	2060	2265	9.0
-Si8	7.5 ± 0.5	1.9 ± 0.4	Metal/few ❍m	1860	2271	17.7
-Si14	14 ± 0.5	3.8 ± 1.1	Metal/few ❍m	1760	2279	23.2
CKC-Ti2	2.0 ± 0.5	0.7 ± 0.2	TiC/ < ❍m	1940	2381	16.4
-Ti8	8.5 ± 0.5	3.2 ± 0.7	Metal/few ❍m	2300	2612	13.9
-Ti16	16 ± 0.5	5.0 ± 1.2	TiC/ < ❍m	2510	3194	20.8
CKC-W10	10[b]	0.9 ± 0.1[c]	Metal/few ❍m	4890	–	–
CKC-Ni10	7.5 ± 0.5[c]	3.0 ± 0.5[c]	Metal/few ❍m	2370	2867	17.3
CKC-Ti8/B17	8.3 at% Ti 15 at% B	1 at% Ti	TiB_2/ < μm	2261	2808	19.5
CKC-Ti13/B27	14.3 at% Ti 28 at% B	2-3 at% Ti	TiB_2/ < μm	2684	3204	16.2
CKC Reference (No dopants)	–	–	–	2060	2260	9.3
CKC Reference (for TiB_2 batch)[d]	--	--	--	2025	2260	10.4
Union Carbide HPG99 (As-deposited pyrolytic graphite)	–	–	–	2200	2260	2.7
Ringsdorf EK98 (Isotropic fine grain graphite)	–	–	–	1860	2260	20.4

[a] The number following the symbol of the dopant element represents the nominal bulk concentration in at.%.
[b] Nominal concentration of tungsten was estimated from the measured density and assuming the porosity of the CKC reference specimen.
[c] Ion-beam analysis performed by Dr. P. Franzen, IPP, Garching, Germany, using RBS (private communication).
[d] The reference material for the TiB2-doped graphites is slightly different from the original reference.

This table belongs to Chapter 1: UTIAS contribution on "Formation and Characterization of CKC Doped Graphites.." by Haasz et al.

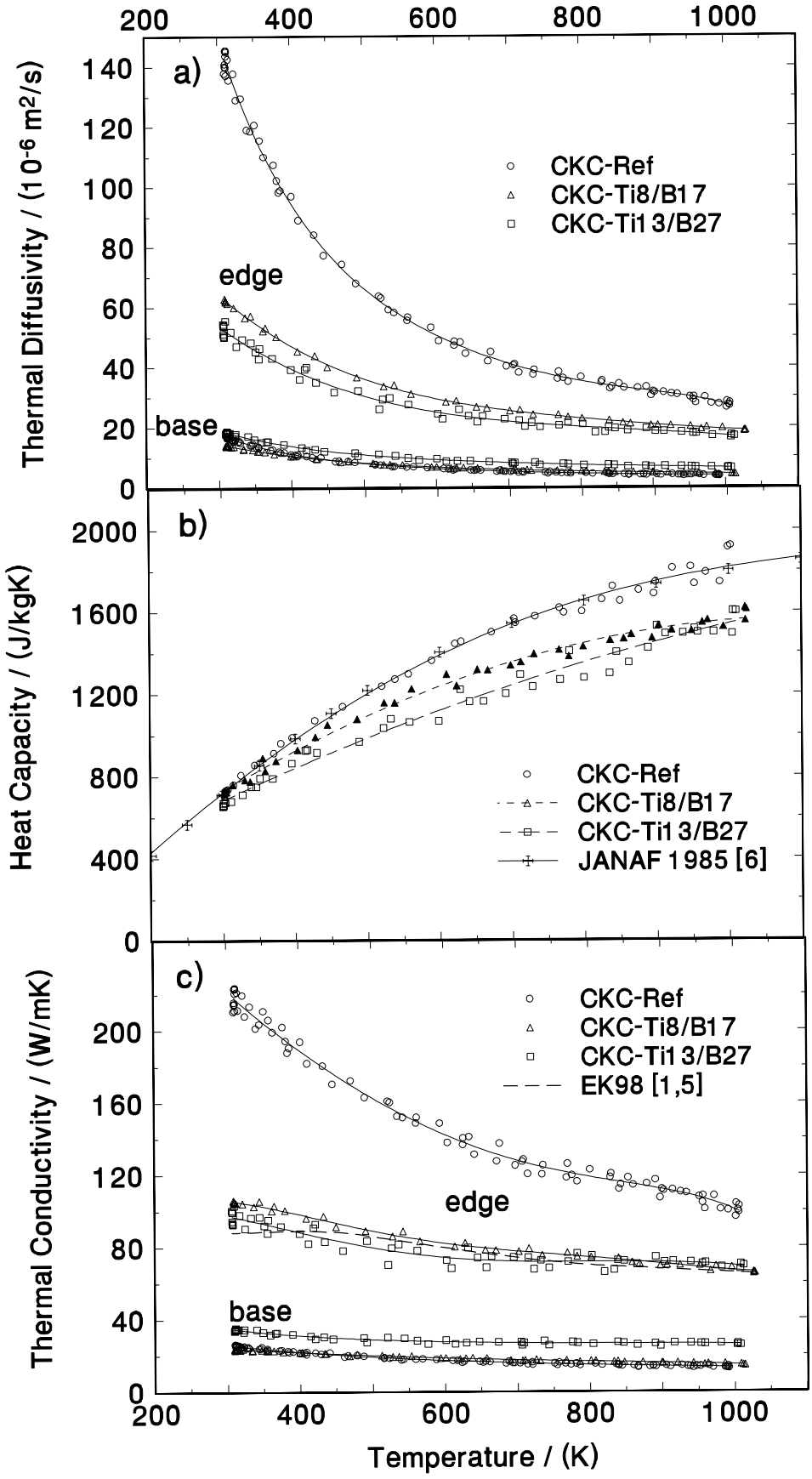

Fig. 1. Thermal properties of TiB2-doped CKC specimens [4]: (a) thermal diffusivity, (b) heat capacity and (c) thermal conductivity derived from the data in (a) and (b). Results for EK98 are from [1,5].

REACTIONS BETWEEN HYDROGEN-CONTAINING CARBON FILMS AND SUBSTRATE METALS AT ELEVATED TEMPERATURE

K. ASHIDA, K. WATANABE
Hydrogen Isotope Research Center,
Toyama University, Japan

Abstract. Changes in physicochemical properties of hydrogen-containing carbon films deposited on beryllium, molybdenum and tungsten were studied by means of infrared, Raman, x-ray photoelectron (XPS) and thermal desorption (TDS) spectroscopy as well as x-ray diffraction (XRD). Infrared and Raman spectroscopy showed that as-prepared hydrogen-containing films were composed of carbon atoms with sp^2 and sp^3 hybridized orbitals, where hydrogen was bound to carbon as -CH_3 and >CH_2. Vacuum heating of the carbon films caused two major thermal desorption peaks. One appeared at about 715 K, irrespective of substrate metals, and the other at higher temperatures, depending on the substrates; 873, 1050 and 1173 K for Be, Mo and W, respectively. The low temperature peak was composed of H_2, CO and hydrocarbons, whereas the high temperature peaks consisted essentially of H_2. The former was due to the reaction of the carbon films with adsorbed water, and evaporation of volatile fragments and/or thermal decomposition of the films. On account of the XPS and XRD observations, the latter was attributed to a solid-state reaction between the films and the substrates to form M_2C (M=Be,Mo,W). Good linear relations were found between the reactivity and material properties of the substrates, such as melting point, surface tension, etc. The over-all kinetics of the solid-state reaction could be explained by a nucleation-growth model.

1 Introduction

Low-Z materials such as beryllium, boron and carbon have been widely used in tokamaks to improve plasma confinement parameters by the reduction of radiation losses [1, 2]. Their high erosion rates through physical and chemical sputtering, evaporation, etc., however, are giving rise to a serious problem for their use as protective tiles on the inner wall of tokamaks. On the other hand, high-Z materials such as molybdenum and tungsten have attracted great attention to compensate for low-Z materials with their durability against high heat loading and particle fluence [3].

Installation of two or more plasma facing materials is common now in many tokamaks to control plasma surface interactions, but poses a new problem concerning fuel recycling and inventory, which relate to the physiochemical properties of co-existing layers consisting of low- and high-Z materials. An understanding of the properties of co-existing layers is indispensable for material selection in designing the next generation tokamaks.

In the present study, hydrogen-containing carbon films were prepared on metal substrates of Be, Mo and W to simulate changes in physiochemical properties of hydrogen-containing carbon depositing on the first wall and/or divertor of tokamaks. The properties of the co-existing layers and their changes with heat loading were studied by means of infrared, Raman, x-ray photoelectron (XPS), x-ray diffraction (XRD) and thermal desorption (TDS) spectroscopies.

2. Experimental

2.1 Sample preparation

Hydrogen-containing carbon films were prepared on beryllium, molybdenum and tungsten as well as silicon and quartz plates by inductive RF discharge [4]. Hereafter, they are denoted as C(H)/M (M=Be, Mo, W), C(H)/Si and C(H)/SiO_2, respectively, in the present paper. The samples C(H)/M were used for observing solid-state reactions between the hydrogen-containing carbon and substrates, C(H)/Si for infrared and Raman spectroscopy, and C(H)/SiO_2 for a referencing standard. The size of each plate was 10 × 10 × 0.5 mm. Methane and ethylene of pure grade were used as working gases for deposition of hydrogen-containing carbon films on these substrates. The gases were purchased from Sumitomo Seika and the purities of both gases were guaranteed as 99.99%. They were used without further purification. The devices for sample preparation and its procedures were the same as C(H)/Be and C(H)/Mo. They are described elsewhere [4, 5, 6].

2.2 Measurements

The change in the total pressure was measured during the discharge and the change in the gas composition was analyzed using the QMS by sampling a part of gas through a variable leak valve. The QMS had been calibrated for H_2, H_2O, CO, CO_2, CH_4 and C_2H_4 by using high purity gases except H_2O, which was supplied from a wet molecular sieve bed.

The characteristics of deposited carbon films were analyzed by FT-IR and Raman spectroscopies. Namely, the C(H)/Si samples were taken out from the preparation system to air and set into their respective sample holders. The spectra were measured at room temperature with 2 cm^{-1} resolution. Thermal desorption spectra were measured for both C(H)/M and C(H)/SiO_2 samples. They were taken out to air and set into a quartz sample tube of a high vacuum system installed with a pre-calibrated mass spectrometer. The sample was heated linearly with time at a rate of 9K/min up to 1273K by use of an electric furnace, where the temperature was measured with a thermocouple attached to the sample tube.

The solid-state reaction between the deposited carbon film and the substrate was measured by XPS through the change in surface composition with vacuum heating. C(H)/M samples taken out from the sample preparation system was set into the sample holder for XPS. The system could be evacuated down to 10^{-8} Pa. Then the sample was heated at a given temperature for 10 min and cooled down to room temperature for measurements. The sample could be heated ohmically up to 1273K, where the temperature was measured with a thermocouple attached to the tungsten substrate.

3 Results

3.1 Characterization of hydrogen-containing films

To determine the composition of hydrogen-containing films, the changes in total and partial pressures with time were measured by using a pressure gauge and the QMS. Figure 1 shows a typical example of the changes observed during the discharges in methane. In this case, the discharge yielded hydrogen and ethylene as the main gaseous products. The hydrogen pressure increased continuously with time, while ethylene pressure reached a maximum and

then decreased gradually. At the end of the discharge, the total pressure increased to 48 Pa, while the composition of the gas was 87% H_2, 8% CH_4 and 5% C_2H_4. In the case of ethylene discharge, hydrogen and acetylene were produced as the main gaseous products, but the acetylene formed a peak and disappeared at the end of the discharge, where the gas phase consisted of essentially hydrogen (95%) with a minor amount of ethylene (5%), and the total pressure was 25 Pa [7]. On account of these changes in the gas phase, the compositions of the carbon films prepared were evaluated as [H]/[C] = 1.7 and 1.4 for the methane and ethylene discharges, respectively.

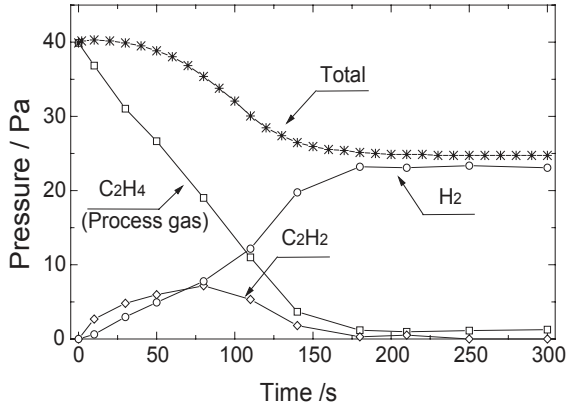

Fig. 1. Pressure changes during discharge of CH_4

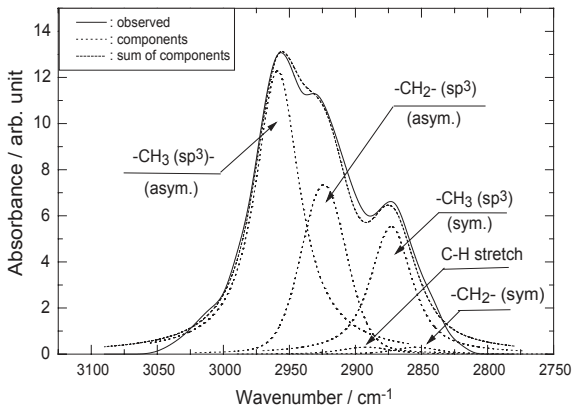

Fig. 2. FT-IR spectrum observed for C(H)/W prepared by methane discharge

Figure 2 shows a FT-IR spectrum in the frequency region of the C-H stretch bands [8], observed for the film prepared by the methane discharge. Essentially the same spectrum was

found for the film prepared by the ethylene discharge. The spectrum could be deconvoluted into three major components, which peaked at 2925, 2875 and 2960 cm^{-1}. They were assigned to symmetric -CH_3, asymmetric >CH_2 and asymmetric -CH_3 stretching vibrations, respectively. Similar band structures were observed for amorphous carbon films [9] and graphite irradiated by keV-energy hydrogen ions [10]. The Raman spectrum of the as-prepared film in a region of 1000 - 1700 cm^{-1} showed a similar structure to that of so-called amorphous carbon and mainly consisted of two components. One of them peaked at 1300 and the other at 1600 cm^{-1}. The former could be attributed to the C-C single bond and the latter to the C=C double bond. In addition, it should be mentioned that similar Raman spectra have been observed for graphite irradiated with hydrogen ions [11]. These observations showed that the C-C and C=C bonds make the principal structure of the as-prepared carbon films, which contain hydrogen amounting [H]/[C] =1.4 - 1.7 as -CH_3 and >CH_2.

3.2 Thermal desorption

Figure 3 shows an example of thermal desorption spectra, which was observed for the C(H)/W film prepared by the methane discharge, where only such species as H_2, CO and H_2O are plotted for simplicity. The relatively high background pressure of H_2O was due to the poor vacuum conditions of the system. The spectra showed two distinct peaks; a low temperature peak centered at about 723K and a high temperature peak at about 1173K. In the low temperature region, other species attributable to hydrocarbons such as CH_x, C_2H_x, and C_3H_x formed peaks of similar intensities as CO. On the other hand, the H_2 peak asserted its preeminence over CO in the high temperature region where no hydrocarbon peaks appeared at all. It should be mentioned that a desorption peak at the low temperature region was also observed for the C(H)/SiO_2 samples, whereas no high temperature H_2 peak appeared. Similar phenomena have also been observed for C(H)/Mo [6] and C(H)/Be [4], although the peak temperatures differ from each other. Small peaks of H_2 and CO observed at about 910K were ascribed to the tungsten substrate, because they also appeared from a tungsten plate but not from a quartz glass plate and the sample tube itself. These peaks were presumably due to reactions of surface contaminants of the tungsten plate (O and C) and water vapor in the system.

3.3 Change in surface and bulk compositions

The surface composition of the carbon films and the chemical state of surface elements were analyzed by XPS to observe their changes with heat loading. The samples were heated in vacuum at a given temperature for 10 min., and cooled down to room temperature for measurement. Similar procedures were repeated step by step up to 1273K. Figure 4 shows an example of the change in the surface composition, which was observed for a C(H)/W sample prepared by the methane discharge. It is seen that the surface composition was almost constant below 600K. Above 600K, the oxygen concentration started to decrease and disappeared at 873C. The carbon concentration began to decrease at 973K and reached 38% at 1273K. On the contrary, tungsten appeared only after the heating at 773K and then increased to 62% at 1273K. During this process, the C1s peak shifted to the lower binding energy side and the $W4f_{7/2}$ moved up with increasing temperature, and their energies agreed well with those identified as carbide.

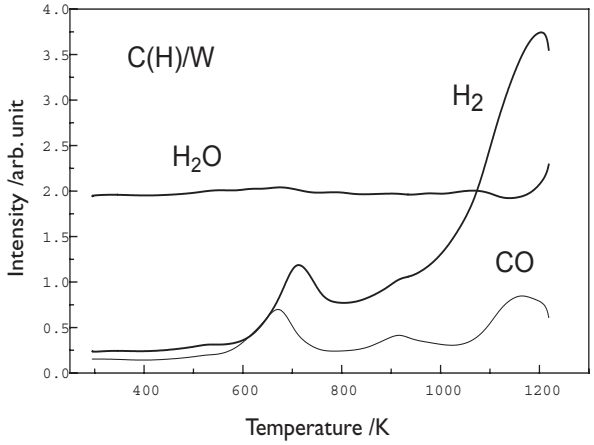

Fig. 3. Thermal desortion spectra of predominant species for a C(H)/W film

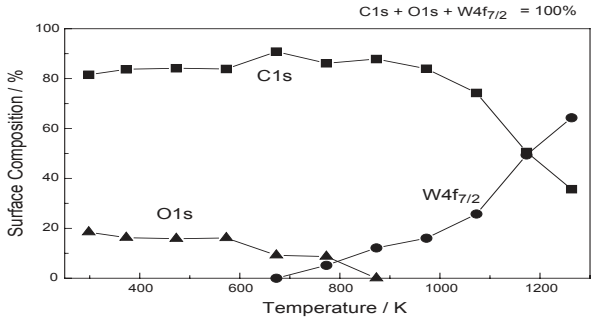

Fig. 4. Change in surface composition with vacuum heating of C(H)/W prepared by methane discharge

On the other hand, the O1s peaks identified as -OH and -CO types kept their peak positions till they disappeared from the surface. These observations indicate that a metallic carbide of W_2C is formed as a final reaction product in the case of C(H)/W. The formation of W_2C was also confirmed by XRD. Similarly, the final products were found to be Be_2C for C (H)/Be [5] and Mo_2C [6] for C(H)/Mo.

4 Discussion

4.1 Gas evolution mechanisms

Hydrogen ion-implanted graphite, which might show similar IR spectrum with the hydrogen-containing films as shown in Fig.2, gives hydrogen desorption peaks only above 923K [12]. Accordingly, the hydrogen evolution in the low temperature region shown in Fig.3 was ascribed to reactions between the film and water adsorbed as $H_2O(a)$ and/or OH(a). Namely, the hydrogen evolution in the low temperature region was described as

$$[-CH_n-]_m + x\,H_2O(a) \rightarrow x\,C(O) + (x + m'\ n'/2)H_2, \quad (1)$$

$$[-CH_n-]_m + x\,OH(a) \rightarrow x\,C(O) + ((x + m'\ n')/2)\,H_2, \quad (2)$$

$$(n = 0 \sim 3,\ m > m',\ n > n'),$$

$$C(O) \rightarrow CO(gas), \quad (3)$$

where [-CH_n-]$_m$ represents the as-deposited hydrogen-containing carbon film, $H_2O(a)$ and OH(a) an adsorbed water and a hydroxyl molecules, respectively, and C(O) a carbon site occupied by adsorbed oxygen. The adsorbed $H_2O(a)$ and OH(a) molecules appear to arise partly from the air exposure of the sample during the transfer from the preparation apparatus to the XPS system and partly from the presence of residual water vapor in the TDS system. The release of hydrocarbons appears simply due to evaporation of volatile fragments of the as-deposited carbon film or its thermal decomposition.

On the other hand, the hydrogen release in the high temperature region is due to the solid-state reaction of the carbon film with the substrate to form W_2C, which was identified by x-ray diffraction analysis. On the basis of these observations, it can be concluded that the solid-state reaction between them is described as [7]

$$[-CH_{n"}-]_{m"} + y\,W \rightarrow (y/2)\,W_2C + (m'"\ n'"/2)\,H_2, \quad (4)$$

$$n" = 0 \sim 3,\ m" > m'",\ n" > n'", \quad (5)$$

where $[-CH_{n"}-]_{m"}$ is the product of reactions which occur in the low temperature region. These reaction schemes are essentially the same as those proposed for the solid-state reaction of hydrogen-containing carbon on beryllium [5] and molybdenum [6]

4.2 Effect of substrate material

As mentioned above, C(H)/Be, C(H)/Mo and C(H)/W give the respective metallic carbides as Be_2C [4, 5], Mo_2C [6] and W_2C [7] by vacuum heating. The ease of carbide formation, however, differs considerably from each other.

For example, Table shows the difference in the hydrogen desorption peaks in the low and high temperature regions. It can be seen that the peak temperature in the high temperature

Table 1. Comparison of H_2 desorption peak temperatures in the low and high temperature regions

	Low Temp.(K)	High Temp. (K)
C(H)/W	723	1173
C(H)/Mo	703	1050
C(H)/Be	723	873
C(H)/SiO_2	713	None

region increases with increasing atomic number of the substrate material, whereas the one in the low temperature region is kept almost constant around 723K for each substrate.

Table 2. Comparison of characteristic temperatures defined by [H]/[M] ratios determined by XPS

	C(H)/W	C(H)/Mo	C(H)/Be
Halfway Temp. (K)	1173	1073	823
Compl. Temp. (K)	1273	1173	873

Table shows another example of the substrate dependence of the solid-state reaction observed by XPS, where one of the characteristic temperatures was defined as the temperature at which the ratio, [C]/[M], became equal, and the other was the temperature at which the ratio attained to [C]/[M] = 1/2, corresponding to the completion of carbide formation as M_2C, where M denotes Be, Mo or W. Hereafter, they are denoted as the halfway and the completion temperatures, respectively. Both of them increased with an increase in the atomic number of substrate materials.

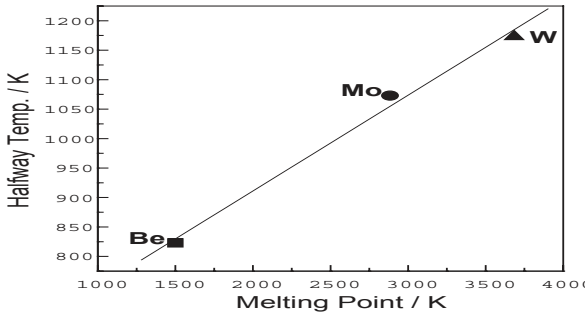

Fig. 5. Plots of the halfway temperature againt the melting points of substrate materials

The halfway temperatures are plotted in Fig.5 against the melting points of substrate materials. It resulted in a good straight line. A similar relation was found for the completion temperature. These characteristic temperatures also showed simple relations with surface tension and other physicochemical properties of the substrate metals. This figure indicates that the reaction between the hydrogen - containing carbon films and the substrate metals becomes progressively faster on the substrate having a lower melting point. In addition, it is worthwhile to mention that the solid-state reaction appears not to be due to a diffusion limited process, because the diffusion constants of carbon in molybdenum and tungsten are almost equivalent [13] and no appreciable difference between them should be expected for the characteristic temperatures and the hydrogen desorption peak temperature.

4.3 Reaction kinetics

The kinetics of the solid-state reaction between the deposited carbon films and the substrates was analyzed by a random nucleation and subsequent growth model [14, 15]. According to Hulbert, in the case of two dimensional crystal growth, the extent of reaction x at time t is described as

$$-\ln(1-x) = \pi h \int_{t'=0}^{t'=t} ID(t-t')\, dt', \tag{6}$$

where h is the thickness of the film, I the nucleation rate per unit volume and D the diffusion constant of reacting material. The extent of reaction is defined by the ratio of the volume of product crystallites to that of non-reacted reactant matrix, where the product crystallites are grown from product nuclei yielded at time t'. The nucleation can be assumed to obey the first order kinetics. Then, the number of nucleation sites remaining at time t is given by

$$N_t = N_0 \exp(-f\,t), \tag{7}$$

where N_0 is the initial number of nucleation sites per unit volume, f the nucleation frequency per site. Then, the nucleation rate per unit volume is

$$I = f\,N_t = fN_0 \exp(-f\,t) \tag{8}$$

Substituting Eq.(8) into Eq.(6) gives

$$\begin{aligned} -\ln(1-x) &= (\frac{\pi h N_0 f D}{2}) \exp(-f\,t)\, t^2 & (9)\\ &= k_{app} \exp(-f\,t)\, t^2 & (10)\\ k_{app} &= (\frac{\pi h N_0 f D}{2}) \end{aligned}$$

Isothermal reaction curves for C(H)/Be [5] were analyzed by Eq.(10) with a non-linear fitting method. Figure 6 compares the observed and calculated reaction curves for C(H)/Be at two different temperatures. The calculated curves were obtained by using the apparent rate constant k_{app} and the nucleation frequency f evaluated from the non-linear fitting, where D was estimated by taking account of the thickness of deposited carbon films ($h \approx 5 \times 10^{-5}$ cm) with an assumption of $N_0 = 10^{23}/cm^3$. The agreement between them is quite good. Namely, the

reaction kinetics is well explained by the nucleation-growth model. In addition, it is seen that the nucleation frequency, f, is very small and then the exponential term in Eq.(10) is essentially unity under the experimental conditions. Therefore, Eq.(10) can be approximated as

$$-\ln(1-x) = k_{app}\, t^2 \tag{11}$$

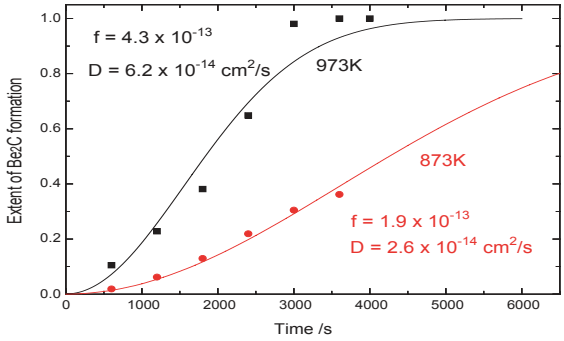

Fig. 6. Comparison of observed and calculated reaction curves for C(H)/Be

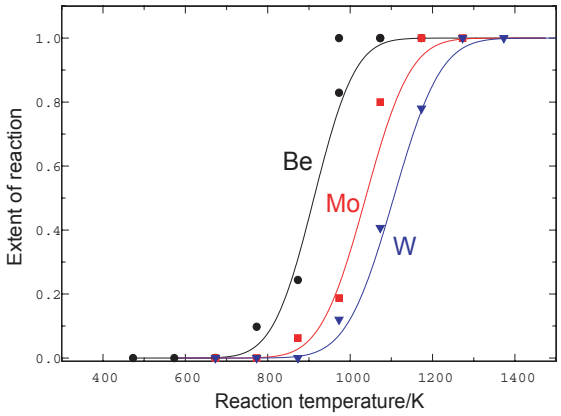

Fig. 7. Analysis of reaction curves for C(H)/M (M=Be,Mo,W)

This equation appears to be also valid for C(H)/Mo and C(H)/W. Accordingly, it can be applied for analysis of a reaction curve as shown in Fig.4, which was taken by heating a sample for a given period of time to higher prescribed temperatures step-by-step. Figure 7 shows the results of analyses of this kind of reaction curves observed for C(H)/M(M=Be,Mo,W) [4, 5, 6, 7], where the extent of reaction, x, is normalized to unity at the completion of reaction to form M_2C; the dots indicate experimental data and the lines are calculated reaction

curves by using the apparent rate constants determined from the analyses. The analyses by the nucleation-growth model reproduced fairly well the observed reaction curves, indicating that the hydrogen-containing carbon film reacts with the substrate metals through the same reaction mechanism and the difference in the reactivity can be ascribed to the differences in the nucleation frequency as well as carbon diffusivity for respective systems.

5 Conclusions

Changes in physicochemical properties of hydrogen-containing carbon films deposited on beryllium, molybdenum and tungsten with vacuum heating were studied by means of FT-IR, Raman, thermal desorption and x-ray photoelectron spectroscopies along with x-ray diffraction analysis. The conclusions obtained are summarized as follows:

1. The hydrogen-containing carbon films prepared by plasma CVD in methane and ethylene consisted of C-C and C=C bondings comprising sp^2 and sp^3 hybridized orbitals. Hydrogen was principally bound to carbon as $>CH_2$ and $-CH_3$. These characteristics were essentially the same for both of the carbon films prepared in methane and ethylene.

2. The vacuum heating of the deposited carbon films formed two major desorption peaks. One appeared about 715 K, being composed of H_2, CO and hydrocarbons, irrespective of substrate metals. The other was observed at higher temperatures, depending on the substrate metals as 873, 1050 and 1173 K for Be, Mo and W, respectively. The high temperature peaks essentially consisted of H_2. The low temperature peak could be ascribed to reactions of the carbon films with adsorbed hydroxyl and water molecules, and evaporation of volatile fragments of the carbon films and/or their thermal decomposition. On the other hand, the high temperature peaks were attributed to the reaction of the films with the substrate metals, which yielded H_2 and M_2C (M=Be, Mo, W) as reaction products.

3. A linear relation was found for the reactivity of carbon films with substrate metals. This relation strongly suggests that the solid-state reaction between them is not due to a diffusion limited process, but attributable to a random nucleation and subsequent growth mechanism.

4. The nucleation-growth model could explain well the reaction kinetics observed for all of the systems studied in the present work, C(H)/M (M=Be,Mo,W).

REFERENCES

[1] R. Behrisch, A. P. Martinelli, S. Grigull, R. Grotzschel, D. Hildebrandt, and W. Schneider, *J. Nucl. Mater.*, 220-222 (1995) 590

[2] A. Sagara, Y. Hasegawa, and et al., *J. Nucl. Mater.*, 241-243 (1997) 972

[3] V. Philipps and R. Nue, *J. Nucl. Mater.*, 241-243 (1997) 227

[4] K. Ashida, K. Watanabe, and T. Okabe, *J. Nucl. Mater.*, 241-243 (1997) 1060

[5] K. Ashida and K. Watanabe, *Fusion Engn. Design*, 37 (1997) 307

[6] K. Ashida, K. Watanabe, I. Kitamura, and S. Ikeno, *J. Nucl. Mater.*, 266-269 (1999) 434

[7] K. Ashida, , K. Fujino, T. Okabe, M. Matsuyama, and K. Watanabe, *J. Nucl. Mater.*, in press

[8] B. Dischler, *E-MRS Meeting, June 1989, Vol. XVII*, p. 189

[9] S. Chiu, S. Turgeon, B. Terreaul, and A. Sarkissian, *Thin Solid Films*, 359 (2000) 275

[10] Y. Gotoh and S. Kajiura, *J. Nucl. Mater.*, 266-269 (1999) 1051

[11] K. Ashida, K. Kanamori, M. Matsuyama, and K. Watanabe, *J. Nucl. Mater.*, 137 (1986) 288

[12] K. Ashida, K. Ichimura, M. Matsuyama, and K. Watanabe, *J. Nucl. Mater.*, 128-129 (1984) 792

[13] The Japan Institute Metals, *Metal Databook 2nd Ed.*, Muruzen, Tokyo, Japan, 1984.

[14] J. H. Sharp, G. W. Brindely, and B. N. Narahari Achar, *J. Am. Ceram. Soc.*, 49 (1966) 379

[15] S. F. Hulbert, *J. British Ceram. Soc.*, 6 (1969) 11

INVESTIGATION OF PLASMA INTERACTION WITH CARBON BASED AND MIXED MATERIALS RELATED TO NEXT-GENERATION FUSION DEVICES

M.I. GUSEVA, Yu.V. MARTYNENKO, S.N. KORSHUNOV

Institute of Nuclear Fusion, Russian Research Center "Kurchatov Institute",
Moscow, Russian Federation

Abstract

Carbon-carbon composites, tungsten and beryllium are considered at present as candidate-materials for International Thermonuclear Experimental Reactor (ITER). The presence of various materials, as the divertor and the first wall components, will unavoidably result in the formation of mixed layers on the surfaces of plasma facing components. In this review, processes of plasma interaction with these materials and layers formed by mixing of the materials are considered. Mixed W-Be and W-C layers were prepared by deposition of two species atoms upon a substrate under simultaneous sputtering of two targets by 20 keV Ar^+-ions. The thickness of the deposited mixed layers was 100–500 nm.

The most important processes investigated here are:

a) erosion at threshold energies and at various temperatures,
b) erosion at plasma disruption,
c) surface modification at normal operation regime and disruption,
d) the influence of the surface modification on material erosion,
e) erosion product formation at plasma disruption (dust creation),
f) hydrogen isotopes retention in materials.

An experimental method of determination of sputtering yield under ion bombardment in the near-threshold energy range has been developed. The method is based on the use of special regimes of field ion microscopic analysis. The method has been used for measurement of the sputtering yield of C-C composite, technically pure tungsten, tungsten oxide and mixed W-C layer on the tungsten by deuterium ions. The energy dependences of the sputtering yield of those materials by deuterium ions at energies ranging from 10 to 500 eV was investigated. Temperature dependences of pure and B-doped C-C composites erosion by deuterium ions were investigated. Material erosion was studied in a steady state plasma at the LENTA facility with parameters close to those expected at normal operation of ITER, and in the MKT plasma accelerator simulating plasma disruption. Surface modifications of graphite materials and tungsten under steady state and power pulsed plasma irradiation are described. Erosion products were investigated in the experiments on the plasma disruption simulation in two accelerators (MKT and MK-200) with different energy densities. The studies of energy flux density influence under the pulsed deuterium plasma effect on graphite, as well as those of simultaneous irradiation of two different targets (W and C-C composite) on the erosion product morphology, were realized. Deuterium retention in tungsten, graphite, as well as in W-C and W-Be mixed layers was investigated as a result of steady state plasma exposition and power pulsed plasma irradiation.

1. INTRODUCTION

According to the updated ITER scenario, graphite materials and tungsten will be used as materials for the divertor, while beryllium is the candidate for the first wall. Therefore these materials and their mixed layers are of particular interest. However there is insufficient data

on the erosion of these materials and on the deuterium - tritium inventory in the ITER operation regime.

In the last few years at the Kurchatov Institute investigations of C-C composite, tungsten and their mixed layers as well as Be-C and Be-W mixed layer erosion were performed. The deuterium retention was studied also. This work was supported under IAEA Contract No. 10098. The results of these investigations [1–5], are presented in this paper.

A second aspect of the current paper is the investigation of near threshold energy sputtering. The new method of sputtering yield determination, based on a special regimes of field ion microscopic analysis, was developed. The sputtering yields of W, C-C composite and W-C layer on tungsten by deuterium ions with energies 10–50 eV were measured.

The temperature dependence of carbon materials is of particular interest because of chemical sputtering and radiation enhanced sublimation, which take place at different temperatures and have different erosion rates under hydrogen isotope bombardment for various carbon materials. This dependence was studied for a C-C composite, which is one of the most perspective carbon materials. The B doped C-C composite was studied also, because B doping reduces chemical sputtering.

In spite of the fact that the plasma disruptions in tokamaks are violations of a normal current pulse production, the development of an instability causing the ejection of a practically whole plasma volume onto the wall has not been prevented yet. It is expected that about 1000 plasma disruptions could take place during the designed ITER service life. In this connection, the experiments on the study of a combined effect of stationary and high power pulsed plasmas simulating the ITER operation under normal operating conditions with plasma disruptions on the plasma facing materials are of interest. The erosion of the materials under disruption was simulated in the MKT plasma accelerator. The material erosion and surface modification under high power plasma pulses were investigated. Erosion products were studied also.

The erosion product at disruption is of interest because most of the material removed from graphite is dust with particle size from 0.01 μm up to 40 μm. The size and quantity of the dust particles are important from safety and environmental points of view. The surface modification at successive stationary deuterium plasma and high power pulsed plasma irradiation have shown an influence on the erosion rate. In the investigation it was observed and explained that joined C-C composite and W target increase graphite particle emissions as compared with a C-C composite target.

The surface modification under steady state plasma exposition and disruption affects the erosion rate and requires revision of some data. Therefore investigations of successive irradiation in steady state and power pulsed plasma in various sequences were performed.
The disruption after steady state plasma exposition was shown to strongly decrease the deuterium retention.

The deuterium retention in carbon coated tungsten and in mixed layers of W-C, W-Be was investigated.

The reviewed problems show that all the peculiarities of fusion device operation can influence and should be taken into account in data used for the device.

2. SPUTTERING BY DEUTERIUM IONS IN THE NEAR-THRESHOLD ENERGY RANGE

2.1. Experimental technique

The field ion microscope is based on processes taking place in electric fields with strength of 10^8–10^{10} V/m. The main element of the field ion microscope is a needle-like sample (cathode) and a fluorescent screen as the anode. One can realize the processes of evaporation and desorption in strong electric fields, along with autoionization. In such cases, the surface atoms are removed at any temperature. The phenomenon of desorption is similar, in principle, to that of evaporation by the field. The differences between the evaporating fields and the desorbing ones are related to a different nature of the bond among the particles removed from the surface.

Field ion microscopy analysis of samples has been completely optimized and standardized [4] for the study of tungsten and tungsten-based composite materials. The appearance of single vacancies on the surfaces of irradiated samples was registered, primarily, by the high-accuracy measurements of the variation in general brightness of the images (measurements of the value of desorption current were taken from a micro-channel plate placed in front of the fluorescent screen of the microscope), and only rarely by direct visual observation.

The experiments were performed in the field ion microscope [1]. For sample irradiation the technique of pulsed two-step reversal of high strength polarity was developed and applied. Ionization of the gas, serving simultaneously for an image-forming purpose, occurred by the mechanism of electron impact at the same time a short high-voltage pulse of reverse (negative) polarity was fed, and the generation of autoelectrons by the sample took place. The duration of such "ion-generating" high-voltage pulses did not exceed 0,1 μs, with an amplitude of 5 kV. Together with the high-voltage pulse, a low-voltage negative pulse was applied to the sample with pulse duration being ≥10 μs, while the amplitude corresponding to the preset energy of bombarding ions varied from 10 to 500 V with step size of 10 V. Concurrently various check analyses were conducted, which realized various sequences of pulses and their parameters.

Implementation of cleaning the surface from the adsorbed particles and films formed in the process of measuring the sputtering yield "in situ" allowed us to carry out measurements of sputtering from an atomic-pure surface.

The procedure of measuring the sputtering yield included the following operations:

a) manufacture of pointed samples and their installation in the field ion microscope capable of ensuring three duties of operation: as a proper field ion microscope, as a desorption ion microscope, and as a field-emission microscope;
b) evacuation of the microscope with subsequent deuterium filling; initially a vacuum of 3×10^{-9} Torr was reached, after deuterium filling the pressure was between 10^{-6} and 10^{-5} Torr;
c) preliminary field-ion and (or) desorption microscopic analysis of an initial surface (the stage I in the Figure 1), its cleaning by evaporation in the field in order to make the atomic clean and atomic smooth surface (magnitude of the evaporating field is 2.8 V/A);

d) ionization of the deuterium gas, which serve at the same time as an imaging gas, by an electron impact of field-electrons generated from the needle edge at an instant of high voltage short pulse of inverse polarity (the stage II in the Figure 1);

e) needle edge surface irradiation by D^+ - ions, providing the pulsed alternation of the voltage polarity at the sample; the energy of bombarding ions is controlled by a change in the amplitude and duration of a direct pulse (the stage III in Figure 1). Points 5 and 6 were repeated many times to receive sufficient dose;

f) repeated field-ion and (or) desorption microscopic analysis of the irradiated sample surface in order to identify single vacancies in it, i.e. direct count of the sputtered atoms (the stage IV in Figure 1);

g) evaluation of sputtering yields corresponding to the given energy of bombarding ions. For the same sample the operations (c)-(g) were repeated many times. The number of "irradiating" voltage pulses was varied from 10 to a few hundred in cases of low values of the sputtering yields.

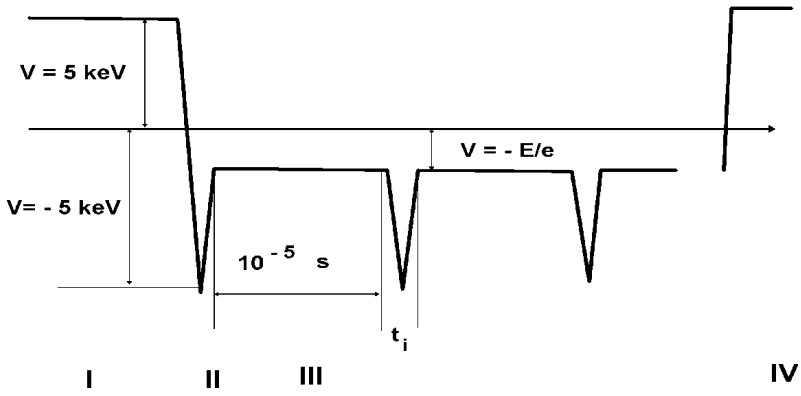

Figure 1. The scheme of the needle potential during sputtering measurement experiments in the field ion microscope: I – field ion image of the surface before sputtering; II – electron impact ionization, t_i; III – sputtering, $N = 14.4nJr\sigma t$; IV – field ion image of the surface after sputtering.

Field ion images were obtained by using deuterium as an image gas. During stage I when a high positive voltage was applied to the needle, deuterium molecules were polarized, attracted to the needle edge, dissociated and ionized and then accelerated to the fluorescence screen where an image was obtained. At stage II a high negative voltage was applied to the needle, which resulted in high field electron emission. Accelerated electrons ionized the deuterium atoms. The duration of high negative voltage pulses, t_i, is short enough to prevent ion acceleration during this stage.

The number of ions created during the ionizing pulse was calculated on the base of formula:

$$N = 14.4\cdot(J\cdot t_i/e)\cdot r\cdot\sigma(V), \qquad (1)$$

where $(J\cdot t_i/e)$ is the number of electrons emitted during the ionizing pulse, r is the radius of needle edge, $\sigma(V)$ is the ionization cross section at electron energy E = eV, and V is the needle voltage during the ionizing pulse.

At stage III sputtering of the needle edge by ions created during stage II was performed. Duration of stage III was chosen to be long enough to attract all of the created ions to the needle. The needle potential during stage III was $V = E_d/e$, where E_d is the energy of deuterium ions required for the investigation.

At stage IV an image of the needle edge after sputtering was received and the number of new vacancies was calculated. The sputtering yield was a ratio of the created vacancies to N·k, where k is the number of ionizing pulses. The needle during the experiment remained at room temperature.

The needlepoint samples of tungsten were produced by electrochemical etching in 1,5N solution of NaOH at 5–10 V D.C. Fibres of C-C composite UAM-95-3D were taken as needle samples for the sputtering yield measurements. The fibres were specially worked out to make a sharp needle edge with radius ≤ 100 nm as required by field ion microscopy.

To produce an oxide layer on the tungsten surface the samples were heated under atmosphere up to the temperature of ~750^0C. The films of a W-C mixture were produced by collection of the products of simultaneous tungsten and graphite sputtering by 20 keV Ar^+-ions on the needle-like and massive samples.

The thickness of oxidized and mixed layers, their roughness and a chemical composition were determined with the profilemeter made by Sloan Instruments and by the Auger electron spectroscopy (AES), in combination with the layer-after-layer etching from massive samples. Phase composition of the targets was investigated using X ray analysis of crystalline structure in the sliding beam geometry.

2.2. Results and discussion

In Table I the experimental results of sputtering threshold energies by deuterium and helium ions for pure W, mixed W-C layer and for tungsten oxide are compared with those of the published experimental and theoretical data [6,7].

TABLE I. THE MEASURED THRESHOLD ENERGIES FOR SPUTTERING COMPARED TO LITERATURE VALUES

No.	Material	Ion	T (K)	E_{th} (eV) experimental	E_{th} (eV) experimental [6–9]	E_{th} (eV) theoretical
1	W	D^+	293	160	175 [11]; 178 [7]	201 [7]; 160 [10]
2	W-C	D^+	78–293	150		
3	WC	D^+			171 [7]; 150 [11]	
4	Tungsten oxide	D^+	293	65	<18 [6]	

No significant differences are observed between the values of E_{th} for W and mixed W-C layers bombarded with D^+-ions. The results for W and W-C layers are in a good agreement with an earlier measurement of threshold energy for sputtering of W and WC by D^+-ions [8,9].

The threshold energy for sputtering of tungsten oxide by deuterium ions measured by field ion microscopy technique is 65 eV, in contrast to the $E_{th} \cong 18$ eV in [6], where tungsten oxide is produced during irradiation with D^+-ions under a background oxygen pressure of 8×10^{-5} Torr and the yield is measured by the weight loss method. A low E_{th} is obtained due to an assumed low surface binding energy ($E_B = 0.3$ eV) of the tungsten oxide molecules [6]. In our experiments on the surface of tungsten a stable oxide film, ~50 nm thick is produced. An estimate of the surface binding energy from [6] gives its value of ~1.1 eV.

The drastic increase of the sputtering threshold energy by D^+-ions for tungsten oxide layer observed by means of the new technique may also be attributed to the differences of the composition of the sputtered particles between these two methods. The new method identifies only W -vacancies, i.e. counts only the W sputtered atoms, and the weight loss method registers all sputtered surface atoms, including adsorbed atoms and molecules.

2.2.1. Sputtering yield of W, WO, W-C

The Auger electron analysis of the mixed W-C layer shows that in the layer, ~10^4 nm thick, W and C are distributed uniformly and the oxygen impurity on the surface does not exceed 9.5%. As a result of tungsten heating in air, the WO-layer thickness on tungsten is ~50 nm.

The energy dependences of sputtering yields for tungsten by deuterium ions are given in Figure 2 (curve 1).

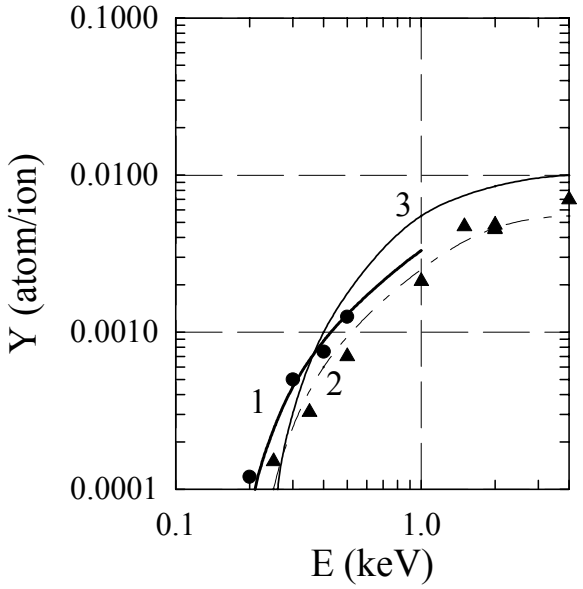

Figure 2. Energy dependence of the sputtering yield of tungsten bombarded with deuterium ions: (1) this work, experimental data (●) for W-D^+; (2) experimental data (▲) for W-D^+ [7]; (3) calculated data for W-D^+ [7].

In Figure 2 in addition to our experimental results, experimental (curve 2) and calculated (curve 3) energy dependences of sputtering yield for combination W-D^+ are presented. The sputtering yields of tungsten, measured by various techniques are rather close to each other, being in sufficiently good agreement with the theoretical curve. The energy dependences of the sputtering yields for the redeposited W-C layers and WC [7] also practically coincide (Figure 2). The energy dependence of the sputtering yield of tungsten

oxide by deuterium ions (curve 1) is given in Figure 3. For comparison, on the same graph, the experimental data by Roth et al. [6] for the tungsten sputtered by D^+-ions under oxygen pressure of 8×10^{-5} Torr (curve 2), as well as those for pure tungsten (curve 3), are given. In the energy range <100 eV, the sputtering yields for tungsten irradiated under high pressure of oxygen essentially exceed the corresponding sputtering yields measured by the field ion microscopy technique. At E > 350 eV the sputtering yield values for tungsten oxide measured by weight loss technique (curve 2) approach the sputtering yields for W (curve 3). This means that, when the sputtering yield rises up to 3×10^{-4} at./ion under experimental conditions [6], the oxide film on the tungsten surface has been sputtered by D^+-ions.

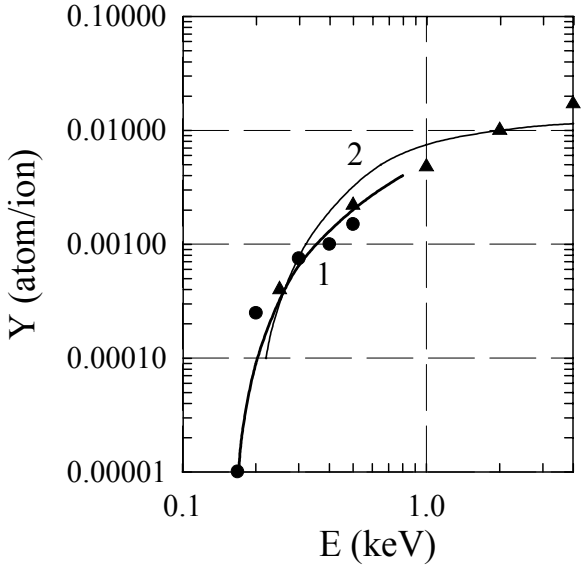

Figure 3. Energy dependence of the sputtering yield of mixed W-C layer on tungsten (1) and WC (2) [7,10] bombarded with deuterium ions: (●) - this work, experimental data for mixed W-C layer; (▲) - experimental data for WC [7,10].

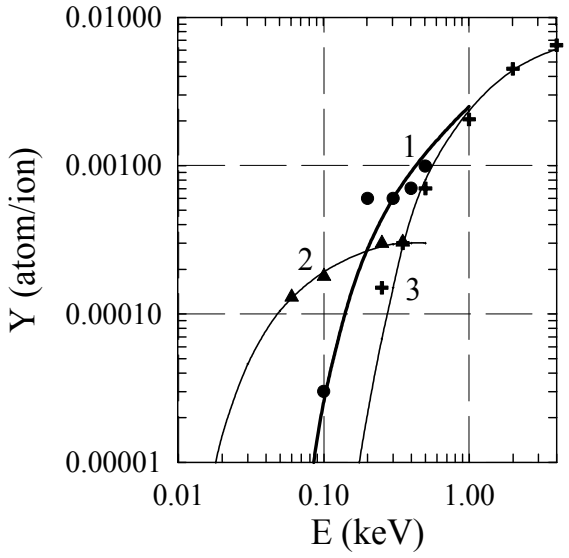

Figure 4. Energy dependence of the sputtering yield of tungsten oxide (curve 1), (curve 2) - from [1] and tungsten (curve 3) bombarded with deuterium ions:(●) - this work, experimental data for tungsten oxide;(+) - this work, experimental data for tungsten;(▲) - experimental data for W-D^+ under oxygen pressure of 8×10^{-5} Torr [1].

2.2.2.Sputtering yield of C-C composite

The experimental results are listed in Table II. The experimental errors are a statistical spread of the various measurement results.

TABLE II. MEASURED SPUTTERING YIELD DATA

D^+ ion energy	Experimental sputtering yield (atom/ion)	Sputtering yield (atom/ion) (data of [6] for pyrolytic graphite)
10 eV	$(5 \pm 3)\cdot 10^{-3}$	$7 \cdot 10^{-3}$
20 eV	$(5 \pm 3)\cdot 10^{-3}$	
50 eV	$(5 \pm 3)\cdot 10^{-3}$	
100 eV	$(6 \pm 3)\cdot 10^{-3}$	
200 eV	$(6 \pm 3)\cdot 10^{-3}$	$8 \cdot 10^{-3}$

The Table II shows: 1) rather high sputtering yield at low energies, 2) weak energy dependence of the sputtering yield in the investigated energy range. It should be noted that the theoretical threshold energy for graphite physical sputtering by D^+ ion is 24.3 eV [10].

Therefore we conclude that the chemical sputtering is the main erosion process at considered energy at room temperature. The chemical sputtering at energies as low as 10 eV indicates that hydrocarbides are formed at low energy deuterium ion bombardment on the surface.

Our data are a little lower (although the difference is within the statistical spread) than that of [6]. It can be explained by a more perfect crystalline structure of the carbon fibre than the structure of pyrolytic graphite, which has a higher number of free bounds and more easyily creates hydrocarbides. We can expect that the filling graphite in C-C composites is sputtered faster. Unfortunately our method does not allow measurement of filling graphite sputtering yield.

Thus, the main results of the sputtering investigation in the near threshold energies are:

1. The drastic increase of the sputtering threshold energy of W oxide bombarded with D^+-ions was observed. The sputtering threshold, E_{th}, measured by field ion microscopy technique is equal 65 eV.
2. The energy dependences of sputtering yield for pure W and for mixed W-C layer on tungsten bombarded with D^+-ions correspond to the earlier published data for W and WC.
3. No sputtering threshold of the C-C composite by deuterium ions was observed down to 10 eV.
4. The sputtering yield of the C-C composite by deuterium ions is weakly dependent on ion energy in the energy range 10–200 eV, being equal to $(5–6)\cdot 10^{-3}$ atom/ion.
5. The obtained results are interpreted as chemical sputtering. The hydrocarbides are formed at deuterium ion bombardment on the graphite surface.

3. TEMPERATURE DEPENDENCE OF PURE AND B-DOPED C-C COMPOSITES EROSION UNDER 3-KEV D^+ IONS BOMBARDMENT

The five-dimensional C-C composite, 5Dk, was taken for investigation. The doped C-C composite contains 0.5% atomic Boron. Irradiation was performed at the ion accelerator ILU-5 with mass separation. The deuterium ion energy was 3 keV and the current density was $1.2 \cdot 10^{16}$ ion/cm^2. Independent heating controlled the temperature of the target. The erosion rate was measured by weight loss method.

3.1. Results and discussion

The temperature dependence of sputtering yields for pure and B-doped C-C composite is shown in the Figure 5.

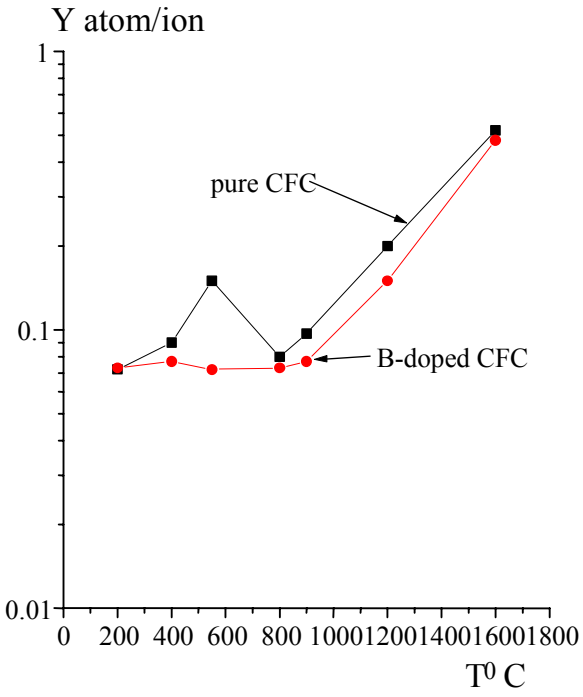

Figure 5. Sputtering yield temperature dependence of pure and B-doped C-C composite under the bombardment by D^+- ions.

The chemical sputtering of pure C-C composite has a maximum at the temperature interval 400^0–700^0 C, the maximal erosion yield in this region being 0.15 atom/ion. The radiation- enhanced sublimation is observed at temperatures higher than 900^0 C. The erosion rate increases with temperature increase in this region up to 0.52 atom/ion at 1600^0 C.

The chemical sputtering of B-doped C-C composite is ~ 2 times lower in its maximum as compared with pure composite, maximum of the chemical sputtering being shifted towards the lower temperature. The maximal erosion rate in the region of chemical sputtering is observed at 400^0 C and is equal 0.076 atom/ion. The beginning of radiation-enhanced sublimation is shifted towards the higher temperature as compare with pure C-C composite. The erosion rate increases with temperature increase in this region up to 0.48 atom/ion at 1600^0 C.

Thus, B-doped C-C composite has lower erosion yield under deuterium ion bombardment than pure C-C composite both at the temperature of chemical sputtering and at the temperature of radiation-enhanced sublimation.

The surfaces of C-C composite after sputtering at different temperatures are shown in Figure 6. The samples sputtered at 200 ^{0} C had smooth fibre surfaces. It showed a surface process of physical sputtering .The samples sputtered at 400^0 C and particular at 550^0 C had rather eroded surfaces. According to [13] the chemical sputtering mechanism follows. Implanted hydrogen atoms bind with displaced interstitial carbon atoms and form hydrocarbide molecules, which diffuse to the surface where their desorption occurs.

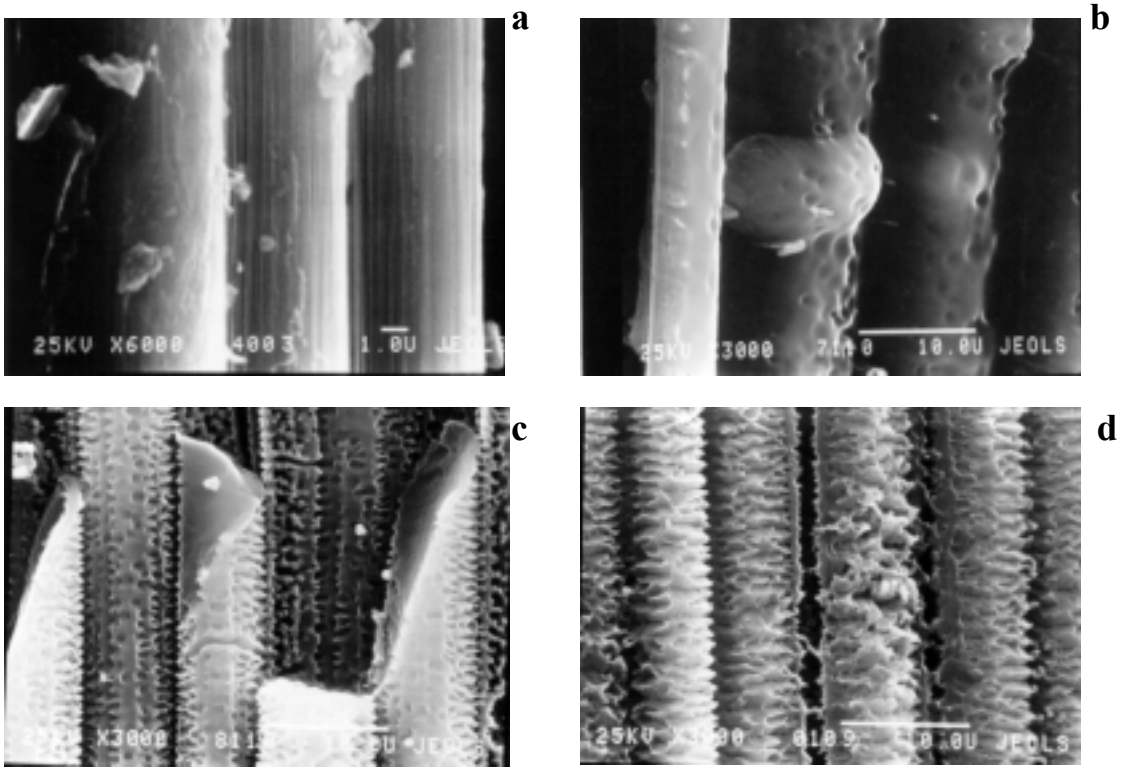

Figure 6. Surface structure of C-C composite: a – before sputtering, b – after the sputtering at 200^0 C, c – after the sputtering at 400^0 C, d – after the sputtering at 550^0 C.

We assume that besides diffusion, gas atoms of hydrocarbides can coalescence in bubbles. Interconnection of the bubbles results in channel formation, which entering to the surface, create such eroded surface topography. This topography is like a sponge structure observed at high temperature helium ion irradiation, when blistering is replaced with sponge like structure. In that case the sponge structure is formed by channels, which promote helium release. Thus we can assume that direct hydrocarbide atoms at chemical sputtering take place.

The main results of the investigation of C-C composite erosion are:

1. The pure C-C-composite erosion has all the known features of graphite erosion: physical sputtering, chemical sputtering and radiation enhanced sublimation.

2. Surface structure of C-C composite after irradiation at the temperature of chemical sputtering shows that hydrocarbides atoms release from the sample depth through channels.
3. The chemical sputtering of B-doped C-C composite is 2 times lower in its maximum as compare with pure composite, maximum of the chemical sputtering being shifted towards the lower temperature.
4. The beginning of radiation enhanced sublimation for the B-doped composite is shifted towards higher temperature as compared with pure composite.
5. B-doped C-C composite has lower erosion yield under deuterium ion bombardment than pure C-C composite both at the temperature of chemical sputtering and at the temperature of radiation enhanced sublimation.

4. MORPHOLOGICAL FEATURES OF EROSION PRODUCTS FOR GRAPHITE AND TUNGSTEN TARGETS EXPOSED BY POWERFUL PLASMA FLOWS

The experiments were done in the plasma accelerator MKT, at a deuterium plasma density of about 10^{15} cm^{-3} and at the maximal ion energy of 1–2 keV. The energy flux density was equal to 300 kJ/m^2, pulse duration was 60 μs long. After 10 pulses, the total energy flux density to the target was at the level of 3 MJ/m^2. For studying a plasma flux energy intensity effect on the erosion product morphology, some experiments were done in the MK-200 plasma accelerator at the energy flux density within the range 10–15 MJ/m^2 per pulse at the pulse duration equal to 50 μs. Similar to the experiments in the MKT-accelerator, the number of discharges was equal to 10. As a result the energy flux intensity was (2–3) x 10^5 MW/m^2, 30–50 times above the value in the experiments with the MKT-accelerator. Impurity-free graphite, MPG-8, was used in those experiments as a target, its morphological erosion product features under irradiation in the MKT-accelerator were studied previously in detail [2,14].

The samples of MPG-8 graphite, as well as tungsten and C-C composite, UAM-92-5-D trademark were used in the experiments.

The erosion, evaporation, and sublimation products were collected upon the plates of monocrystalline silicon and on the basalt filter located in a plasma flux shadow around the targets under exposure. In the MK-200 accelerator experiment the incident plasma interacted with a graphite lattice. In this case the conditions for the material erosion were, naturally, different from those which existed in the plasma interaction with a flat target. This scheme was chosen to protect the products of erosion and the collectors against the plasma flux effect. In a given case, some fraction of the produced graphite particles passes through the lattice orifices and gets out of the plasma. Due to this circuit-diagram we managed to collect the graphite pieces produced under high (10–15 MJ/m^2) fluxes.

For studying the erosion and sublimation products the techniques of transmission electron and scanning microscope, electron transmission diffraction, X ray spectral analysis were used.

Studying the filter, some layers, including 2–3 fibres laying with the particles deposited on them, were traced with both the scanning microscope and with the transmission electron one. One should note that the erosion product morphology study with the transmission microscopy has a great advantage over the scanning one, since it gives an opportunity to study their nature by the electron transmission diffraction.

4.1. Results

4.1.1. Energy flux density effect on the erosion products sizes.

Some typical microphotographs of one of the basalt filter parts and of the MPG-8 graphite pieces captured on it after 10 deuterium plasma pulses, at energy flux density 0.25 MJ/cm^2 per pulse in MKT accelerator, are given in Figure 7.

The particles and flakes of various shapes, from 0.01 μm to 40 μm in size, are registered on the filter. In Figure 8 the graphite erosion product size distribution is shown per unit size. The size distribution has two maxima in the range 0.01–0.03 μm and 2–4 μm. The "tail" of the distribution is expanded up to 40 μm, that unambiguously confirms the brittle destruction of graphite.

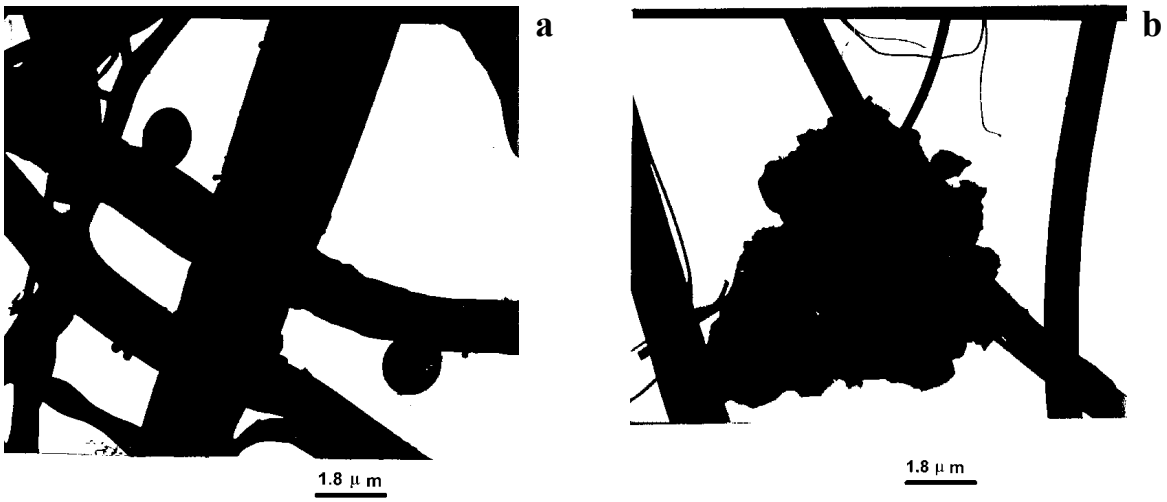

Figure 7. Microphotographs of a basalt filter with the erosion products of MPG-8 graphite after the irradiation by the pulsed plasma flux with the energy density 0.25 MJ/m^2 per pulse, t = 50μs, pulses number is 10, as flakes (a) and spheres (b).

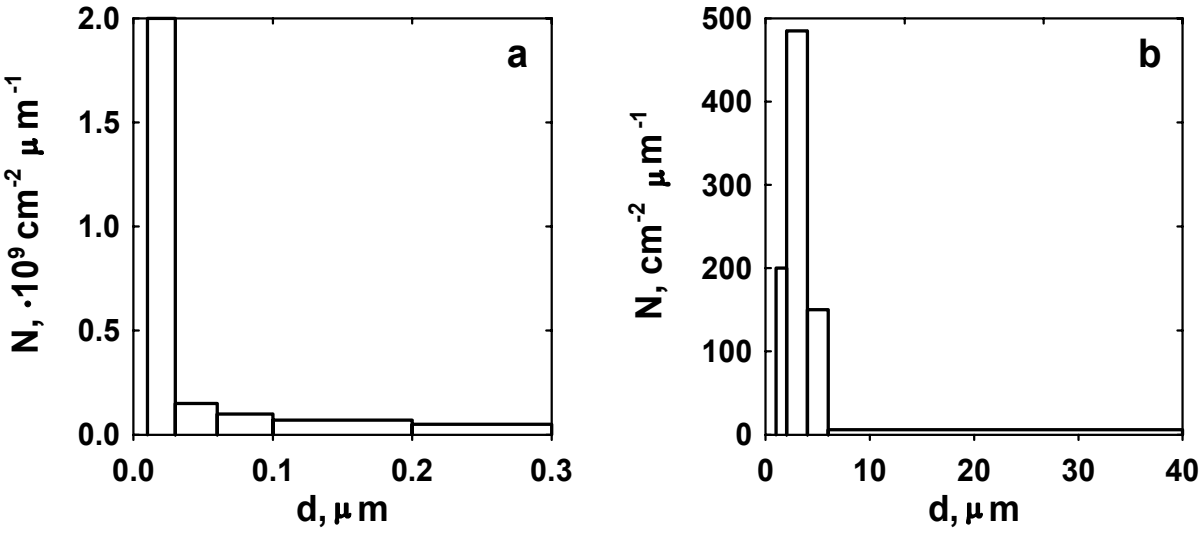

Figure 8. Erosion product size distribution of the MPG-8 graphite per a size unit in the ranges: 0.01 μm ≤ R_1 ≤ 0.3 μm (a) and 1μm ≤ R_2 ≤ 40 μm (b) after an effect of the deuterium plasma pulse with the energy density 0.25 MJ/m^2 per pulse, t= 50μs, in MKT accelerator.

Figure 9 illustrates the electron microscope microphotographs of MPG-8 graphite erosion products deposited upon different parts of the basalt filter after 10 deuterium high power plasma pulses in the MK-200 accelerator. The erosion products are characterized by various shapes and by an essential difference in size. We managed to fix both large pieces (up to 4 μm) and sub-micron ones (> 0.25 μm) on the basalt fibers. Along with the graphite flakes of an irregular shape (Figure 9a) some graphite pieces of an almost spherical geometry are seen (Figure 9b).

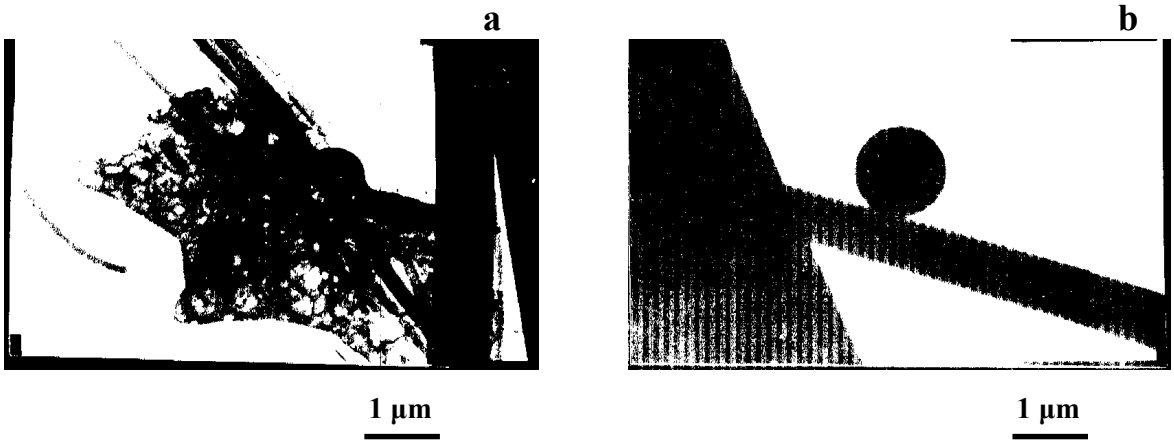

Figure 9. Electron-microscopic photographs of MPG-8 graphite erosion products after irradiation by the deuterium plasma in MK-200 (10–15 MJ/m^2 per pulse, t = 50μs,10 pulses).

Thus, in accordance with the results obtained in the MKT accelerator, confirming the presence of large flakes (up to 40 μm) and sub-micron particles (from 0.01 μm in size), in the experiment at MK-200 accelerator under an effect of the plasma fluxes of an essentially greater power, the micron (~ 4 μm) and sub-micron (>0.25 μm) particles were also registered.

4.1.2. Erosion products under simultaneous plasma effect on the W and C-C composite targets.

Studies of the samples with electron and scanning microscopes have allowed one to register the particles, < 0.1 μm up to 20 μm in size, upon the collectors after simultaneous irradiation of W and CFC. The basalt filter microphotograph with the captured laminated flakes, of uniform thickness, is shown in Figure 10a. According to the data of a transmission electron microscope, such flakes are about 1μm thick. On the photograph (Figure 10b) one can see, along with the places of laminated configuration, spherical drop phase particles, their diameters are in the range 0.1–1 μm.

The results of the spectral X ray analysis of round particles show that such particles are tungsten. The erosion products of irregular shape are pieces of graphite. Thus, elements W and C, belonging to both irradiated targets, were unambiguously registered among the erosion products.

The particle distribution in size for the case of simultaneous irradiation of W and CFC are represented in Figure 11.

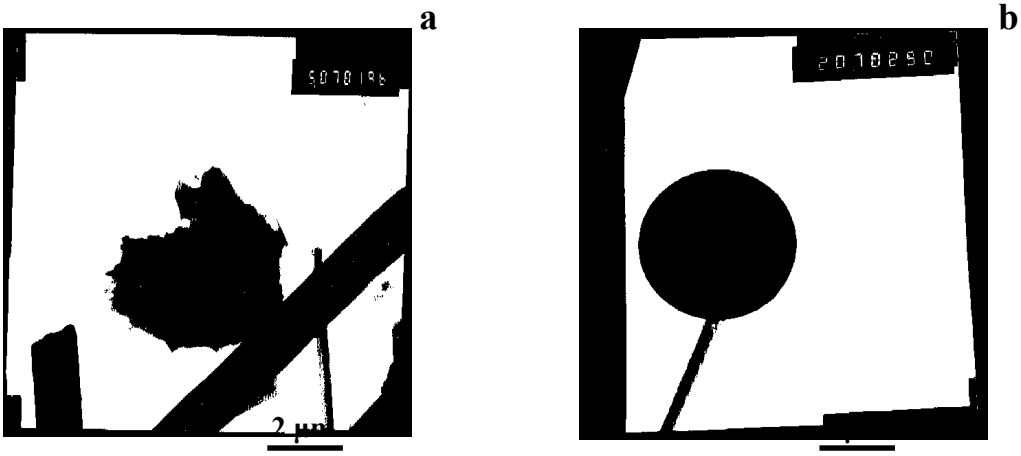

Figure 10. Microphotographs of W and CFC target erosion products collected on the basalt filter after simultaneous irradiation by the pulsed plasma flux (0.3 MJ/m^2 per pulse, t = 50 μs,10 pulses).

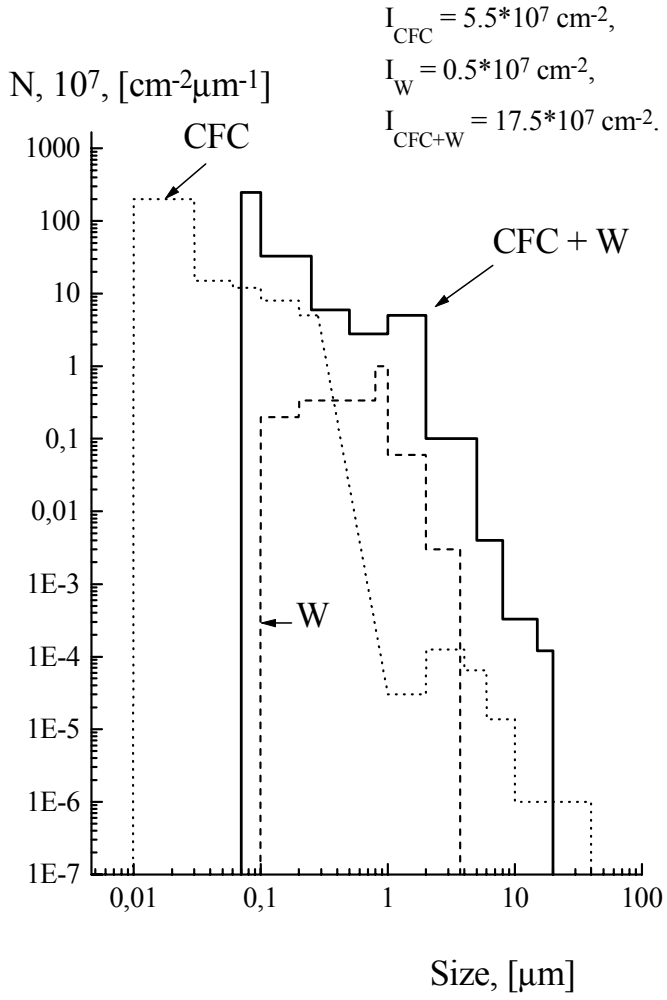

Figure 11. Erosion product size distribution after an effect of the pulsed plasma flux with the energy density 0.3 MJ/m^2 per pulse, t= 50μs, pulses number is 10 on the W+C-C composite target, on C-C composite target and that after the pulsed plasma flux with the energy density 0.45 MJ/m^2 per pulse, t= 50μs, pulses number is 20 on W target.

These distributions have the following features:

1. The number of particles is considerably higher than that for the target from C-C composite or W only. The total number of all size particles collected from 1 cm^2 of the collector is equal $5.5 \cdot 10^7 cm^{-2}$ (for C-C composite target), $17.5 \cdot 10^7$ cm^{-2} (for W+ C-C composite target) and $0.5 \cdot 10^7$ cm^{-2} (for W target).

2. The distribution is "narrower" than that for C-C composite target, i.e. the particles smaller than 0.07 μm and larger than >20 μm (which were see for C-C composite target) are absent.

One should note that in the case of the W target one maximum (in the range 0.2–0.8 μm) only is observed and the maximal size of drops does not exceed 4 μm. In the case of joint targets the range of erosion product size becomes narrower on both sub-micron and micron sizes. It is evident that a shift in erosion product size distribution occurs due to C-C composite particles and flakes, since the W-drops diameter range is within 0.2–4 μm.

Thus, the experiments confirm the fact that both the plasma energy flux and the composition of the shielding plasma affect the erosion product number and size.

4.2. Discussion of the results

Most of the experimental results can be explained if one takes into account the shielding plasma effect on the emitted particles. First of all one should consider effects of heating and cooling of the particles to determine the possibility of particles disappearing due to evaporation in the shielding plasma.

Let us estimate the energy balance on a particle in the shielding plasma. The energy flux, Q, coming to a particle surface consists of the kinetic and potential energies of ions, electrons and radiation.

The main cooling process is evaporation. The radiation of the particle can be neglected, since at the temperature of interest it is much smaller than the cooling due to evaporation.

For particles with size < 5 μm one can neglect the time of heat propagation through the particle.

The particle vapor shielding may be neglected also, since an average free path of ions and electrons is much longer than the particle size.

Hence it follows that the particle surface movement velocity, U_-, due to evaporation, can be found from the energy balance equation:

$$Q = U_- \cdot N \cdot H, \qquad U_- = Q/N \cdot H, \tag{1}$$

where N is the number of atoms per unit volume, U_-

Along with evaporation of the particle a redeposition of carbon atoms on the particle surface is also possible. Velocity of particle surface due to redeposition:

$$U_+ = \xi \cdot n_{pl} \cdot v_i / N, \tag{2}$$

where n_{pl} is the number of carbon ions (or atoms) in the shielding plasma per unit volume, v_i is the velocity of carbon ions (or atoms), N is the number of atoms per unit volume of the particle, ξ is the sticking coefficient of the carbon ions coming to the particle surface. The estimation shows that $U_+ \approx U_-$, although the uncertainty of the estimation is rather great. In any case, the presence of the flakes, ~ 1 μm thick, and the thickness being independent of irradiation condition, confirms the fact that the evaporated layer thickness is considerably lower than 1 μm.

At the same time, a possible mechanism of overheating instability can result in explosion of small particles. A particle in a plasma is charged to the potential $\varphi \approx T_e \cdot \ln(v_e/v_i) \approx 4.5 \cdot T_e$ (v_e is the electron velocity, T_e is the electron temperature in the shielding plasma), which equalizes the arrival of positive charges (brought by ions) and that of negative (brought by electrons). If a particle is heated to a temperature at which thermal electron emission starts (for small particles field electron emission in the field $E = \varphi/r$ is possible), each emitted electron is replaced by an electron from the plasma. Emitted electrons bring away from the particle the energy ~ w (w is the work function), whereas plasma electrons bring to the particle the energy ~ ·φ. At φ > w particle heating occurs. In this case the equation describing particle temperature rise is

$$(4\pi/3)\cdot r^3 \cdot 3N \cdot dT/dt = 4\pi \cdot r^2 \{Q - U_- \cdot N \cdot H + (\varphi - w) \cdot j(T)\} = \\ = 4\pi \cdot r^2 \{Q - N \cdot H \cdot c \cdot \exp(-H/T) + (\varphi - w) \cdot A \cdot T^2 \cdot \exp(-w/T)\} \qquad (3)$$

where A is the Richardson constant. The particle temperature is expressed in energetical units, hence at high temperature the heat capacity of the particle is 3 per atom. We take into account that if an evaporated surface is not in equilibrium with surrounding vapor

$$U_- = c \cdot \exp(-H/T), \qquad (4)$$

where c equals approximately the sound velocity. The sublimation energy, H, is higher than the work function, w, hence at T< w the heating caused by electron emission prevails over evaporation cooling. The solution of equation (3) gives the temperature of the particle as a function of time, t, divided by particles radius, r, (see Figure 12). For the calculation given in Figure 12 the following parameters are used: A =100 A/cm^2·K^2, w =4.7 eV, H =7.3 eV, Q =50 kW/cm^2, the initial temperature of the particle equals 0.3 eV. The curve 1 represents T(t/r) dependence for (φ-w) = 0. In this case the temperature reaches the value ~ 0.519 eV determined by equation (1). The curve 2 represents T(t/r) dependence for (φ-w) = 1 eV. The curve 3 represents T(t/r) dependence for (φ-w) = 0.3125 eV. The Figure 12 shows that characteristic time of micron-size particle heating is less than 100 μs.

One can see the very strong influence of the value (φ-w) on the T(t/r) dependence.

For small particles the electric field, $E = \varphi/r$, decreases the work function and promotes electron emission. The work function decrease is [15]

$$\delta w = e^{3/2} \cdot E^{1/2} = e^{3/2} \cdot (\varphi/r)^{1/2}, \qquad (5)$$

where e is the electron charge. For φ = 5 eV and r = 1 μm δw ≈ 0.1 eV. One can account for the electric field by replacing (φ-w) with (φ-w)·exp(δw/T).

Thus the small particles are overheated with much a higher rate and can reach a temperature at which a particle explosion occurs. Therefore in the particle size distribution, particles with a radius lower than a critical radius, r_{cr}, are absent, r_{cr} increasing with increase of electron temperature, T_e, of the shielding plasma.

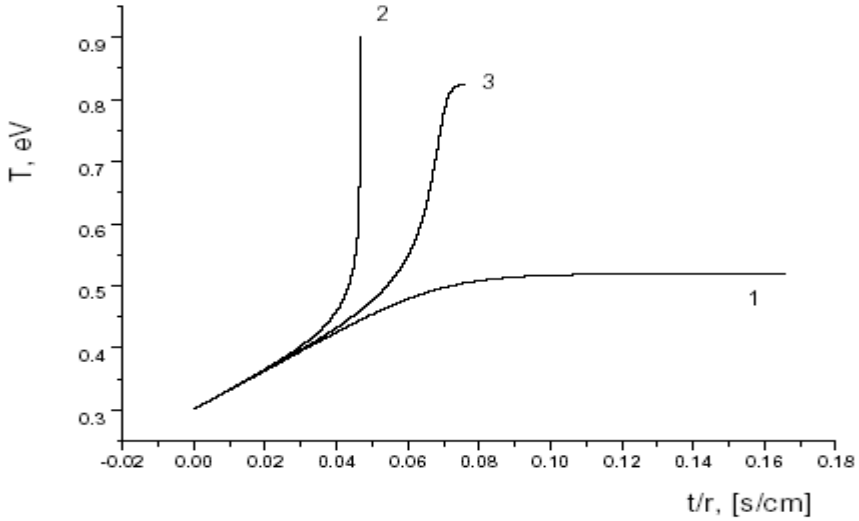

Figure 12. The temperature of a particles as a function of t/r. The curve 1 represents T(t/r) dependence for (φ-w) = 0. The curve 2 represents T(t/r) dependence for (φ-w) = 1 eV. The curve 3 represents T(t/r) dependence for (φ-w) = 0.3125 eV.

In the case of a combined target, including tungsten and graphite, the plasma has a higher radiation, higher T_e near the target surface and, as a result of that r_{cr} rises in comparison with a purely carbonic plasma, and a maximum in the sub-micron particle size distribution is shifted to the range of large sizes. Indeed, under C-C composite erosion, the maximum of particles in a sub-micron range is within 0.02–0.03 μm, meanwhile the particles of such size, under joint irradiation of W plus the C-C composite, were not detected.. One should note that an increase in the power incident on the target surface results also in a reduction of a maximal graphite flakes size. The mechanism of emerging such flakes is the following [15]. In a surface layer, as a result of heating, a compressive stress arises with the pressure $p = K\cdot\alpha\cdot\Delta T$ (K is the compression module, α is the thermal expansion factor, ΔT is the temperature difference between this layer and that located below. The stressed layer energy per surface unit is equal $W_p = h\ p^2\cdot(1-\nu)/E$, where ν - Poisson coefficient, E - elasticity module. When W_p exceeds the surface energy, W_s, separation of a part of this layer from layer located under it takes place. The zone of separation propagates with velocity

$$v = (2W_p/9.1\cdot\rho)^{1/2}\cdot(E/p)^{1/4}, \quad (6)$$

where ρ is the material density. The separated layer is bent to relax the stress, the propagation velocity of the bending equal to the transversal wave velocity in a film

$$c = k\sqrt{\frac{h^2 E}{3\rho(1-\nu^2)}},\ k = 2\pi/\lambda\ . \quad (7)$$

At first, when the separated part is small in size, λ, the velocity of the wave, c, is greater than velocity of separation, v. With an increase in λ, the velocity, c, reduces and, at the

propagation of the bending lags behind the zone of detachment, vibration of detached part of a film are excited.

$$\lambda \cong \lambda_1 \cong 2\pi h \sqrt{\frac{2E}{I(1-\nu^2)p}} \qquad (8)$$

These vibration results in the rupture of the film, when the energy of vibration, equal to about W_p, is sufficient for rupture along the perimeter of the separated film part, $W_p > W_s \cdot h/\lambda$. We assume that the relationship (8) determines the maximal flake size, λ_1. Hence, it follows that $\lambda_1 \propto T^{-1/2}$, and the maximal flake size is reduced with temperature rise. It was really observed at transition from C-C composite target to combined C-C composite + W target (higher radiation of shielding plasma with W ions), and at transition to higher pulse power in MK-200 facility. The particle acceleration in shielding plasma with a pressure gradient, ΔP, is equal:

$$dv/dt = \Delta P/\rho \qquad (9)$$

For an estimation, let us assume that $\Delta P \cong P/l$, where l is the shielding plasma width, and $P=n \cdot T_1$ (T_1 is the ion temperature in the plasma). Hence, one obtains the particle velocity by the end of the pulse ($\tau = 5 \times 10^{-5}$ s) $v \approx 10$ cm/ s. Thus, the particles are able to move from the surface during the pulse to distance, $v \cdot t \approx 5$ μm, only. It means that the electron temperature near the target surface determines particles surviving. For longer pulses, as it is expected under plasma disruptions, all other parameters being equal, the particles fly through the shielding plasma for the time, $t = 10^{-3}$ s, attain the velocity, $v \approx 10^3$ cm/s and move the distance ~ 0.5 μm. Increase in the power and duration of the pulse can also result in an increase in minimal particle size and in a reduction of the maximal size, and, at a rather high parameter of shielding plasma, in the complete disappearance of surviving graphite particles.

Thus, the main results of erosion products investigation for graphite, W, C-C composite are:

1. Micron and sub-micron size particles, balls and flakes were observed to be removed from graphite surface under both MKT and MK-200 plasma pulses.
2. Electron diffraction shows the graphite crystal structure of the particles.
3. Joined C-C composite and W target increases graphite particle emission as compared with C-C composite target.
4. Increase of deuterium plasma flow or shielding plasma radiation results in an increase in minimal collected particle size and in decrease maximal flake size.
5. Theoretical estimation shows that at high enough power density of deuterium plasma flux and at long pulse all the graphite particles can be exploded in shielding plasma.

5. SURFACE MODIFICATION AND EROSION OF CARBON BASED MATERIALS

For determining the service life of the first wall and that of a divertor, until recently some experiments were done to study erosion of the candidate materials under stationary plasma conditions or to imitate plasma disruption by the pulsed high power plasma fluxes.

For imitation of the expected ITER-operating conditions the samples of C-C composite were initially exposed to high doses in a stationary deuterium plasma, then irradiated by the pulsed high power D plasma and then again exposed in a stationary deuterium plasma.

The Russian composite C-C composite, UAM-92-5D, was taken for investigation. This C-C composite contains 0.15% by wieght Ti. Samples of RGT-type graphite were used in experiments.

The exposition in steady state deuterium plasma was performed in the LENTA facility with a beam plasma discharge at irradiation temperatures of 1000^0 C for C-C composite and 770^0 C or 1150^0 C for RGT-type graphite. The energy of deuterium ions was 200 eV. The current densities to the target were equal to $2.4 \cdot 10^{17}$ ion/cm^2 s and $5 \cdot 10^{17}$ ion/cm^2 s for C-C composite and RGT-type graphite, correspondingly. The doses of deuterium ions were $5 \cdot 10^{21}$ ion/cm^{-2} and $\cdot 10^{22}$ ion/cm^2, correspondingly. The erosion rate was measured by weight loss method. Several measurements were performed and the average yield was taken as a result.

Later the samples were irradiated in the MKT- plasma accelerator at the deuterium plasma density of about 10^{15} cm^{-3} and at the maximal ion energy of 1–2 keV. The energy flux density was equal to 0.25 MJ m^{-2}. The pulse duration was 60 μs, the number of pulses was equal to six.

5.1. C-C composite erosion and surface modification

Sputtering yield of C-C composite by 200 eV deuterium ions measured by weight loss after exposition in LENTA facility is 0.5 atom/ion. The temperature of C-C composite at exposition was in the range of radiation enhanced sublimation, therefore the measured sputtering yield is higher than that for physical sputtering, calculated to be 0.0144 atom/ion [7].

The SEM pictures of various parts C-C composite surface after exposition in steady state plasma are shown in the Figure 13 (a) and (b). One can see rough eroded surfaces in each case.

The Figures 14 (a) and (b) show pictures of various parts of theC-C composite surface after exposition in steady state plasma and followed irradiation in MKT plasma accelerator. Droplets and rather large melted pieces are seen on each part of the surface. Between the melted parts one can see the surface which was not melted. The melted parts can be identified as titanium carbide, which has a lower melting point than graphite. The thickness of the melted parts is not higher than ~ 1μm.

The Figures 15 (a) and (b) show the SEM pictures of various parts of theC-C composite surface after exposition in steady state plasma, then irradiation in MKT plasma accelerator and then again exposition in steady state plasma. The area of the melted surface decreases as compared to Figures 14 (a, b), but nevertheless some melted droplets are seen on the surface. The surface between the melted parts is like that after steady state plasma exposition.

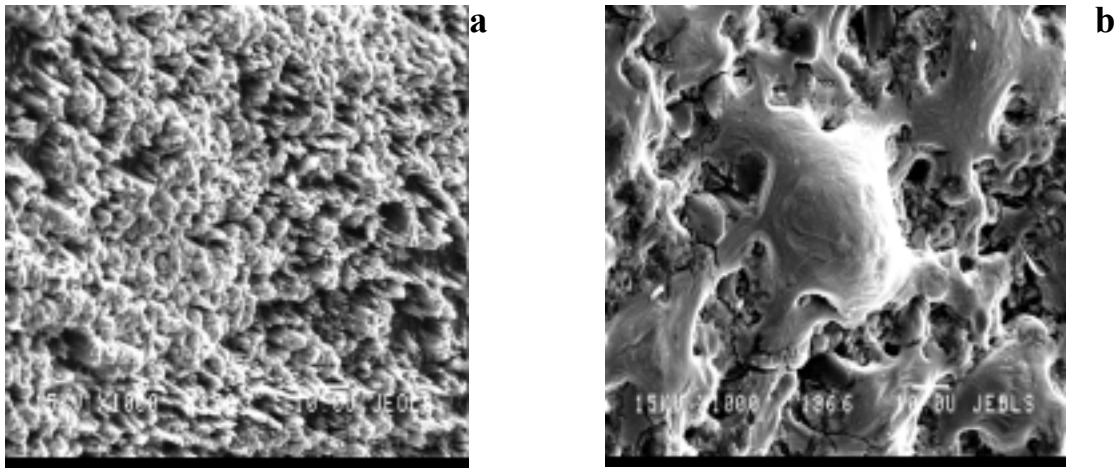

Figure 13. SEM photographs of the various parts C-C composite surface after irradiation by steady state (200 eV, $5 \cdot 10^{25}$ m^{-2}, 1000 C) deuterium plasma.

The calculated thickness of the sputtered layer at steady state plasma exposition is ~ 100 μm. It is much higher than the thickness of the layer modified by irradiation in the MKT plasma accelerator. Therefore the irradiation in the plasma accelerator does not influence sputtering in a steady state plasma. The melted droplets of titanium carbide have lower sputtering yield and part of them remain on the surface even after removing the much thicker layer of pure graphite. In ITER the dose at the graphite part of the divertor during one pulse will be even higher then in our experiment and the disruption will not affect sputtering during the normal regime operation.

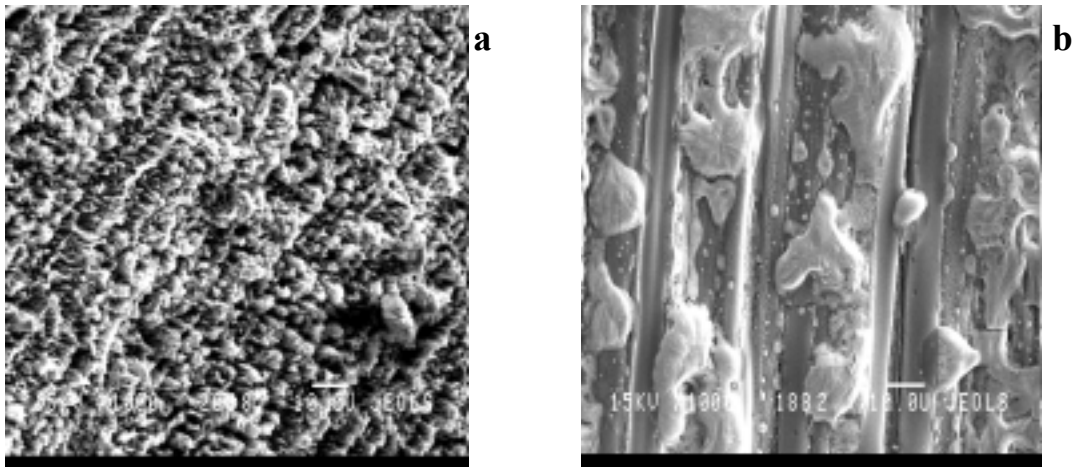

Figure 14. SEM photographs of the various parts C-C composite surface after irradiation by steady state (200 eV, $5 \cdot 10^{25}$ m^{-2}, 1000 C) plasma and followed irradiation by pulsed (0.25 MJ/m^2 per pulse, 60 μs, 6 pulses) deuterium plasma.

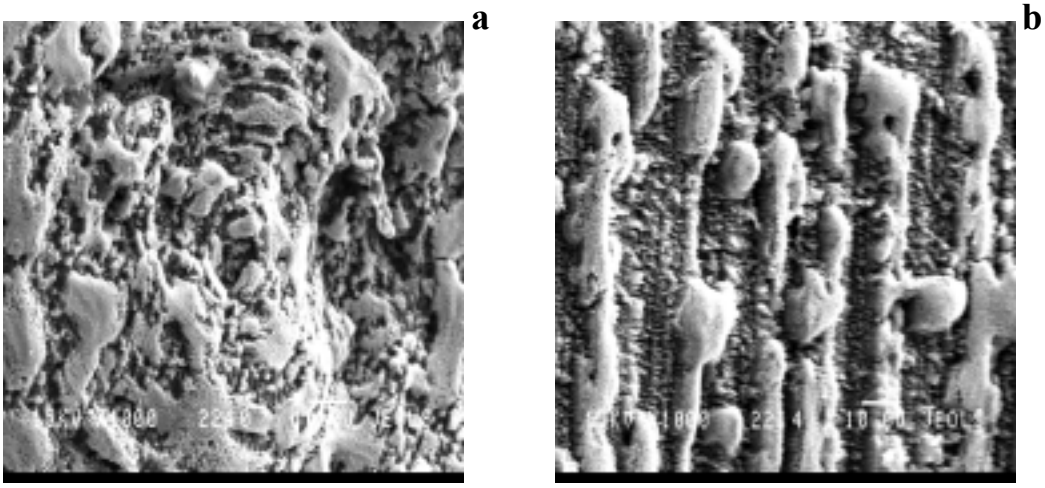

Figure 15. SEM photographs of the various parts C-C composite surface after irradiation by steady state (200 eV, $5 \cdot 10^{25}$ m^{-2}, 1000^0 C) plasma, followed irradiation by pulsed (0.25 MJ/m^2 per pulse, 60 μs, 6 pulses) deuterium plasma and then again irradiation by steady state (200 eV, $5 \cdot 10^{25}$ m^{-2}, 1000^0 C) plasma

Thus, main results of C-C composite investigation are:

1. The exposition of C-C composite in steady state plasma with parameters close to that in ITER divertor shows all the known features of graphite erosion: physical sputtering, chemical sputtering and radiation enhanced sublimation.
2. The sputtering yield of C-C composite by deuterium ions with the energy 200 eV at the temperature 1000^0 C is 0.5 atom/ion.
3. Disruption simulation in the MKT plasma accelerator results in erosion of about 0.1 μm layer and in the appearance of a melted layer on part of the C-C composite surface. The melted materials is identified as titanium carbide. The thickness of the melted layer is ~ 1μm.
4. The exposition of C-C composite in steady state plasma after plasma accelerator irradiation gives the same sputtering yield as before plasma accelerator irradiation if the sputtered layer exceeds the thickness of the layer modified by plasma accelerator irradiation.
5. Taking into account normal operation pulse duration of 400 s, one can expect sputtered layer thickness much higher than depth of the layer modified at disruption and hence neglect the influence of disruption on C-C composite sputtering during the normal operation.

5.2. RGT-type graphite erosion and surface modification

A relief characteristic for the growth of whiskers is developed upon the RGT graphite surface sputtered by extra high deuterium ion doses. Figure 16a illustrates a characteristic structure of the RGT graphite surface after its bombardment by 200 eV D^+- ions at 770^0C.

The condition for the emergence of whiskers is the presence of an impurity in the material under sputtering. In this case, it is related with different sputtering yields for graphite together with the particles of TiC present in it. The size of the produced whiskers is about 10 μm. Slits are seen between whiskers. The formation of such a developed structure upon the graphite surface is a result of interaction among the processes of sputtering, redeposition and surface diffusion. Relief of the surface is brush-like.

The subsequent effect of six high power deuterium plasma pulses results in an inessential change in the surface structure (Figure 17a). Upon the surface the configurations known as “balls with the legs” are produced. From the comparison of the surface structures, which have been developed under the influence of steady state (Figure 16a) and successive steady state and pulsed plasma (Figure 17a), we can conclude that the surface formed by deuterium ions with high dose sputtering is thermally stable. The developed structure is considerably different than that formed after irradiation only by the pulsed plasma flux [2].

Figure 16b illustrates the surface structures of the graphite sample irradiated by deuterium steady state plasma at the temperature 1150^0 C. The surface microstructure differs from that which is being formed upon the surface of the same graphite exposed in the LENTA deuterium plasma at the temperature of 770^0 C, all other conditions being equal. Such an effect is provided by different erosion processes at different temperatures of the target: physical sputtering takes place at 770^0C and the radiation-enhanced sublimation of graphite takes place at 1150^0 C. As a result of an effect by high deuterium ion fluence on the graphite surface, the periodic structure with a honey-comb morphology of a terrace-type was produced. These terrace-type structures are being developed across the whole surface of the grain. The size of terraces varied in the range from 0.5 to 2.5 μm .

Along with the formation of a recurring structure, somewhere on the surface one can see separate pieces of a “husk” which are probably produced as a result of the sublimed graphite back-diffusion and of its condensation upon the target.

After the joint effect of steady state and pulsed plasmas the surface topography is essentially changed (Figure 17b). The periodic relief produced after an effect of the steady state plasma is destroyed. One can see the traces of chipping and brittle destruction.

Thus, the graphite erosion during disruption is determined by the temperature of preliminary steady state plasma irradiation. At the temperature when the physical sputtering takes place the brush-like structure is developed on the surface. This structure is stable under thermal shock. At the temperature T > 1000 C when the radiation enhanced sublimation takes place the periodic terrace-type structure with lentil-like grains appears after steady state plasma exposure. Most of the lentil-like grains are weakly bounded one with another and can be easily removed under disruption.

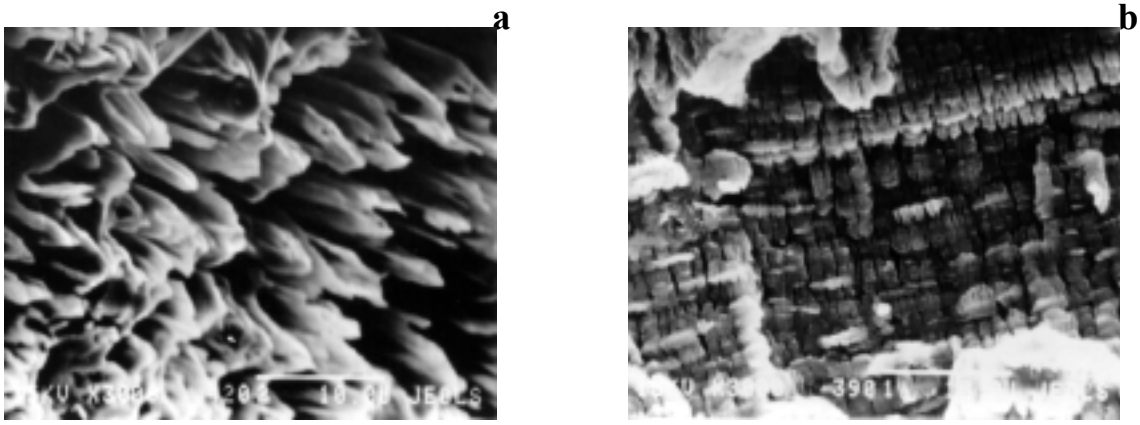

Figure 16. SEM photographs of the RGT graphite surface after irradiation by steady state (200 eV, 10^{26} m^{-2}) deuterium plasma at 770^0C (a) and 1150^0C (b).

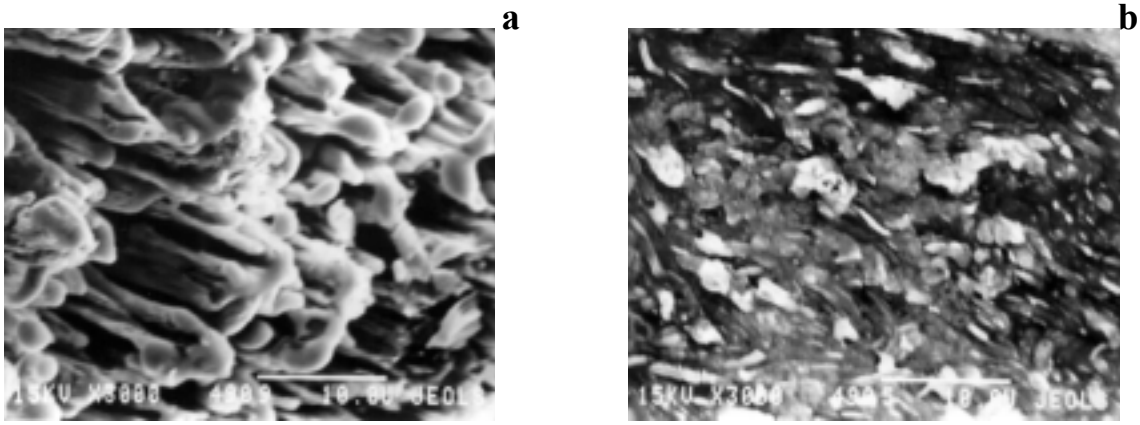

Figure 17. SEM photographs of the RGT graphite surface: (a) - after irradiation by steady state (200 eV, 10^{26} m^{-2}, 770^0C) + pulsed (0.25 MJ/m^2 per pulse, 60 μs, 6 pulses) deuterium plasmas; (b) - after irradiation by steady state (200 eV, 10^{26} m^{-2}, 1150^0C) + pulsed (0.25 MJ/m^2 per pulse, 60 μs, 6 pulses) deuterium plasmas.

6. DEUTERIUM BEHAVIOUR IN TUNGSTEN AND GRAPHITE AT COMBINED STEADY-STATE AND POWER PULSED PLASMA FLOW ACTION

Samples of tungsten and those of RGT graphite, including 7 weight percents of titanium, were used in the experiments. The mixed W-C layers were produced in the ILU accelerator [4] by simultaneous sputtering of tungsten and that of the impurity-free MPG-8 graphite with Ar^+-ions having the energy of 20 keV. A beryllium collector 15 mm in diameter was placed at a distance of 25 mm from the tungsten and graphite targets set at the angle of 60^0 to the ion beam. The temperature in the process of irradiation was sustained at the level of 600 K.

The tungsten and RGT graphite samples were exposed in steady state deuterium plasma of the facility with the plasma beam discharge up to a fluence of 10^{26} m^{-2} corresponding to one pulse of a current in ITER. The current density to the target was equal to $5 \cdot 10^{21}$ m^{-2} s^{-1}, the deuterium ion energy was ~ 200 eV. The temperature in the process of tungsten irradiation was sustained at the level of 550^0 C , two characteristic temperatures, 770^0 C and 1150^0 C, were chosen for sustaining different processes of graphite erosion and hydrogen diffusion into it, respectively. A part of the samples irradiated in the steady state plasma served for realizing the studies. Other samples underwent an additional irradiation in the electrodynamic plasma MKT-accelerator at deuterium plasma concentration of 10^{21} m^{-3} and at the maximal ion energy of (1–2) keV. The pulse duration was equal to 60 μs, the number of pulses was varied from 6 to 10. The energy flux densities to the targets were 0.25 MJ/m^2 per pulse, 0.5 MJ/m^2 per pulse and 0.9 MJ/m^2 per pulse. In the experiments with the mixed W-C layers deposited on beryllium the energy flux density was reduced to 0.2 MJ/m^2 per pulse and the number of pulses did not exceed two, since the film was completely removed with their increase.

The deposited layer thicknesses were determined with a Sloan Instruments Dektax profilometer. The experiments with tungsten targets were also performed in the opposite order: pulsed-steady state plasma.

After each treatment by plasma fluxes the studies of target surface microstructure with the JEOL scanning microscope and chemical surface composition by the Rutherford back scattering technique in the Van-de-Graaf accelerator were done. The back-scattered He^+-ions- at an angle of 170^0-with the energy of 1.2 MeV were registered with a surface-barrier detector.

For determining the distribution profiles in the irradiated targets the elastic recoil detection analysis technique was used. The He^+-ion beam with the energy 2.2 MeV was incident on the sample under study at an angle of 15^0 to its surface, the recoil atoms were registered at an angle of 30^0 to the initial He^+-ion incidence direction. The energy spectra measurements with standard calibration samples were done to produce the absolute values of deuterium atom concentrations.

6.1. Experimental results

6.1.1. Deuterium retention in tungsten

Some profiles of the deuterium distribution in the tungsten exposed under steady state plasma (curve 1) and those after additional irradiation of the same sample by the pulsed plasma flux (curve 2) are given in Figure 18. At the irradiation temperature of 550^0 C and at the irradiation duration of 6 hours the distribution profile, given in Figure 18 (curve 1), is determined by the deuterium diffusion to the surface and depthward. This is confirmed by the presence of the "tail" in a distribution expanding to 60 nm deep at the maximum 10 nm deep, meanwhile $R_p+\Delta R_p$ = 3.3 nm for the deuterium introduced with the energy of 200 eV into tungsten, according to the calculation by the TRIM - code. The deuterium diffusion coefficient estimation, done on the basis of the experimental profile given in Figure 18 (curve 1), provides $1.7\cdot10^{-19}$ m^2 s^{-1}. The integral deuterium concentration in the surface layer is equal $1.5\cdot10^{20}$ m^{-2}. It means that a considerable amount of deuterium diffuses to the surface and is released into vacuum. An additional irradiation of the tungsten samples by ten pulses of the deuterium plasma with the energy density of 0.5 MJ/m^2 per pulse results in an abrupt drop in the deuterium content within the tungsten. The integral concentration of deuterium in it drops down to $2\cdot10^{19}$ m^{-2}, i.e. approximately by one order of magnitude in comparison with the deuterium concentration in the sample after an exposure in plasma within the LENTA facility. The deuterium distribution profile shift towards the tungsten surface confirms the fact that the deuterium diffusion takes place to the surface only. A great part of deuterium, as a result of the plasma disruptions, will escape the tungsten into vacuum and some part of deuterium will be accumulated within a narrow surface layer only.

The deuterium escape outside, as a result of the high power thermal effect, is provided by melting, cracking of a tungsten surface layer and by its flaking, as shown in Figure 19.

The irradiation of the tungsten samples in the opposite order: by a flux of the pulse plasma first and, then, by low energy deuterium ions were carried out. Deuterium was not registered after an effect by 10 plasma pulses with the energy density 0.9 MJ/m^2 per pulse. In that case (Figure 20), the surface layer of tungsten was melted, bulged and had a bad thermal contact with the substrate.

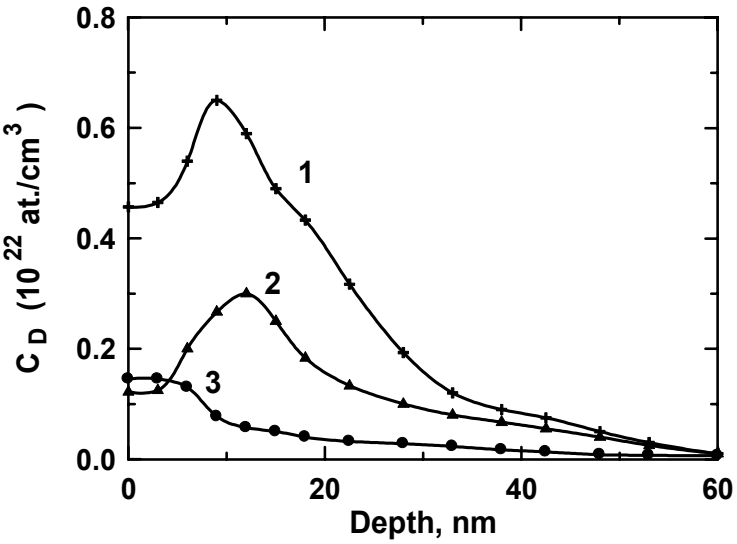

Figure 18. Depth distribution of D in tungsten: (1) - after irradiation by steady state (200 eV, 10^{26} m^{-2}, 550^0 C) deuterium plasma; (2) - after irradiation by steady state (200 eV, 10^{26} m^{-2}, 550^0 C) + pulsed (0.5 MJ/m^2 per pulse, 60 μs, 10 pulses) + steady state (200 eV, 10^{26} m^{-2}, 550^0 C) deuterium plasmas; (3) - after irradiation by steady state (200 eV, 10^{26} m^{-2}, 550^0 C) + pulsed (0.5 MJ/m^2 per pulse, 60 μs, 10 pulses) deuterium plasmas.

Flaking of large (~ 100 μm) areas of the surface layer was observed, as well as the melting and bulging of W in lower-located layers. The melting of W confirms the fact that surface temperature attained ~ 3500 K that provided the absence of D in W samples after such high power thermal plasma effect. At subsequent exposure of W by steady state plasma, twice smaller amount of D was captured in damaged surface layer of W than that under similar irradiation conditions of an initial tungsten (See, Figure 18, curve 2). The integral deuterium concentration was $7 \cdot 10^{19}$ m^{-2}.

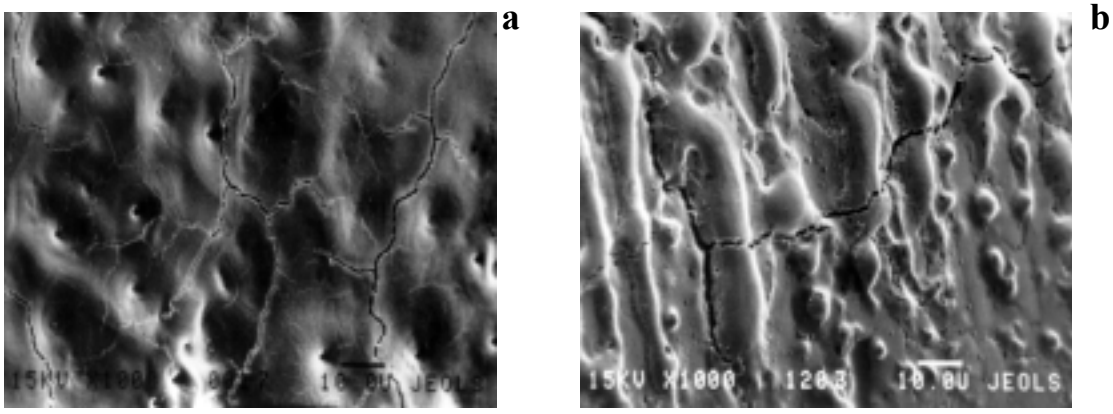

Figure 19. SEM photographs of the tungsten surface after irradiation by steady state (200 eV, 10^{26} m^{-2}, 550^0 C) + pulsed (0.5 MJ/m^2 per pulse, 60 μs, 10 pulses) deuterium plasmas.

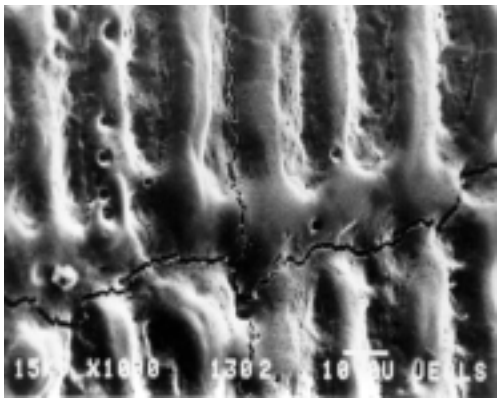

Figure 20. SEM photographs of the tungsten surface after irradiation by pulsed (0.9 MJ/m^2 per pulse, 60 μs, 10 pulses) deuterium plasma.

The result of measuring the retained deuterium in tungsten under its irradiation by the steady state and pulsed deuterium plasma fluxes are summarized in Table III.

TABLE III. DEUTERIUM RETENTION IN TUNGSTEN UNDER IRRADIATION BY STEADY STATE (E = 200 eV, $T_{IRR.} = 550^0$ C , D = 10^{26} m^{-2}) AND PULSED PLASMAS

No	Irradiation	Energy density, kJ/m^2	Integral concentration, m^{-2}	Ratio D/W
1	Steady state plasma		$1{,}5\cdot10^{20}$	0,110
2	Pulsed plasma	900	-	-
3	Steady state + pulsed plasma	500	$2\cdot10^{19}$	0,025
4	Pulsed + steady state plasma	900	$7\cdot10^{19}$	0,032

From an analysis of Table III and Figure 18 one can conclude that the plasma disruptions will assist in a considerable reduction in the saturating concentration of deuterium in tungsten and in a deuterium diffusion outside. As a result of the joint steady state and pulsed plasma effect, the amount of deuterium atoms respective to tungsten ones is about 3.5–4.5 times reduced in comparison with the ratio D/W after an exposure in the steady state plasma at 550^0 C.

6.1.2. Deuterium retention in the carbon-coated tungsten

Figure 21 shows element distributions in W target with carbon coating and topography pictures of the samples before and after pulsed plasma irradiation. Plasma treatment results in full destruction of carbon layer with a thickness of 250 nm, however, a 100 nm carbon enriched layer remains near the W substrate. It is the modified W-C layer with deuterium distribution shown in Figure 22. The comparison with similar data for pure tungsten leads to the conclusion that carbon layer deposition on tungsten during the exposure in a steady state plasma does not practically influence the deuterium retention in tungsten at plasma disruption.

Figure 22 shows deuterium depth distribution in carbon-coated tungsten after ten pulses of deuterium plasma with the energy density 0.9 MJ/m^2 per pulse. One can see that D is situated in a surface layer with thickness of 150 nm and its total concentration is $3\cdot10^{19}$ m^{-2}. No deuterium diffusion into the W depth is observed.

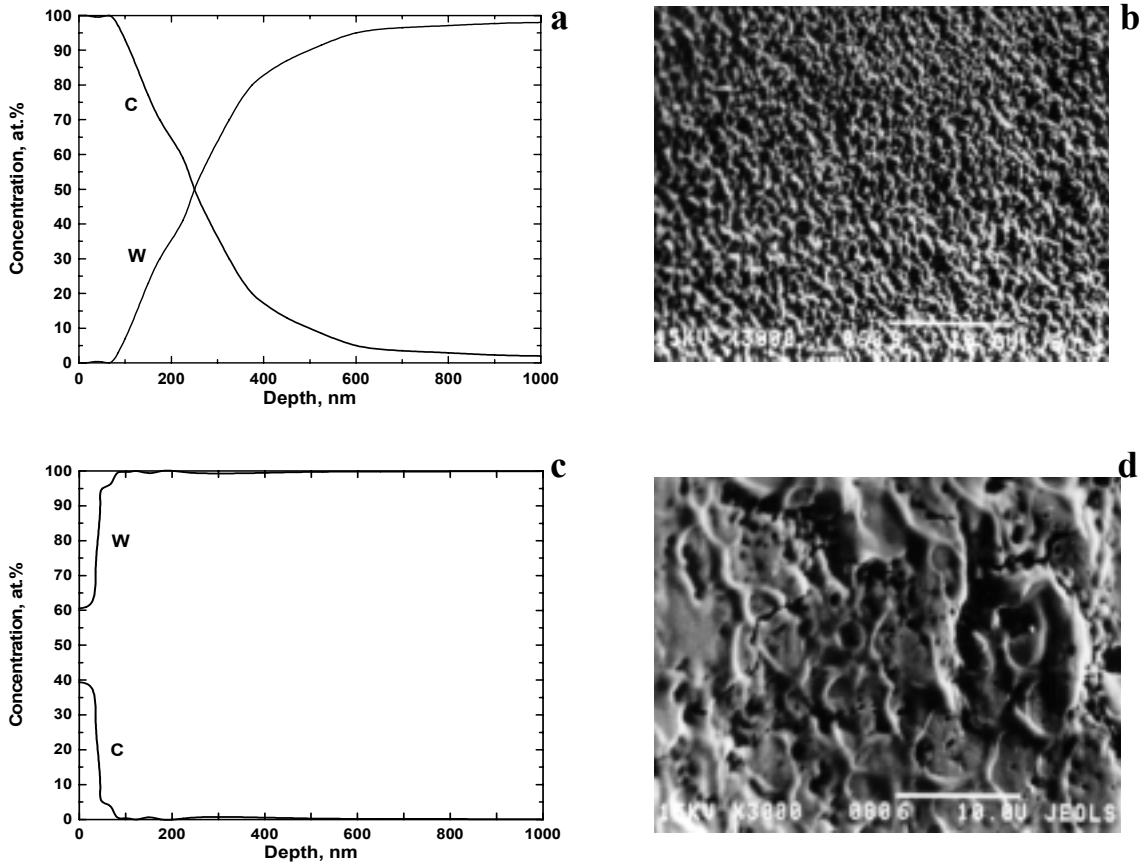

Figure 21. Depth distribution of elements in carbon-coated tungsten and corresponding SEM photographs of the sample surfaces before (a,b) and after (c,d) irradiation by power pulsed (0.9 MJ/m^2 per pulse, 60 μs, 10 pulses) deuterium plasma.

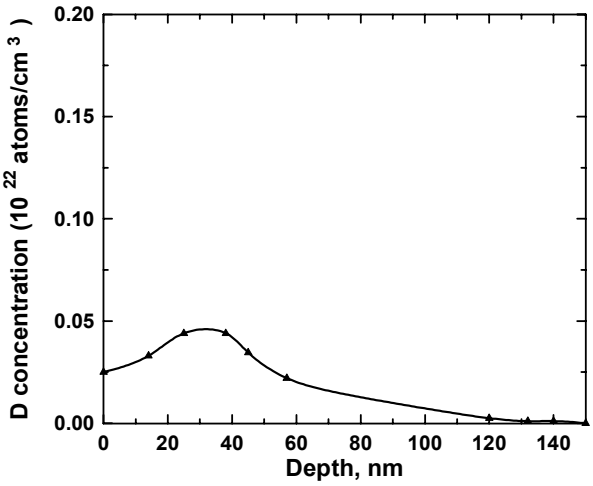

Figure 22. Depth distribution of deuterium in carbon-coated tungsten after irradiation by power pulsed (0.9 MJ/m^2 per pulse, 60 μs, 10 pulses) deuterium plasma.

6.1.3. Deuterium retention in the RGT graphite

The deuterium distribution profiles in the RGT graphite samples irradiated by deuterium ions with the energy 200 eV up to the fluence 10^{26} m^{-2} at the temperatures 770^0 C (curve 1) and 1150^0 C (curve 2), as well as those after an additional effect of six deuterium plasma pulses, at the energy fluxes of 0.25 MJ/m^2 (curves 3,4), upon these targets, are given in Figure 23. The nature of D distribution in the graphite samples exposed in steady state plasma is provided by the different mechanism of hydrogen isotope diffusion in graphite at the temperatures 770^0 C and 1150^0 C. The captured deuterium concentration at 1150^0 C, when diffusion through the grain volume takes place, is essentially higher than that at 770^0 C, when deuterium diffuses, mainly, through open channels. The curve (2) maximum is shifted depthward respective to the curve 1. D concentration in vicinity to the surface (curve 2) is smaller than that on the curve 1, that is provided by a greater D diffusion rate throughout the volume deep into the sample and towards the surface.

The subsequent irradiation by the pulsed plasma results in an abrupt deuterium concentration reduction in both samples of graphite. However, the deuterium distribution in the RGT graphite has a different nature in the samples exposed in the steady state plasma at various temperatures. Such an effect is provided by different graphite surface erosion processes at the temperatures under study, as a result of bombarding by D^+-ions with the energy of 200 eV and, respectively, by the different produced graphite surface topographic. At 770^0 C, a physical sputtering of graphite surface takes place and a relief characteristic for the growth of whiskers (Figure 16a) is being developed upon the surface sputtered by a super high deuterium ion fluence. At 1150^0 C, under conditions of radiation-enhanced graphite sublimation, a periodic structure of a terrace-type (Figure 16b) is being produced upon the surface [2].

As a result of the joint effect of steady state and pulsed plasmas the microstructure of the developed surface with whiskers is almost unchanged (slightly-changed): melting of the whisker ends is only observed (Figure 17a), meanwhile one can see the evidence of chipping and brittle destruction upon the graphite surface instead of the periodic relief produced after irradiation with D^+-ions at 1150^0 C (Figure 17b). Along with the deuterium escape outside, as a result of diffusion, the nature of deuterium distribution (Figure 23, curve 3) for this case confirms the deuterium distribution profile shift from the depth to the surface of a graphite target, as a result of the surface layer removing under a heat effect by the pulsed plasma. An increase in temperature, as a result of a high power thermal effect under pulsed irradiation, resulting in melting of the TiC-whiskers, causes a reduction in the deuterium concentration in graphite (curve 2) due to the deuterium back diffusion.

Table IV presents the integral deuterium concentration in the RGT graphite at various temperatures of irradiation by D^+-ions with the energy of 200 eV up to the fluence 10^{26} m^{-2} and after an additional effect by six deuterium plasma pulses with the energy density equal 0.25 MJ/m^2.

Thus, the production of whiskers under bombardment of the RGT graphite with the deuterium ions at a temperature corresponding to the physical sputtering of graphite assists in a reduction of the integral deuterium concentration by the order of magnitude under subsequent pulsed plasma effect. Produced brush-like surface structure turned out to be a thermostable one under subsequent effect of a heat shock accompanying the plasma pulse. The ratio D/C is reduced more than by the order of magnitude under joint steady state and pulsed plasma effect.

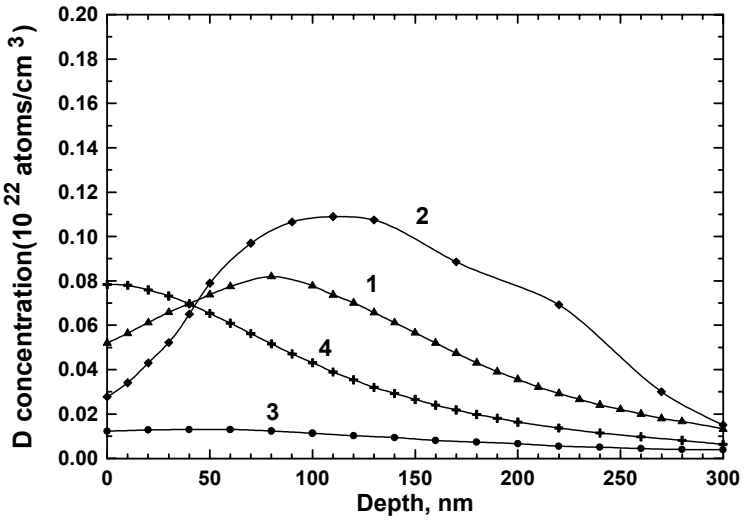

Figure 23. Depth distribution of D in RGT graphite: 1 - after steady state (200 eV, 10^{26} m^{-2}) deuterium plasma irradiation at 770^0 C ; 2 - after steady state (200 eV, 10^{26} m^{-2}) deuterium plasma irradiation at 1150^0 C ; 3 - after irradiation by steady state (200 eV, 10^{26} m^{-2}, 770^0 C) + pulsed (0.25 MJ/m^2 per pulse, 60 μs, 6 pulses) deuterium plasmas; 4 - after irradiation by steady state (200 eV, 10^{26} m^{-2}, 1150^0 C) + pulsed (0.25 MJ/m^2 per pulse, 60 μs, 6 pulses) deuterium plasmas.

TABLE IV. DEUTERIUM RETENTION IN THE RGT GRAPHITE

No	Irradiation	Temperature of steady state plasma irradiation, ^{0} C	Integral concentration, m^{-2}	Ratio D/C
1	Steady state plasma	770	$1{,}90 \cdot 10^{20}$	0,0870
2	Steady state plasma	1150	$2{,}70 \cdot 10^{20}$	0,1000
3	Steady state + pulsed plasma	770	$1{,}60 \cdot 10^{19}$	0,0067
4	Steady state + pulsed plasma	1150	$1{,}16 \cdot 10^{20}$	0,0084

6.1.4. Deuterium retention in the mixed W-C layer

Some studies of peculiarities in the deuterium retention in the coating made of the W-C mixture upon beryllium under pulse plasma effect were done. The chemical composition of the mixed W-C layer, measured by RBS technique, is shown in Figure 24.

The coating, 250 nm thick, includes ~50%W and ~50%C. The preliminary exposure of the W-C layer in a steady state plasma simulating one pulse of a current in ITER (D = 10^{26} m^{-2}) has not been done, since the film, 250 nm thick, is unavoidably sputtered under conditions of the study. The pulsed plasma irradiation of W-C layer is done under softer operating conditions in comparison with the plasma parameters under irradiation of tungsten and graphite targets. After irradiation by two plasma pulses at the energy density 0.2 MJ/m^2 per pulse, a partial film destruction (Figure 25b) is observed.

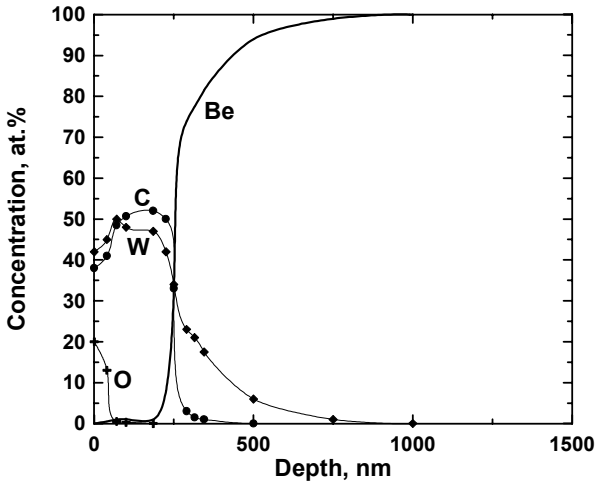

Figure 24. Depth distribution of elements in mixed W-C layer deposited on Be substrate before pulsed deuterium plasma irradiation.

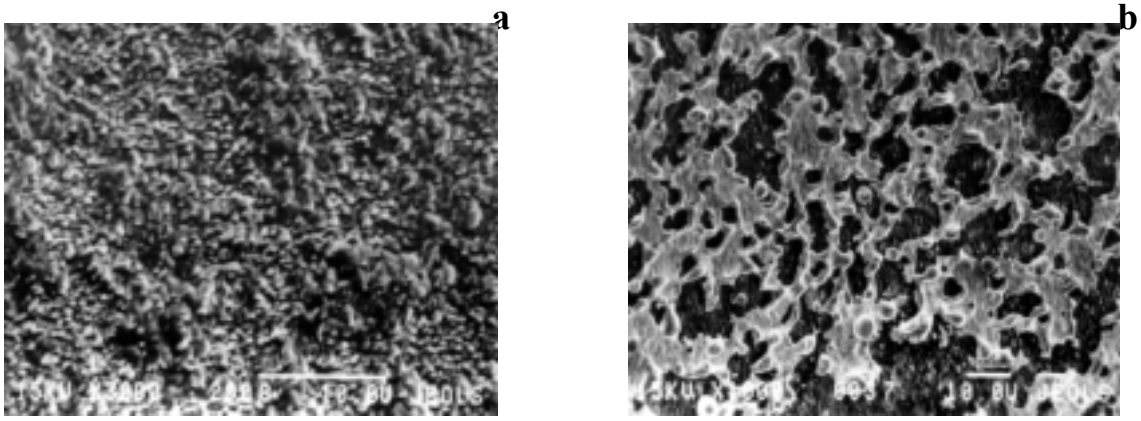

Figure 25. SEM photographs of the mixed W-C layer surface before (a) and after irradiation by pulsed (0.2 MJ/m^2 per pulse, 60 μs, 2 pulses) deuterium plasma (b).

According to the observed surface topography, the energy RBS spectra measured at its different parts also confirm the presence of differences in the chemical composition of the target surface layers. Element distributions in a surface target layer after an effect of the pulsed plasma for the areas with the retained coating (a) and for the areas without coating (b) are given in Figure 26.

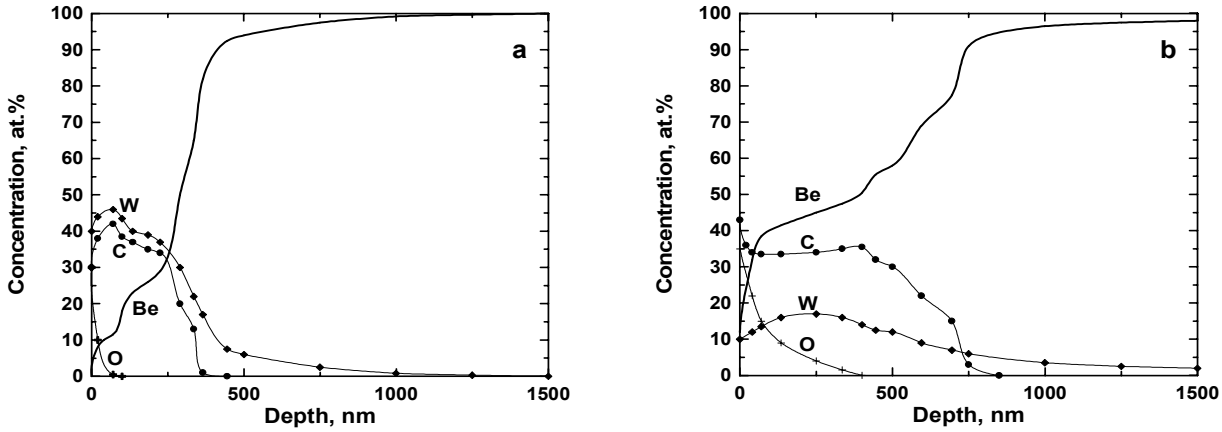

Figure 26. Depth distribution of elements in mixed W-C layer deposited on Be substrate after irradiation by pulsed (0.2 MJ/m^2 per pulse, 60 μs, 2 pulses) deuterium plasma for the areas with the retained coating (a) and for the areas without coating (b).

As seen in Figure 26a, the beryllium diffusion into the coating is observed. In the areas where the film is absent the coating element penetration deep into the beryllium backing occurs. It is characteristic that heavy tungsten atoms penetrate much deeper than the atoms of carbon. Probably, such an effect can be provided by the leakage of the melted tungsten into the melted beryllium under the pressure produced by a plasma flux under disruption as "viscous fingers" [4]. Moreover, there are some areas, where the film is completely removed from the backing surface, probably, as a result of bad adhesion, and the beryllium backing composition practically has not been changed.

D distribution profiles for various target areas after plasma effect are shown in Figure 27.

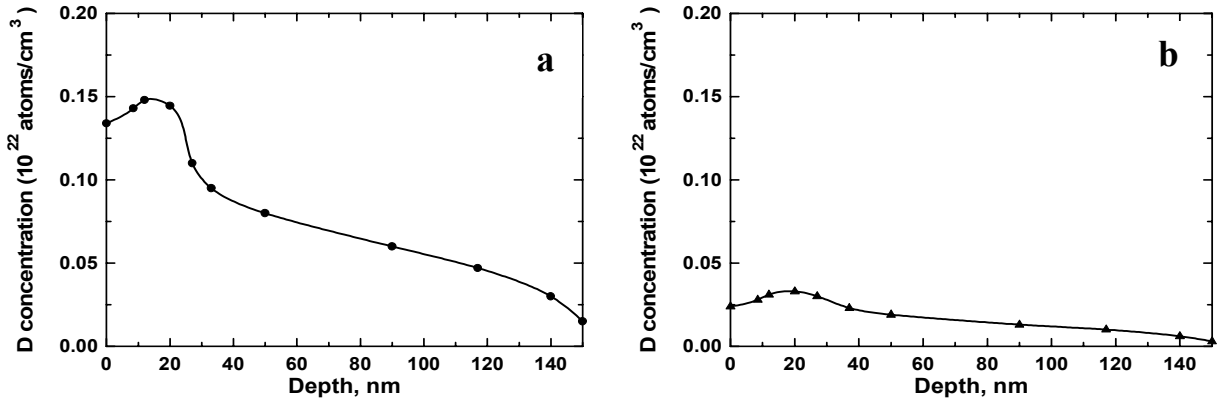

Figure 27. Depth distribution of D in mixed W-C layer deposited on Be substrate after irradiation by pulsed (0.2 MJ/m^2 per pulse, 60 μs, 2 pulses) deuterium plasma for the areas with the retained coating (a), and for the areas with the completely removed coating (b).

The integral D atom concentrations are varied in the range (1.1–1.3)·10^{20} m^{-2}. In the Be surface layer, where the coating has been removed, only the tail to the deuterium distribution remained (Figure 27b), its integral concentration is reduced to 3·10^{19} m^{-2}.

Thus, the combined steady state and power pulse deuterium plasma effect on the W and graphite results in a reduction of retained D in comparison with steady state plasma irradiation only.

Under bombardment of tungsten and under that of carbon-coated tungsten by a flux of high power pulsed (0.9 MJ/m^2 per pulse, 10 pulses, 60 μs long each) deuterium plasma deuterium is not detected in tungsten, but in the presence of a carbon film the integral deuterium concentration is equal $3 \cdot 10^{19}$ m^{-2}. The deuterium is distributed in a modified surface layer with thickness of 150 nm.

Production of W-C coating on Be at normal operating conditions and its removal under disruptions will assist in a reduction of D retention in Be and will prevent the deuterium diffusion into the material depth.

7. DEUTERIUM RETENTION AND EROSION OF MIXED W-Be LAYER ON Be IN EXPERIMENTS ON PLASMA DISRUPTION SIMULATION

Targets of electrolytically-pure tungsten and those of commercial powder-compacted beryllium of TShP-type were used in these experiments. The mixed W-Be layers were produced in the ILU accelerator [4]. The mixed-material samples underwent an irradiation in the electrodynamic plasma MKT-accelerator at the D plasma concentration of 10^{21} m^{-3} and at the maximal ion energy of (1–2) keV. The pulse duration was 60 μs. In experiments with the mixed (W-Be) layers on Be the energy flux density was 0.2 MJ/m^2 per pulse and the number of pulses did not exceed two, since the film was completely removed with their increase. After each treatment by pulsed plasma fluxes the studies of target surface microstructure with the JEOL scanning microscope and chemical surface composition by the Rutherford back scattering technique in the Van-de Graaf accelerator were done. The Van-de-Graaf accelerator was also used for determination of the deuterium depth distribution profiles in the mixed W-Be layers by the ERDA method [2]. Basalt fibre filters were used for collection of the erosion products. The morphological characterization of dust particles were investigated by means of transmission and scanning electron microscopy (JEOL).

7.1. Deuterium retention in mixed W-Be layer

Some studies of peculiarities in the deuterium retention in coating made of the W-Be mixture on Be substrate under pulsed plasma effect were done. The thickness of the mixed W-Be layer was ~500 nm. The chemical composition of the mixed W-Be layer, measured by RBS technique, is shown in Figure 28a. The coating contains up to 35% W by atom, up to 35% Be and up to 30% O. The W-Be layer irradiation by the pulsed plasma is done under softer operating conditions in comparison with the plasma parameters under irradiation of tungsten and graphite targets [2].

After irradiation by two plasma pulses at the energy density 0.2 MJ/m^2 per pulse, film is melted and removed completely from the local surface areas up to 30 μm in diameter. W-Be coating surface topography before and after an exposure in D pulsed plasma is shown in Figure 29. The energy RBS spectra measured at its different parts also confirm the presence of differences in the chemical composition of the target surface layers. For the surface areas with the removed film Be surface concentration is about 75% by atom, W – about 15%, O - about 10% and the penetration of W and O atoms up to 1250 nm in depth of Be substrate is observed (Figure 28b). There are some areas, where the film is completely removed from the backing surface, probably, as a result of bad adhesion, and the Be substrate composition has not been changed. For the surface areas with the melted film the beryllium diffusion into the

coating is observed (Figure 28c). As result, Be surface concentration increase up to 90% by atom, W and O concentration decrease about 3 and 2 times.

Deuterium distribution profiles for various target areas after plasma effect are shown in Figure 30.

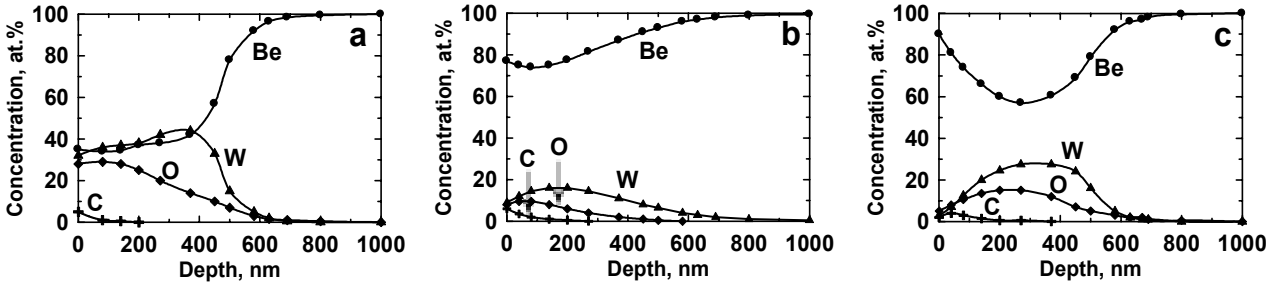

Figure 28. Depth distribution of elements in mixed W-Be layer deposited on Be substrate before (a) and after irradiation by pulsed (0.2 MJ/m^2 per pulse, 60 μs, 2 pulses) deuterium plasma for the areas with the removed (b) and retained coating (c).

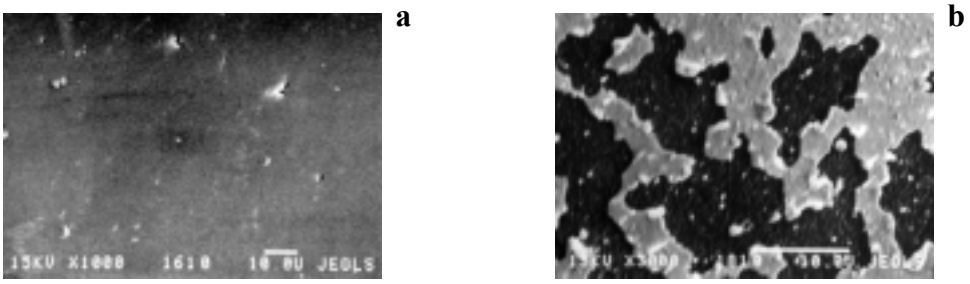

Figure 29. SEM photographs of the mixed W-Be layer before (a) and after irradiation by pulsed (0.2 MJ/m^2 per pulse, 60 μs, 2 pulses) deuterium plasma (b).

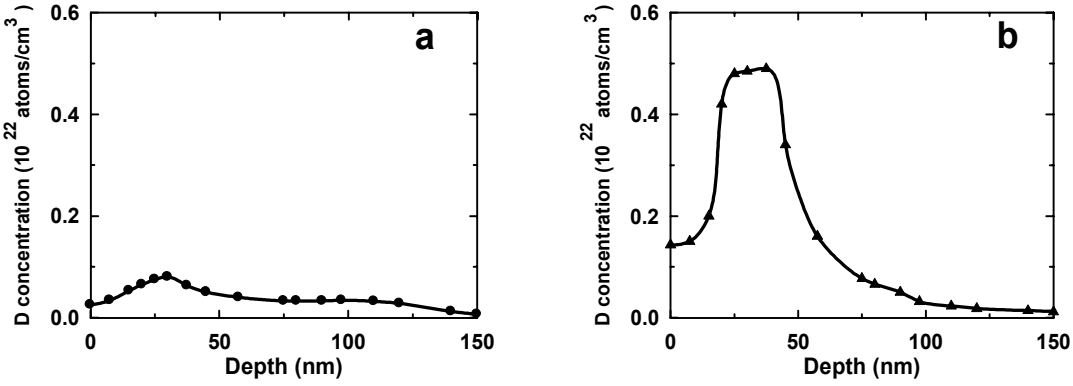

Figure 30. Depth distribution of deuterium in mixed W-Be layer deposited on beryllium substrate after irradiation by pulsed (0.2 MJ/m^2 per pulse, 60 μs, 2 pulses) deuterium plasma for the areas with the removed (a) and retained coating (b).

For retained melted areas of the mixed W-Be layer deuterium is situated in the surface layer with thickness of 150 nm and its integral deuterium atom concentration is equal to $2.2 \cdot 10^{20}$ m^{-2}. No deuterium diffusion into the beryllium backing depth is observed. In the

surface beryllium layer, where the coating has been removed and the backing composition hasn't been changed, only the tail to the deuterium distribution remained (Figure 30a), deuterium integral concentration is reduced in comparison with that for retained layer and it's equal $0.6 \cdot 10^{20}$ m^{-2}. One should note that the deuterium concentration reduction in the vicinity to the sample surface also means a reduction in the deuterium accumulation in the whole sample, as well as that in its penetrability [4].

7.2. Erosion products of mixed W-Be layer

The particle distributions with respect to their sizes are presented as histograms in Figure 31. Total distribution has two maxima located in the ranges 0.1–0.2 μm and 2.5–5.0 μm, respectively. Erosion products captured upon the basalt collector have mainly a round drop configuration (Figure 32) and its maximal size is about 20 μm in diameter. The results of study of erosion products confirm the melting of the mixed W-Be layer on Be under irradiation by pulsed power plasma flux.

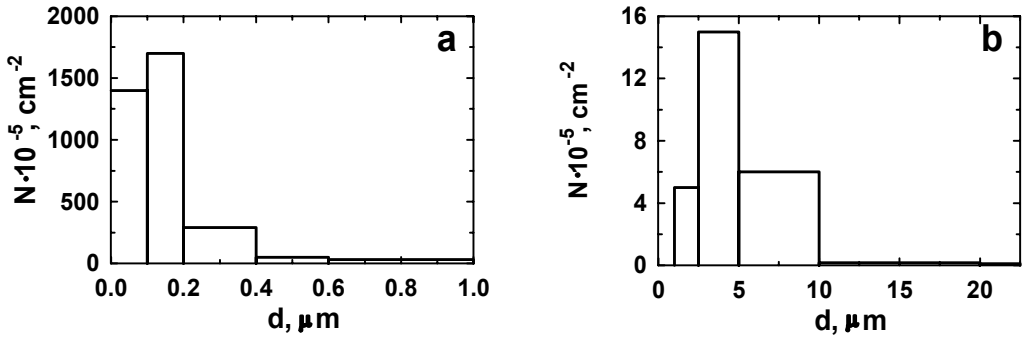

Figure 31. Size erosion product distributions in the ranges 0–1 μm (a) and 1.0–22.5 μm after irradiation of W-Be layer on Be by pulsed (0.2 MJ/m^2 per pulse, 60 μs, 2 pulses) deuterium plasma.

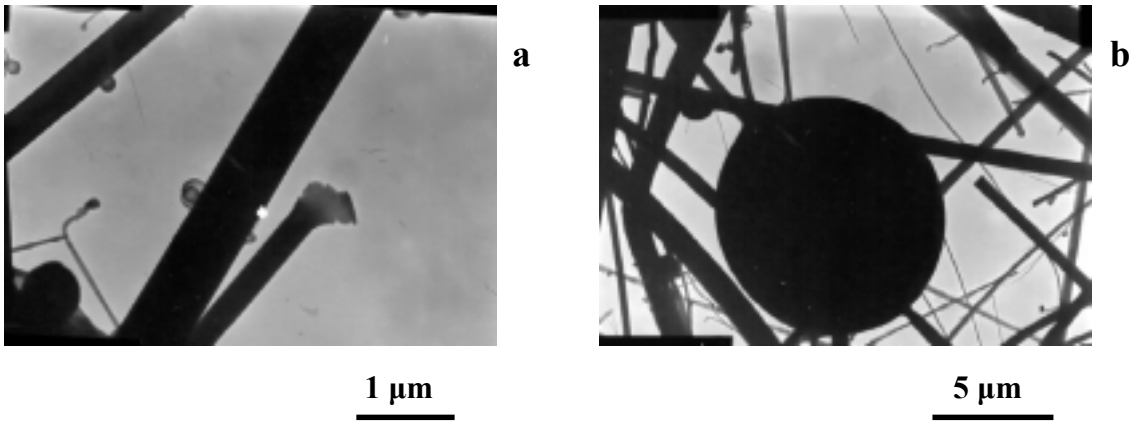

Figure 32. Electron microphotographs of the filters with the small (a) and large (b) erosion product particles after irradiation of mixed W-Be layer deposited on Be by pulsed (0.2 MJ/m^2 per pulse, 60 μs, 2 pulses) deuterium plasma.

Thus, after high power pulsed deuterium plasma irradiation of mixed W-Be layer on Be deuterium is distributed in a modified surface layer with thickness of 150 nm. The absence of D in Be substrate is provided by D escape outside, as a result of the mixed layer melting.

Production of W-Be coating on Be at normal operating conditions and its removing under disruptions will assist in a reduction in a D retention in Be and will prevent the D diffusion into the material depth. The size distribution of W-Be coating erosion products has two maxima in the ranges 0.1–0.2 μm and 2.5–5.0 μm, particles attain a maximal size of about 20 μm in diameter and have a drop-like configuration.

8. CONCLUSIONS

1. A new precise method of low sputtering yield determination based on field ion microscopy is developed. The results received by this method are:

a) no sputtering threshold of C-C composite by deuterium ions, sputtering yield is weakly energy dependent in the energy range 10–200 eV and equals $(5–6)\cdot10^{-3}$ atom/ion;

b) the measured threshold energy for tungsten oxide is 65 eV instead of <10 eV reported earlier[1–5], whereas sputtering yields of pure W and W-C layer are in agreement with previous investigations.

2. The study of the temperature dependence of pure and B-doped C-C composite erosion rate by 2-keV deuterium ions shows:

a) all the known features of graphite erosion: physical sputtering, chemical sputtering and radiation enhanced sublimation, the maximal chemical sputtering yield being equal 0.18 atom/ion and situated at 600^0 C, the physical sputtering yield being equal 0.07 atom/ion;

b) the boron doped C-C composite has 2 times lower chemical sputtering and the beginning of radiation enhanced sublimation for boron doped C-C composite is shifted on ~100^0 C towards the higher temperature as compared with pure C-C composite.

3. Investigation of materias erosion under power pulsed plasma flow simulating disruption shows:

a) erosion rate of C-C composite under the disruption increases in joined C-C composite and W target as compare with C-C composite target due to increase of shielding plasma radiation;

b) an essential effect of RGT graphite surface modification at steady state plasma exposition on the subsequent erosion under plasma disruptions is shown, the exposition at the temperature of physical sputtering being to decrease the erosion, whereas exposition at the temperature of radiation enhanced sublimation being to increase the erosion;

c) on the other hand the irradiation in plasma accelerator does not influence sputtering in steady state plasma because the thickness of the sputtered layer during one pulse of normal operation is much higher than the thickness of the layer modified during the disruption.

4. The plasma disruption reduces concentration of deuterium in tungsten. As a result of the joint steady state and pulsed plasma effect, the amount of deuterium atoms respective to tungsten ones is about 3.5–4.5 times reduced in comparison with the ratio D/W after an exposure in the steady state plasma at 550^0 C.

5. The production of whiskers under bombardment of the RGT graphite with the deuterium ions at a temperature corresponding to the physical sputtering of graphite results.

6. Production of W-C and W-Be coating on the beryllium at normal operating conditions and its removing under disruptions will assist in a reduction in a deuterium retention in beryllium and will prevent the deuterium diffusion into the material depth.

7. The reviewed problems show that data about surface erosion and deuterium retention are sensitive to the peculiarities of fusion device operation and it should be taken into account.

REFERENCES

[1] GUSEVA, M.I., SUVOROV, A.L., KORSHUNOV, S.N., LAZAREV, N.E., J. Nucl. Mater. **266–269** (1999) 222.

[2] MARTYNENKO, Yu.V., GUSEVA, M.I., VASILIEV, V.I., GUREEV, V.M., DANELYAN, L.S., PETROV, V.B., KHRIPUNOV, B.I., SOKOLOV, Yu.A., STATIVKINA, O.V., STOLYAROVA, V.G., STRUNNIKOV, V.M., J. Nucl. Mater. **258–263** (1998) 1120.

[3] KORSHUNOV, S.N., VASILIEV, V.I., GUSEVA, M.I., GUREEV, V.M., DANELYAN, L.S., KULIKAUSKAS, V.S., MARTYNENKO, Yu.V., PETROV, V.B., STRUNNIKOV, V.M., KHRIPUNOV, B.I., in Proceedings of The International Workshop on Hydrogen Recycle at Plasma Facing Materials (UTNL-R 0380) University of Tokyo, Tokyo, Japan 1998, 161.

[4] KORSHUNOV, S.N., VASILIEV, V.I., GUSEVA, M.I., GUREEV, V.M., DANELYAN, L.S., ZATEKIN, V.V., KULIKAUSKAS, V.S., Fusion Technology **38** (2000) 357.

[5] GUSEVA, M.I., GUREEV, V.M., DANELYAN, L.S., KORSHUNOV, S.N., KULIKAUSKAS, V.S., MARTYNENKO, Yu.V., MOSKOVKIN P.G., ZATEKIN, V.V., in Book of Hydrogen Recycling at Plasma Facing Materials (WU, C.H., Ed.), Kluwer Academic Publisher, Netherlands 2000, 265.

[6] ROTH, J., BOHDANSKY, J., OTTENBERGER, W., in Report of Data on Low Energy Light Ion Sputtering, Max-Planck-Institut für Plasmaphysik, Report IPP 9/26, Germany 1979.

[7] ECKSTEIN, W., GARCIA-ROSALES, C., ROTH, J., OTTENBERGER, W., in Report of Sputtering Data, Max-Planck-Institut für Plasmaphysik, Report IPP 9/82, Germany 1993.

[8] ROTH, J., BOHDANSKY, J., BLEWER, R.S., OTTENBERGER, W., J. Nucl. Mater. **85–86** (1979) 1077.

[9] ROTH, J., ECKSTEIN, W., GUSEVA, M., Fusion Engineering and Design **37** (1997) 465.

[10] J. ROTH, J. BOHDANSKY, A.P. MARTINELLI, in Proceedings of 1 Conference on Ion Beam Modification of Materials, Budapest, Hungary, 1978, p. 1541.

[11] ROTH, J. ECKSTEIN, W., BOHDANSKY, J., J. Nucl. Mater. **165** (1989) 199.

[12] MACH, B.V., HAASZ, A.A., DAVIS, J.W., J. Nucl. Mater. **241–243** (1997) 1147.

[13] VIETZKE, E., FLASSKAMP, K., PHILIPPS, V., J. Nucl. Mater. **128–129** (1984) 545.

[14] GUSEVA, M.I., GUREEV, V.M., KORSHUNOV, S.N., J. Nucl. Mater. **220–222** (1995) 957.

[15] CARTER, G., MARTYNENKO, Yu.V., MOSCOVKIN, P.G., Thin Solid Films **287** (1996) 275.

PLASMA-MATERIAL INTERACTION FOR MIXED PLASMA-FACING MATERIALS IN FUSION REACTORS STUDIED IN TEXTOR-94

E. VIETZKE[1], W. BIEL[1], H.G. ESSER[1], T. HIRAI[1], A. HUBER[1], A. KIRSCHNER[1], M. LEHNEN[1], T. OHGO[2], K. OHYA[3], V. PHILIPPS[1], A. POSPIESZCZYK[1], J. RAPP[1], M. RUBEL[4], U. SAMM[1], B. SCHWEER[1], J. VON SEGGERN[1], G. SERGIENKO[5], T. TANABE[6], M. WADA [7], P. WIENHOLD[1]

[1]Institut für Plasmaphysik, Forschungszentrum Jülich GmbH, Euratom Association, Trilateral Euregio Cluster, Jülich, Germany,
[2]Department of Physics, Fukuoka University of Education, Munakata, Fukuoka, Japan
[3]Faculty of Engineering, The University of Tokushima, Tokushima, Japan
[4] Alfvén Laboratory, Royal Institute of Technology, Association Euratom-VR, Stockholm, Sweden
[5] Inst. For High Temperatures, "IVTAN", Moscow, Russian Federation
[6]Center of Integrated Research in Science and Engineering, Nagoya University, Nagoya, Japan
[7]Department of Electronics, Doshisha University, Kyotanabe, Kyoto, Japan

Abstract

In an overview, the main erosion and redeposition results of some mixed materials, such as amorphous Si/C-films („siliconization"), Si-doped CFC (NS31), B_4C coated copper, are shortly presented in comparison to carbon from test limiter investigation in TEXTOR discharges. In the first two cases, the C and O flux on the toroidal limiter is reduced and no SiD_x formation at a limiter temperature of 550 K has been observed. The surface temperature of the B_4C coated copper limiter reach 1200 K by a power load of 4 MW/m^2. No severe delamination of the B_4C coating occurred after 80 exposures. For a direct comparison twin limiters experiments of C/W and W/Ta were performed. The Dγ line of the reemitted D flux is about 25% larger on C than on W. The redeposition of C on initially pure W limiter is modeled by the ERO-TEXTOR code. The built-up of the net-deposition zone and the net erosion zone on the W limiter is in agreement with experimental observations.

1. Introduction

The main activities in this project were concentrated to analyse erosion and deposition processes including local particle transport, to study the hydrogen recycling and to investigate the behaviour of several test limiters made from different materials or from different doped carbon during TEXTOR discharges. The materials investigated in comparison to pure carbon were thin boron or silicon films on all walls (so called boronisation and siliconisation), silicon-doped CFC material (NS31), tungsten and tungsten-coated graphite, tantalum and thick B_4C coated copper as limiter material. NS31 is a reference material for the lower divertor target foreseen for ITER and B_4C coated copper is foreseen for the first wall of the stellarator W7-X in Greifswald.

2. Silicon-carbon material

2.1. Siliconisation

The siliconisation results in a reduction of oxygen impurity and also initially in a suppression of the carbon content in the plasma [1] as seen in Fig. 1. Silicon is released mainly by physical sputtering, no significant SiD_4 release was observed at a wall temperature of 300 °C and also the Si deposition on C surfaces affects not significantly the hydrocarbon formation (Fig. 2).

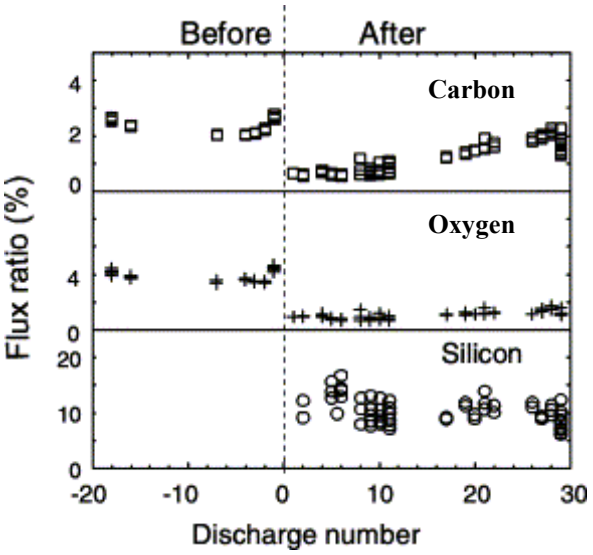

Fig. 1. Evolution of the relative flux ratios before and after siliconisation of carbon, oxygen and silicon measured on the ALT toroidal limiter as a function of shot number. The data are from a density of 3×10^{13} /cm^3 with 1.3 MW nuclear beam heating (co-injection).

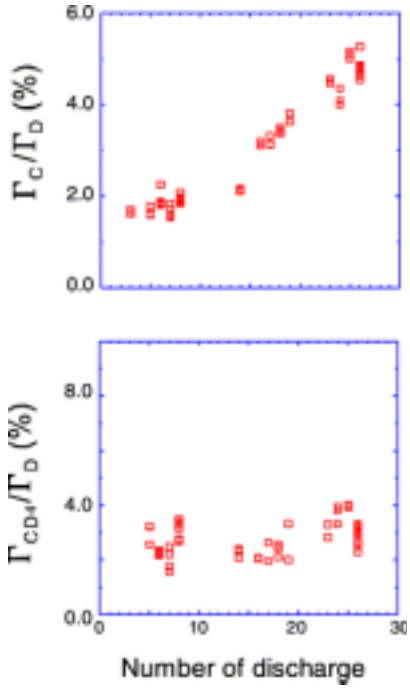

Fig. 2. Development of the C^+ and CD flux ratio as function of the discharge number for a graphite test limiter inserted in a freshly siliconised TEXTOR environment.

However, the silicon deposited at the wall has large influence on the plasma performance. It gave access to high density ($1.7\times n_{Greenwald}$) due to postponed MARFES and improved the energy confinement ("RI-mode" with radiation from intrinsically sputtered Si) [2].

2.2. Silicon-doped CFC material:

Silicon doped CFC material (NS31) was exposed as a test limiter in TEXTOR-94 [3]. In Fig.3 some results are shown in comparison to pure graphite. It was found that the methane formation is slightly reduced compared to that on a pure graphite target. The yield is between

2-3% over the whole range of plasma densities while on graphite the yield increases with plasma density. At the highest densities (~$5x10^{19}m^{-3}$) the reduction factor reaches about 2. The overall carbon ion flux from the silicon doped graphite limiter is only slightly reduced compared to graphite limiters. Although the material contains only about 1-1.5% of Si, a remarkable Si/D flux between 0.12% and 0.4% was observed spectroscopically. A measurable chemical erosion in the form of SiD_x has not been found. At surface temperatures exceeding about 1500°C (see Fig. 4) silicon evaporation begins to overcome the sputtered Si-flux leading to an increase of the Si concentration in the plasma and of the total radiation losses. Surface analysis revealed the formation of microcracks and holes. A depletion of silicon was observed in areas of the highest power load with values of 0.03% in and 0.02% between the fibres. Part of the released silicon was found on the limiter surface in the vicinity of the tangency point.

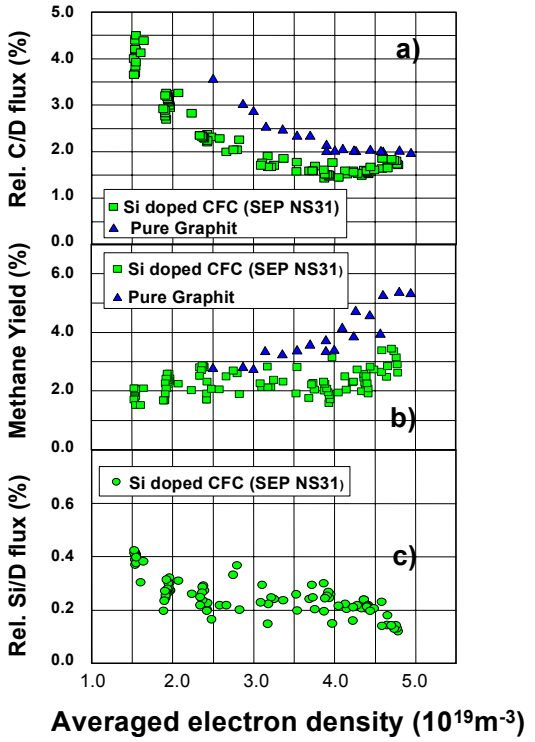

Fig. 3. Evolution of the relative flux ratios of carbon (a), methane (b) and silicon (c) measured from pure graphite and Si doped CFC limiters as function of the averaged electron density.

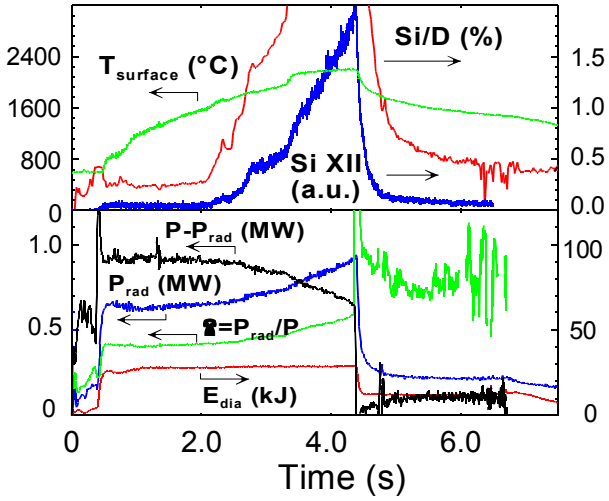

Fig. 4. Example of a discharge with silicon evaporation from a test limiter made of Si-doped CFC (SEP NS31). The figure shows the time traces of the local silicon fluxes from the limiter (Si/D), the line integrated radiation of Si XII emission, the local surface temperature of the limiter measured at the location of maximal power loading, the energy loss due to plasma radiation (P_{rad}), the radiation level $\gamma=P_{rad}/P$, the diamagnetic energy E_{dia} and the convective power on the test limiter P- P_{rad}, respectively.

3. Twin limiter experiments

Twin limiter experiments allow comparing two different material properties in edge plasma directly. First, carbon and tungsten have been investigated and compared as plasma-facing material [4-8]. With the same D-flux impinging on carbon and tungsten surface, the intensity of the Dγ-line is about 20-30% larger on carbon. This can be explained by the different hydrogen reflection properties and a different branching ratio of hydrogen release as atom or molecule. A post mortem analysis showed no carbon layer ($<10^{15}$C/cm^2) in the erosion region of the tungsten limiter. However, during the plasma exposure a carbon flux is spectroscopically observed on both sides, where the maximum intensity of the CII flux from the carbon surface is only ≈20% larger than that from the tungsten surface. This demonstrates that the majority of the carbon release from both surfaces is due to recycling of carbon impurities in the plasma edge and that only a small part of the detected carbon is due to bulk erosion of the graphite limiter. The amount of carbon, which is released in form of hydrocarbons from the tungsten surface is negligible compared to the graphite surface. The heat depositions on both sides under the same plasma conditions is about 30% larger on the carbon surface compared with the tungsten surface. This can be explained by the different energy reflection coefficients.

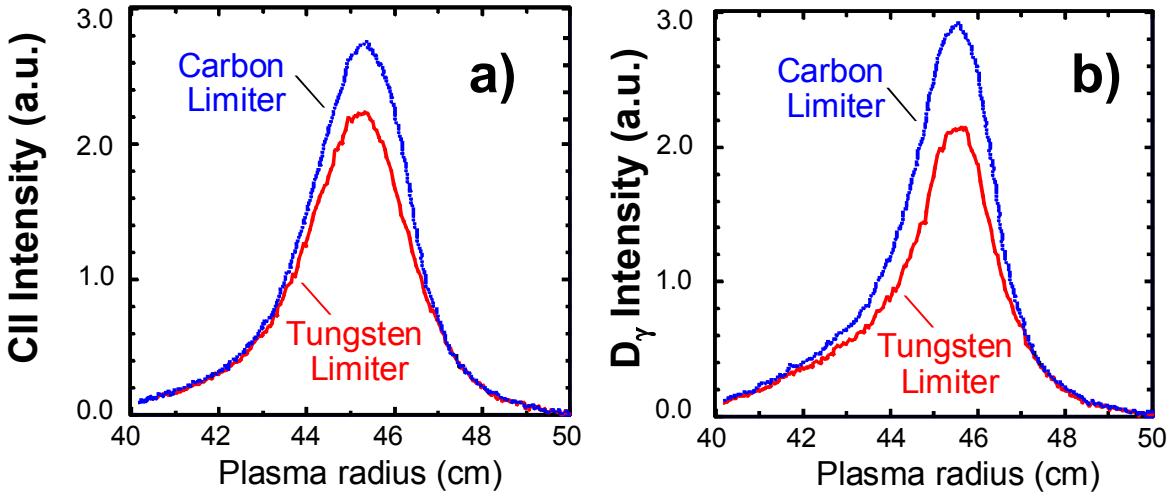

Fig. 5. Radial distributions of CII (a) and D_γ (b) from tungsten and carbon limiters.

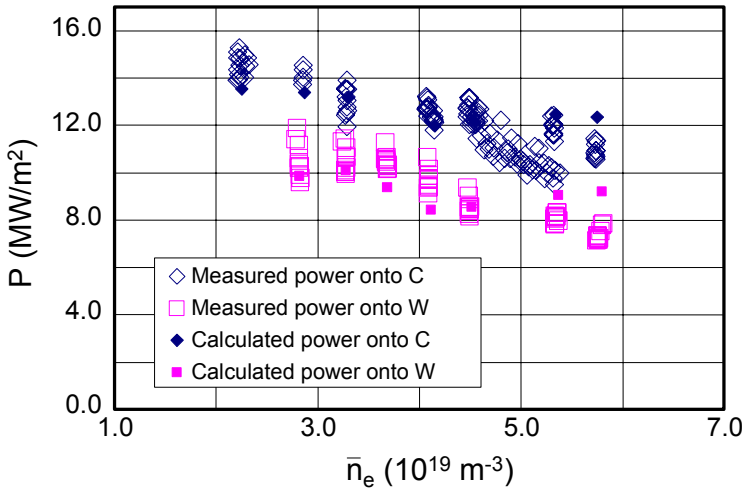

Fig. 6. Density dependence of the absorbed heat flux onto C- and W-limiters.

The disadvantage using tungsten is its difficult machining. Another high-Z material, tantalum, has a high ductility with the great advantage of easy machining, but it forms hydrides at relatively low temperature. Thus, Ta-W twin limiter experiments have been started in order to compare the hydrogen recycling on these high Z materials and their behaviour under high power exposure [9].

Both materials have similar masses and therefore similar reflection coefficients for hydrogen. But, Ta is an exothermic hydrogen occluder and W an endothermic one. Thus, different hydrogen release properties are expected. The figure 7 shows the temperature dependent D_β light intensity in front of Ta and W surfaces. In case of Ta, the D_β intensity is increasing with temperature above 1300K. The decay length of the emitted D_γ light from Ta surface along the minor radius became shorter above 1300 K. These might be explained by a continues change from molecular hydrogen releases at low temperature over a mixture of molecular and atomic hydrogen to pure atomic release at high temperatures, as it is observed in hydrogen/deuterium release process from carbon surfaces [10,11].

Another result in this comparison is surface temperature excursion. Under a comparable power fluxes, the surface temperature evolution during plasma exposure is different for Ta and W: Ta surface reached up to 2100 K and W up to 1600 K. This difference is due to the difference in thermal conductivities (Ta: 58 $Wm^{-1}K^{-1}$, W: 177 $Wm^{-1}K^{-1}$).

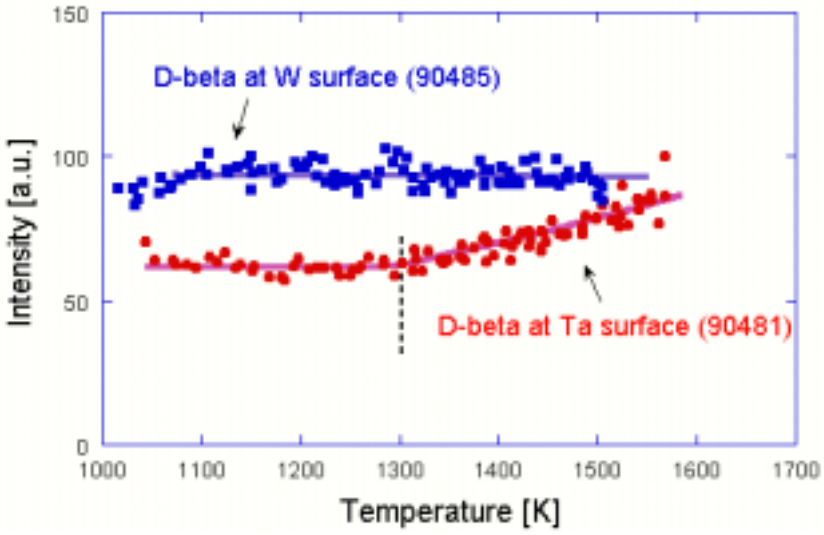

Fig. 7. D_β emission from Ta and W as a function of surface temperature measured by a pyrometer. Above 1300K, D_β emission from the Ta surface is linearly increasing with the surface temperature.

The surface temperatures of the Ta limiter increased shot by shot under the same comparable D-flux, which is due to a degradation of the thermal conductivity. It is associated with significant surface modification such as grain growth, cracking, recrystalization and plastic deformation due to heat load. On the other hand, the thermal properties of W did not show degradation over a number of discharges. As one can expect from the result, W did not had serious modification on it and still had a shiny surface, which is the same as previous experiments [12,13].

Post-mortem analyses have also been carried out. Microstructural observation at the cross section showed that significant grain growth, recrystalization and plastic deformation due to thermal stress occured. Surface analysis indicated that the deuterium concentration was less than 0.1% in subsurface region. Accordingly, even though Ta has exothermic properties, the impact of deuterium in Ta would not be significant, as long as the temperature was kept at high temperature (above 700 K in these experiments).

4. B_4C-coated copper limiter

For the W7-X Stellarator experiment, a first-wall concept with actively cooled stainless-steel panels as plasma-facing components with low atomic number coatings, in particular boron carbide (B_4C) layers, are being developed [14]. The aim of the B_4C coating is to avoid accumulation of high-Z impurities in the plasma during steady-state operation. It allows

continuous boronisation of the walls with its advantages of low chemical sputtering and oxygen gettering.

Similar limiter blocks have been inserted through lock systems, exposed to higher heat loads and diagnosed in detail in- and ex-situ as well. The surface temperature excursion during an plasma exposure is shown in Fig. . The plasma was heated auxiliary by two neutral beams of 1.5 and 1.3 MW/m^2. The resulting load on the test limiter amounted to 4MW/m^2. The 170 µm thick B_4C layer was rapidly heated up to 1000 °C and cooled down as the pyrometer signals show. The surface layer withstood such an exposure and did not detach from the copper. Increasing of the deposited heating power above 8 MW/m^2 lead to melting of the B_4C coating (see Fig. 9 in [14]).

In order to test this wall concept in a comparable plasma surrounding, the five top and bottom poloidal carbon limiter blocks in TEXTOR have been replaced by copper tiles coated with a 170 µm vacuum plasma sprayed B_4C layer and exposed permanently at a position 1 cm behind the last closed flux surface for several months under various plasma conditions.

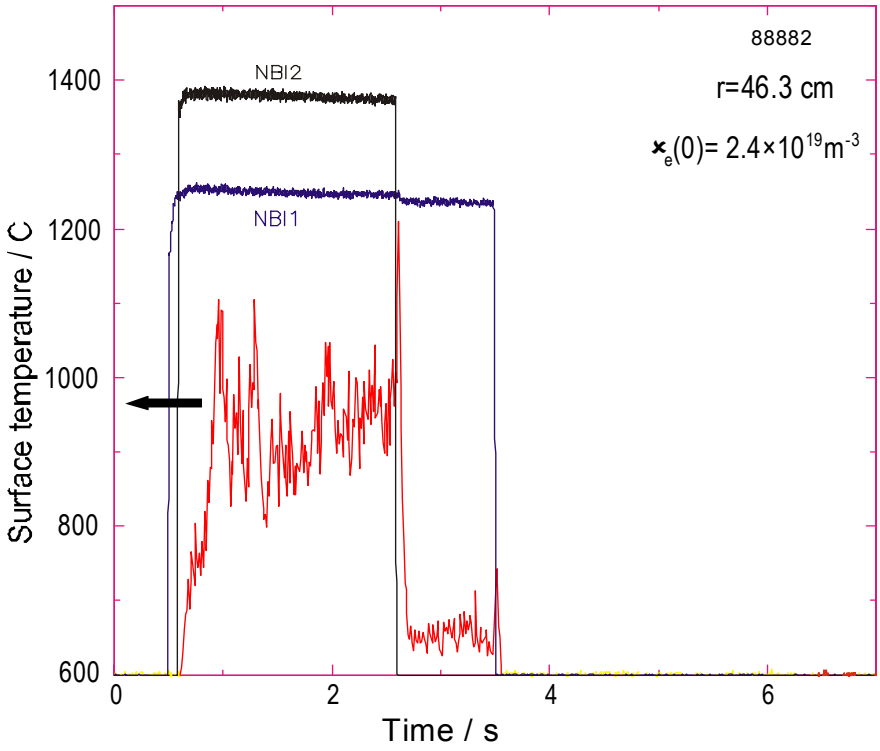

Fig. 8. The surface temperature excursion of a test limiter (made of copper coated with 170 µm B_4C) during exposure in TEXTOR near the last-close flux surface. The plasma was heated auxiliary by two neutral beams of 1.5 and 1.3 MW/m^2. The resulting load on the test limiter amounted to 4 MW/m^2.

No disturbance of plasma performance due to surface charging of the B_4C coatings with low electrical conductivity was found [14,15]. Concerning erosion and hydrogen inventory the limiters behave in general as every low Z object in a carbon surrounding and show similar properties as a pure graphite surface. The hydrogen inventory may be higher. During the discharges, video observation showed the emission of glowing particles from the limiter surfaces presumably due to arcing [14].

Distinct craters developed on the coating on both limiter types down to the copper bulk and are assumed to be caused by electrical arcs. It is not clarified yet and is subject of further investigations whether the arcs are triggered by surface or surface roughness or whether the electrically insulating B_4C layer triggered the enhanced arc formation. The arc probability measured across the surface of the top poloidal limiter seems to be affected by adjacent obstacles rising into the SOL which trigger predominantly bipolar arcs. They are observed during the whole discharge and not only at the start or the end. It seems that the changes of resistivity by e.g. melting suppresses further arcing. In the course of the experiments the craters are covered by carbon deposition from the graphite surrounding. No negative influence of the arcing on the properties of the coating and on the plasma behaviour could be evaluated so far. The temperature of the coating during a plasma discharge rises and decays extremely fast indicating that the heat contact from the coating to the substrate determine the thermal response of the coating rather than the heating of the copper bulk. However, despite reaching the melting temperature of the B_4C coating and cracking no severe delamination of the coating occurred (see Fig.9). Plastic deformation of the copper and high adhesion strength of the coating seems to compensate the thermomechanical stresses resulting from the mismatch in thermal expansion.

5. Modelling of erosion and deposition processes by the ERO-TEXTOR code

Simulating erosion and redeposition processes in fusion devices lead to a better understanding of the involved processes. The 3-dimensional Monte-Carlo code ERO-TEXTOR [16,17] has been developed to model the plasma-wall-interaction and the transport of eroded particles in the vicinity of test-limiters exposed to the edge plasma of TEXTOR.

Fig. 9. The surface of a test limiter (made of copper coated with 170 µm B_4C) after 80 exposures in TEXTOR near the last-close flux surface. The melting zone is clearly seen especially in the magnification at the right hand side where also a number of craters are visible possibly caused by electrical arcs.

Important problems concerning the lifetime of various wall materials (high Z vs. low Z) under different plasma conditions and the transport of eroded impurities into the main plasma can be treated with the ERO-TEXTOR code. Recently, the divertor geometry was implemented to carry out simulations for JET, ASDEX and ITER [18].

An important effort is the development of an adequate surface model for mixed materials and erosion. The following figure shows as one example the simulated surface composition of an initially pure tungsten limiter (spherically shaped) which was exposed to the edge plasma of TEXTOR. Carbon as main impurity of the background plasma can be deposited at the limiter surface. The spatial distribution of the carbon and tungsten concentration after having reached equilibrium inside the interaction layer is a result of the local erosion and deposition fluxes. At the locations where the carbon concentration is less than 100%, the incoming carbon flux (sum of background flux and redeposition) is in balance with the outgoing carbon flux. Only the tungsten in these regions suffers a continuously erosion. The built-up of net-deposition zones at the toroidal edges (100% carbon) and a net erosion zone in the middle part of the limiter is in agreement with experimental observations [19].

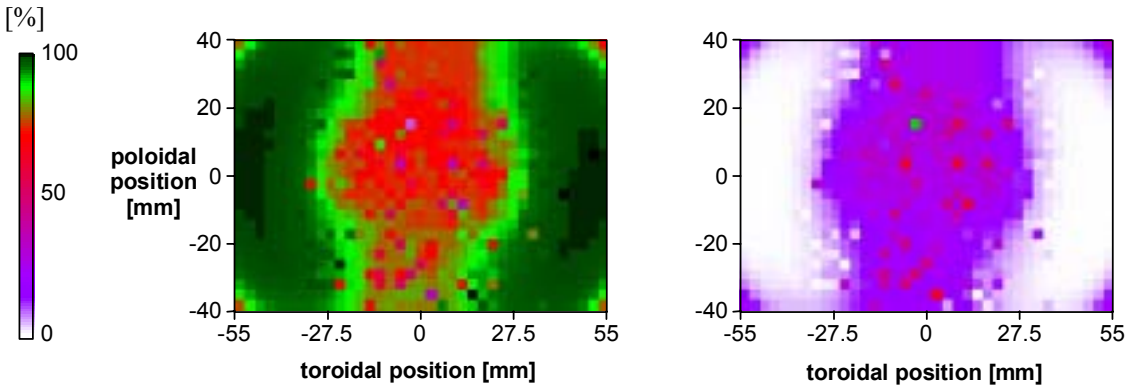

Fig. 10. Distribution of carbon (left) and tungsten (right) inside the interaction layer of an initially pure tungsten limiter after having reached stationarity. The pictures show a top view of the limiter. The plasma parameters of a typical ohmic shot of TEXTOR-94 were used as described in [17].

REFERENCES

[1] V. Philipps, A. Huber, H.G. Esser, A. Pospieszczyk, B. Schweer, J. von Seggern, W. Biel, J. Rapp, J. Nucl. Mater. 290-293 (2001) 1190–1194.

[2] J. Rapp, W. Biel, H. Gerhauser, A. Huber, H.R. Koslowski, M.Lehnen, V.Philipps, A. Pospieszczyk, D. Reiser, U. Samm, G. Sergienko, M.Z. Tokar, R. Zagórski, J. Nucl. Mater., 290-293 (2001) 1148–1154.

[3] A. Huber et al., to be published.

[4] A. Huber, V. Philipps, A. Pospieszczyk, A. Kirschner, M. Lehnen, T. Ohgo, K. Ohya, M. Rubel, B. Schweer, J. von Seggern, G. Sergienko, T. Tanabe, M. Wada, J. Nucl. Mater. 290-293 (2001) 276–280.

[5] K. Ohya, R. Kawakami, T. Tanabe, M. Wada, T. Ohgo, V. Philipps, A. Pospieszczyk, A. Huber, M. Rubel, G. Sergienko, N. Noda, J. Nucl. Mater. 290-293 (2001) 303-307.

[6] M, Rubel, V. Philipps, A. Pospieszczyk, H. Renner, Proc. 28th EPS Conference on Controlled Fusion and Plasma Physics, Madeira, Portugal, June 2001.

[7] T. Tanabe, T. Ohgo, M. Wada, M. Rubel, V. Philipps, J. von Seggern, K. Ohya, A. Huber, A. Pospieszczyk, B. Schweer, Fusion Engineering and Design 49-50 (2000) 355–362.

[8] M. Rubel, T. Tanabe, V. Philipps, B. Emmoth, A. Kirschner, J. von Seggern, P. Wienhold, J. Nucl. Mater. 283-287 (2000) 1089–1093.

[9] T. Hirai, V. Philipps, A. Huber, M. Wada, T. Tanabe, T. Ohgo, P. Wienhold, J. von Seggern, A. Pospieszczyk , G. Sergienko, To be presented at and published in the Proc. of the 10th International Conference on Fusion Reactor Materials (ICFRM-10).

[10] A. Pospieszczyk, Ph. Mertens, G. Sergienko, A. Huber, V. Philipps, D. Reiter, D. Rusbueldt, B. Schweer, E. Vietzke, P. T. Greenland, J. Nucl. Mater. 266-269 (1999) 138–145.

[11] J. W. Davis, A. A. Haasz, J. Nucl. Mater., 223 (1995) 312–315.

[12] V. Philipps, A. Pospieszczyk, A. Huber, A. Kirschner, J. Rapp, B. Schweer, P. Wienhold, G. Van Oost, G. Sergienko,T. Tanabe, K. Ohya, M. Wada, T. Ohgo, M. Rubel, J. Nucl. Mater. 258-263 (1998) 858–864.

[13] T. Tanabe, T. Ohgo, M. Wada, M. Rubel, V. Philipps, J. von Seggern, K. Ohya, A. Huber, A. Pospieszczyk, B. Schweer, TEXTOR team, Fusion Engineering and Design, 49-50 (2000) 355–362.

[14] S. Kötterl, H. Bolt, H. Greuer, J. Linke, M. Mayer, V. Philipps, A. Pospieszczyk, H. Renner, M. Rödig, J. Roth, B. Schweer, D. Valenza, Physica Scripta T91 (2001) 117–123.
[15] A.Pospieszczyk et al., to be published.
[16] U. Kögler, J. Winter, Jül-Report 3361, Forschungszentrum Jülich GmbH, Jülich 1997.
[17] A. Kirschner, V. Philipps, J. Winter, U. Kögler, Nucl. Fus., Vol. 40, No. 5 (2000), 989.
[18] A. Kirschner, A. Huber, V. Philipps, A. Pospieszczyk, P. Wienhold, J. Winter, Nucl. Mat. 290–293 (2001), 238.
[19] A. Kirschner et al., to be published.

FORMATION AND EROSION OF MIXED MATERIALS

Ch. LINSMEIER, J. ROTH, K. SCHMID
Max-Planck-Institut für Plasmaphysik, EURATOM Association,
Garching bei München, Germany

Abstract

The formation of compounds between wall materials and plasma impurities at the first wall of fusion devices involves a broad spectrum of species and interaction parameters such as ion energies, surface temperatures, impurity concentrations. Most of these parameters are hardly controllable in fusion experiments. To elucidate formation and erosion mechanisms, well-controlled laboratory experiments are described. In the first part of this review, carbide formation for the elements Be, Si, Ti and W is reported for thin carbon films on pure substrates. At room temperature, carbide formation is found in all systems up to a monolayer carbide coverage. For larger carbon amounts, elementary carbon films are formed. At elevated temperatures, the carbide formation is determined by thermochemistry and carbon transport by diffusion. For metallic carbides (W, Ti), strong carbon diffusion into the bulk substrate takes place at high temperatures. Several carbide phases are observed as a function of temperature. For ionic (Be) and covalent (Si) carbides, stable and stoichiometric carbide layers up to temperatures close to the respective melting points are formed. The second part of this review describes phase formation and erosion processes by impurity ion bombardment. For carbon ion impact, layer deposition, carbide formation and carbon diffusion processes depend on the parameters substrate temperature, angle of ion incidence and ion energy. This is shown in detail for carbon ion impact on tungsten. A reproduction of experimental results is possible after the determination of the concentration-dependent diffusion coefficient of carbon in tungsten. Finally, simultaneous bombardment of surfaces by multiple species is discussed for the combinations carbon-hydrogen and carbon-oxygen, experimentally carried out by CH_3^+ and CO^+ bombardments of tungsten and beryllium, respectively. Complex dynamic processes are observed as a function of particle fluence and substrate temperature.

Introduction

The formation of mixed materials relevant to fusion first walls is a complex process involving a broad spectrum of particle species, particle energies, material temperatures, just to mention some. Under real conditions during plasma discharges in a fusion experiment these parameters are hardly controllable. Moreover, analytical methods are limited, especially those which probe the chemical composition and state of the surface as well as depth profiles. Nevertheless, at JET an attempt was started a decade ago with the Fast Transfer System to employ ion and photoelectron spectroscopies *in vacuo* [1]. The fundamental properties of the interaction of potential wall materials and impurities from the plasma, however, can only be studied under full control of all experimental parameters. Therefore, studies have to be carried out under well-defined conditions which are achieved in ultra-high vacuum (UHV) environments. The goal of those studies is both the full control of all experimental parameters and their limitation to only a few parameter variations during specific experimental series. Through this approach we aim at gaining full understanding of the behavior of systems consisting of two to several elements under variation of incoming particle energies, sample temperatures, surface morphologies or chemical reaction conditions.

In the first part of this paper we summarize studies carried out recently concerning the formation of carbides in binary systems of carbon and several elements relevant for nuclear fusion. Specifically, we investigate materials used or under consideration for plasma facing components or wall conditioning procedures. In particular, we will discuss the formation of carbides of the elements beryllium, silicon, titanium and tungsten. In the second part, the influence of the intermixing and compound formation during carbon bombardment on the erosion properties of potential plasma facing materials is presented. Multi-species ion bombardment is simulated by using CH_3^+ or CO^+ ions.

I. Formation of mixed materials

Since carbon is an ubiquitous contamination at all surfaces, experiments to study the chemical interaction of surfaces with carbon require the thorough cleaning of the samples and experimental procedures fully under UHV conditions. Experimental details are given in ref. [2,3] and are only shortly described here. Carbon is provided as a surface layer at thicknesses between submonolayer coverage and several nm [2]. The analysis of the chemical and physical processes during the carbide formation at the surfaces is carried out mainly by photoelectron and ion spectroscopies. Main tool is X ray photoelectron spectroscopy (XPS) which probes core-level photoelectron binding energies and therefore yielding elemental identification of the electron-emitting atom, including its chemical environment. Ion spectroscopies comprise of techniques available from a 3 MV tandem accelerator, e.g. Rutherford backscattering spectrometry (RBS). In the experimental setup ARTOSS we combine both electron and ion spectroscopies together with sample cleaning and preparation facilities [3]. High-resolution XPS measurements are possible in a second UHV system, equipped with both a dual anode (Mg/Al) X ray source and a monochromatic Al X ray source [4]. This chamber is connected to a preparation chamber where films can be evaporated onto the samples and thermal treatments are carried out under UHV conditions. The samples used for the carbide formation studies are a beryllium (0001) single crystal, a silicon (100) waver, and polycrystalline foils of titanium and tungsten.

1. Room temperature reactivity

The C 1s peaks deposited at room temperature on the four elements Be, Si, Ti and W are plotted in Fig. 1 without background subtraction. The shaded area marks the binding energy regime where elementary carbon binding energies appear. The carbide binding energies (taken from the literature for Ti, Si, and W [5] and from a separate experiment for Be [6]) are shown in Fig. 1 by vertical lines. In all four cases a stoichiometric carbide is formed at the surface at room temperature. In the Ti case intensity is detected between the narrow TiC peak at 281.8 eV and the broadened elementary carbon signal at 284.2 eV. Photoelectron intensity at this binding energy around 282.6 eV between TiC and elementary carbon originates from substoichiometric Ti carbides like Ti_8C_5 or Ti_6C_5 [7,8]. The width of the peak originating from stoichiometric TiC equals the experimental resolution for this measurement and is considerably smaller than both the elementary and the substoichiometric carbide signals. A sharp XPS signal can only be observed for a phase which not only possesses exact stoichiometry but also exhibits a well-ordered and uniform local environment of the atoms giving rise to a photoelectron peak of identical energy. In this case of a carbon layer on Ti a well-ordered and stoichiometric TiC layer develops. In addition, substoichiometric carbides are present, however, only producing a broad range photoelectron intensity of smaller magnitude than for the TiC phase.

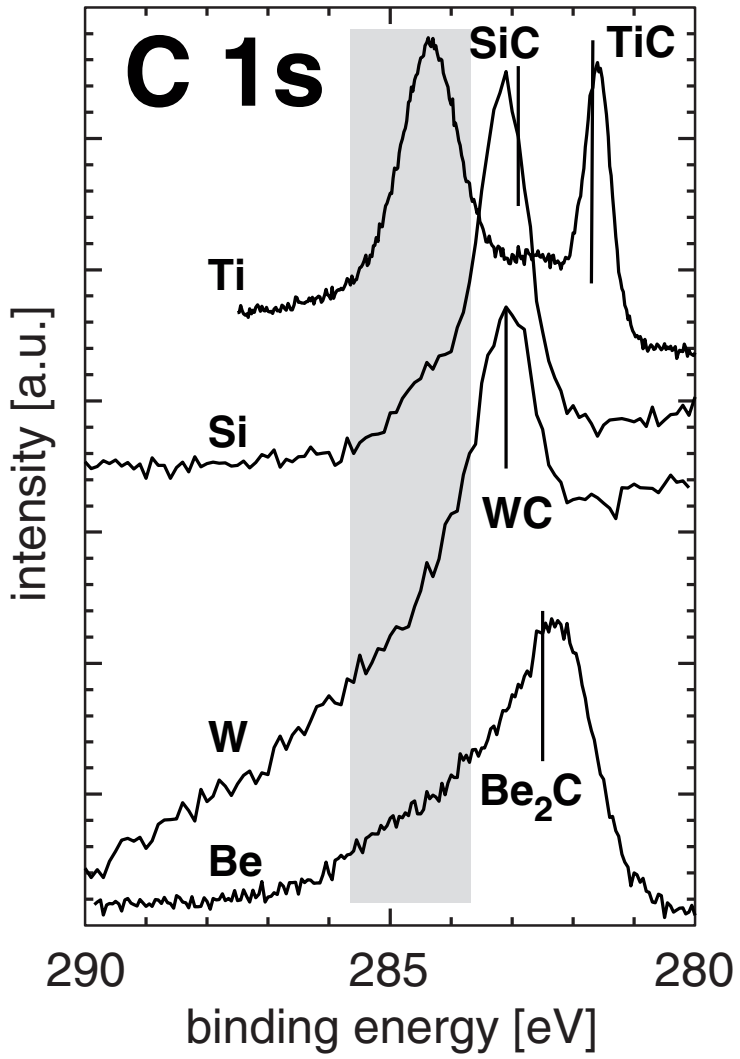

Fig. 1. Carbide formation at 300 K at the interface between elementary carbon layers and Ti, Si, W, and Be substrates. The C coverages are: approximately 2 ML C on Ti_{poly} and Be (0001); below 1 ML C on Si (100) and W_{poly}.

The formation of carbides is also observed for the three other elements (Si, W and Be) under study here. In all cases we find that for sub-monolayer carbon amounts the deposited carbon leads to a photoelectron peak at carbide binding energies. When the amount of carbon on the surface is increased, intensity in the elementary binding energy range appears. We conclude that impinging carbon atoms readily react with elementary surfaces. As soon as a monolayer of carbide has formed, this chemical interaction stops and further carbon deposited on the surface retains its elementary character. The carbon directly at the interface between substrate and adsorbed layer exhibits a charge density distribution which is characteristic for the respective carbide. A similar behavior is also observed for molybdenum [9].

The variation of the chemical state of deposited carbon with increasing carbon amounts on a Be surface is shown in Fig. 2. Plotted is the integrated intensity of the total C 1s binding energy range and the respective elementary and carbidic carbon intensities after depositing increasing amounts of carbon from an electron beam evaporation source. The carbon coverage is determined by RBS using ^{4}He at 600 keV. At the smallest carbon coverage, almost all C 1s intensity is localized at the carbide binding energy. With increasing carbon deposition, the

carbide amount increases up to a coverage of 1.2 ML. Further increase of the total carbon at the surface does not lead to the formation of further Be_2C. However, the carbon remains in the elementary chemical state. Therefore it can be concluded that at room temperature no diffusion through the adlayer takes place. Neither diffuses beryllium from the substrate through the formed carbide layer and reacts with freshly deposited carbon, nor is the elementary carbon at the surface able to diffuse through the formed Be_2C monolayer and reach metallic beryllium. Therefore, the carbide formation reaction stops after roughly one monolayer for Be_2C has been formed at the C–Be interface.

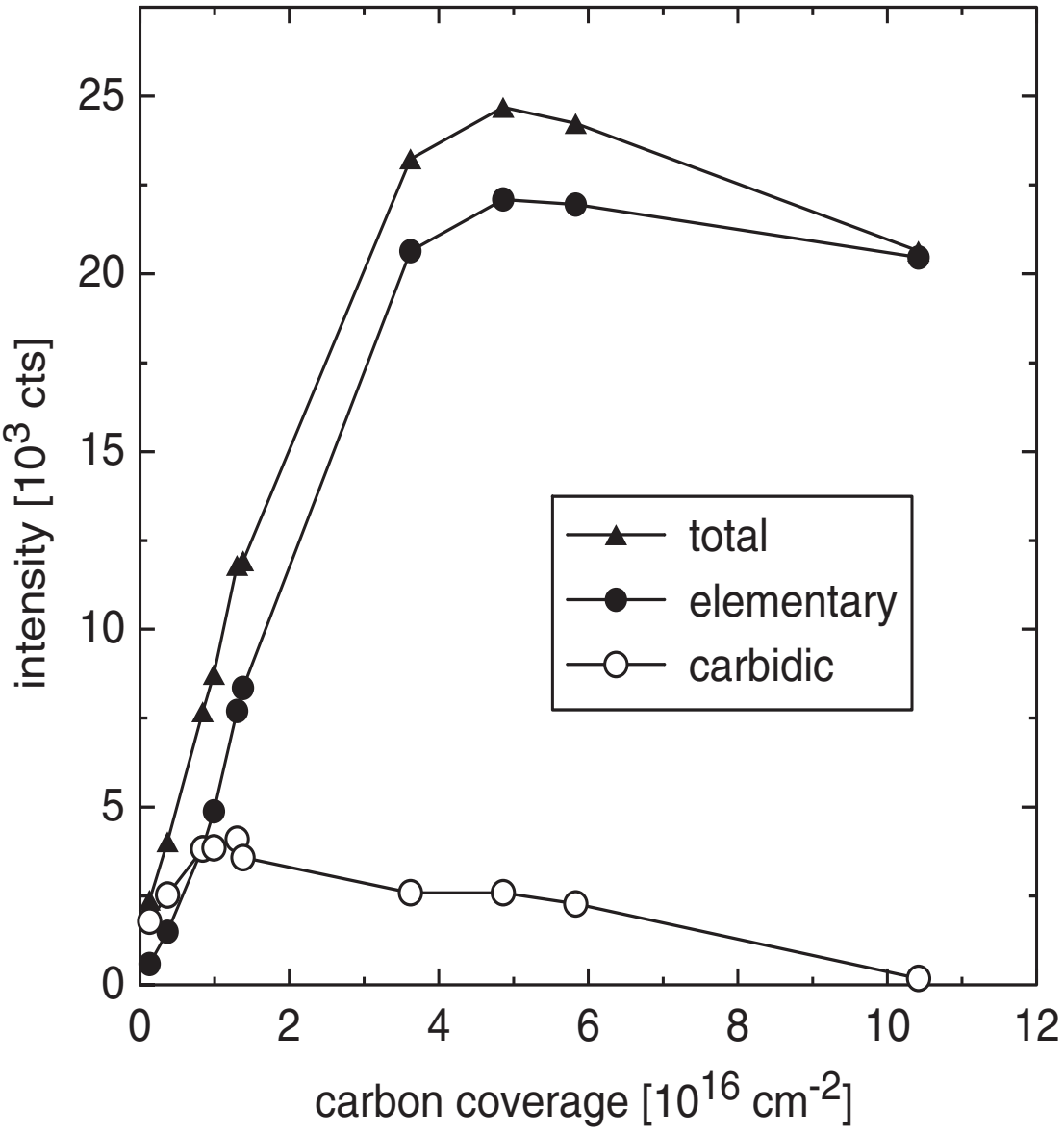

Fig. 2. XPS intensity in the C 1s region for a C/Be sample, plotted as a function of deposited carbon amount. The total C intensity can be separated in carbide and elementary C fractions.

With further increasing carbon coverage the carbide intensity actually decreases after the Be_2C monolayer has formed. This indicates that the carbide is situated at the very interface between the Be surface and the deposited carbon layer. The carbide photoelectrons from the C–Be interface are therefore attenuated on their way to the spectrometer through the elementary carbon overlayer. The attenuation of the photoelectrons is also visible in the

elementary and total C 1s intensities. With increasing carbon coverage the total carbon intensity rises almost linearly up to $3x10^{16}$ cm^{-2}. Above a carbon coverage of $4x10^{16}$ cm^{-2} the intensity levels off since the total depth of information for XPS (limited by the inelastic mean free path of photoelectrons) is reached. The maximum in the carbon intensity at a carbon coverage around $5x10^{16}$ cm^{-2} indicates a change in the surface morphology during the carbon deposition. The growing carbon layer initially exhibits a rough surface. Due to the roughness more carbon atoms are exposed compared to a flat surface. The decreasing carbon intensity above $5x10^{16}$ cm^{-2} suggests a flattening of the carbon layer around this fluence.

2. Carbide formation at elevated temperatures

The limited mobility of carbon or beryllium at room temperature limiting the carbide amount formed during these experiments to approximately one monolayer is also visible in Fig. 3. This figure shows the amount of carbon which has reacted to Be_2C as a function of the total carbon amount deposited at the surface, for sample temperatures between 300 K and 673 K. The bisecting line in this diagram thus indicates the quantitative formation of Be_2C. The intensity from the XPS measurements is calibrated against the RBS data thus giving absolute numbers for the carbon areal density. The measurements at 300 K and 373 K in Fig. 3 are very similar in initial slope and final carbide amount.

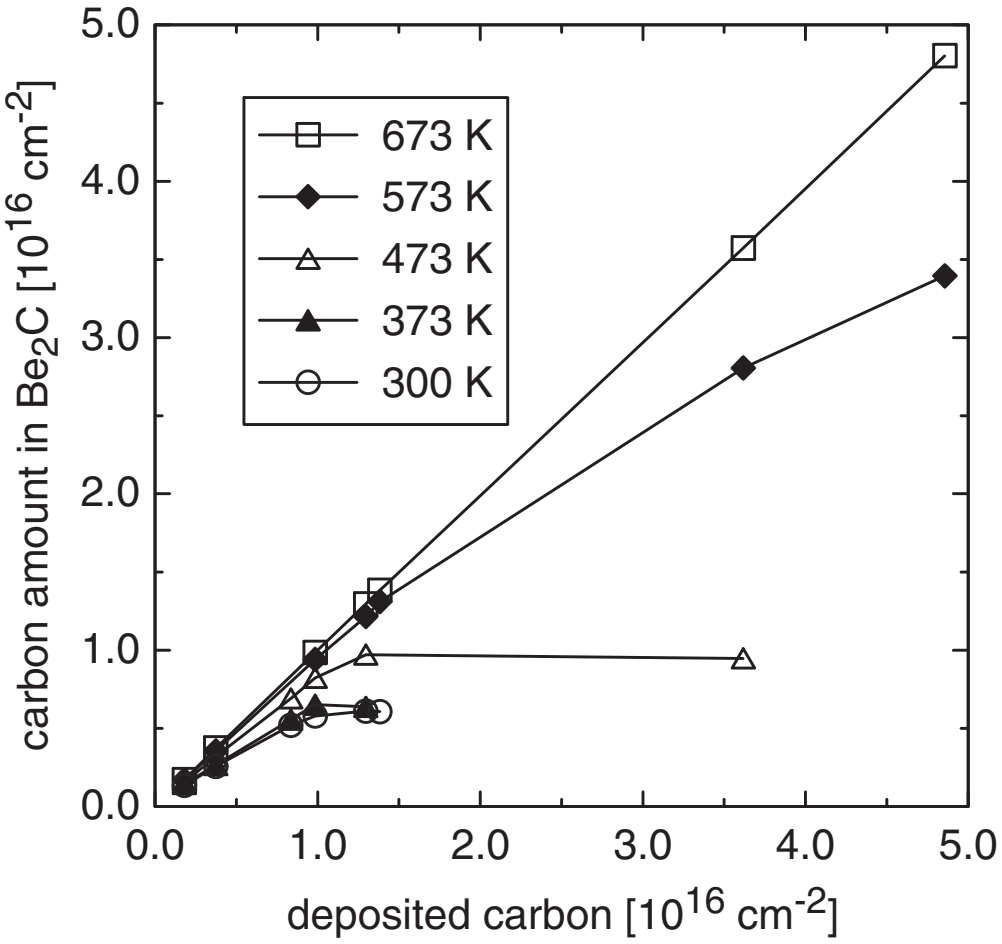

Fig. 3. Total amount of carbon bound in Be_2C at each temperature step as a function of the initially deposited carbon amount at 300 K. The data points at equal temperatures (but different samples) are connected to guide the eye.

The initial slope at these temperatures deviates notably from the bisecting line. This indicates that from the deposition start on the carbide formation is incomplete. There is always carbon deposited elementarily at the surface. The final amount of carbide indicated by the leveling of the curves is reached after carbon deposition of $1x10^{16}$ cm^{-2}. The carbidic carbon amount of $6x10^{15}$ cm^{-2} corresponds to 5.6 ML of Be_2C, calculated with a Be_2C bulk density of 1.90 g cm^{-3}. The reaction between carbon and beryllium at 473 K is still not quantitative from the start on. However, more carbon reacts with beryllium at this temperature and the final amount of carbide reached after the deposition of $1.3x10^{16}$ cm^{-2} corresponds to 12.2 ML Be_2C. Already at the substrate temperature of 573 K almost all deposited carbon reacts with beryllium initially. The curve starts to bend from the 45° line after a carbon amount of approx. $1.5x10^{16}$ cm^{-2}. Within these measurements no constant Be_2C amount is reached. This is also true for the experiment at a Be substrate temperature of 673 K. The amount of carbon converted to Be_2C corresponds in the whole range examined to the total amount deposited at the surface. All data points lie well on the bisecting line. These measurements demonstrate that the amount of carbide is characteristic for a given temperature, provided that sufficient elementary carbon is available. A similar behavior was described by Miller for titanium layers on carbon [10].

RBS measurements which probe the total amount of carbon on beryllium substrates show that the carbide layer formed at the metal surface is stable up to temperatures of 900 K [11]. Neither diffusion of carbon into the Be bulk nor diffusion of Be metal through the carbide surface layer is observed. The stability of the carbide layer on Be is explained by the nature of the chemical bond in Be_2C. This compound is of ionic nature where the solid constituents are Be^{2+} and C^{4-} ions, respectively. Diffusion of one lattice species through the solid requires to overcome the Coulomb barrier between ionic species.

A different diffusion behavior of carbon can be expected for transition metals (e.g. W, Ti) which form metallic carbides. These carbides are characterized by a lattice structure defined by metal atom packings. Carbon atoms are positioned at sites defined by the metal atom structure, e.g. octahedral sites ion the case of TiC or trigonal prismatic sites in WC. Since there are equal amounts of those sites and metal atoms, a complete occupation of all sites in the metal lattice by carbon atoms defines the composition *M*C (e.g. WC, TiC). In subcarbides (e.g. W_2C), half of the octahedral sites of a W hcp (hexagonal close packed) structure are occupied by carbon, usually in an ordered way. However, since there is a number of energetically equivalent sites within arrangements defined by spheres packing, diffusion between these equivalent sites is easily possible. The small energy barriers between the sites are also the reason why some transition metals not only form compounds of exact stoichiometry. Phases with varying stoichiometry exist. This is the case for Ti, where the TiC phase has a compositional range of 32 to 48.8 at.% C [12].

The composition changes and carbon diffusion for a carbon film on tungsten at different temperatures are shown in Fig. 4. Fig. 4a shows the composition of the surface layer accessible by XPS, calculated from the C 1s and W $4f_{7/2}$ photoelectron peaks. The result of the C 1s deconvolution is shown in detail for the temperature range 873 K to 1373 K in Fig. 4b. Beginning at room temperature, the chemical state of carbon is elementary with a very small contribution of WC which stems from the carbide layer at the C–W interface. The elementary carbon itself shows two states: most of the carbon (roughly 2/3) features an ordered graphitic configuration, whereas a minor part (1/3) is also graphitic, but with a locally disordered structure [13]. This disordered graphite converts into an ordered phase during temperatures up to 870 K. The total amount of carbon in the surface layer stays constant. The carbide fraction

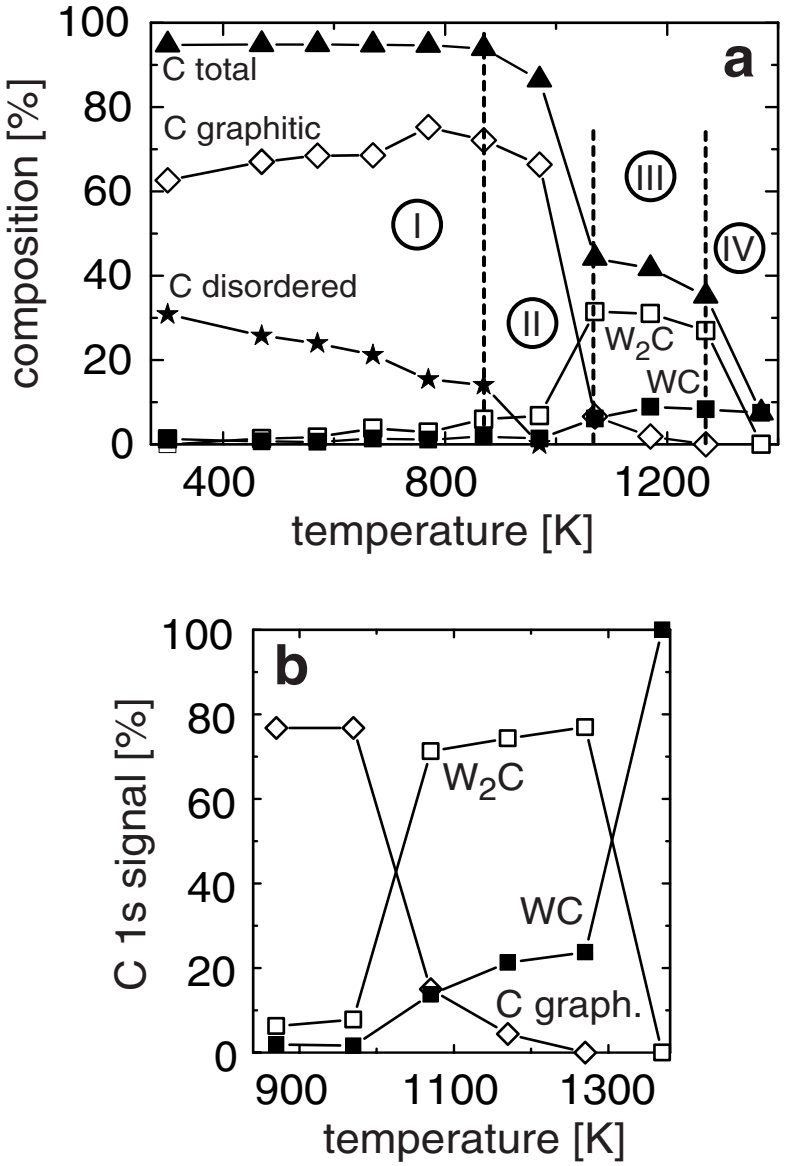

Fig. 4. (a) Surface composition of a 1.5 nm carbon film deposited on tungsten, as a function of annealing temperature. The dashed lines indicated the four phases during the carbidization process on tungsten. (b) Relative fractions of the C 1s intensity within the temperature range where major carbide amounts are formed.

increases only slightly up to this temperature. At 970 K a chemical reaction between elementary carbon and metallic tungsten sets in. In the C 1s spectrum a new binding state is necessary to fit the experimental data and the W $4f_{7/2}$ peak shifts to higher binding energies, indicating carbide formation. The total carbon intensity starts to decrease. Between 1070 K and 1270 K the carbon is predominantly bound in W_2C with decreasingly smaller fractions of elementary carbon and an increasing part of carbon in bound WC. In this temperature regime the loss of carbon from the surface layer is reduced after the strong drop around 1000 K. The surface layer still contains around 40 at.% of carbon. Another significant change in the carbon content is observed after heating the sample to 1370 K. The total C 1s intensity decreases and the W $4f_{7/2}$ signal is dominated by metallic tungsten. Carbon is diffused into the tungsten bulk to a substantial degree.

As indicated in Fig. 4a the temperature range can be divided into four regions. In phase (I) only carbide formed during the sample preparation exists. Disordered parts of carbon in the elementary carbon layer order with increasing temperature. Phase (II) starts between 870 K and 970 K. A part of elementary carbon reacts with tungsten under W_2C formation. The total amount of carbon within the XPS analysis depth significantly decreases. At 1070 K a transition from phase (II) to phase (III) occurs. In this phase W_2C dominates which is particularly obvious in Fig. 4b which shows the relative parts of the carbon chemical states in the C 1s integral. W_2C is formed by carbon atoms located at the octahedral sites in a hcp W arrangement. To form W_2C from W and C from the deposited layer, transport of C atoms to these sites is necessary. This explains the strong decrease of the C 1s signal upon W_2C formation. Besides W_2C also WC develops where carbon is located in trigonal prismatic sites in a hexagonal primitive W packing. After the W_2C formation further decrease of the carbon amount is slowed down until the transition from phase (III) to phase (IV) at 1270 K. In phase (IV) all carbon exists as WC. The total carbon amount within the XPS analysis region has further decreased strongly.

The strong decrease of the carbon intensity during the thermal treatments of a 1.0 nm carbon layer on polycrystalline Ti is shown in Fig. 5. After deposition, the carbon is predominantly elementary, only at the C–Ti interface TiC is present. The carbide fraction rises from 2 at.% at 300 K to 18 at.% after heating the sample to 670 K. At higher temperatures the total carbon intensity significantly decreases. In the spectrum after 770 K only 38 at.% of the initial C 1s intensity are present. The peak is shifted completely to the binding energy of TiC at 281.8 eV and the part of subcarbide (denoted by Ti_xC_y) rises to 18 at.%. The C 1s intensity after the 870 K treatment has almost vanished, it remains only 0.7 at.% of the initial value at 300 K. The total intensity after the 870 K treatment is located at

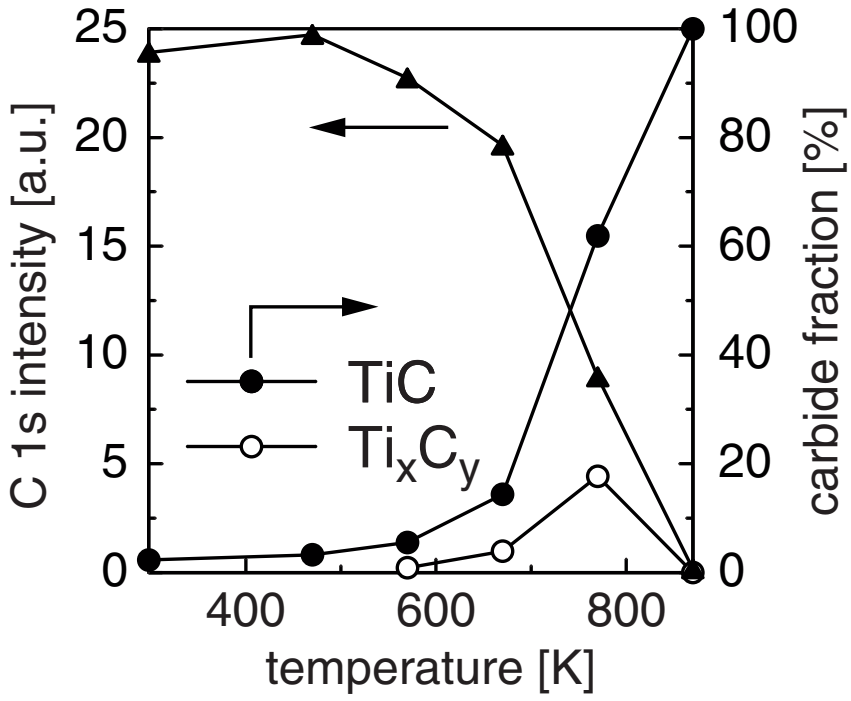

Fig. 5. XPS temperature profile from a 1.0 nm C layer on polycrystalline Ti. Plotted are the carbide and subcarbide contributions to the total C 1s intensity (circles) and the decrease of the total C 1s intensity (triangles).

the TiC binding energy, no elementary carbon or carbon in Ti subcarbides are present. TiC is a metallic carbide, similar to WC. However, during the phase transition from metallic Ti over subcarbides with varying stoichiometry, the host atoms remain in their hcp structure and the carbide stoichiometry is determined by the degree of occupation of the octahedral sites by carbon atoms. This explains the broad phase range of the subcarbides and also the truly substoichiometric nature of TiC where always carbon vacancies exist.

The interaction of carbon with elemental surfaces of Be, Ti and W is determined both by the chemical reaction between carbon and the metals and by the diffusion of carbon in the substrate material. All carbides discussed here have negative enthalpies of formation, listed in Table 1. The formation of carbides from the elements releases energy and therefore takes place spontaneously if carbon and metal atoms are both available. The availability in the layered samples under study here is in turn governed by the diffusion of carbon towards the metal (or metal diffusion into the carbon layer). Besides chemical driving forces for atom mobility the structure of the solid and types of chemical bonds are crucial. As soon as a carbide has formed at the interface (which takes place spontaneously upon deposition of carbon on the clean metal surfaces) the atoms must diffuse through a growing carbide layer. This diffusion is easily possible in case of the transition metals Ti and W, which form metallic carbides. Here, carbon atoms occupy void lattice sites in the metals' host structure which is best described in both cases by packings of spheres. Many energetically equivalent sites are present in the host lattice. Therefore, only a small activation barrier has to be overcome for carbon atoms changing sites. Since we start with a layered structure, both entropic and chemical driving forces lead to the dilution of carbon atoms in the bulk metals at elevated temperatures. In the case of tungsten structural rearrangements are necessary during the transition from metallic tungsten (body centered cubic, bcc) to W_2C (hexagonal close packing, hcp) and WC (hexagonal primitive). The two carbide phases can be well distinguished in the experiment during the temperature increase. Such a restructuring is not necessary in the Ti system, since metal and carbides all have hcp structures. Since no restructuring is necessary during the metal-carbide transition, this may be the reason that the subcarbide phase is not specifically visible during the carbide formation reaction. In contrast to the metallic carbides of Ti and W, Be_2C is an ionic solid. Diffusion of species here means that ions must travel through the lattice whereby Coulomb forces have to be overcome. The experiments show that the carbide layers on Be substrates are stable up to 900 K. This observation correlates well with this picture. In Fig. 6 the elements Be, Ti and W are compared during the carbide formation. Plotted are the C 1s intensities (normalized to the value after carbon deposition at 300 K) for increased sample temperatures. Also plotted as a reference are the results of a similar experiment using Au as substrate. Gold is inert towards carbide formation and carbon is insoluble in gold [12]. Therefore, no intensity drop due to compound formation or carbon diffusion into the Au bulk is expected. For the reactive metals an initial phase can be identified starting at room temperature in which only small carbon losses take place. They can be interpreted by some intermixing between carbon and substrate material. After this initial phase all three metals exhibit a characteristic temperature where the carbon intensity drops significantly. We identify this phase with quantitative carbide formation. At the end of this temperature region all available carbon is chemically in the carbidic state. For Be and W a final phase can be identified where the C 1s intensity drop stops or at least strongly slows down. In case of Be the carbon intensity stays at a high level indicating the stability of the formed carbide. No diffusive losses to the bulk take place for this ionic carbide. For W, only a small amount of carbide is present at the surface. The majority of the carbon has been lost by diffusion into the bulk substrate. In the case of Ti, this final phase lacks completely. Diffusion of carbon in Ti is so strong that finally only traces for TiC remain detectable in the surface layer.

Table 1. Free enthalpies of formation (ΔG_f) for binary carbides of Ti, Be and W [14].

Compound	**ΔG_f [eV]**
TiC	-1.88
Be_2C	-1.19
WC	-0.40
W_2C	-0.23

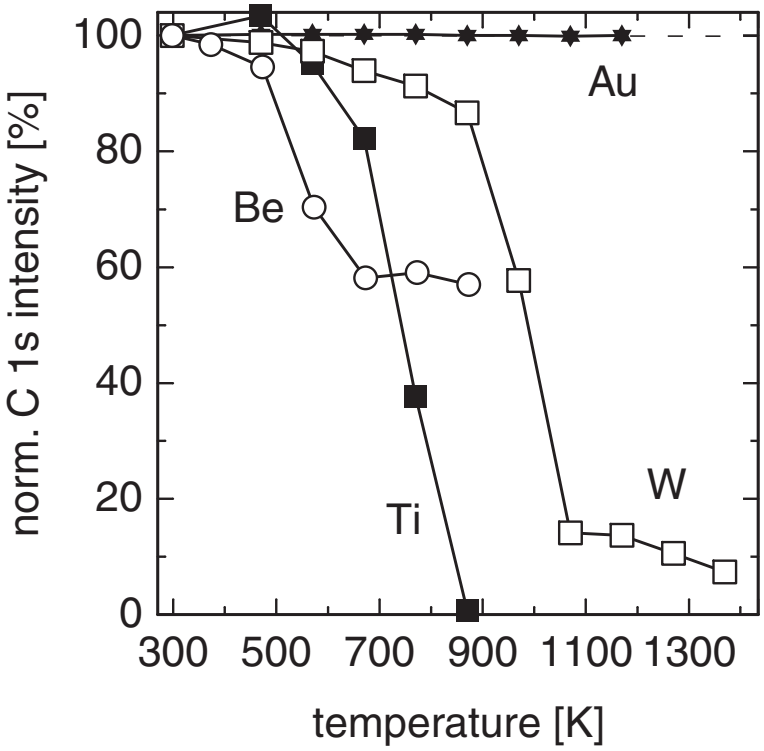

Fig. 6. Changes in the XPS C 1s intensities during annealing of thin carbon films deposited at 300 K on the indicated materials. The curves are normalized to the initial carbon intensity (100 %).

II: Erosion behavior of mixed materials

In fusion devices the deposition of non-recycling impurity atoms will always be in the form of energetic ions. Therefore implantation and phase formation will proceed simultaneously with ion induced erosion. In the following this situation will be discussed for the bombardment of typical plasma facing materials, such as W, Be, Ti and Si, with carbon ions.

1. Estimates from kinetic Monte Carlo code simulations

First investigations [15] on the dependence of the erosion yield of W under carbon ion bombardment have been performed previously at room temperature and interpreted using the Monte-Carlo Code TRIDYN [16]. The erosion and deposition processes occurring during C bombardment were investigated by *in situ* monitoring of the samples weight change as a

function of the applied C fluence. Fig. 7a shows the weight change of a W sample due to carbon bombardment at different angles of incidence. The typical shape of the weight change observed in these experiments can be seen in the 0° or 35° graphs in Fig. 7a. Initially the sample's weight decreases due to W erosion, moves through a transition point and then starts to increase again. The occurrence of the transition point an the proximate increase of the samples weight is due the deposition of C. This formation of a C layer is dominated by the carbon self sputtering yield . At normal incidence, carbon self sputtering is always below unity and protective layers build up. At grazing angles of incidence the self sputtering yield increases above unity, leaving the substrate surface open for continuous erosion as can be seen in the 70° graph in Fig. 7a [15]. The limits for W erosion and C deposition in the parameters space of energy and angle of incidence is shown in Fig. 7b. The agreement of the transition from deposition to erosion with calculations of the energy and angle of incidence where the sum of self sputtering yield and reflection coefficient is equal to unity [17] underlines the importance of the self sputtering yield of carbon. These code calculations cannot take into account effects of enhanced surface temperatures, such as the diffusion of carbon in the bulk W, carbide phase formations or the radiation enhanced sublimation (RES) of carbon, which dominates the self sputtering at enhanced temperatures.

These processes lead to a temperature dependence of erosion by carbon. Diffusion and RES introduce additional C loss channels from the surface thereby hindering the formation of a protective C layer. They can inhibit layer formation above a certain temperature threshold and lead to continuos erosion of the substrate material. For all materials under examination here carbon will accumulate at the surface at room temperature, thus forming a protection layer for erosion and the steady state erosion yield of the substrate material will be zero. However, the surface will no longer be that of the substrate material originally intended, but a carbon surface! With increasing temperature the formation of carbides can change the erosion behavior of the substrate material by increasing the surface binding energy of the atoms which governs sputtering at a given energy and angle of incidence. This is especially true for carbides with a high energy of formation like Be_2C and SiC.

From the results presented in section I estimates for the influence of diffusion and phase formation can be obtained The sputtering yield of Be and Si, which form stable carbides at 500 K and 1100 K, respectively, is expected to be reduced compared to the clean material. In the case of Ti and W diffusion becomes fast enough to leave the surface almost unchanged by the implanted carbon atoms at temperatures above 800 K and 1000 K, respectively. For Au no phase formation or inward diffusion could be found up to 1500 K and the deposition of carbon layers should prevent erosion at all temperatures.

2. Temperature dependence of W erosion due to carbon ion bombardment

The temperature dependence of erosion / deposition due to carbon ion bombardment has been investigated in detail for W, Ta, Pt and Au [18] and examples will be given here for the C^+/W system. Fig. 8 shows the fluence dependence of the weight change of a W sample bombarded at normal angle of incidence with 2.4 keV C^+ ions at different temperatures.

While at room temperature the data agree well with the behavior shown in Fig. 7a, already at 773 K a slower weight increase is observed at high fluences. This is an indication of an enhanced self sputtering yield after the deposition of a carbon layer on the W surface and must be interpreted in terms of RES of carbon [18,19]. With further increasing temperature

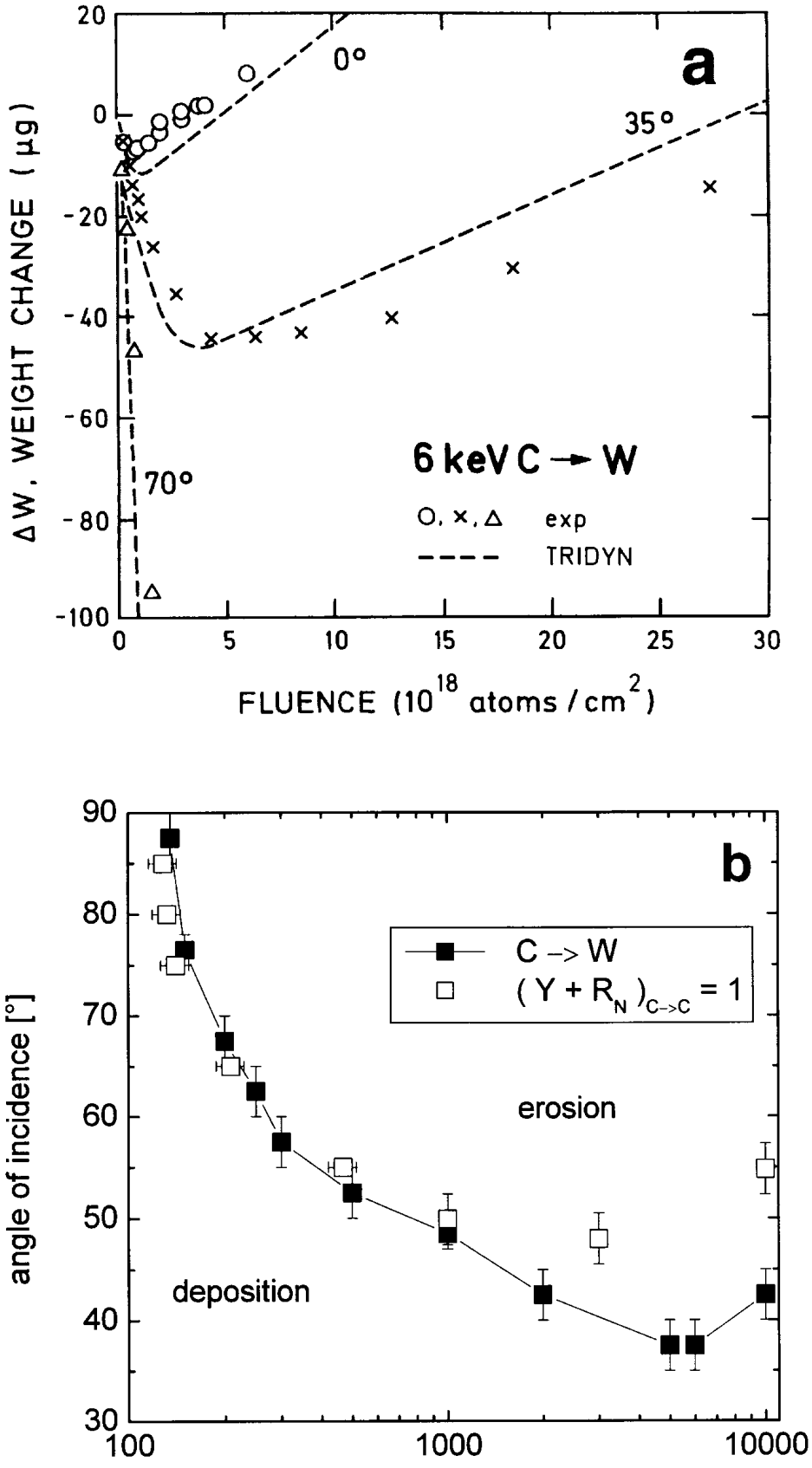

Fig. 7. C^+ ion bombardment of tungsten. a) weight change as a function of applied carbon fluence for 0°, 35° and 70° angles of incidence (with respect to surface normal) b) angular and energy dependence of the transition from erosion to deposition.

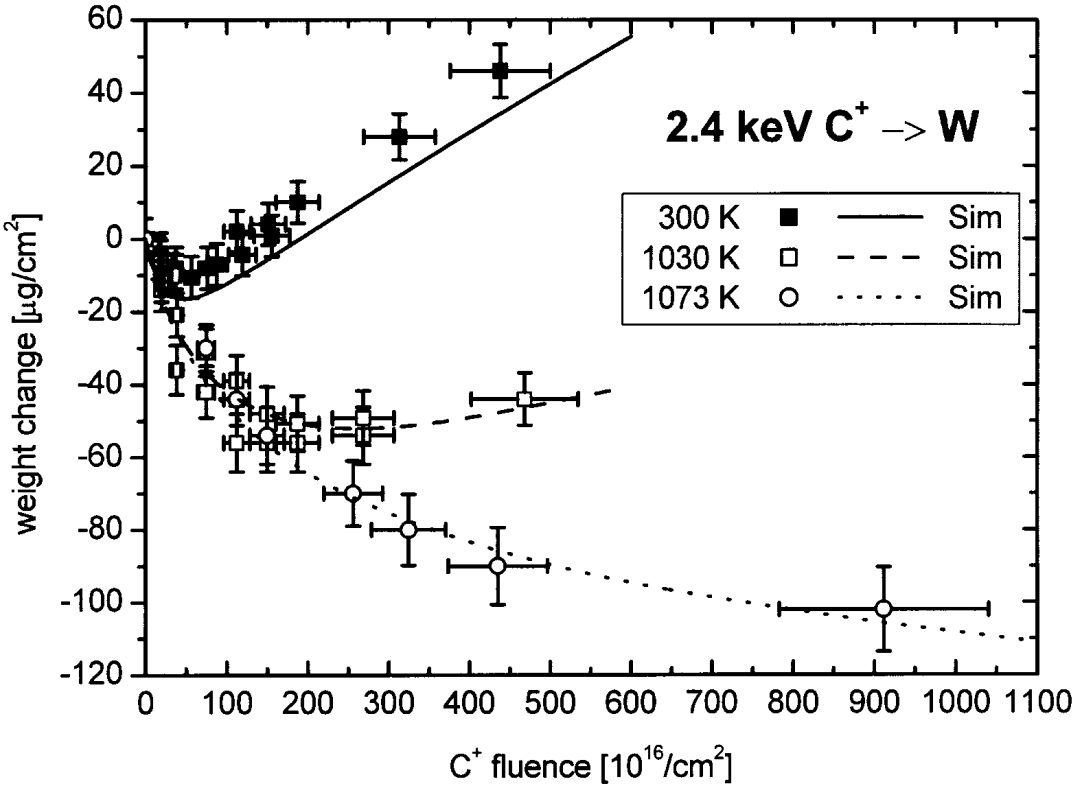

Fig. 8. Comparison of experimental and simulated weight change data of 2.4 keV C^{+} → W in the temperature range from 300 K to 1073 K.

the initial weight loss extends to higher fluences. This can be interpreted as the manifestation of carbon diffusion into W in competition with carbon implantation, thus leaving the surface exposed to erosion to higher carbon fluences. The final weight increase has again a smaller slope due to the RES increase with temperature [19,20]. In order to simulate the observed behavior in separate experiments the RES erosion yields and the diffusion coefficient of carbon in W are determined from the interdiffusion of carbon layers on W samples at elevated temperatures. Measurements of the carbon self sputtering yield demonstrate that the effect of RES extends down to room temperature and must be taken into account for all elevated temperatures [18]. The data is collected in Fig. 9 and agrees well with literature data for the RES yield at higher temperatures [19,20]. The diffusion coefficients are found to be strongly depended on carbon concentration, decreasing more than an order of magnitude for carbon concentrations above 30 at.% in the investigated temperature range up to 1173 K [21]. In Fig. 10 the concentration dependent diffusion coefficient D(C) for low C concentrations [21] is compared with literature data [22]. Literature data are quite scattered and the low concentration values of D(C) from [21] lie between literature data for diffusion of C in W and in WC. At temperatures above 1200 K the diffusion of carbon is so fast that a carbon ion flux of 1.5×10^{14} $cm^{-2}s^{-1}$ is insufficient to result in complete surface coverage. The surface remains uncovered by carbon at high fluences and continuous weight loss occurs. The lines shown in Fig. 8 were obtained by computer calculations that took into account the simultaneous erosion/deposition and diffusion processes by coupling the Monte-Carlo code TRIDYN [16] with the new diffusion code DIFFUSEDC [18]. In this coupled approach the application of a certain fluence Φ is approximated by discrete fluence steps $\Delta\Phi$ and time steps Δt. Each step starts with a TRIDYN calculation during which the implantation of a fluence

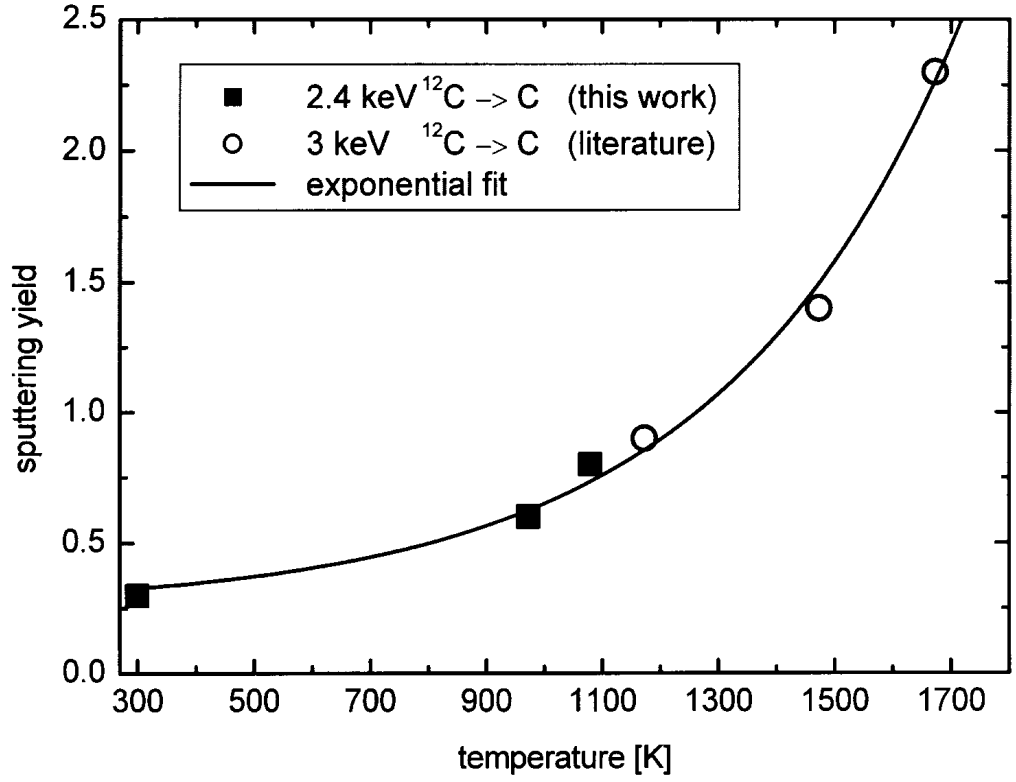

Fig. 9. Temperature dependence of the C self sputtering yield together with an exponential fit to the available data.

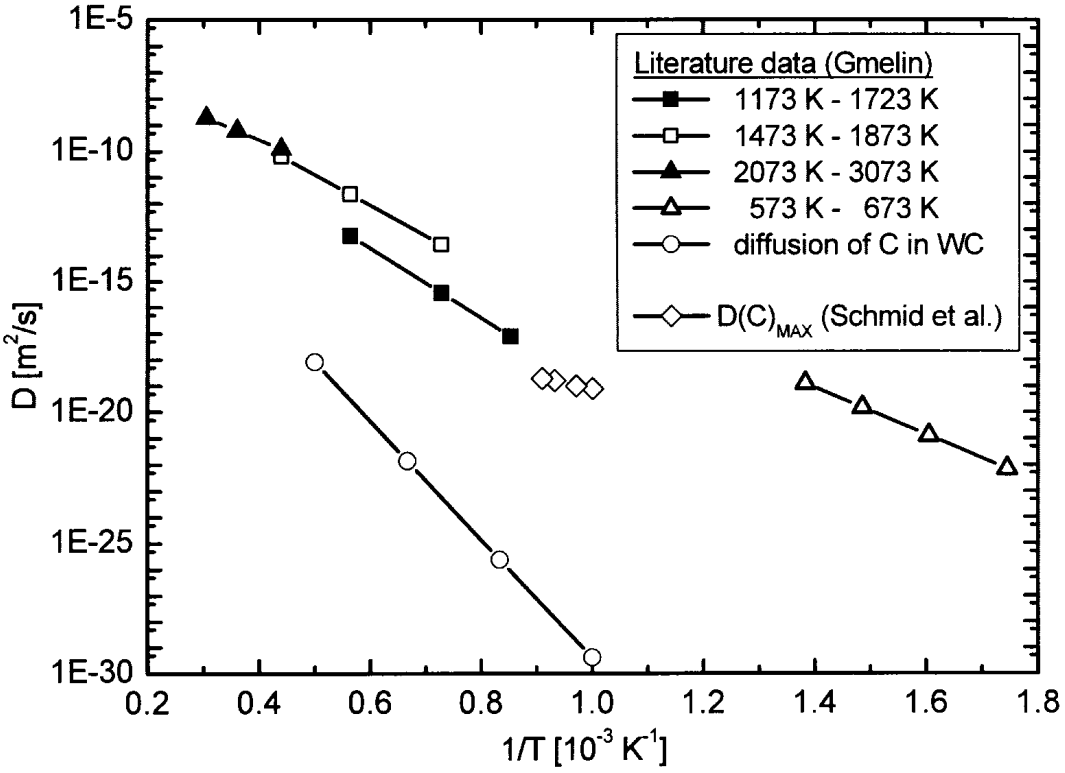

Fig. 10. Summary of available data on diffusion of C in W and C in WC.

$\Delta\Phi$ is simulated, thereby taking the enhanced carbon erosion due RES into account by reducing the surface binding energy. The resulting carbon depth profile then serves as the input into a DIFFUSEDC calculation during which the evolution of the implanted carbon due to diffusion during a time period Δt is simulated. The result of this calculation in turn serves a input in the next TRIDYN run. This cycle is repeated N times with $N = \Phi/\Delta\Phi$. In this calculations the discretization parameters $\Delta\Phi$ and Δt were chosen small enough that the implantation and diffusion processes can be considered to occur simultaneously. The agreement of the curves and the experimental data without additional free fitting parameters indicates the diffusion and RES are the responsible processes for the temperature dependence of erosion/deposition.

Other high-Z target materials yield qualitatively similar results but are different in details. For Ta, carbon diffusion coefficients are known to be about two orders of magnitude smaller than for W, thus making diffusion negligible in the temperature range up to 1200 K. The experimental data show a strongly reduced erosion phase at small fluences and a deposition phase in agreement with the temperature dependent RES yields. Bombardment of Au results in a carbon layer deposition at any temperature up to 1073 K, which starts to flake off at high fluences [18].

3. Multi-species ion bombardment

In fusion devices, typically, the plasma facing components are bombarded simultaneously by different ion species. Together with the flux of impurity ions, such as carbon, oxygen or atoms from wall materials, a much larger flux of fuel ions, i.e. hydrogen isotopes, impinges onto the surface. In order to simulate the simultaneous impact of carbon and hydrogen ions, CH_3^+ ions were used in comparison with C^+ ions [19]. The CH_3^+ energy was chosen at 3 keV such that the carbon ions obtain the same energy as in the case of single C^+ bombardment at 2.4 keV. The equivalent energy for hydrogen is 200 eV. In Fig. 11 the fluence dependence of erosion by CH_3^+ is compared to C^+ ions. Already at 300 K an increased erosion yield for CH_3^+ is found. CH_3^+ at 1000 K leads to continuos weight loss of the sample. In simulations of the erosion/deposition due to CH_3^+ the additional erosion (physical + chemical) due to the incident 200 eV hydrogen atoms must be taken into account. In this case TRIDYN may simulate the physical sputtering yield, while additional chemical erosion effects [23] must be taken into account separately. Chemical erosion is therefore added as an additional step (YCHEM) in the TRIDYN + DIFFUSEDC coupling cycle described above. In YCHEM the carbon depth profile calculated by TRIDYN is modified according to a given chemical sputtering yield analogous to the dynamic surface relaxation performed by TRIDYN. In order to simulate the results of CH_3^+ bombardment on W depicted in Fig. 10, two types of calculations were performed. At 300 K where diffusion is negligible only TRIDYN+YCHEM is used with chemical erosion yield of 4%. The high temperature bombardment at 1000 K is simulated using the full sequence TRIDYN+DIFFUSEDC+YCHEM. The agreement with the experimental data in excellent. The resulting code package now allows the simulation of erosion/deposition in divertor or first wall conditions under fusion experiments which cannot be reproduced directly in ion beam experiments.

The simultaneous impact of different impurity ions, such as C^+ and O^+, is simulated by bombardment with CO^+ ions. As substrate in this case Be was chosen [24,25] and the CO^+ ion energy was 3 keV.

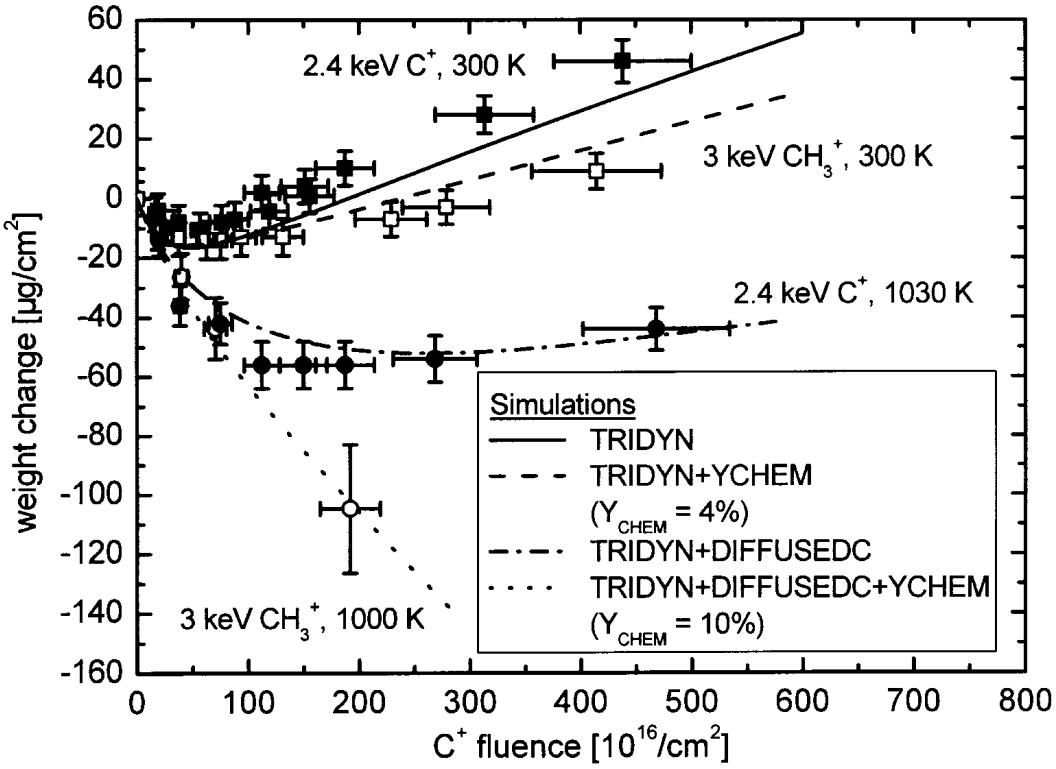

Fig. 11. Comparison of the temperature dependence of the W samples weight change during C^+ and CH_3^+ bombardment.

While at room temperature a carbon layer is deposited, as in the case of W, CO^+ bombardment results in a saturation of the deposited amount of both C^+ and O^+. The erosion of carbon by oxygen ions is higher than unity [26] such that a surface concentration less than 100 at.% C results in an eroded carbon flux equal to the incident CO^+ ion flux. Such a high erosion yield must be due to chemical re-erosion of deposited carbon by oxygen atoms, where CO and CO_2 formation is found [26,27]. Chemical phase analysis shows a surface layer of BeO intermixed with amorphous carbon [28]. The coverage does not protect the Be substrate from erosion. At room temperature continuous weight loss of the Be sample prevails (Fig. 12).

The erosion yield of Be increases with increasing surface temperature up to 473 K, indicating a reduced Be coverage by carbon. This may be due to enhanced C erosion or by diffusion of Be to the surface. At further elevated temperatures initially a weight increase occurs, turning into erosion at high fluences. Depth profiling of C and O after reaching steady state erosion reveals the increasing interdiffusion of Be with C and O which results in the initial weight increase.

Conclusions

Under bombardment with non-recycling impurities the surfaces of pure materials used as plasma-facing component will be modified. This modification has been investigated for the case of bombardment by carbon ions or CO^+ and CH_3^+ molecules. Substrates investigated are Be, Si, Ti, and W.

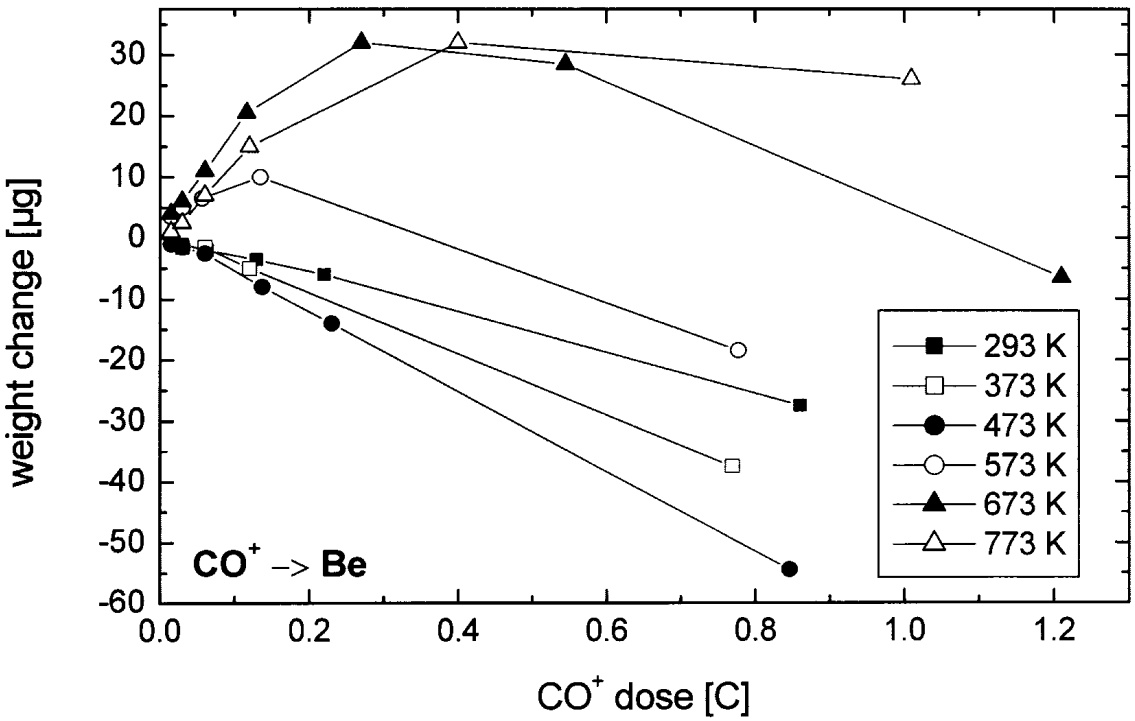

Fig. 12. Weight change of a Be target during 3 keV CO^+ bombardment in the temperature range from 293 K to 773 K.

The chemical interaction of carbon with these materials is investigated by deposition of elementary carbon layers and subsequent thermal treatment. The processes of chemical phase formation (carbidization) and diffusion have been analyzed by X ray photoelectron spectroscopy. Carbide formation was observed in all cases. Carbon diffusion into the bulk at elevated temperatures is observed for the transition metals Ti and W. For Be and Si, however, which are forming ionic and covalent carbide compounds, respectively, no carbon diffusion into the bulk takes place. For W and Ti, both subcarbides and carbides with different stoichiometries are identified.

At room temperature and normal angle of incidence on all elements a carbon layer is deposited by C^+ ion bombardment, protecting the underlying substrate from erosion. At elevated temperatures the formation of compounds and carbide phases occur. The temperatures where carbide formation sets in correlates with the heat of formation of the different carbides. Simultaneously, interdiffusion of implanted carbon atoms and substrate atoms occur.

These modifications at elevated temperatures have strong influence on the erosion behavior of the substrate. Transitions from deposition to erosion occur at elevated temperatures and a detailed investigation is presented for the case of C^+ and CH_3^+ bombardment of W. The transition temperature depends on the diffusion coefficient for carbon into W and on the temperature dependent self sputtering yield of carbon. Using these data the erosion behavior can be simulated in a modified TRIDYN code and extrapolated to the conditions in future fusion reactors.

Multi-species ion bombardment were simulated using CO^+ and CH_3^+ ions and show additional complications due to the chemical interaction of the incident species. In order to simulate multi-species bombardment as expected in fusion plasma conditions dual beam

experiments will have to be performed where ion fluxes can be varied independently. Additionally, drastic differences are expected with respect to hydrogen retention and diffusion in mixed material surfaces and needs to be investigated.

REFERENCES

[1] J.P. Coad, H. Bergsåker, S. Burch, G. Kaveney, F. Lama, G.F. Neill, J. Partridge, J.C.B. Simpson, and J. Vince, J. Nucl. Mater. 176&177 (1990) 145.
[2] Ch. Linsmeier, J. Luthin, and P. Goldstraß, J. Nucl. Mater. 290-293 (2001) 25.
[3] Ch. Linsmeier, P. Goldstraß, and K.U. Klages, Physica Scipta T 94 (2001) 28.
[4] S. Miller, G. Berning, H. Plank, and J. Roth, J. Vac. Sci. Technol. A 15 (1997) 2029.
[5] J.F. Moulder, W.F. Stickle, P.E. Sobol, and K.E. Bomben, *Handbook of X ray Photoelectron Spectroscopy*, Ed. J. Chastain, Perkin-Elmer Corp., Eden Prairie (1992).
[6] P. Goldstraß and Ch. Linsmeier, Nucl. Instrum. and Meth. B 161-163 (2000) 411.
[7] B.V. Khaneko, S.Ya. Golub, and M.P. Arbuzov, Kristallografiya (1980) 112.
[8] N.V. Dzhalabadze, B.G. Eristavi, N.I. Maisuradze, and E.R. Kuteliya, The Physics of Metals and Metallurgy 86 (1998) 59.
[9] P. Reinke and P. Oelhafen, Diamond Relat. Mater. 8 (1999) 155.
[10] S. Miller, PhD thesis, Universität Bayreuth (1997).
[11] P. Goldstraß, K.U. Klages, and Ch. Linsmeier, J. Nucl. Mater. 290-293 (2001) 76.
[12] T.B. Massalski, H. Okamoto, P.R. Subramanian, L. Kacprzak, *Binary Alloy Phase Diagrams*, 2nd Ed., Version 1.0, ASM International, Materials Park, Ohio (1996).
[13] J. Luthin and Ch. Linsmeier, Surf. Sci. 454–456 (2000) 78.
[14] I. Bahrin, *Thermochemical Data of Pure Substances*, 3rd Ed., Vol. 1&2, Weinheim (1995).
[15] J. Roth, W. Eckstein, J. Bohdansky J. Nucl. Mater. 165 (1989) 193.
[16] W. Möller, W. Eckstein, Computer Physics Communications 51 (1988) 355-368.
[17] W. Eckstein, J. Nucl. Mater. 281 (2000) 195.
[18] K. Schmid, PhD Thesis, Universität Bayreuth (2002).
[19] K. Krieger, J. Roth, J. Nucl. Mater. 290-293 (2001) 107.
[20] J. Roth, J. Bohdansky, W. Ottenberger, J. Nucl. Mater. 165 (1989) 193.
[21] K. Schmid and J. Roth, J. Nucl. Mater. 302 (2002) 96.
[22] Gmelin Handbook, W, Suppl. Vol. A 5b (1993).
[23] J. Roth, J. Nucl. Mater. 266-269 (1999) 51.
[24] P. Goldstraß, PhD thesis, Universität Bayreuth (2000) and IPP-Report 9/126 (2000).
[25] P. Goldstraß, W. Eckstein, and Ch. Linsmeier, J. Nucl. Mater. 266-269 (1999) 581.
[26] E. Hechtl, J. Bohdansky, J. Roth J. Nucl. Mater. 103&104 (1981) 333.
[27] E. Vietzke, A.A. Haasz, in: "Physical Processes of the Interaction of Fusion Plasmas with Solids" Eds: W.O. Hofer, J. Roth (Academic Press London 1996) p. 135.
[28] P. Goldstraß, Ch. Linsmeier, J. Nucl. Mater. 290-293 (2001) 71.

EROSION OF DOPED GRAPHITES AND DIII-D TOKAMAK TILES

A.A. HAASZ, J.W. DAVIS, A.Y.K. CHEN, P.B. WRIGHT,
R.G. MACAULAY-NEWCOMBE

Abstract

Results are presented on the effect of dopants in graphite on chemical erosion and radiation-enhanced sublimation (RES). Threes sets of experiments are presented. (i) One set of erosion experiments was performed with specimens fabricated by Ceramics Kingston Ceramique Inc. (CKC). Of all the CKC specimens studied, boron doping with ≥8 at% surface concentration (<1 μm) provides the best resistance to hydrocarbon formation; up to a factor of 5 reduction in the CH_4 yield is observed. Somewhat smaller improvements have been seen for the Ti and Si-doped specimens. The most significant reduction in RES is observed for specimens with 13.8 at% B and specimens with 5.0 at% Ti surface concentrations (<1 μm); reductions of factors of 3-5 have been seen at 1800 K. (ii) The second set of experiments was directed to the study of chemical erosion of three specimens taken from the DIII-D tokamak: from the outer midplane, the lower divertor and the upper divertor. Extensive surface diagnostics was performed on these specimens and the measured chemical erosion yields were assessed in conjunction with the surface composition. Implications for the spectroscopic measurements in DIII-D are considered. (iii) The third set of experiments dealt with the chemical erosion of B-doped graphite due to combined H^+ and O^+ irradiation. A key observation is that the presence of oxygen ions in the O^+-$H^+ \rightarrow$C/B irradiation case seems to reduce the CH_4 yield suppression effect of boron, causing the CH_4 yield to increase during simultaneous O^+ and H^+ irradiation, compared to H^+-only impact. By comparison, for the O^+-$H^+ \rightarrow$C (undoped graphite) case, the CH_4 yield *decreases* during simultaneous O^+ and H^+ irradiation due to the O^+-induced methane break-up effect. There is also evidence of suppressed water production in the O^+-$H^+ \rightarrow$C/B system.

1. Chemical Erosion and RES of Doped Graphites

Graphite is being planned for high heat flux areas in the divertor of next-step fusion devices, such as ITER, because of its excellent thermo-mechanical properties. However, graphite's major drawbacks are its erosion and hydrogen retention characteristics. In order to improve graphite's erosion resistance, doping with other elements has received extensive attention. We have studied the effect of doping on chemical erosion, radiation-enhanced sublimation (RES), and hydrogen retention using specially fabricated specimens provided by a Canadian company, Ceramics Kingston Ceramique Inc. (CKC). Our study has also included an assessment of the thermal behaviour of the doped materials. Based on the thermal transport results for these materials [1], the specimens were found to be highly anisotropic. Here we shall provide results on chemical erosion and RES. Surface composition analysis, thermal diffusivity, and H-retention results are presented elsewhere in this book.

1.1. Chemical Erosion of Doped Graphites

Erosion experiments were performed using CKC specimens doped with B, Si, Ti, W, and TiB_2. The doped specimens were exposed to H^+ ions of 30eV-1keV energy. Hydrocarbon reaction products were measured by residual-gas-analysis (RGA) as a function of specimen temperature in the range 300-1000 K [2]. In general, specimens with dopant concentrations

higher than a few at.% at the surface lead to reduced hydrocarbon formation over undoped graphite at and above the temperature corresponding to the maximum chemical erosion yield. Figure 1 shows the temperature profiles of the CH_4 yields under 1 keV H^+ irradiation of the CKC B-, Si-, Ti-, and W-doped specimens at various surface dopant concentrations and graphite-plane orientations. The surface concentrations of dopants corresponding to specimen designations in Fig. 1 are given in Table 1. Of all the specimens studied, boron doping with ≥8 at.% surface concentration (<1 μm) provides the best resistance to hydrocarbon formation. Compared to pure graphite, a factor of 5 reduction in the CH_4 yield is observed. A somewhat smaller improvement (~ a factor of 2 reduction in CH_4 yield) is seen for the 4-5 at.% surface concentration Ti and Si specimens.

SEM photographs of the unirradiated and irradiated regions of the specimens reveal that irradiation affects mostly the carbon matrix and produces a fine-scale roughening of the irradiated regions compared to the flake structure of the unirradiated regions. There is no observable evidence that the structure and the distribution of the dopant particulates are affected by H^+ irradiation. EDX analysis also shows that irradiation does not significantly alter the dopant concentration.

Table 1. Dopant concentrations the CKC graphite specimens [2,4]

SPECIMEN DESIGNATION	DOPANT CONCENTRATION	
	Bulk/(at. %) depth > ~ 1 μm	Surface/(at. %) depth < 1 μm for B depth < 0.1 μm for Si and Ti
CKC-B2	2.0 ± 0.9	1.2 ± 0.6
-B10	9.4 ±1.6	7.9 ± 2.4
-B20	20.1 ± 3.6	13.8 ± 2.2
CKC-Si3	3.0 ± 0.5	0.7 ± 0.2
-Si8	7.5 ± 0.5	1.9 ± 0.4
-Si14	14 ± 0.5	3.8 ± 1.1
CKC-Ti2	2.0 ± 0.5	0.7 ± 0.2
-Ti8	8.5 ± 0.5	3.2 ± 0.7
-Ti16	16 ± 0.5	5.0 ± 1.2
CKC-W10	10	0.9 ± 0.1
CKC-Ni10	7.5 ± 0.5	3.0 ± 0.5
CKC-Ti8/B17	8.3 at% Ti 15 at% B	1 at% Ti
CKC-Ti13/B27	14.3 at% Ti 28 at% B	2-3 at% Ti

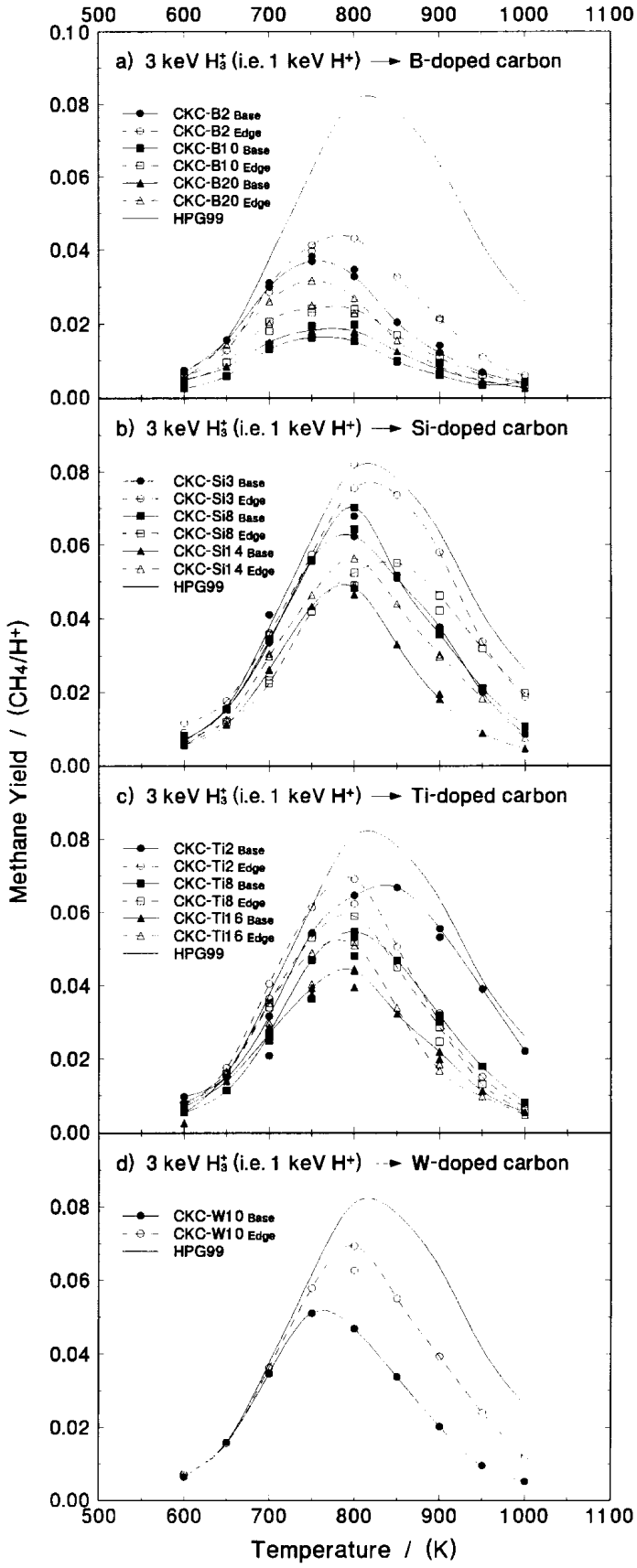

Fig. 1. Temperature dependence of the methane yield for 1 keV H^+ bombardment of the CKC doped specimens. Dopants: (a) B, (b) Si, (c) Ti, and (d) W [1]. The HPG99 yield is shown for comparison [5].

As will be seen below, doping with Ti leads to a significant reduction in RES. Therefore, to benefit from boron's effect on chemical erosion reduction and titanium's effect on RES reduction, we have asked CKC to fabricate specimens using TiB_2 as dopant. The measured chemical erosion yields of TiB_2-doped graphite, with 20% TiB_2 and "base" orientation, under 30 to 1000 eV H^+ irradiation, are shown in Fig. 2 [3]. As with the other dopants discussed above, the chemical erosion yield – both the methane and the total chemical yields – are lower than the yields corresponding to pure graphites. For H^+ energies ≥ 300 eV and temperatures ≥ 700 K, the erosion yield was reduced by a factor of 4 to 10 for the doped materials. This implies that the dopants do play a role at 'high energies' in the chemical erosion process. On the other hand, for lower ion energies and low specimen temperatures, the effect of the dopant was much less pronounced. In fact, for the 30 eV H^+ case, the yield reduction was comparable to the reduction in carbon content, implying that the presence of the dopants plays no role in the erosion mechanism at 'low energies.'

2. Chemical Erosion of DIII-D Wall and Divertor Tiles

Spectroscopic erosion data from the DIII-D tokamak show some striking long-term trends [6]. CD emissions – an indicator of chemical erosion – at the lower divertor have decreased by as much as two orders of magnitude near the inner strike point over a period of 5–6 years. This reduction might be related to the regular boronizations of the vessel or some other plasma conditioning process. On the other hand, the measured carbon influx at the midplane indicates erosion yields comparable to pure graphite [6]. To further investigate these observations, controlled laboratory experiments have been performed at UTIAS on tile specimens removed from DIII-D [7,8].

2.1. Characterization of DIII-D Tile Specimens

Three specimens from the DIII-D tokamak were investigated: (1) MP3 from the outer midplane, (2) B3 from the lower divertor, and (3) UD4 from the upper divertor. All specimens were UCAR-TS-1792 (ATJ) graphite, and were present in the tokamak through the 1993-1999 operational period [6]. The MP3 tile sample had a thick, non-uniform layer of plasma-deposited boron on the surface, which gave it a reddish colour. SEM analysis revealed a globular, porous surface typical of plasma-deposited films [7]. Cross-sectional SEM indicated the film thickness to be ~2 μm, which is consistent with EDX measurements, as well as the amount of boron deposited on the inner vessel wall of DIII-D during its numerous boronizations. XPS and SIMS analyses of the surface show a boron/carbon film of up to ~100 nm thickness, containing ~20-40 at% carbon, indicating that there is a small net deposition of carbon from the plasma onto the midplane tiles.

Specimen B3 from the lower divertor had a bluish-grey hue and was streaked with arc tracks from tokamak operation [8]. Surface analysis revealed a very thin amorphous boron-carbon plasma-deposited film on the surface, consisting mainly of carbon, a few at% of nitrogen, oxygen, boron, and traces of metals. Although the exact film thickness could not be deduced, XPS and RBS analyses indicate a film thickness in the range of 5-20 nm. The upper divertor sample UD4 was grey in colour, and also had the appearance of a typical plasma-deposited film [8]. SEM analysis showed large (~10-100 μm) crystals on the surface. EDX indicated that these might be boron oxide (or possibly boric acid). The underlying film was found to be primarily carbon with a small amount of oxygen (and by inference, boron). The film thickness was estimated from oxygen exposure experiments to be ~?? [8].

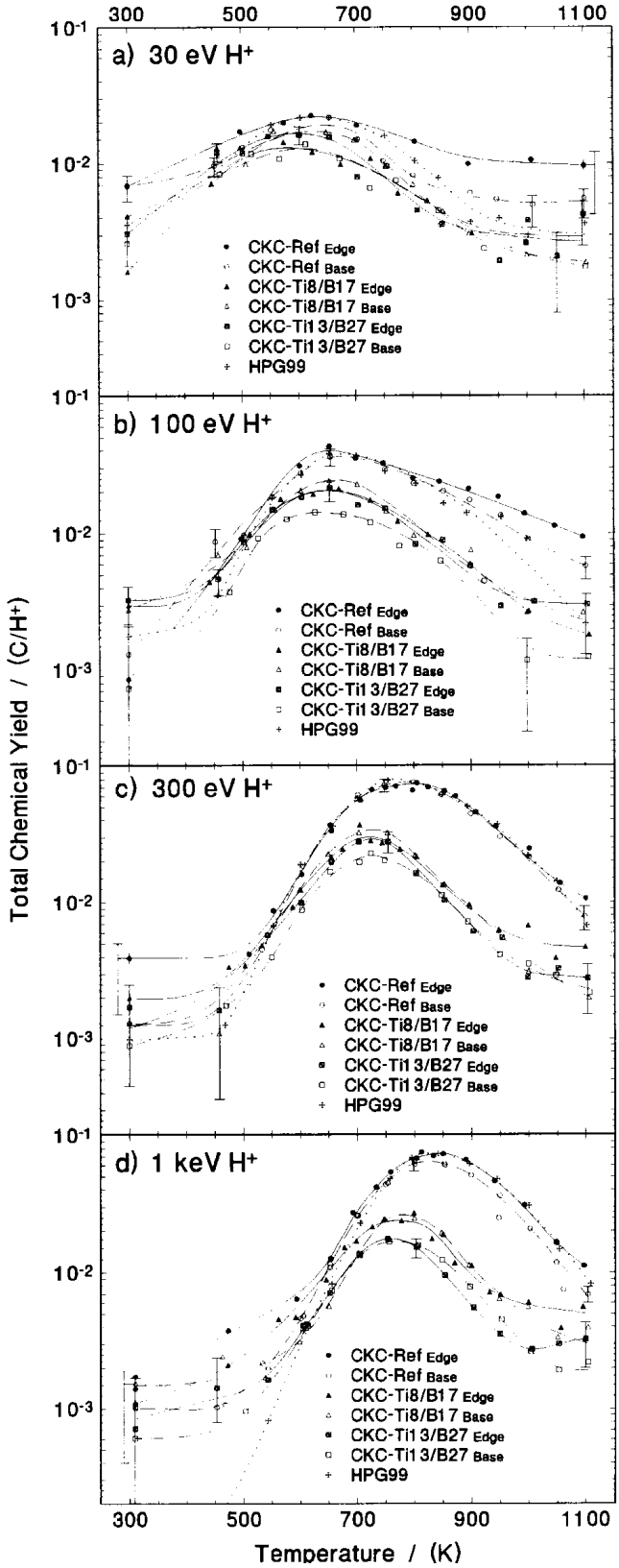

Fig. 2. Temperature dependence of the total chemical erosion yields of CKC-20% TiB_2-doped graphite, based on the sum of the measured hydrocarbon yields for CH_4, C_2H_2, C_2H_4, C_2H_6, C_3H_6 and C_3H_8. Undoped CKC reference and pure HPG99 pyrolytic graphite are shown for comparison. H^+ energies: (a) 30 eV, (b) 100 eV, (c) 300 eV, and (d) 1 keV [3].

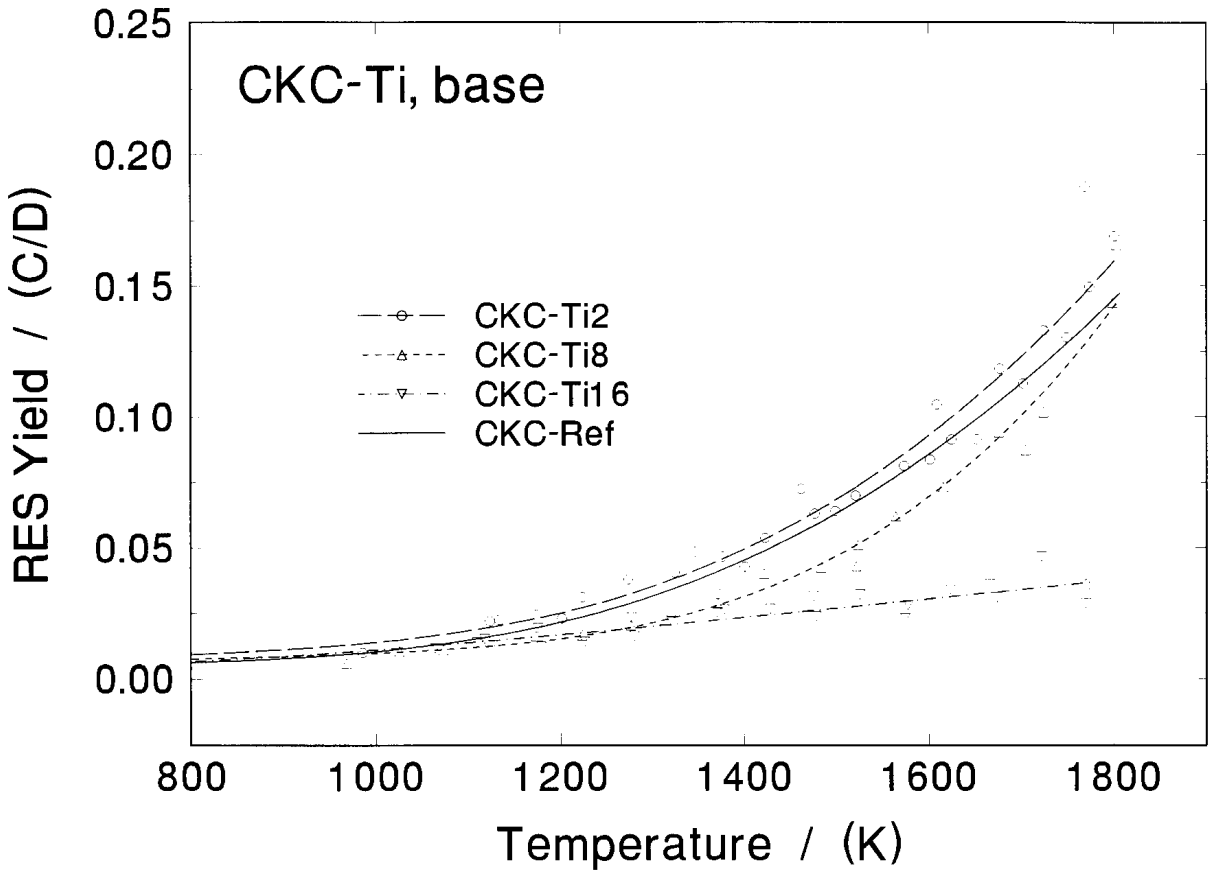

Fig. 3. Temperature dependence of the RES yields for the 'base' orientation of the CKC Ti-doped graphite at various surface dopant concentrations for 1 keV D^+ bombardment with a flux of 10^{19} D^+/m^2s and a fluence of 6×10^{21} D^+/m^2 [4].

2.2. Chemical Erosion of DIII-D Tile Specimens due to D^+ Impact

All chemical erosion experiments of the DIII-D tile specimens were performed with a low-energy ion gun at 50 eV and 200 eV D^+ impact energies, and 300-700 K specimen temperature. The hydrocarbon products of chemical erosion (CD_4, C_2D_2, C_2D_4, C_2D_6, C_3D_6, and C_3D_8) were measured in the residual gas using a quadrupole mass spectrometer (QMS). QMS calibration was performed *in-situ* with known leaks of CD_4, C_2D_2, and C_3D_6. The relative sensitivities of C_2D_2, C_2D_6, and C_3D_8 were estimated from previous calibrations [9].

Midplane Specimen MP3

Figure 4 shows the methane and total carbon (ΣC_iD_j) erosion yields for 50 eV impact as a function of fluence at temperatures of 300, 500 and 700 K. The general trend in fluence dependence is similar for all temperatures. At lower fluence, similar to that received during a typical shot at DIII-D ($<10^{22}$ D^+/m^2), the chemical erosion yield is similar to that of both pure and B-doped graphite [7]. The yields decrease by a factor of ~2 as the fluence is increased, which might be attributed to preferential removal of carbon from the film, leading to a boron enriched layer at the surface. However, the chemical erosion yields do not decrease to zero with increasing fluence, but reach a steady state, which may imply that the erosion is limited by the diffusion of carbon to the film surface or by the removal of boron [7]. The increase in steady-state erosion yield with increasing specimen temperature suggests that carbon diffusion through the a:B/C film may play an important role [7]. Extrapolating these results to the DIII-

D tokamak, where typical shots correspond to fluences $<10^{22}$ D^+/m^2, the thin B/C layer is not expected to be removed. Consequently, the erosion yield at the tokamak midplane could appear to be similar to graphite for the duration of the discharge [7] – in agreement with the observed spectroscopic measurement [6].

Upper Divertor Specimen UD4

Erosion experiments were performed at 200 eV and 300 K for fluences up to ~$3x10^{22}$ D^+/m^2. The erosion yield was found to be independent of fluence, and therefore subsequent measurements were made at a fluence of ~$3x10^{21}$ D^+/m^2; see Fig. 5.

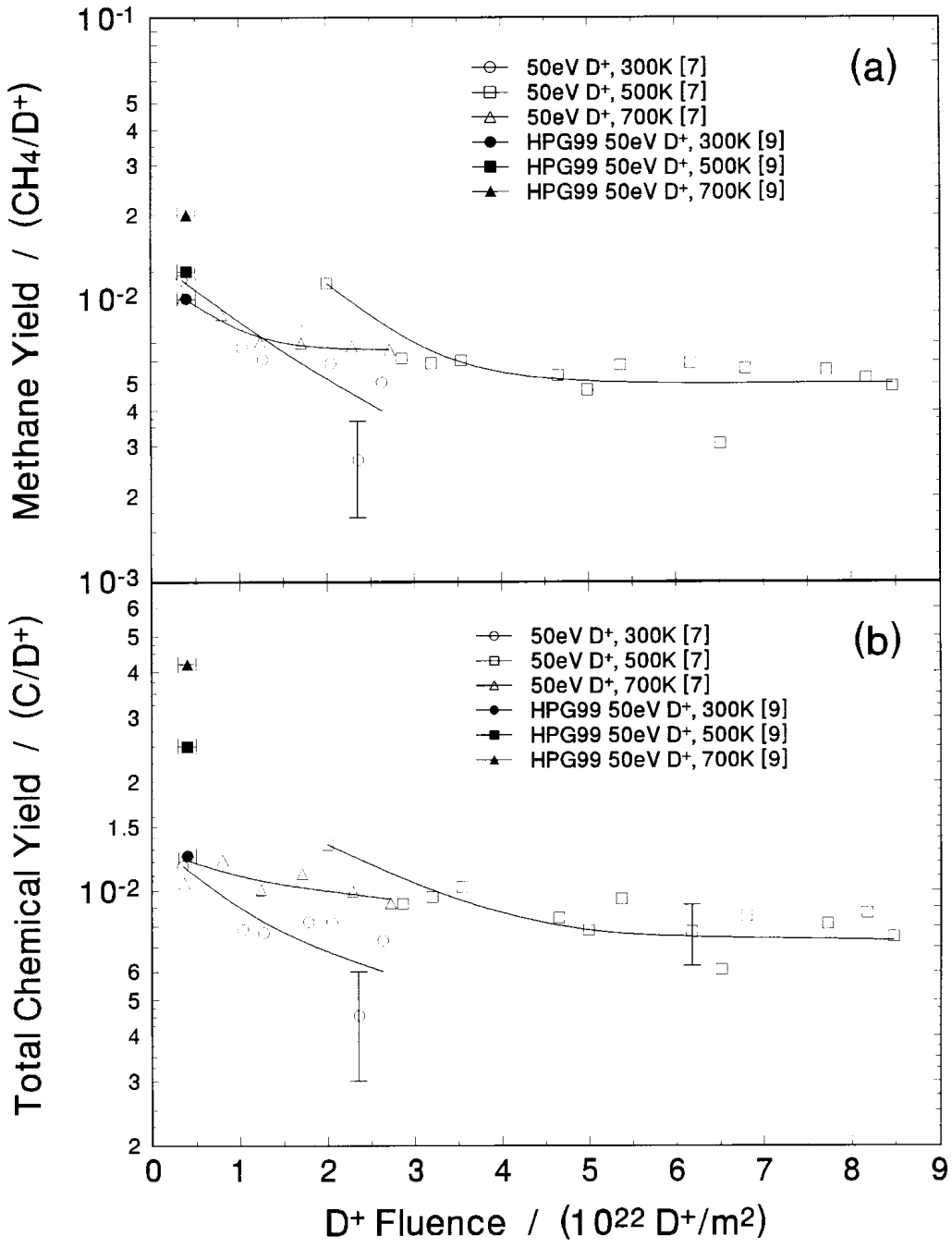

Fig. 4. Fluence dependence of (a) methane yields and (b) total carbon yields for 50 eV D^+ impact on DIII-D specimen MP3 [7]. Chemical erosion yield of pyrolytic graphite is shown for comparison [9].

For 200 eV D^+ irradiation, at 300 K, the erosion yield is slightly higher than that of pyrolytic graphite, possibly due to the amorphous nature of the film. At 500 K the yields are virtually the same. However, at 700 K, the erosion yield is less than that of pyrolytic graphite. Here the erosion yield is similar to that of boron-doped graphite, where we see the suppression of the high temperature reaction channel at higher temperatures and energies [8]. For 50 eV D^+ irradiation, again the erosion yield is higher at 300 K. It can also be seen that there is a larger contribution from the heavier hydrocarbons, which one expects to see when the ion energy is reduced [9]. However, at 500 K and 700 K, the erosion yields are similar to that of graphite. This is consistent with boron-doped graphite, where for lower incident energy there is little to no suppression of the chemical erosion yields at higher temperatures [3].

Lower Divertor Specimen B3

Chemical erosion experiments were conducted on an inner divertor specimen with 50 eV D^+ and 500 K temperature. At very low fluence, the chemical erosion yield reached a steady-state value comparable to that of pure graphite. Upon visual examination of the specimen, it was seen that the film had been completely eroded through to the graphite substrate. Whatever B-containing film was on the surface, it was removed sufficiently quickly that reliable measurements could not be made. In the DIII-D divertor region where this particular specimen came from, there was a mix of inner strike point (ISP), private-flux, and outer strike point (OSP) exposure. During double-null plasmas, B3 was actually at the OSP, and it is probable that at the time of removal this region was more like net erosion than net deposition, leading to the exposure of the graphite substrate [8].

3. Chemical Erosion of Boron-Doped Graphite due to H^+ and O^+

Oxygen is often one of the main intrinsic impurities in the plasma of current fusion devices with carbon first walls. Therefore, the synergistic reactions of oxygen-containing ions and the hydrogenic fuel with carbon materials play an important role in the complex process of plasma-wall interaction. Adding boron to graphite has been shown to lead to CH_4 yield reductions of as much as a factor of 5 [2,3]. The erosion of B-doped graphite under conditions of simultaneous bombardment by O^+ and H^+ ions was studied using an independently controlled high-flux, low-energy, mass-analyzed dual-beam ion accelerator [10]. The beam energies were in the ranges 0.7 – 3 keV H^+ and 5 keV O^+, with the resulting beam range ratio (R_H / R_O) being between ~ 1 (beams overlapping) and ~ 6 (beams nearly separated). Beam fluxes were in the range ~$2.5–4.8\times10^{19}$ H^+ / m^2s and ~ $0.3–1.8\times10^{19}$ O^+ / m^2s, with the flux ratio (Φ_O / Φ_H) being in the rage ~ 0.1 – 0.5 [11-13]. The effect of varying the ion range ratio and flux ratio on the reaction product yields was investigated [11-14].

Two types of boron-doped carbon specimens were used. One was cut from a block of CKC B-doped graphite [4], manufactured from finely ground graphite (10–45 μm) mixed with an organic binder with boron added as B metal particulates of ~μm size. The specimen used (CKC-B20) contains about 20 at.% B in the bulk (depth >1 μm), and about 14 at.% B on the surface (depth <1 μm). The other specimen (USB15) was a fine-grain (~0.01μm) boron-doped graphite manufactured by NII Grafit, USSR with a density of ~ 2000 kg/m^3 and a uniform distribution of 15 at.% boron. Pyrolytic graphite specimen (HPG99) was also studied under the same irradiation conditions for comparison.

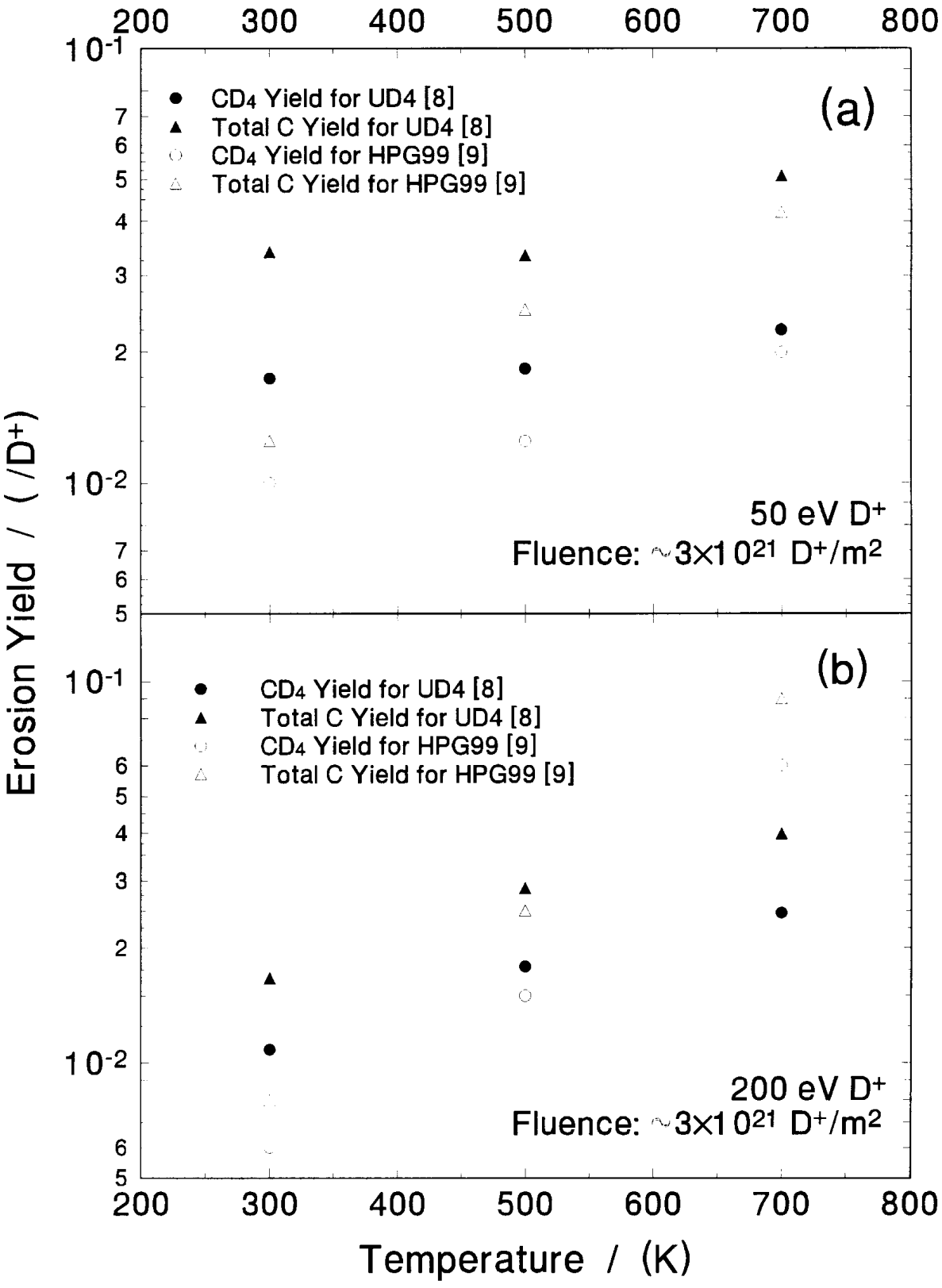

Fig. 5. Methane and total chemical erosion yields of DIII-D specimen UD4 for (a) 50 eV D^+ and (b) 200 eV D^+ impact at 300 K, 500 K, and 700 K [8]. Chemical erosion yield of pyrolytic graphite is shown for comparison [9].

3.1. Chemical Erosion: CH_4 Yield

The presence of oxygen ions in the O^+-H^+→C/B irradiation case [C/B represents B-doped carbon] seems to reduce the CH_4 yield suppression effect of boron, causing the CH_4 yield to increase during simultaneous O^+ and H^+ irradiation, compared to H^+-only impact [2]; see Fig. 6. By comparison, for the O^+-H^+→C (undoped graphite) case, the CH_4 yield *decreases* during simultaneous O^+ and H^+ irradiation due to the O^+-induced methane break-up effect [12,15]. The resulting CH_4 yield during simultaneous O^+ and H^+ irradiation in the O^+-H^+→C/B system more than compensates for the O^+-induced methane break-up effect. We postulate that the combined presence of oxygen and boron on the inner surfaces of graphite leads to a reduction of hydrogen recombination, and in turn, to an increase in CH_4 formation [12]. A general trend of higher methane increase for the beam-separated case was also observed. This can be explained by noting that higher methane reduction in the O^+-H^+→C system is expected for the beam-overlapping case due to the interference of the O^+ with the formation of methane precursors, in addition to the O^+-induced methane breakup. Thus, the resulting CH_4 increase in the O^+-H^+→C/B system is expected to be relatively less for the beam-overlapping case, consistent with the observed results [12].

3.2. Chemical Erosion: H_2O, CO and CO_2 Yields

As with the pure graphite (HPG99) case [11], no re-emission of O or O_2 was observed in the line-of-sight QMS detection mode for both the O^+→C/B and O^+-H^+→C/B irradiation of the CKC-B20 and USB15 specimens. Also, as in the O^+-H^+→C system [11], a reduction of CO and CO_2 yields was seen during simultaneous O^+ and H^+ irradiation, compared to O^+-only impact. In the O^+-H^+→C/B system, there seems to be a shift in the distribution of CO and CO_2 yields, i.e., generally higher CO yields and lower CO_2 yields, compared to the O^+-H^+→C case.

Furthermore, similar to the O^+-H^+→C (HPG99) case [11], water production was also observed for the O^+-H^+→C/B case [13,14]. However, there is evidence of suppressed water production in the O^+-H^+→C/B system. Figure 7 shows the H_2O yields of both O^+-H^+→C and O^+-H^+→C/B cases at 800 K, as a function of beam flux ratio Φ_O/Φ_H for two ion range separation cases (beams overlapping and separated). Water production at $\Phi_O/\Phi_H \sim 0.1$ is markedly smaller in the O^+-H^+→C/B system than in the O^+-H^+→C system [13]. For other flux ratios, no consistent trend is seen.

To explain the observed water yield reduction in the O^+-H^+→C/B irradiation case, we postulate the presence of H-O-containing complexes at the end of the O^+ range, created by attaching mobile hydrogen atoms [16] and the implanted oxygen to carbon or boron on the internal surfaces. The C-attached complexes form 'water precursors,' which during thermal or ion-induced desorption can release H_2O molecules. The B-attached complexes, on the other hand, have much less probability of releasing H_2O due to the higher stability of the B-O bond. Instead, B_xO_y and H/H_2 might be released during thermal or ion-induced desorption. In other words, the presence of B reduces the H and O supplies by providing competing reaction paths that do not produce water. This hypothesis is consistent with the observed reduction of water yield for the O^+-H^+→C/B case [13].

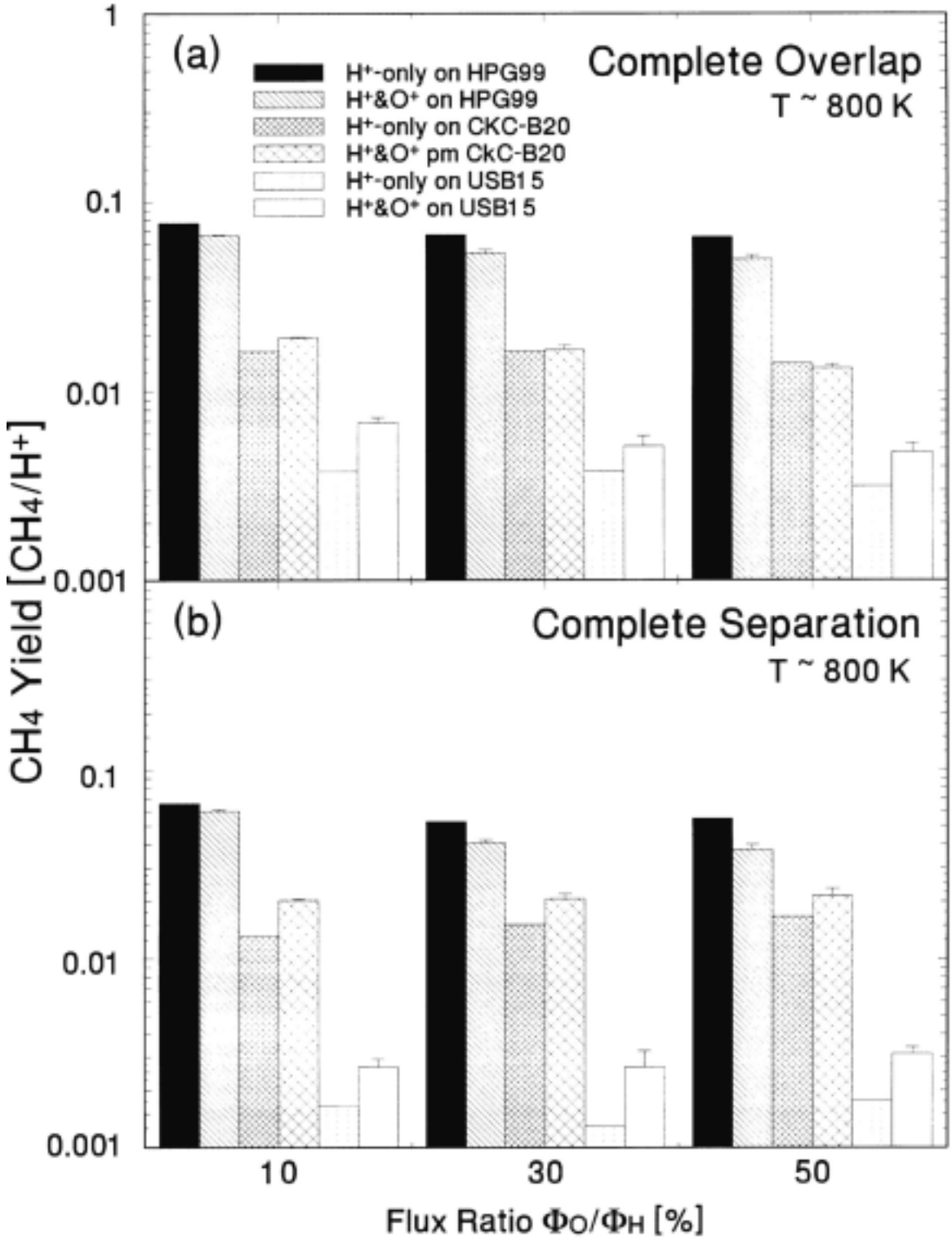

Fig. 6. CH_4 yields of both O^+-$H^+ \rightarrow C$ and O^+-$H^+ \rightarrow C/B$ irradiations as a function of beam flux ratio Φ_O/Φ_H for two ion range separation cases: (a) beams are completely overlapping (E_O = 5 keV, E_H = 0.7 keV, $R_H/R_O \sim 1$), and (b) beams are completely separated (E_O = 5 keV, E_H = 3 keV, $R_H/R_O \sim 6$). The oxygen flux Φ_O is fixed at ~3 $\times 10^{18}$ O^+/m^2s, while the hydrogen flux Φ_H varies from 0.6 – 3.1 $\times 10^{19}$ H^+/m^2s [12].

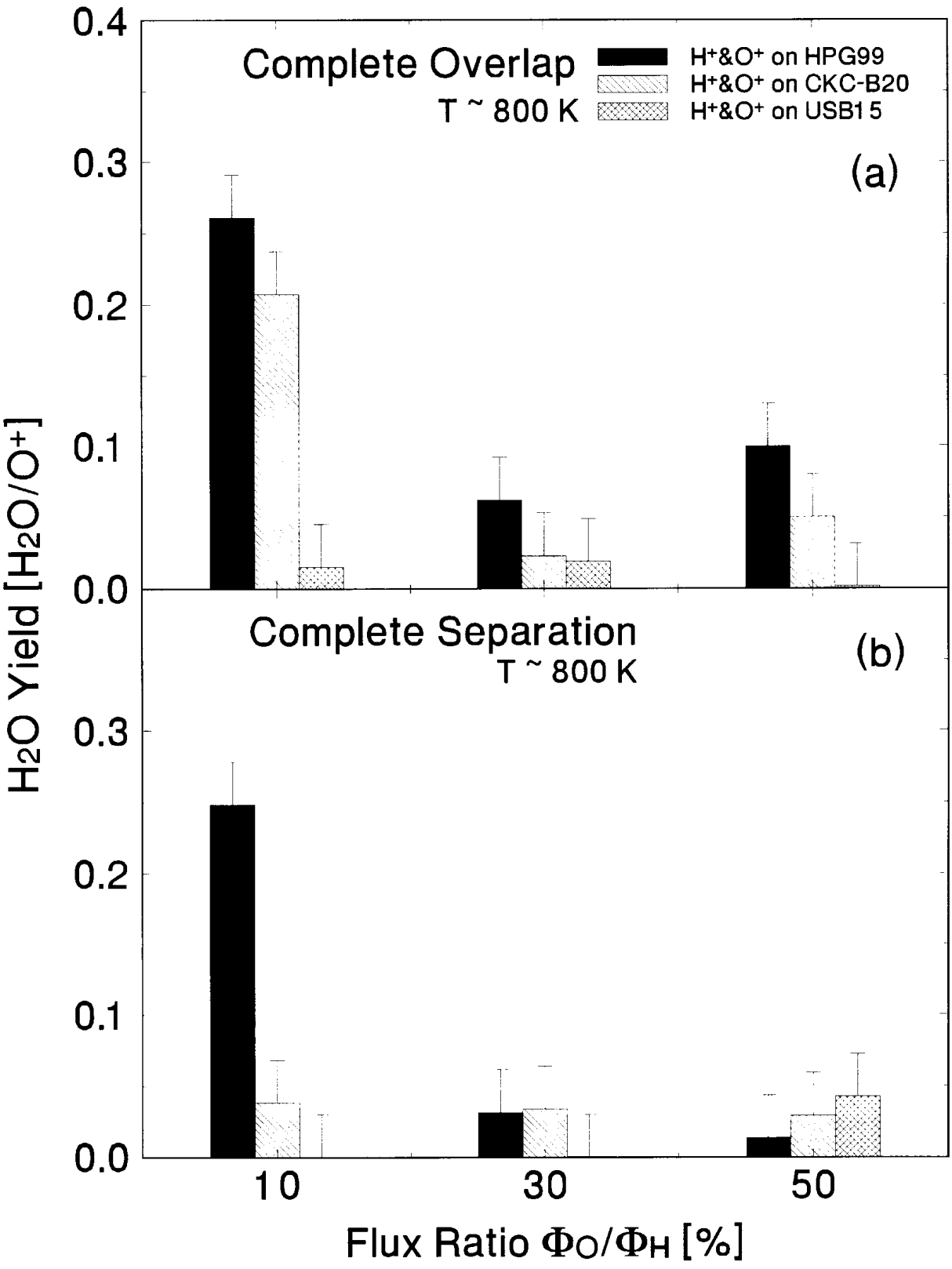

Fig. 7. H_2O yields for both O^+-$H^+ \rightarrow C$ and O^+-$H^+ \rightarrow C/B$ irradiations as a function of beam flux ratio Φ_O/Φ_H for two ion range separation cases: (a) beams are completely overlapping (E_O = 5 keV, E_H = 0.7 keV, $R_H/R_O \sim 1$), and (b) beams are completely separated (E_O = 5 keV, E_H = 3 keV, $R_H/R_O \sim 6$). The oxygen flux Φ_O is fixed at $\sim 3 \times 10^{18}$ O^+/m^2s, while the hydrogen flux Φ_H varies from $0.6 - 3.1 \times 10^{19}$ H^+/m^2s [13].

REFERENCES

[1] B.N. Enweani, J.W. Davis, A.A. Haasz, "Thermal diffusivity/conductivity of doped graphites," J. Nucl. Mater. 224 (1995) 245–253.

[2] A.Y.K. Chen, A.A. Haasz, J.W. Davis, "Comparison of chemical erosion yields of doped graphites," J. Nucl. Mater. 227 (1995) 66–75.

[3] J.W. Davis, A.A. Haasz, "Chemical erosion of CKC TiB_2-doped graphite," J. Nucl. Mater. 255 (1998) 214–221.

[4] P. Franzen, A.A. Haasz, J.W. Davis, "Radiation-enhanced sublimation of doped graphites," J. Nucl. Mater. 226 (1995) 15–26.

[5] A.A. Haasz, J.W. Davis, "Comparison of the chemical erosion of carbon/carbon composites and pyrolytic graphite," J. Nucl. Mater. 175 (1990) 84–89.

[6] D.G. Whyte et al., "Reductions in divertor carbon sources in DIIID," J. Nucl. Mater. 290-293 (2001) 356.

[7] J.W. Davis, P.B. Wright, R.G. Macaulay-Newcombe, A.A. Haasz, C.G. Hamilton, "Chemical erosion of boronized films from DIIID tiles," J. Nucl. Mater. 290–293 (2001) 66–70.

[8] P.B. Wright et al., to be published.

[9] B.V. Mech, A.A. Haasz, J.W. Davis, "Isotopic effects in hydrocarbon formation due to low-energy H^+/D^+ impact on graphite," J. Nucl. Mater. 255 (1998) 153–164.

[10] A.A. Haasz, J.W. Davis, "Synergistic chemical erosion of graphite due to simultaneous bombardment by H^+ and other low-Z ions using a dual-beam accelerator," Nucl. Instrum. Methods B83 (1993) 117–124.

[11] A.Y.K. Chen, J.W. Davis, A.A. Haasz, "Chemical erosion of graphite due to simultaneous O^+ and H^+ irradiation," J. Nucl. Mater. 266-269 (1999) 399–405.

[12] A.Y.K Chen, A.A. Haasz, J.W. Davis, "Methane formation in graphite and boron-doped graphite under simultaneous O^+ and H^+ irradiation," J. Nucl. Mater. 290–293 (2001) 61–65.

[13] A.Y.K. Chen, A.A. Haasz, J.W. Davis, "Water formation in graphite and boron-doped graphite under simultaneous O^+ and H^+ irradiation", to be published.

[14] A.Y.K. Chen, "Chemical erosion of graphite due to simultaneous H^+ and O^+ irradiation," Ph.D. Thesis, University of Toronto, 2001.

[15] A.A. Haasz, S. Chiu, P. Franzen, "Methane breakup during H^+/He^+- graphite interactions," J. Nucl. Mater. 220-222 (1995) 815–818.

[16] S. Chiu, A.A. Haasz, "Molecule formation due to sequential and simultaneous exposure of graphite to H^+ and D^+," J. Nucl. Mater. 196–198 (1992) 972–976.

MIXED-MATERIAL EROSION PROCESSES IN PISCES

R.P. DOERNER and the PISCES Team
Center for Energy Research, University of California San Diego,
La Jolla, California, United States of America

Abstract

The formation of mixed-material layers on plasma-facing components is a complicated process governed not only by the material properties of the surfaces (such as temperature, reflection coefficients and sputtering yield), but also on the conditions in the adjacent plasma (redeposition probability and impurity content). Experiments have been conducted to understand the conditions under which these layers will form and their growth rate. Once the surfaces form they can drastically effect the erosion behavior of the underlying substrate material. Erosion behavior of mixed-material layer on beryllium, tungsten and carbon surfaces are presented.

I. Introduction

The PISCES-B plasma device [1] has examined the formation conditions and properties of mixed-material surface layers that can form on plasma-facing components. The formation of the layers is a complicated process governed not only by the material properties of the surfaces (such as temperature, reflection coefficients and sputtering yield), but also on the conditions in the adjacent plasma (redeposition probability and impurity content). This work has focused primarily on the Be/C system [2,3], although some work using the W/C system [4,5] has also been performed. In this section, we first discuss the formation conditions for a carbon-containing mixed-material layer. The implications for erosion of both carbon on beryllium and beryllium on carbon will then be examined.

The PISCES-B device has been modified to investigate mixed-materials in several ways. An impurity gas puffing system has been installed in the target interaction region. To date experiments have focused on puffing deuterated methane (CD_4) into the plasma. In addition, a beryllium gettering ball can be inserted upstream in the plasma column to seed the plasma with beryllium as it flows toward the target.

II. Layer Formation and Growth

The formation of any surface layer is a competition between deposition and removal processes. Deposition from a plasma will be influenced by such factors as the impurity concentration of the plasma, the sticking coefficient of the impurity (and hence the type of impurity - molecular, atomic, ionic) on the surface, the incident energy of the impurity and probably many others. Removal will be influenced by chemical bonding on the surface, the plasma ion energy, the probability of redeposition and again probably many other factors. Influential in both the removal and deposition processes is the temperature of the surface. The temperature will determine the chemical structure of the surface as well as the interdiffusion of impurities and the bulk material. At elevated temperatures, molecules such as carbides are more likely to form and impurities deposited in the near surface region can more easily diffuse away from the surface and become less likely to be removed. Therefore, it is more

likely to form a surface layer at higher temperatures, all other variables being constant. In principle, a study of the formation of mixed-material surface layers should include variations of all of these quantities. In practice, this work focused on variations of the temperature of the surface and the concentration of impurities in the incident plasma to develop a two dimensional map that would help determine under which conditions mixed-material layers are likely to form.

In a plasma without impurities, a mixed-material layer will not form regardless of the sample temperature. When the impurity concentration is high, deposits will grow at any temperature. These two conditions can be seen in Figure 1, showing film formation conditions in PISCES-B. At low impurity concentrations, 0.2% carbon (without CD_4 injection), films do not form at any temperature. At impurity concentrations of 3% carbon (using CD_4 puffing), films form during room temperature exposures. Deuterium plasmas with 100 eV ion energy bombardment of the surface are used to generate the data in this graph. The ion flux varies from a low of 1×10^{21} $m^{-2}s^{-1}$ up to 2×10^{22} $m^{-2}s^{-1}$ and is related to the temperature of the surface. Exposure times range from 1000 up to 7200 sec. (i.e. 2 hours). The difficulty of the definition of what constitutes film formation arises for the region between these two extremes.

For lack of a better definition, a surface concentration of at least 50% carbon is used in Figure 1 to define when a mixed-material surface layer formed on a sample. It should be noted that some of the 'clean' data points in Figure 1 had a carbon surface concentration of up to 30%. Also, several of the high-temperature 'coated' surfaces were measured to consist entirely of carbon and oxygen, without any evidence of the underlying beryllium substrate. The surface concentration may be somewhat misleading, however, because many of the films that were formed in a transition region were observed to crack and flake off. A region indicative of this transition from clean to coated surfaces is sketched on the figure.

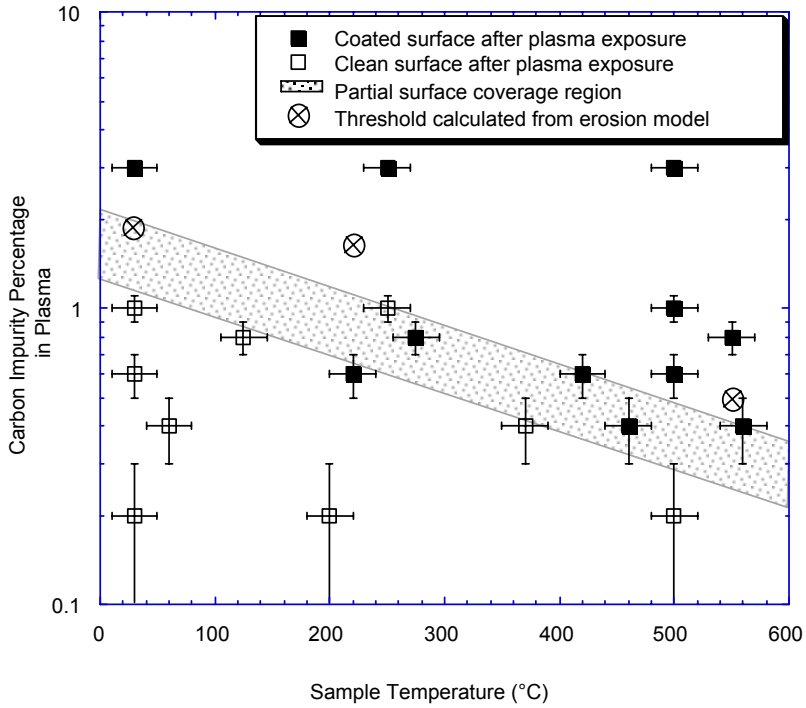

Figure 1. Carbon-containing mixed-material layer formation conditions (in surface temperature and plasma carbon concentration) for beryllium exposed to 100 eV deuterium ion plasma bombardment. A transition region is observed between the region where clean and coated surfaces result. An analytic model based on the erosion and deposition rate of the carbon is shown to predict the observed behavior.

The growth rate of the film was measured under the condition of 0.8% carbon impurity concentration at a sample temperature of 550°C. The layer thickness is measured using a profilometer at a location on the sample where the surface film had exfoliated from the substrate revealing the beryllium surface below. Figure 2 shows a SEM picture of a region of the sample where such an exfoliation occurred. The predominantly carbon containing film is clearly seen partially covering an apparently clean beryllium surface below.

If the growth rate of the film is determined by the diffusion rate of the underlying substrate through the impurity layer, the thickness will have a time to the one half dependence [6]. If the growth rate is determined by the arrival rate of the impurity atoms at the surface, a constant growth rate in time is expected. Figure 3 compares these two growth rate models (normalized at the measured data point at 3 microns) with the measured film thickness obtained from the samples exposed in PISCES-B. The linear growth rate model more closely matches the experimental results, meaning that the impurity arrival rate at the surface governs the growth rate of the film.

This can be further verified by examining experiments performed using the W/C system. Downstream CD_4 puffing was also used to simulate carbon impurities in a deuterium plasma at various tungsten substrate temperatures. Although not as systematically performed as the Be/C system just described, Figure 4 shows the distribution of experiments performed at various carbon concentrations and substrate temperatures. At the impurity level of about 1% CD_4, measured by the gas analyzer, no carbon deposition was observed in the plasma exposed substrates at temperature below 700 K. When the substrate temperature was increased to 850 K, carbon particles started to form on the tungsten surface, mostly along sharp edges that serve as the nucleation sites. These results are in general agreement with the findings using the Be/C system and bolster the assertion that chemistry only plays a dominant role in the transition region between clean and coated behavior.

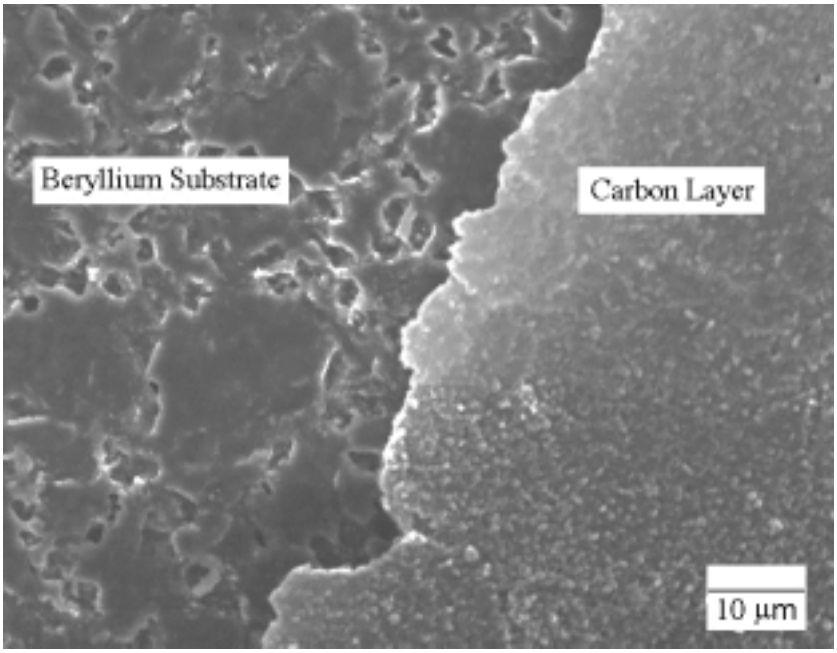

Figure 2. SEM photograph showing the edge region of a carbon-containing film which has cracked and fallen off the beryllium substrate. The substrate is seen to have the appearance of a 'clean' beryllium surface.

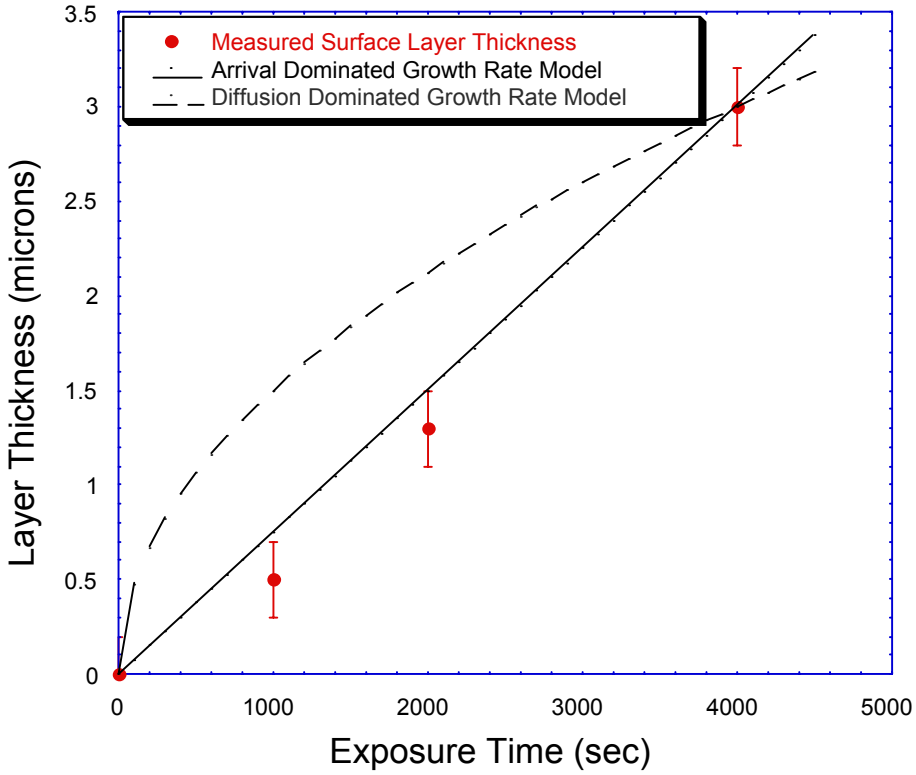

Figure 3. The measured mixed-material layer thickness in PISCES-B is governed by the arrival rate of carbon atoms at the surface (constant growth in time), rather than by the diffusion of bulk atoms through the surface layer (thickness proportional to $t^{1/2}$).

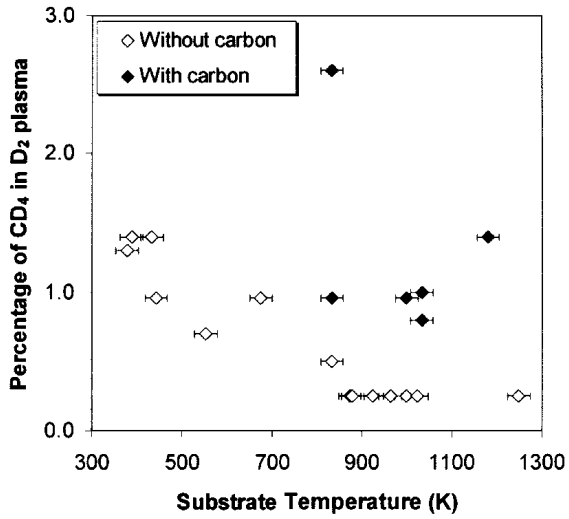

Figure 4. Carbon film formation on tungsten substrates under various conditions.

III. Erosion Behavior

The effect of a carbon-containing mixed-material layer on the erosion of beryllium has been described in [7], where the layer appears close to the diffusion limited growth regime described above, but where lack of an impurity concentration measurement hampered the interpretation of the results. The reduction of the erosion of beryllium (Figure 5) was attributed to two factors. First, as carbon covers parts of the plasma bombarded surface, the

amount of beryllium exposed to the plasma is reduced, but this does not account for the entire reduction. A fraction (26%) of the carbon was measured to be bound up in beryllium carbide bonds that act to inhibit the loss of beryllium because of the increased binding energy of the carbide. The combination of these two effects resulted in a factor of 3-4 reduction in the erosion yield of beryllium in a mixed-material layer. The formation of mixed-material layers on the ITER first wall can, therefore, have beneficial consequences for the lifetime of the wall.

The other question is to what extent beryllium eroded from the first wall and upper baffle will be transported into the divertor and influence the erosion of the graphite divertor dump plate. Calculations have estimated the amount of beryllium that will be deposited on the ITER dump plates [8].

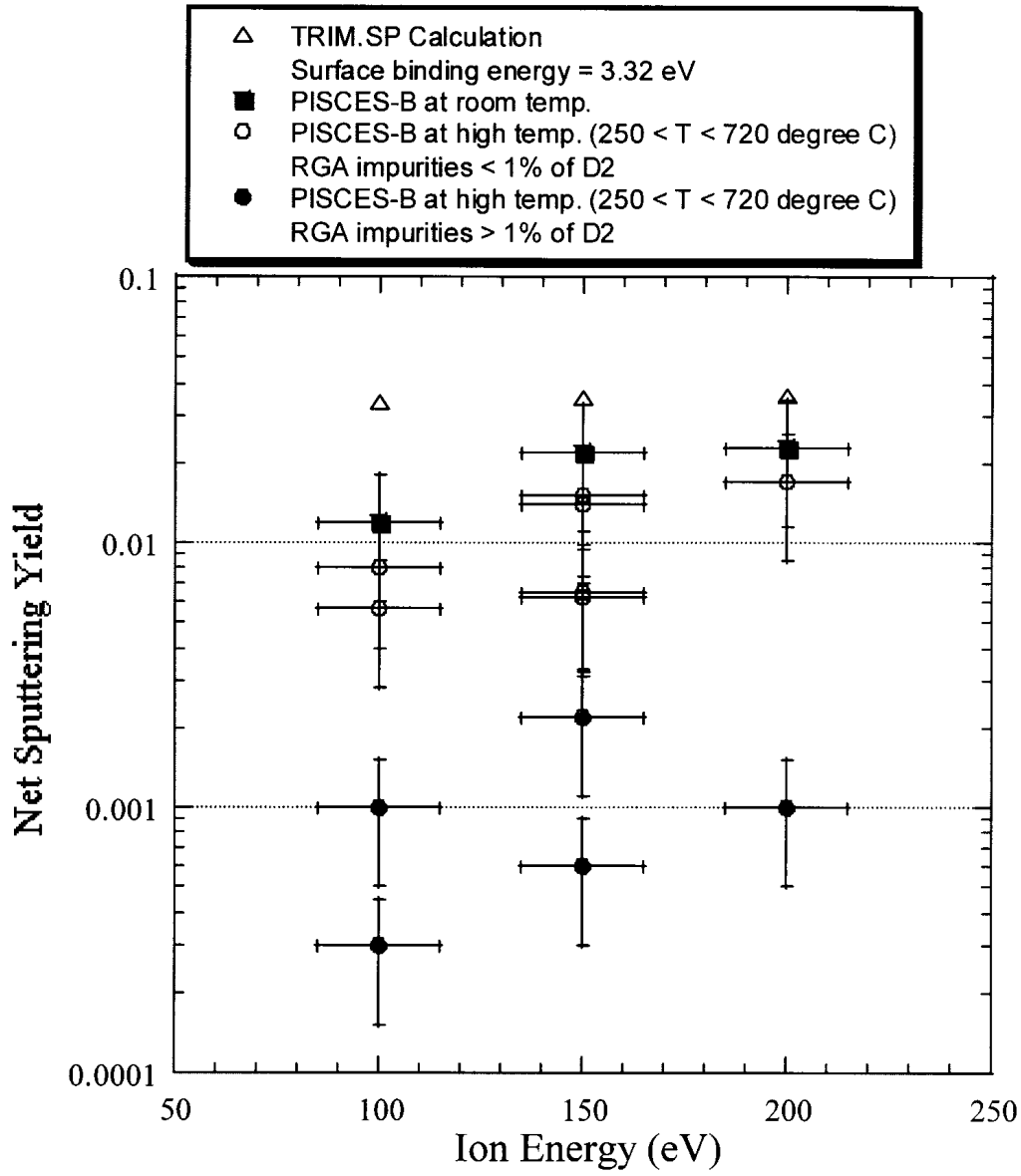

Figure 5. Measured sputtering yield of beryllium exposed to deuterium plasma bombardment under different surface temperature conditions and plasma impurity concentrations. Theoretical sputtering yield of beryllium from the TRIM code is also plotted for comparison.

One would expect to observe at least a reduction in carbon erosion proportional to the amount of beryllium surface coverage on the divertor plate. However, it might also be possible for the beryllium to act much like a dopant in the graphite [9] and to further reduce the chemical erosion from the dump plate.

This effect has been investigated by lowering the beryllium getter into the PISCES-B deuterium plasma column. As the temperature of the getter increases, beryllium begins to evaporate from the surface and is ionized in the adjacent plasma. The ionized beryllium will then flow along with the plasma to a graphite sample inserted into the target region. The CD band intensity emitted from the plasma can be used as a relative measure of the change in the chemical erosion of the graphite as the concentration of beryllium on the surface changes.

The experimental conditions during the measurements were: ion flux = $1x10^{22}$ $m^{-2}s^{-1}$, ion bombarding energy = 60 eV, electron temperature = 25 eV and carbon surface temperature = 400°C. The CD band emission is insensitive to small changes in the electron temperature in this range [10], so the CD band emission is a reliable indication of the chemical erosion of the graphite. The discharge was periodically terminated and the sample analyzed in-situ with AES to determine the surface concentrations of beryllium and carbon. A small amount of oxygen, about 10%, was also usually detected on the surface. The discharge was then reinitiated for a period of time and then the CD band intensity remeasured, followed by additional surface analysis. The resultant graph is shown in Figure 6. Also plotted in Figure 6 is the expected chemical erosion based purely on the fractional carbon surface coverage. As can be seen, the beryllium that will be eroded from the first wall and transported to the ITER divertor will act to inhibit the formation of hydrocarbons. For reference purposes, the chemical erosion rate from a SiC doped graphite (NS-31), as measured in PISCES, is also shown in the figure.

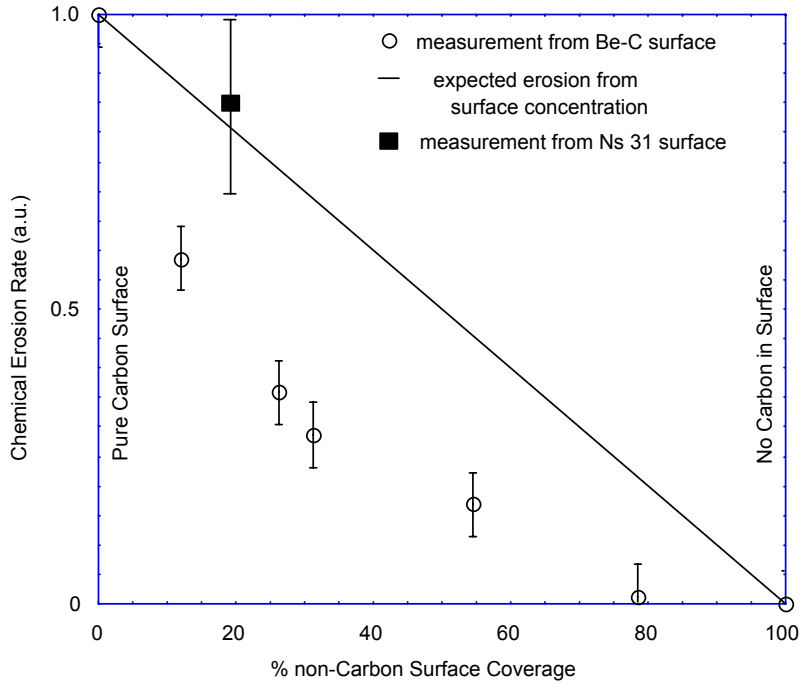

Figure 6. The influence of uniform and non-uniform mixing, or doping, of a graphite surface can be seen by comparing the non-uniform NS 31 doped graphite to a graphite sample uniformly coated with beryllium. The solid line indicates the linear change expected from varying the surface concentration of carbon.

IV. Summary

The PISCES research program in the area of mixed-materials has attempted to develop an understanding of this complicated phenomenon in an actual plasma environment. In addition to identifying several key variables that can play a role in the formation of these surface layers, the effect these layers have on the plasma interaction behavior have been documented. Finally, it is realized that mixed-materials can have either beneficial or detrimental effects for plasma-facing components and, where possible, some insight into these competing effects is described.

REFERENCES

[1] Y. Hirooka, et al., J. Vac. Technol. A 8 (1990) 1790.
[2] R.P. Doerner et al., J. Nucl. Mater. 266-269 (1999) 392.
[3] R. P. Doerner et al., Physica Scripta T81 (1999) 35.
[4] F.C. Sze, R.P. Doerner and S. Luckhardt, J. Nucl. Mater. 264 (1999) 89.
[5] F.C. Sze, L. Chousal, R.P. Doerner and S. Luckhardt, J. Nucl. Mater. 266-269 (1999) 1212.
[6] N. F. Mott and R. W. Gurney, Electronic Processes in Ionic Crystals, Dover Publications Inc., New York, 1964.
[7] J. Won et al., J. Nucl. Mater. 241-243 (1997) 1110.
[8] J. N. Brooks et al., J. Nucl. Mater. 266-269 (1999) 58.
[9] J. Roth, J. Nucl. Mater. 145-147 (1987) 87.
[10] Y. Ra et al., J. Vac. Sci. Technol. A 8 (1990) 1783.

H RETENTION IN DOPED GRAPHITES AND C^+-IMPLANTED W, AND THERMO-OXIDATIVE REMOVAL OF TOKAMAK CODEPOSITS

A.A. HAASZ, J.W. DAVIS, M. POON, R.G. MACAULAY-NEWCOMBE,
C.G. HAMILTON

Abstract

Results are presented on hydrogen retention in doped graphites and C^+-implanted tungsten. Also discussed are experiments aimed at removing deuterium from tokamak codeposits by thermo-oxidation. (i) For the B- and Ti-doped specimens fabricated by Ceramics Kingston Ceramique Inc., D retention, as a function of fluence, was similar to the undoped CKC graphite; the Si- and W-doped specimens, on the other hand, display a much stronger increasing dependence on fluence. At this point, it is not clear whether the increased retention is due to a direct chemical effect of the dopants or due to changes in the material structure, which lead to enhanced diffusion of D into the bulk. (ii) Particle induced erosion of multi-material plasma-facing structures in ITER will be inevitable, leading to cross-contamination of all surfaces. Two of these materials, W and C, display significantly different hydrogen retention and recycling properties, leading one to inquire whether the re-deposition or implantation of C on W will significantly alter its hydrogen recycling properties. With various combinations of C^+ and D^+ fluences, one may obtain one of three different domains for D retention: D retention in a graphitic surface layer; D retention in a tungsten carbide region; and D retention in pure W. (iii) The accumulation of tritium due to the codeposition of eroded C and the tritium fuel on tokamak vessel components is causing major concerns for the operation of next-step fusion devices such as ITER. Various methods have been proposed to remove the tritium from these codeposits, but to date the only demonstrated effective method is to remove the codeposits together with the tritium by thermo-oxidation. Reaction product analysis shows that essentially all of the D is removed via D_2O formation, and C is removed by the formation of CO and CO_2. No D_2 or methane formation was seen. Thermo-oxidation of various tokamak codeposits produced very similar trends in D removal as a function of O_2 exposure time. At 623K oxidation temperature, a large decrease in D content is seen over the first hour, followed by a much slower decrease over the remainder of the experimental run; at 523 K, removal rates are about an order of magnitude lower.

1. Deuterium Retention in CKC Doped Graphites

Graphite is being planned for high heat flux areas in the divertor of next-step fusion devices, such as ITER, because of its excellent thermo-mechanical properties. However, graphite's major drawbacks are its erosion and hydrogen retention characteristics. In order to improve graphite's erosion resistance, doping with other elements has received extensive attention. We have studied the effect of doping on chemical erosion, radiation-enhanced sublimation (RES), and hydrogen retention using specially fabricated specimens provided by a Canadian company, Ceramics Kingston Ceramique Inc. (CKC). Our study has also included an assessment of the thermal behaviour of the doped materials. Here we shall provide results on H retention. Surface composition analysis and thermal diffusivity, and erosion results are presented elsewhere in this book.

The retention behaviour of 1 keV D^+ ions in graphites doped with B, Ti, Si and W, was compared with D^+ retention in pure graphites for temperatures 300-1000K, and for fluences of 10^{21}- 4×10^{24} D/m^2 [1].

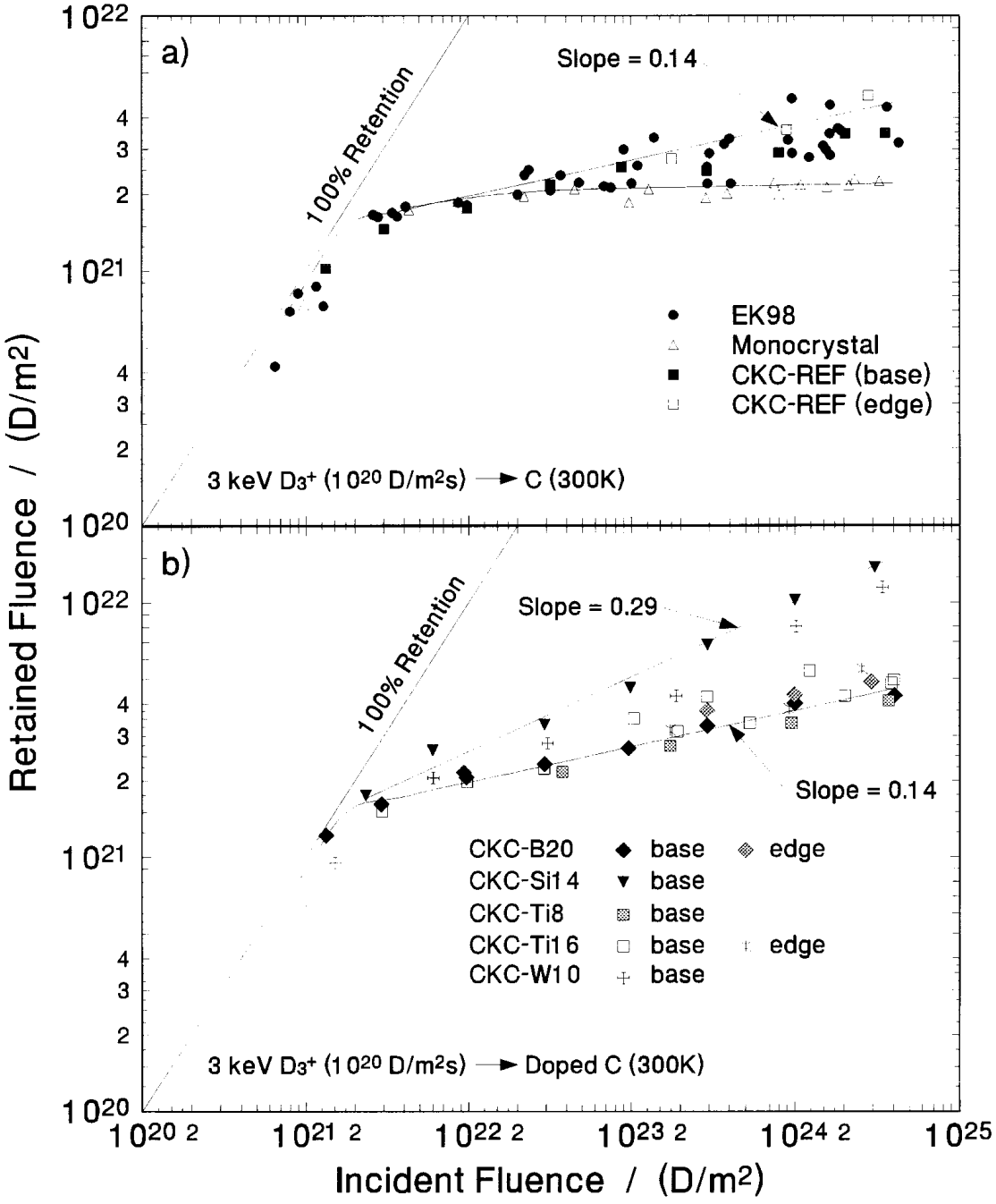

Fig. 1. TDS measurements of D retention in (a) undoped graphites and (b) doped graphites as a function of D^+ fluence.

Included in the pure graphites was the CKC reference material manufactured by the same technique as the doped graphites. The retention in this undoped reference material was found to be similar to that in EK98, with nearly 100% retention of D^+ for fluences of up to ~ 10^{21} D/m^2, followed by a much slower increase with fluence; see Fig. 1(a).

For the B- and Ti-doped specimens, D retention was similar to the undoped materials; see Fig. 1(b). The Si- and W-doped specimens, on the other hand, display a much stronger increasing dependence on fluence. At this point, it is not clear whether the increased retention is due to a direct chemical effect of the dopants or due to changes in the material structure,

which lead to enhanced diffusion of D into the bulk. Amounts retained as a function of implantation temperature were not greatly different from EK98, with all materials displaying very little retention above 1000K.

2. Deuterium Retention in C^+-Implanted Tungsten

Particle induced erosion of multi-material plasma-facing structures in ITER will be inevitable, leading to cross-contamination of all surfaces. Two of these materials, tungsten and carbon, display significantly different hydrogen retention and recycling properties, leading one to inquire whether the re-deposition or implantation of C on W will significantly alter its hydrogen recycling properties.

2.1. Surface Analysis of the C^+-Implanted Tungsten Specimens

Surface analysis by XPS was performed on the C^+-implanted tungsten specimens [here referred to as W/C] to determine the surface structure created by the C^+ pre-implantation [2]. Significant amounts of tungsten carbide (10%) and graphite (21%) were seen on the surface of the low C^+ fluence (10^{21} C^+/m^2) implanted specimen. A large amount of graphite (48%) with very little tungsten carbide (<1%) was found on the surface of the high C^+ fluence (10^{22} C^+/m^2) specimen. These results suggest a progressive surface evolution with increasing C^+ fluence, from a pure W surface, to a tungsten carbide region at low C^+ fluence, and finally to a graphite surface layer at high C^+ fluences.

For C^+ implantation at 300 K, RBS surface analysis shows just over half of the implanted C in the near-surface, suggesting diffusion of C into the bulk even at room temperature [2]. With an increase in temperature to 500 K, the amount of C in the near-surface is decreased (only one-third of the implanted fluence), implying even greater diffusion into the bulk. For the higher C^+ fluence implant at 300 K, RBS shows a tail of C, ~2 at% extending 170 nm into the specimen, whereas the same implant at 500 K shows a longer tail of C, ~1 at% extending 300 nm into the bulk.

2.2. The Effect of Pre-Implanted C on D-Retention in W

The effect of pre-implanted C on D retention in W was investigated using polycrystalline W foils [25 μm thick, 99.95 wt% pure, annealed at T>1470 K for 1 hr]. The pre-implantation was performed with 1 keV C^+ ions to fluences of 10^{21} C^+/m^2 and 10^{22} C^+/m^2 at 300 K and 500 K. Using this newly created W/C structure, a D retention study with 1.5 keV D_3^+ (500 eV/D^+) ions was performed as a function of incident D^+ fluence and implantation temperature [2]. Thermal desorption spectroscopy was used to determine the amount of D trapped in the W/C specimens.

The retention results are shown in Fig. 2. Results for pure polycrystalline tungsten are included for comparison [3]. For the lower fluence C^+ pre-implantation (10^{21} C^+/m^2) at 300 K, one will note, at low D^+ fluences, a strong decrease in retention compared to the pure W data; see Fig. 2(a). However, at higher D^+ fluences, the W/C specimens exhibit the same retention as the pure W. For the same C^+ fluence, but implanted at an elevated temperature of 500 K [Fig. 2(b)], the significant decreases noted in Fig. 2(a) are not observed. In fact, for subsequent D^+ implants at 300 K, the results are the same as the pure W case; on the other hand, subsequent D^+ implants at 500 K on the W/C specimens give retention values a factor of 3 lower than the pure W, independent of the incident D^+ fluence. With the higher fluence C^+

implant (10^{22} C^+/m^2) at 300 K and 500 K [Fig. 2(c)], the results again show a completely different retention behaviour. In this case, D retention in the W/C specimens is higher than in pure W for low D^+ fluences. At higher D^+ fluences, the 300 K results follow the same retention values found in pure W. However, the W/C specimens at 500 K show a large decrease in retention at intermediate D^+ fluences; then, as the incident D^+ fluence increases, the retention also increases, but the amount retained is still about 5 times lower than the pure W case.

2.3. Discussion of Observed Retention Results

In order to explain the observed trends in the D retention curves, one must also consider the effects of both the C^+ pre-irradiation and the subsequent D^+ implantation on the W/C structure. The incident D^+ ions will preferentially erode the C atoms from the surface such that the surface evolution resulting from the C^+ implantations is reversed: from graphite, to tungsten carbide at low D^+ fluences, and finally to pure W at high D^+ fluences. Thus, with various combinations of C^+ fluences and D^+ fluences, one may obtain one of three different domains for D retention: (i) D retention in a graphitic surface layer; (ii) D retention in a tungsten carbide region; and (iii) D retention in pure W.

The effect of the first region occurs with a high-fluence C^+ implant followed by a D^+ implant at low fluences [Fig. 2(c)]. In this region, retention is greater than in pure W due to high trapping in the graphitic film. In fact, these retention values are comparable to D retention in pure graphite [4]. The influence of the tungsten carbide, region (ii), can be seen for low-fluence C^+ implants followed by low-fluence D^+ implants [Fig. 2(a)], or for high-fluence C^+ implants followed by intermediate D^+ fluences [Fig. 2(c)]. Retention in these cases is below the levels seen in pure W, suggesting that tungsten carbide formation may lead to lower D retention. Two possible explanations can be envisioned for this observed result: (a) the presence of tungsten carbide on the surface may promote surface recycling of D, and (b) the formation of tungsten carbides reduces the number of 'sites' available for trapping D.

From Fig. 2, it is apparent that D retention in the W/C system is very much dependent on the C^+ implantation temperature. This temperature dependence is believed to be a result of C diffusion. As noted above, RBS surface analysis shows C diffusion into the bulk, extending to170 nm at 300K, and 300nm at 500K. Higher C diffusivity may lead to the formation of tungsten carbides deeper in the bulk, requiring a much higher D^+ fluence to remove C from the bulk. Another possible effect of C diffusion may be the dispersion (or dilution) of tungsten carbides throughout a greater volume, decreasing the local carbide concentration and thus reducing their effect on D retention. Both of these effects can be seen when comparing D retention at 500K after a 300K C^+ pre-implant [Fig. 2(a)] and after a 500K C^+ pre-implant [Fig. 2(b)]. At low incident fluences, the 500K C^+ pre-irradiation lowers D retention only by a factor of 3, whereas the 300K C^+ pre-irradiation lowers D retention by more than a factor of 10 (dilution effect). At the highest fluences in Fig 2(a), the 300K C^+ pre-implant exhibits region (iii), where the carbon and carbides are removed from the specimen to the extent that the W itself dominates retention. However, a factor of 3 lower retention is still present in the 500K C^+ pre-implant case in Fig. 2(b), possibly due to the deeper diffusion effect.

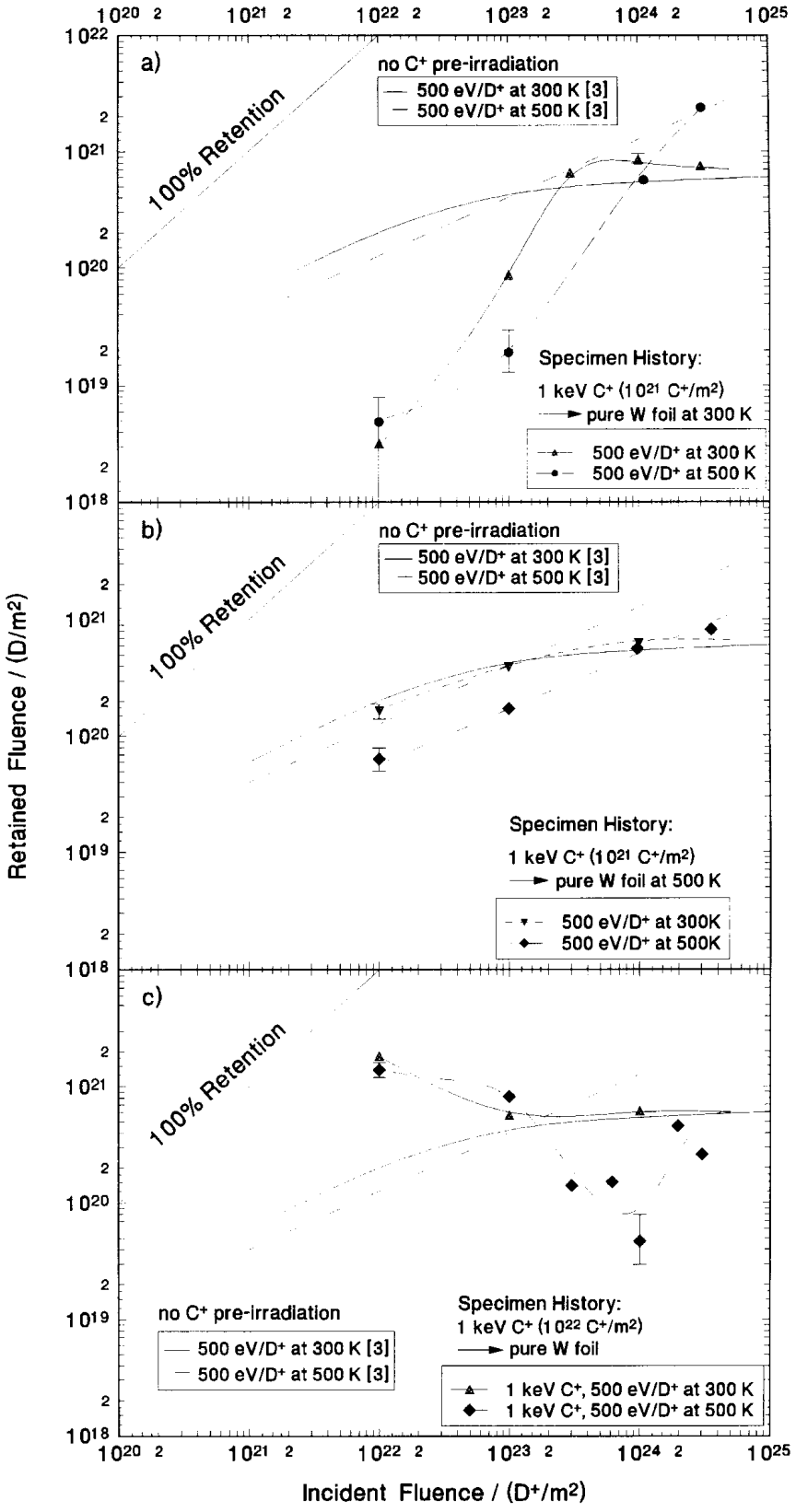

Fig. 2. Deuterium retention as a function of D^+ fluence for a W foil pre-implanted with 1 keV C^+ to different C^+ fluences at different temperatures. (a) 10^{21} C^+/m^2 at 300K; (b) 10^{21} C^+/m^2 at 500K; and (c) 10^{22} C^+/m^2 at 300K and 500K. Lines are drawn through the data corresponding to different C^+ and D^+ implantation temperatures. Reference curves for 500 eV D^+ implantation in pure polycrystalline W [3] are shown for comparison.

methods have been proposed to remove the tritium from these codeposits [5], but to date the only demonstrated effective method is to remove the codeposits together with the tritium by thermo-oxidation [6-8]. From an analysis of the reaction products formed by exposing a laboratory a-C:D film to $^{18}O_2$ at 470K, it was concluded that essentially all of the D is removed via D_2O formation, and C is removed by the formation of $C^{18}O$ and $C^{18}O_2$ [9]. No D_2 or methane formation was seen. Surface analysis of the film after $^{18}O_2$ exposure using XPS and SIMS revealed the presence of carbonyl groups and an increase of hydroxyl groups due to surface oxidation [9]. Thermal oxidation of hydrocarbon polymers provides a plausible reaction mechanism leading to the emission of D_2O, CO_2 and CO, consistent with the observed surface complexes [9]. Extensive laboratory studies of hydrogen removal from codeposited films and D^+-implanted graphite via thermo-oxidation have shown that the release of D occurs in conjunction with C erosion, and the D- and C-removal rates depend strongly on film structure and the temperature of the layer during oxidation [5-9].

As part of this study, some deuterated tokamak films from TFTR [6], JET [7] and DIII-D [7,8], containing significant impurity concentrations, have been studied in our laboratory. Specimens were placed in a heated O_2 atmosphere and the rate of deuterium removal was measured using laser-induced desorption spectroscopy.

3.1. Codeposits Obtained from Tokamaks

TFTR specimens

During the 1985-87 D campaign in TFTR, the POCO AXF-5Q graphite tiles were exposed to a large number of deuterium discharges resulting in regions of extensive erosion and redeposition. During the 1987 opening, in situ analysis of the tiles showed the presence of ~ 2% metallic impurities, mainly Ni [10]. Some tiles were removed for further ex situ analysis for D content [11]. Two specimens were studied in our laboratory, one cut from the surface of tile N3-15 which was in a region of moderate deposition [11], and the other was cut from tile N3-24 which was located at the top of the limiter column. D content measurements for the latter by Wampler et al. [11] indicate ~ $7x10^{21}$ D/m^2, placing it in a region of low deposition.

DIII-D specimens

Specimens were cut from DIII-D tiles, composed of ATJ graphite, which had been in the tokamak from 1993 to 1999, and was exposed to many boronizations resulting B coverage on all internal surfaces. The specimens used in our oxidation experiments were from the upper and lower divertors and the outer mid-plane. The codeposit on the mid-plane tile had an accumulated thickness of 1-2 μm, primarily boron, while the lower divertor tile had a much thinner codeposit, containing a very small amount of B. The lower divertor tile was at a location that was sometimes the inner strike point, and thus the absence of a thick boron layer is not surprising. The upper divertor tile had a film thickness between that of the lower divertor and the mid-plane specimens, and was composed primarily of carbon.

JET specimens

Specimens with a film thickness of ~ 2 μm (cross-sectional SEM) were taken from the JET Mark I divertor, which was in operation from April 1994 to March 1995. The tile location on the divertor was designated 6A, and the surface analysis information of these tiles can be found in [12]. The tile was in place during Be evaporation experiments and thus contained as much as 10 at% Be [12].

3.2. Thermo-oxidation and deuterium content measurements

The deuterium content of the tokamak films was measured by laser thermal desorption spectroscopy following thermo-oxidation at 523-623K in a 2.1kPa oxygen backfill. The thermal desorption procedure made use of a neodymium-glass laser, with a ~0.5 s pulse length and ~ 1 J energy/pulse, to remove the film from a ~1.6 mm diameter spot on the surface. The released deuterium was then measured using a quadrupole mass spectrometer (QMS) monitoring signals at masses 3 and 4.

Thermo-oxidation of the various codeposits produces very similar trends in D removal as a function of time of O_2 exposure. This trend is seen in Fig. 3 in the form of a large decrease in the D content over the first hour, at 623 K, followed by a much slower decrease over the remainder of the experimental run; at 523 K, removal rates are about an order of magnitude lower. The D removal rates, as well as the corresponding estimated C erosion rates for some cases where sufficient information was available, are summarized in Table 1.

The specimens from the DIII-D *divertor* (both upper and lower) behaved in a similar manner; see Fig. 3(c). There is an initial fast removal of the film, followed by a slower rate. While both of these films contained some boron, they were primarily composed of carbon. On the other hand, the DIII-D *outer mid-plane* film specimen was primarily composed of a boron rich layer of ~ 2 μm, with some indication of a thin carbon outer layer. In this case, the O_2 was able to remove only ~25 % of the D, the remainder being locked up by a stable boron layer; see Fig. 3(c).

Table 1. C-erosion and D-removal rates for tokamak codeposits during O_2 exposure

Temp [K]	TFTR/N3-15 [6,7] ~ 5 μm thick (ρ~1900 kg·m^{-3}; D/C~0.35); 16 Torr O_2			TFTR/N3-24 [7] ~ 0.15 μm thick 16 Torr O_2	
	Erosion		D-removal [D/m^{2}h]	Erosion [μm/h][c]	D-removal [D/m^{2}h]
	[μm/h][a]	[C/m^{2}h][b]			
523	0.8	5.7x10^{22}	2x10^{22}	0.07	0.2x10^{22}
573	3.5	29x10^{22}	10x10^{22}		
623	> 10	>70x10^{22}	>25x10^{22}	> 0.5	1.5x10^{22}

Temp [K]	JET divertor 6A [7] ~2 μm thick 16 Torr O_2		DIII-D#B [7] ~ 2 μm thick (ρ~1300 kg·m^{-3}; D/C~0.185); 16 Torr O_2			DIII-D [8] upper&lower divertor and midplane tiles; 16 Torr O_2
	Erosion [μm/h][a]	D-removal [D/m^{2}h]	Erosion		D-removal [D/m^{2}h]	D-removal [D/m^{2}h]
			[μm/h][a]	[C/m^{2}h][b]		
523	0.5	1x10^{22}	0.23	1.5x10^{22}	0.27x10^{22}	
573						
623	3.3	7x10^{22}	3.5	22x10^{22}	4.1x10^{22}	~ 0.6x10^{22}

[a] Erosion rate is estimated from measured D content and SEM photos of film thickness, assuming constant D/C.
[b] C-erosion rate is estimated from measured D content and D/C ratio based on mass-loss measurement.
[c] Erosion rate is estimated from measured D content and an assumed D/C ratio and density based on the TFTR/N3-15 value.

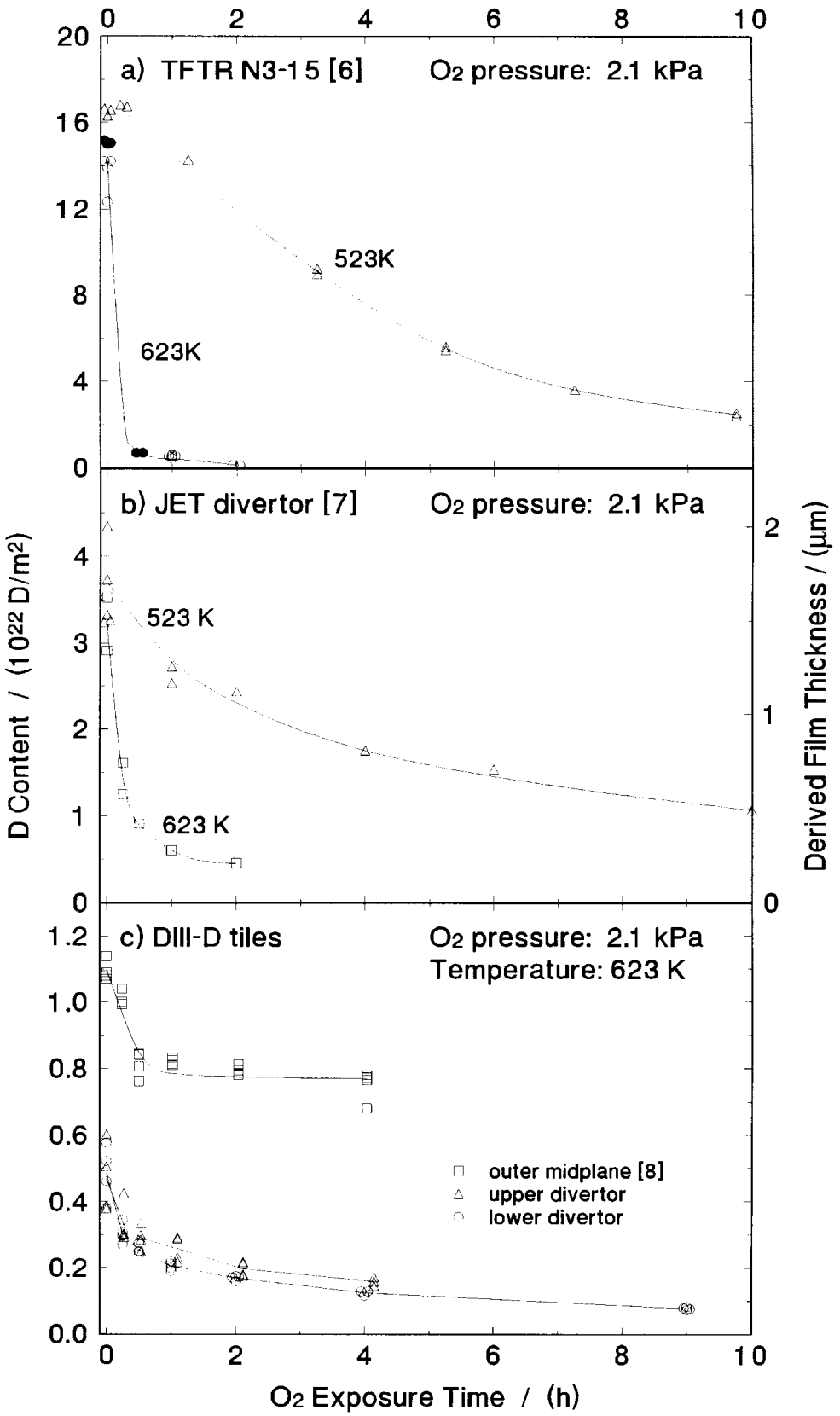

Fig. 3. D content as a function of O_2 exposure for codeposited films obtained from tokamaks. (a) TFTR [6,7], JET [7] and (b) DIII-D midplane [7,8] and upper and lower divertor tiles.

REFERENCES

[1] A.A. Haasz, J.W. Davis, "Deuterium retention in doped graphites," J. Nucl. Mater. 232 (1996) 219-225.

[2] M. Poon, J.W. Davis, A.A. Haasz, "Effect of carbon pre-implantation on deuterium retention in tungsten," J. Nucl. Mater. 283-287 (2000) 1062-1067.

[3] Haasz, Davis, Poon, Macaulay-Newcombe, "Deuterium retention in tungsten for fusion use," J. Nucl. Mater. 258-263 (1998) 889-895.

[4] A.A. Haasz, J.W. Davis, "Fluence dependence of deuterium trapping in graphite," J. Nucl. Mater. 209 (1994) 155-160.

[5] G. Federici, et al. J. Nucl. Mater. 266-269 (1999) 14-29.

[6] J.W. Davis, A.A. Haasz, " The removal of codeposited layers from TFTR tiles by O_2 gas exposure," J. Nucl. Mater. 256 (1998) 65-68.

[7] J.W. Davis, A.A. Haasz, "Oxygen removal of codeposited a-C:D layers from tokamak tiles," J. Nucl. Mater. 266-269 (1999) 478-484.

[8] J.W. Davis, P.B. Wright, R.G. Macaulay-Newcombe, A.A. Haasz, C.G. Hamilton, "Chemical erosion of boronized films from DIII-D tiles," J. Nucl. Mater. 290-293 (2001) 66-70.

[9] A.A. Haasz, S. Chiu, J.E. Pierre, Y.I. Gudimenko, "Thermo-oxidative removal of amorphous hydrogenated carbon films," J. Vac. Sci. Technol. A14 (1996) 178-193.

[10] B.E. Mills, D.A. Buchenauer,A.E. Pontau, M. Ulrickson, J. Nucl. Mater. 162-164 (1989) 343.

[11] W.R. Wampler, B.L. Doyle, S.R. Lee, et al., J. Vac. Sci. Technol. A6 (1988) 2111.

[12] J.P. Coad, M. Rubel, C.H. Wu, J. Nucl. Mater. 241-243 (1997) 408.

HYDROGEN RETENTION IN BERYLLIUM OXIDE

V.KH. ALIMOV
Institute of Physical Chemistry, Russian Academy of Sciences,
Moscow, Russian Federation

Abstract

The paper gives a review of the experimental results on oxidation of beryllium under deuterium (D) ion irradiation and deuterium retention in beryllium oxide. Irradiation of Be with keV D ions as well as D atom exposure in the atmosphere of oxygen-containing molecules leads to oxygen incorporation into the sample. The results of detailed studies on oxygen incorporation into beryllium under 3 keV D ion bombardment at 300 and 700 K are presented in this paper. Furthermore, retention of deuterium implanted in beryllium oxide in the temperature range from at 300 to 700 K is analyzed.

1. INTRODUCTION

Present concepts for ITER-FEAT consider beryllium (Be) as a candidate material for the plasma-facing component of the first-wall system [1]. Sputtering of Be tiles with hydrogen isotope ions and neutrals as well as by impurity atoms leads to codeposition of beryllium, carbon, oxygen and hydrogen isotope atoms at deposition-dominated areas of the wall [2-4]. Due to a high affinity of Be to oxygen [5], beryllium oxide (BeO) formation takes place. Reliable data on the hydrogen behavior in beryllium oxide, in particular, under irradiation are of great importance for the application of Be tiles in fusion devices.

The first reviews of experimental data available for hydrogen isotope trapping and release in pure beryllium were presented around ten years ago [5,6]. Recently, new results regarding hydrogen isotope retention in Be for tokamak plasma-facing application were reviewed in detail [7]. However, the data base on the hydrogen behavior in beryllium oxide is very poor. This paper presents the experimental results on oxidation of Be under D ion irradiation in a controlled oxygen atmosphere (Section 2) and deuterium retention in beryllium oxide (Section 3).

2 OXYGEN INCORPORATION INTO BERYLLIUM UNDER D ION IRRADIATION IN OXYGEN ATMOSPHERE

It is well known that beryllium reacts rapidly with oxygen or oxygen-bearing compounds to form beryllium oxide BeO, with a large exothermic enthalpy of formation (about –600 kJ/mol [8]). A saturated BeO layer has been observed to form on clean Be surface for oxygen exposure of only 10 Langmuirs (L) [9] (1 L is equivalent to 1.3×10^{-4} Pa s). For oxygen exposure of 4×10^{5} L at room temperature the BeO thickness was found to be 1.3-1.4 nm [10]. Under conditions of thermal oxidation at O_2 pressures between 3×10^{-6} and 2×10^{-4} Pa and in the temperature range 300 to 770 K the time dependence of the thickness of the beryllium oxide film obeys a logarithmic law [10]. After air exposure at room temperature, electropolished hot-pressed beryllium is normally covered with a nonporous protective oxide film of about 5-7 nm [11].

The increase of oxygen content in beryllium after D or He ion bombardment under relatively poor vacuum conditions has been observed by Langley [12]. Sixteen years after, Alimov et al. [11] presented results on the oxygen sorption in beryllium irradiated with D and

He ions and then exposed to air and ^{18}O enriched (80%) oxygen at 300 K. The total content of oxygen isotopes in the near-surface layer of a Be sample was measured by electron probe microanalysis (EPMA), whereas depth profiles of deuterium, helium and oxygen isotopes were determined by secondary ion mass spectrometry (SIMS) and residual gas analysis (RGA) in the course of surface sputtering. A comparison of oxygen depth profiles with D/He ion ranges made it possible to establish that the oxygen accumulation in the subsurface layer with a thickness equal to the ion mean range took place after the ion implantation with high fluences (at which the reemission of deuterium/helium appeared). It was suggested that a kind of open porosity developed in the ion stopping zone. Actually, a transmission electron microscopy (TEM) study of the microstructure of Be irradiated with D and He ions in the temperature range 300 to 700 K revealed the development of interconnected bubbles at room temperature and a labyrinth structure of flattened-out wide channels at temperatures ≥500 K [13]. Obviously, this porosity was responsible for the penetration of oxygen-containing molecules into the near-surface layer of the ion implanted Be, which led to the increase of oxygen content after the ion irradiation.

The oxygen incorporation into beryllium under 3 keV D ion irradiation at 300 and 700 K in ^{18}O enriched oxygen atmosphere at pressures ranged 10^{-5} to 10^{-3} Pa was studied by Alimov et al. [14]. They showed that the total amount of incorporated oxygen increases stepwise with D ion fluence (Fig. 1). At the first accumulation stage, the oxygen atoms are incorporated into the surface layers. Values of the O atom incorporation rate at the first accumulation stage are given in Table I. At the second accumulation stage, the development of interconnected gas porosity in the Be matrix and penetration of oxygen molecules through the system of open pores results in the oxidation of a newly formed beryllium surface; in so doing the marked increase of the oxygen content in the ion stopping zone takes place. The maximum content of oxygen incorporated into the surface layers and the bulk (in the implantation zone) increases with the oxygen pressure and decreases when the irradiation temperature increases from 300 to 700 K.

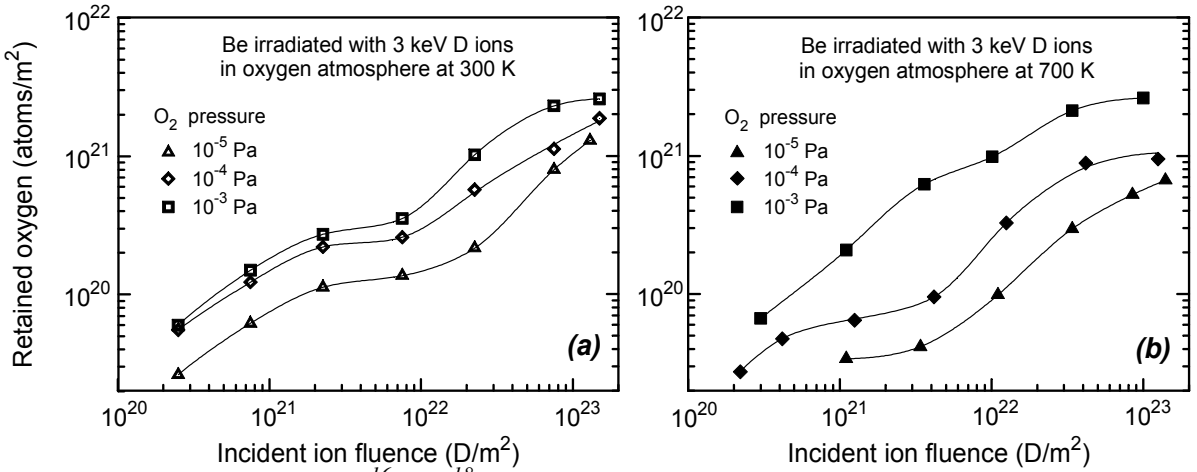

Figure 1. Amount of oxygen(^{16}O + ^{18}O) incorporated into Be irradiated with 3 keV D ions at 300 (a) and 700 K (b) in ^{18}O enriched oxygen atmosphere at pressures indicated as a function of the ion fluence [14].

TABLE I. INITIAL RATES OF INCORPORATION OF ^{16}O AND ^{18}O ATOMS INTO BERYLLIUM (O ATOMS/D ION) UNDER IRRADIATION WITH 3 keV D IONS IN O_2 ATMOSPHERE AT 300 AND 700 K [14]

	$P_{oxygen} = 10^{-5}$ Pa	$P_{oxygen} = 10^{-4}$ Pa	$P_{oxygen} = 10^{-3}$ Pa
T_{irr} = 300 K	0.09±0.03	0.18±0.06	0.20±0.06
T_{irr} = 700 K	<0.03	0.11±0.04	0.19±0.06

Some possible processes for oxygen incorporation into and through existing beryllium oxide layers under ion bombardment at the first accumulation stage can be pointed out. (i) Dissociation of oxygen molecules on the oxide surface. Oxygen atoms or ions would diffuse much easier than molecules through the oxide layer thereby enhancing the incorporation rate. (ii) Radiation enhanced adsorption, causing a larger surface oxygen coverage due to electronic charging of the surface or to an increased number of oxygen adsorption sites on the surface produced by ion sputtering. (iii) Recoil implantation and/or radiation enhanced diffusion of oxygen atoms through defects created under irradiation.

It seems likely that the increase of implantation temperature will cause the amount of oxygen adsorbed on BeO surface to decrease and will cause a reduction in the oxygen incorporation rate. The processes (i)-(iii) would be of major importance for the oxygen incorporation at low D-ion fluences. At high fluences, the formation of an open porosity over the D ion stopping range increases the area of the oxygen interaction with beryllium atoms and hence the oxygen amount in the bulk.

3. DEUTERIUM RETENTION IN BERYLLIUM OXIDE

In close-packed hexagonal (cph) lattices of beryllium oxide, for each oxygen anion O^{2-}, 0.132 nm in radius [15], there are two tetrahedral interstitial sites ($r_t = 0.22r(O^{2-}) = 0.029$ nm) and one octahedral interstitial site ($r_o = 0.41r(O^{2-}) = 0.054$ nm). One of the tetrahedral interstitial sites is occupied by beryllium cation Be^{2+} of 0.034 nm radius [15]. The position of hydrogen in BeO can be different. Taking into account the size of hydrogen atom (atomic radius = 0.078 nm, covalent radius = 0.03 nm) the most probable place for hydrogen location in non-charged state is octahedral interstitial site. Nevertheless, the probability that hydrogen can reside in the empty tetrahedral interstitial site of the anion sublattice or in a cation vacancy (which is also a tetrahedral site) must not be ruled out. It is quite reasonable to suppose that hydrogen is charged positively in a cation vacancy.

A wide range of values for the tritium diffusivity was observed by Fowler et al. [16] in studies of single crystal, sintered and powdered BeO with activation energies ranging from 0.7 to 2.3 eV. The value for the T diffusivity in sintered BeO, $D = 7\times10^{-6}$ exp (-2.1 eV/kT) m^2s^{-1}, which was determined for the temperature range 923-1473 K [16], is generally used for BeO films thermally grown onto a Be substrate. The solubility of deuterium in BeO was determined by Macaulay-Newcombe and Thompson using a technique of deuterium thermal absorption and desorption [17]. They reported the solubility to be given by $S \approx 10^{18}$ exp (-0.8 eV/kT) at.$\cdot m^{-3}\cdot Pa^{-0.5}$ and possibly related to the formation of hydroxide

bonds, because of the similarity of the activation energy, 0.8 eV, to the O-H bond formation energy of 0.81 eV [18].

The experiments on hydrogen absorption by BeO exposed to a hydrogen atmosphere [19] have revealed that hydrogen uptake is not observed below 573 K and that at 573–773 K the hydrogen sorption is not reproducible. The H atom sorption leads to some electron transfer process detected by means of infrared spectroscopic techniques. The H sorption may have produced a chemisorbed protonic species of the type postulated on ZnO [20]. Under subsequent heating, the H species are partly or wholly desorbed as water, possibly causing the formation of anion vacancies [19].

The trapping of ion implanted deuterium (5 keV D^+) in thermally grown BeO films at implant temperatures ranging from 140 to 470 K was investigated by Behrisch et al. [21] using the $D(^3He,H)^4He$ nuclear reaction. The ratio of implanted D to BeO molecules obtained at saturation was found to be 0.34 and 0.24 for implant temperatures of 140 and 300-470 K, respectively.

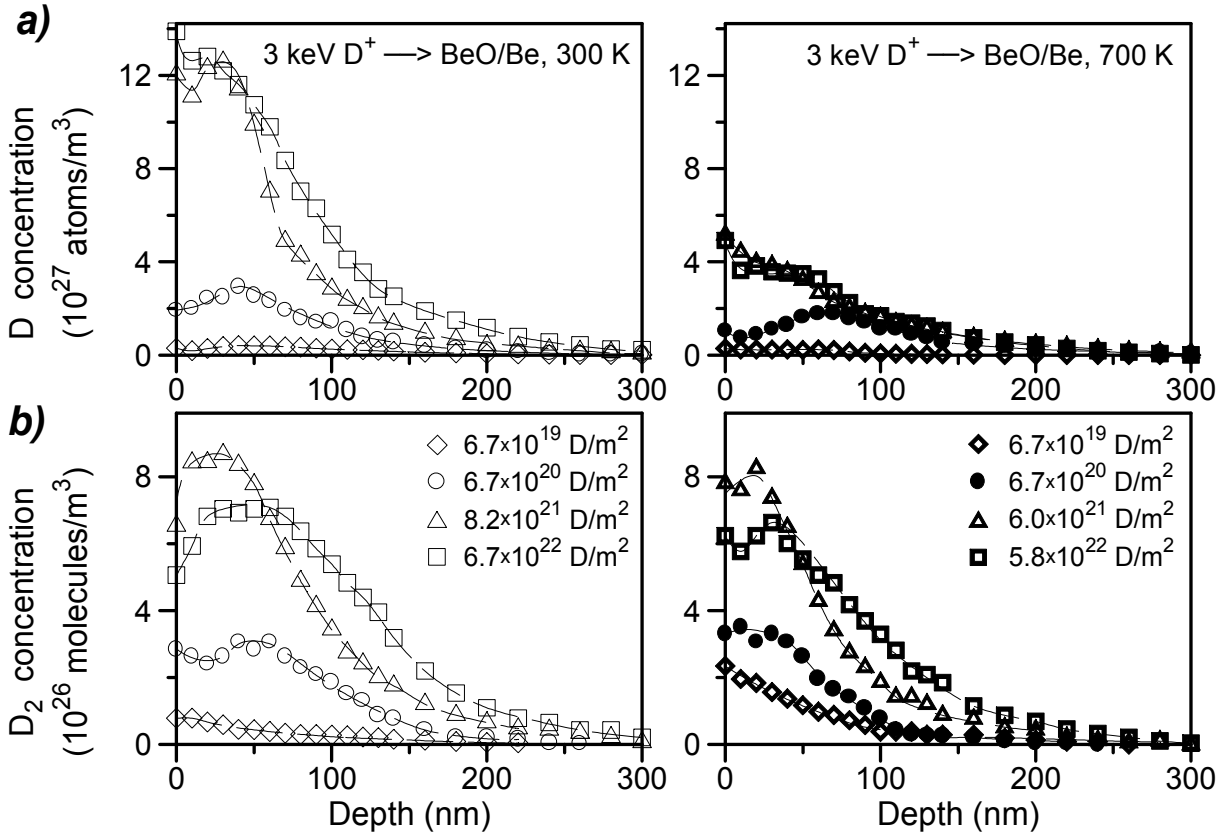

Figure 2. Concentration profiles of deuterium trapped as D atoms (a) and in the form of D_2 molecules (b) in 120 nm layer of BeO on Be substrate implanted with 3 keV D ions at 300 and 700 K [22]. Note that the molecular density of beryllium oxide is approximately 7.2×10^{28} BeO/m^3.

In the experiments performed by Alimov and Chernikov [22], SIMS, RGA and TEM were used to determine the depth concentration profiles of deuterium trapped in beryllium oxide as separate D atoms and D_2 molecules. The oxide layer was grown on polished Be to a thickness of about 120 nm. Deuterium at 3 keV was implanted to a depth of about 50 nm at irradiation temperatures of 300 and 700 K. Depth profiles of D atoms and D_2 molecules in

BeO/Be sample are shown in Fig. 2. TEM analysis have revealed that irradiation at 300 and 700 K leads to the formation of tiny deuterium filled bubbles (0.6-0.7 nm radius, (4-5)×10^{24} m^{-3} volume density). These bubbles together with the intercrystalline gaps are responsible for the accumulation of a molecular fraction of the implanted deuterium. The major part of implanted deuterium is present in BeO film in the form of D atoms (Fig. 3), probably chemically bound to O atoms.

The comparison of the maximum concentrations of D atoms, D_2 molecules and total deuterium present in both states in Be and BeO irradiated with D ions at 300 and 700 K to high fluences (when saturation takes place) is given in Table II. The study of deuterium retention in beryllium [13,23] has shown that a high percentage of deuterium is accumulated in the form of D_2 molecules.

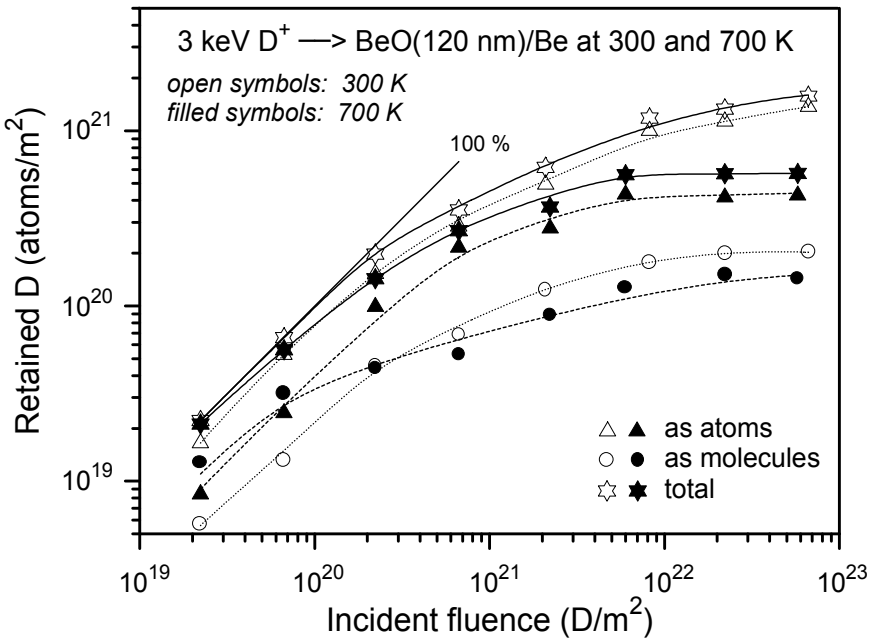

Figure 3. Quantities of deuterium trapped as D atoms and D_2 molecules and the total amount of deuterium within the BeO film of ~ 120 nm in thickness and adjacent metal layers implanted with 3 keV D ions at 300 and 700 K as a function of the ion fluence [22].

TABLE II. MAXIMUM CONCENTRATIONS OF D ATOMS, D_2 MOLECULES AND DEUTERIUM PRESENT IN BOTH STATES IN THE IMPLANTATION ZONE OF BERYLLIUM [13,23] AND BERYLLIUM OXIDE [22] IRRADIATED WITH D IONS AT 300 AND 700 K

	Be		BeO	
	300 K	700 K	300 K	700 K
D atom concentration (D/Be)	0.02	0.01	0.18	0.05
D_2 molecule concentration (D_2/Be)	0.04	0.01	0.01	0.01
Total D concentration (D/Be)	0.10	0.03	0.20	0.07
Gas-induced swelling (%)	1.8	50	0.5	0.6

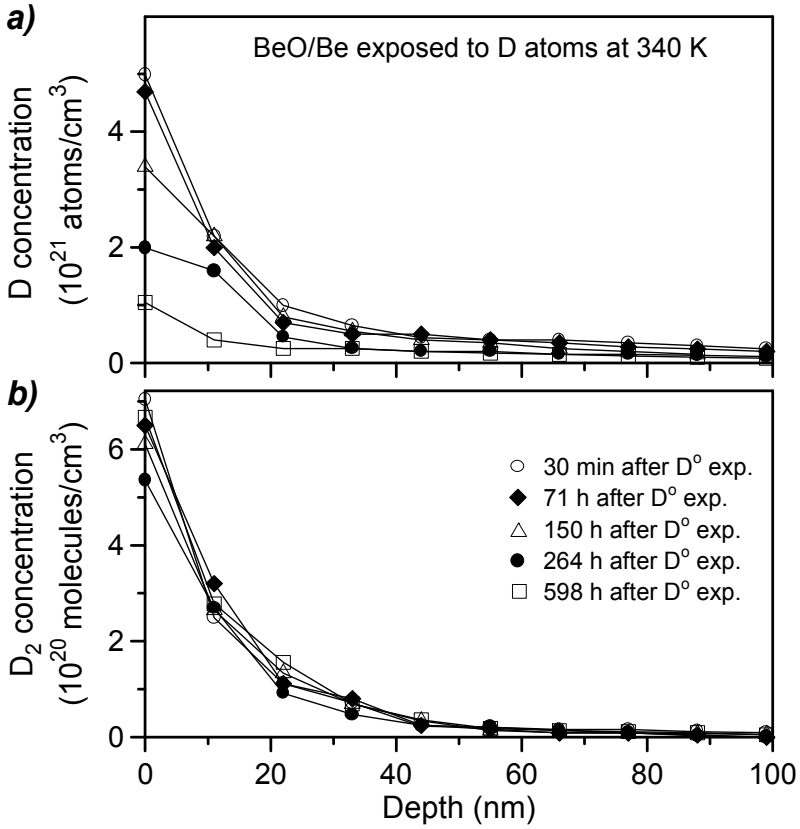

Figure 4. Evolution of D atom concentration (a) and D_2 molecule concentration (b) in BeO/Be sample exposed to D atoms at 340 K to a fluence of ~4×10^{23} D/m^2, as a function of storage time in vacuum at room temperature [25].

As for BeO, the majority of implanted deuterium is retained as D atoms both at 300 and 700 K [22]. Attention is drawn to the fact that the value of gas-induced swelling in BeO at 700 K is two orders of magnitude less then that for Be.

The retention of deuterium in a beryllium oxide layer growing onto a Be substrate during D atom exposure in medium base vacuum (10^{-4} Pa) at 340 and 500 K was measured by Sharapov and Alimov [24,25] using combined SIMS and RGA methods. Results obtained show that deuterium is mainly accumulated as D atoms in the BeO layer about 20 nm in thickness (Fig. 4). Concentration profiles of oxygen were determined by SIMS. The fraction of D_2 molecules in deuterium retention is small and does not exceed 5-10%. The amount of D atoms decreases with time during the sample storage at 300 K in vacuum or air, whereas the D_2 content remains practically constant (Fig. 4). The evolution of D atom content, Q_D, with storage time obeys the equation: $Q_D = Q_D^0 \exp(-f_D t)$, where Q_D^0 is the initial D atom content, t - the elapsed time from termination of D atom exposure, f_D – the decrease rate constant. The value of f_D was determined to be equal to $(3.6\pm0.3)\times10^{-5}$ min^{-1} [25].

It is suggested [18,26] that hydrogen isotope atoms may react with beryllium oxide to form beryllium hydroxide by the chemical reaction

$$2BeO + 2H \rightarrow Be(OH)_2 + Be \quad (1)$$

the S.T.P. formation energy of which is about -0.8 eV [27]. The decomposition of beryllium hydroxide is carried out according to the reaction

$$2Be(OH)_2 \rightarrow 2BeO + H_2O \quad (2)$$

with an activation energy of 61.5 kJ/mol (0.64 eV) [28]. The decrease of D atom content in a BeO layer with time [24,25] (Fig. 4) is thought to be attributable to dehydration of beryllium hydroxide which is formed during simultaneous action of D atoms and oxygen-containing molecules on the Be sample surface. An Arrhenius plot of the dehydration rate constant for beryllium hydroxide is shown in Fig. 5.

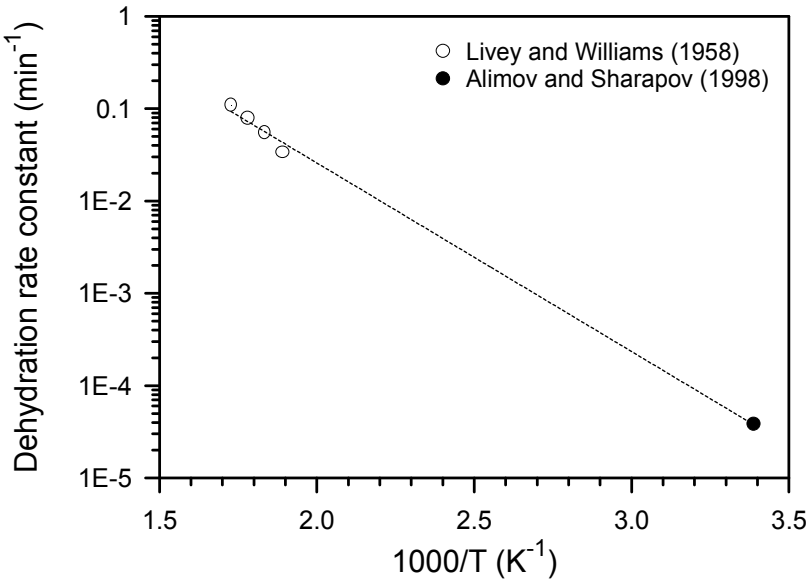

Figure 5. Arrhenius plot of the dehydration rate constant for beryllium hydroxide. The experimental data are taken from Livey and Williams [28] and Alimov and Sharapov [24,25].

The appearance of molecular deuterium in the BeO layer growing during D atom exposure (Fig. 4) is related to accumulation of deuterium atoms at structural defects of oxide layer where they form molecules.

4. CONCLUSIONS

(1) Irradiation of beryllium with D ions in an oxygen-containing atmosphere leads to radiation-enhanced oxidation of beryllium. In the case of irradiation with keV D ions in an O_2 atmosphere, the total amount of oxygen atoms incorporated into Be increases stepwise with D ion fluence. At the first accumulation stage, the oxygen atoms are incorporated into the surface layers. At the second accumulation stage, the development of interconnected gas porosity in the Be matrix and penetration of oxygen molecules through the system of open pores result in the oxidation of new-formed beryllium surface; in so doing the marked increase of the oxygen content in the ion stopping zone takes place. The maximum content of oxygen incorporated into the surface layers increases with the pressure of oxygen-containing molecules.

(2) Irradiation of a BeO layer with keV D ions at 300 and 700 K leads to the formation of tiny deuterium filled bubbles of 0.6-0.7 nm in radius and with volume density of $(4\text{-}5)\times10^{24}$ m^{-3}. These bubbles together with the intercrystalline gaps are thought to be responsible for the accumulation of D_2 molecules. At both irradiation temperatures the D_2 concentration reaches its maximum of 0.01 D_2-molecules/BeO. However, the major part of implanted deuterium is present in BeO film in the form of D atoms, probably, chemically bound to O atoms. The maximal D atom concentration is 0.18 D-atoms/BeO for D ion implantation at 300 K and 0.05 D-atoms/Bo for the implantation at 700 K.

Due to the presence of oxygen-containing molecules as trace impurities, the beryllium oxide layer is formed on the surface of the Be sample exposed to D atoms at elevated temperatures. It has been found that the deuterium atom exposure leads to the deuterium retention in this layer. The majority of deuterium (> 90%) retains as D atoms, the other part is accumulated in the form of D_2 molecules. After termination of D atom exposure the D concentration in BeO layer decreases with time at room temperature. It is supposed that the formation of beryllium hydroxide $Be(OD)_2$ under D atom exposure of a growing BeO layer takes place. The decrease of deuterium concentration with time is explained by dehydration of the beryllium hydroxide.

REFERENCES

[1] FEDERICI, G., BROOKS, J.N., COSTER, D.P., et al., Proc. 14th Intern Conf. on Plasma Surface Interaction in Controlled Fusion Devices (to be published in J. Nucl. Mater).
[2] MARTINELLI, A.P., BEHRISCH, R., PEACOCK, A.T., J. Nucl. Mater. **212-215** (1994) 1245.
[3] BEHRISCH, R., MARTINELLI, A.P., GRIGULL, S., et al., J. Nucl. Mater. **220-222** (1995) 590.
[4] MAYER, M., BEHRISCH, R., PLANK, H., et al., J. Nucl. Mater. **230** (1996) 67.
[5] WILSON, K.L., CAUSEY, R.A., HSU, W.L., et al., J. Vac. Sci. Technol. A **8** (1990) 1750.
[6] WILSON, K.L., BASTASZ, R., CAUSEY, R.A., et al., Suppl. Nucl. Fusion, **1** (1991) 31.
[7] ANDERL, R.A., CAUSEY, R.A., DAVIS, J.W., et al., J. Nucl. Mater. **273** (1999) 1.
[8] KELLEY, K.K., J.Amer. Chem. Soc. **61** (1939) 1217.
[9] HURD, J.T., ADAMS, R.O., J. Vac. Sci. Technol. **6** (1969) 229.
[10] FOWLER, D.E., BLAKELY, J.M., Surface Sci. **148** (1984) 265.
[11] ALIMOV, V.KH., ZALAVUTDINOV, R.KH., GORODETSKY, A.E., ZAKHAROV, A.P., J. Nucl. Mater. **220-222** (1995) 947.
[12] LANGLEY, R.A., J. Nucl.Mater. **85&86** (1979) 1123.
[13] CHERNIKOV, V.N., ALIMOV, V.KH., MARKIN, A.V., ZAKHAROV, A.P., J. Nucl. Mater. **228** (1996) 47.
[14] ALIMOV, V.KH., ZALAVUTDINOV, R.KH., ZAKHAROV A.P., J. Nucl. Mater. **266-269** (1999) 417.
[15] BELIAEV, R.A., Beryllium Oxide, Gosatomizdat, Moscow (1962) (in Russian).
[16] FOWLER, J.D., CHANDRA, D., ELLEMAN, T.S., PAYNE, A.W., VERGHESE, K., J. Am. Ceram. Soc. **60** (1977) 155.
[17] MACAULAY-NEWCOMBE, R.G., THOMPSON, D.A., J. Nucl. Mater. **212-215** (1994) 942.
[18] BILLONE, M.C., DALLE DONNE, M., MACAULAY-NEWCOMBE, R.G., Fusion Eng. Des. **27** (1995) 179.
[19] LOW, M.J.D., RAMASUBRAMANIAN, N., J. Phys. Chem. **70** (1966) 933.
[20] EISCHENS, R.P., PLISKIN, W.A., LOW, M.J.D., J. Catalysis **1** (1962) 180.
[21] BEHRISCH, R., BLEWER, R.S., BORDERS, J., LANGLEY, R., ROTH, J., SCHERZER, B.M.U., SCHULZ, R., Radiat. Eff. **48** (1980) 221.
[22] ALIMOV, V.KH., CHERNIKOV, V.N., J. Nucl. Mater. **273** (1999) 277.
[23] ALIMOV, V.KH., CHERNIKOV, V.N., ZAKHAROV, A.P., J. Nucl. Mater. **241-243** (1997) 1047.
[24] SHARAPOV, V.M., ALIMOV, V.KH., GAVRILOV, L.E., J. Nucl. Mater. **258-263** (1998) 803.
[25] ALIMOV, V.KH., SHARAPOV, V.M., unpublished work.

[26] SHARAPOV, V.M., GAVRILOV, L.E., KULIKAUSKAS, V.S., MARKIN, A.V., J. Nucl. Mater. **233-237** (1996) 870.
[27] CHASE, M.W., Jr., DAVIES, C.A., DOWNEY, J.R., Jr., FRURIP, D.J., McDONALD, R.A., SYVERUD, A.N., JANAF Thermochemical Tables, 3rd ed., Part I, aluminium-cobalt, J. Phys. Chem. Ref. Data (Suppl. 14) (1985) 1.
[28] LIVEY D.T., WILLIAMS, J., Proc. Second UN International Conference on Peaceful Uses of Atomic Energy, Geneva, vol. 5, 1958, 311.

DEUTERIUM RETENTION IN GRAPHITE, TUNGSTEN AND TUNGSTEN-CARBON MIXED MATERIALS

V.Kh. ALIMOV, D.A. KOMAROV, R.Kh. ZALAVUTDINOV
Institute of Physical Chemistry, Russian Academy of Sciences,
Moscow, Russian Federation

Abstract

Deuterium (D) retention in graphite, tungsten single crystal and tungsten-carbon mixed materials implanted with keV D ions has been investigated by means of secondary ion mass spectrometry (SIMS) and residual gas analysis (RGA) measurements. The mixed materials were prepared by chemical vapor deposition (CVD) and reactive magnetron sputtering of carbon-tungsten cathode. In the implantation zone, the maximum D concentration in tungsten and tungsten-carbon mixed materials is lower than that in graphite by one-two orders of magnitude depending on implantation temperature. Deuterium incorporated into the tungsten-carbon mixed materials prepared by magnetron sputtering in a D2 atmosphere is accumulated up to concentrations which are typical for pure tungsten or tungsten carbides but not for graphite inclusions.

1. INTRODUCTION

According to the requirements and selection criteria in the ITER design, the plasma facing material will be chosen from beryllium, carbon fibre composite and tungsten. Physical and chemical sputtering causes erosion of plasma-facing materials and impurity release into the plasma. These elements and hydrogen from the plasma will subsequently be co-deposited back onto the wall and divertor surface forming mixed layers.

In view of the above mentioned fact, not only pure materials such as carbon and tungsten should be studied, but also carbides and mixed carbon-containing materials.

The retention of hydrogen isotopes in the carbon layer has been reviewed in the past by Wilson and Hsu [1] and by Möller [2] and is discussed in numerous other publications. When a hydrogen atom is embedded into graphite (or carbon composite) at temperatures below ~800 K, it is effectively immobile [3,4]. It remains there until the surrounding conditions (temperature or crystalline structure) are altered. Additional atoms are retained in the same manner until a saturation is reached [5]. The hydrogen to carbon ratio in the saturated layer is controlled by the temperature [6] and equals to 0.40-0.65 at 300 K and to about 0.05 at 1150 K [5,7-10]. Direct information on the deuterium-graphite bonding in the implanted layer has been acquired from X ray photoelectron spectroscopy (XPS) and secondary ion mass spectrometry (SIMS) measurements [11-13]. In XPS experiments a chemical shift as well as broadening of the C 1s peak was observed together with the appearance of CD^- and C_2D^- lines in the SIMS spectra. It was also shown that CD^- and C_2D^- lines arise due to the formation of chemical bonds between implanted deuterium and carbon. Considering the trapping of H and D ions one has to bear in mind the evidence that hydrogen molecules are formed in the bulk during implantation and these molecules diffuse to the surface through a highly damage matrix via a network of open paths of subnanometer scale [14,15].

When carbon atoms are sputtered from a graphite or carbon composite surface, they are re-deposited on the surrounding surfaces. As the sputtered atoms arrive at their new location, they are co-deposited with energetic hydrogen isotope ions and neutrals. The characteristics of

the co-deposited layers and other similar coatings are reviewed in Refs. [16-24]. The hydrogen content in the layers can reach value of ~1 H/C [23]. As to chemical composition of the co-deposited layer, summarising the results reported in Refs. [19,25-28] it can be said that the co-deposited carbon-hydrogen layer is primarily amorphous, contains a large amount of hydrogen, has hydrogen formed monohydride with sp^3, sp^2, and sp^1 hybridized carbon atoms in decreasing probability, and has hydrogen that is chemisorbed on the carbon as well.

Few data obtained by different experimental methods have been reported on deuterium inventories in tungsten after implantation of hydrogen isotope ions at energies in the range 0.1 to 8 keV [29-36]. It has been shown that the hydrogen isotope inventory in tungsten materials depends strongly on the material structure at temperatures in the range from 300 to 600 K [32]. More than 70% of the implanted deuterium diffuses into the bulk even at room temperature and is captured by lattice imperfections [32,34,35].

There are only a few works on deuterium trapping in and thermal release from tungsten containing carbon, prepared by chemical vapour deposition (CVD) [37] or by annealing tungsten films kept in contact with carbon films at 1500-1673 K [38,39]. It has been found that the amount of deuterium retained in $W_{0.85}C_{0.15}$ and $W_{0.60}C_{0.40}$ produced by CVD is more than double the value in CVD tungsten free from carbon atoms. In the tungsten layer containing carbon the concentration of retained D atoms is higher than that in pure tungsten by about 20 percent [38] and reaches the value of $\sim 1.5\times10^{28}$ D/m^3 at room temperature [38,39]. The deuterium inventory in tungsten containing carbon steeply decreases with increasing target temperature from 300 to 550 K and reaches the value of pure tungsten at higher temperatures [37]. No data on hydrogen solubility and diffusivity in tungsten carbides are available.

Retention of deuterium implanted at room temperature in pure W single crystal and that pre-irradiated with 40 keV C ions has been studied in Ref [40]. D ion implantation was performed at energies of 10 keV with the range confined in the carbon modified layer and 100 keV with the range exceeding the carbon modified layer. Carbon pre-implantation influences the deuterium retention only if the range of the D ions is confined within the carbon modified surface layer. In this case, deuterium diffusion beyond the ion range distribution does not occur and the retained amount of deuterium is smaller than in the pure W crystal. At D ion energy where the deuterium range exceeds the carbon modified layer the retention occurs in the dislocation zone extending up to 1 μm and the total retained amount is the same for carbon implanted and pure W samples.

The present work was done to study the influence of carbon atoms deposited together with tungsten and deuterium atoms on the retention of implanted deuterium. In order to understand D behaviour in the mixed W-C material, the additional experiments on the study of the deuterium retention in graphite, pure tungsten and tungsten carbide irradiated with D ions were also performed.

2. EXPERIMENTAL

2.1. Implantation of graphite, tungsten and tungsten carbide with D ions

Four types of samples were implanted with D ions:

(i) Highly ordered pyrolytic graphite (HOPG). Samples were prepared by cleaving into plates about 0.5 mm thick and cleaned in ethanol in an ultrasonic bath. Each sample was baked at 1800-1900 K for 15 min using an electron beam.

(ii) A W single crystal with a purity of 99.99 wt% produced by double electron-beam zone melting was used. The samples were cut from a W rod by spark cutting and were 0.6-0.7 mm in thickness. The sample surface was mechanically and electrochemically polished.

(iii) Chemical vapor deposited (CVD) tungsten-carbon coating with atomic ratio of W:C = 75:25, about 10 μm thick. The coating was chemically deposited on copper substrates from a vapor mixture of tungsten fluoride, carbon-containing gases and hydrogen at temperature of 750-900 K. Oxygen concentration in the coating does not exceed 1 at.%. The grain size of the CVD coating is about 1 μm and the surface roughness is 1-2 μm. The chemical composition in the bulk of the CVD coating was determined by Electron Probe Microanalysis (EPMA) in a "Cameca" microanalyzer equipped with two wavelength dispersive spectrometers. The structure of the CVD sample was characterized by means of an X ray diffraction technique. It has been revealed that the CVD coating is comprised of W_2C carbide phase and free tungsten atoms.

(iv) Tungsten-carbon mixed film $W_{0.73}C_{0.23}O_{0.04}$ prepared by dc magnetron sputtering of tungsten cathode in Ar atmosphere (see Section 2.2). Below we will denote this sample as W-C(Ar) mixed film. Characterization of the W-C mixed film by means of Reflected High Energy Electron Diffraction (RHEED) has shown that graphite-like and tungsten crystallites are present in the amorphous structure of the sample.

The samples were mounted on a heatable target holder in a special two-chamber UHV system with a typical background pressure better than 1×10^{-7} Pa. The samples were implanted in the first vacuum chamber with mass-separated D_2^+ at an energy of 6 or 12 keV (that is the samples were implanted with D ions at an energy of 3 or 6 keV) and irradiation temperatures T_{irr} = 300 and 650 K. In order to achieve a uniform implantation over the whole bombardment area, the ion beam of 0.5 mm in diameter was swept electrostatically in the x and y directions over area of 5.5×6.0 mm^2. During measurements of the ion beam current a positive bias of 30 V was applied to the target to suppress the secondary electron emission.

2.2. Deposition of carbon and tungsten-carbon mixed films by reactive magnetron sputtering in D_2 and Ar atmosphere

The samples were prepared using a magnetron sputtering system with a base pressure of approximately 1×10^{-4} Pa. The hydrogenated carbon and tungsten-carbon mixed films were deposited by dc sputtering from graphite and tungsten cathode, respectively, in a D_2 atmosphere. Additionally, a mixed tungsten-carbon film (denoted as W-C(Ar) mixed film) was deposited by sputtering of tungsten cathode in an Ar atmosphere. All sample films were deposited on silicon substrates. The discharge voltage supplied by the stabilizer to the cathode was varied in the range from –360 to -500 V depending on cathode material. The parameters maintained during the deposition of the films are shown in Table I. The seventh column shows the product of the discharge voltage and current.

When the hydrogenated C films were prepared, a considerable amount of carbon was deposited on the walls of the vacuum chamber of the magnetron sputtering system. In subsequent experiments with sputtering of tungsten cathode, the carbon atoms were deposited on the substrate simultaneously with W atoms and O atoms descended from the residual gas, and the films prepared were W-C mixed ones.

TABLE I. DEPOSITION CONDITIONS FOR DC MAGNETRON SPUTTERING OF CARBON AND TUNGSTEN-CARBON MIXED FILMS

Sample	Cathode material	Sputtering gas	Gas pressure (Pa)	Deposition temperature (K)	Cathode to substrate distance (cm)	Sputtering power (V×A)	Film composition	Film thickness (nm)
C film	Graphite	D_2	0.1-0.3	393	10	360×0.5	$C_{0.92}O_{0.08}$	36
C film	Graphite	D_2	0.1-0.3	400	6	400×1.5	$C_{0.85}O_{0.15}$	653
C film	Graphite	D_2	0.1-0.3	683	6	400×1.5	$C_{0.89}O_{0.11}$	73
C film	Graphite	D_2	0.3-0.4	973	6	380×1.5	$C_{0.98}O_{0.02}$	206
W-C film	Tungsten	D_2	1.0	393	10	480×1.5	$W_{0.57}C_{0.23}O_{0.20}$	25
W-C film	Tungsten	D_2	0.5	463	6	500×1.5	$W_{0.51}C_{0.31}O_{0.18}$	258
W-C film	Tungsten	D_2	0.5	563	6	500×1.5	$W_{0.62}C_{0.18}O_{0.20}$	303
W-C film	Tungsten	D_2	0.5	617	6	500×1.5	$W_{0.60}C_{0.23}O_{0.17}$	305
W-C film	Tungsten	D_2	0.5	733	6	500×1.5	$W_{0.61}C_{0.27}O_{0.12}$	364
W-C film	Tungsten	D_2	0.5	833	6	500×1.5	$W_{0.78}C_{0.13}O_{0.09}$	313
W-C film	Tungsten	D_2	0.5	960	6	500×1.5	$W_{0.83}C_{0.10}O_{0.07}$	307
W-C film	Tungsten	Ar	0.1	580	11.5	360×1.0	$W_{0.73}C_{0.23}O_{0.04}$	110

The chemical composition of the deposited films was determined by EPMA. The structure of W-C mixed films was characterized by RHEED. It has been revealed that the W-C mixed films prepared at relatively low temperatures (≤ 563 K) demonstrate amorphous structure with inclusions of graphite-like and tungsten crystallites about 1 nm in size. With the deposition temperature increase, the graphite-like and tungsten crystallites grow in size (up to 10 nm for graphite inclusions and ~100 nm for tungsten crystallites). In the mixed films prepared at temperatures above 733 K, W_2C carbide phase is also observed in the RHEED pattern.

2.3. Deuterium depth profiling

The samples implanted with D ions or prepared by magnetron sputtering were transferred into the second analytical chamber of the UHV system for SIMS measurements of D^- (m/e = 2), C^- (m/e = 12), CH^- (m/e = 13), CH_2^- and CD^- (m/e = 14) secondary ion species and RGA measurements of the partial pressures of HD and D_2 molecules in the course of sputtering of the surface with 4 keV Ar^+. The use of two quadrupole mass spectrometers (QMS) made it possible to register SIMS and RGA signals simultaneously. Partial pressures of HD and D_2 molecules evolved were determined taking into account the background intensities of masses 3 and 4, which were measured with the Ar ion beam switched off.

For highly ordered pyrolytic graphite and W single crystal, the sputtering rate was usually determined as a ratio of the depth of a crater produced by sputtering on the surfaces

(using optical interferometer) to the sputtering time with an accuracy of about 40%. The sputtering rates for CVD tungsten-carbon coating and mixed tungsten-carbon films were assumed to be equal to the sputtering rate of W crystal.

To separate CH_2^- and CD^- signals, a dependence $\frac{CH_2^-}{C^-} = f(\frac{CH^-}{C^-})$ was revealed using SIMS analysis of unirradiated HOPG (Fig. 1). It should be noted that HOPG as manufactured contains a considerable amount of protium. Analyzing D ion implanted graphite and carbon films prepared by magnetron sputtering, the CH^-/C^- ratio was measured and the CH_2^-/C^- ratio was determined using the dependence $\frac{CH_2^-}{C^-} = f(\frac{CH^-}{C^-})$. The CD^-/C^- ratio was obtained by subtraction of the CH_2^-/C^- ratio from the ratio of 14 *m*/*e* to 12 *m*/*e*.

We attribute the appearance of the SIMS D^- signal (or CD^- signal when D ion implanted graphite and D-containing carbon films are analyzed) to the existence of separate D atoms within the matrix. A cause of the D_2 signal appearance seems to be the recombination of D atoms sputtered as well as the direct release of D_2 molecules from the sputtered layers. In order to distinguish the recombination and molecular fractions, the HD and D_2 RGA signals were measured simultaneously. We assume that in the absence of the molecular fraction the intensity of the D_2 signal should be proportional to the square of the intensity of the HD signal. Such a proportionality is observed in fact after D ion irradiation of graphite and beryllium at 300 K up to $\Phi < 1\times10^{20}$ D/m^2 [41,42]. The coefficient of the proportionality, *K*, depends on vacuum conditions and has much in common with that obtained in our experiments with graphite and Be. Regarding *K* as a constant during sputtering in RGA measurements, one can determine the intensity of the signal I_{mol} caused solely by the release of molecular deuterium:

$$I_{\mathrm{mol}} = I_{\mathrm{D_2}} - K(I_{\mathrm{HD}})^2,$$

where $I_{\mathrm{D_2}}$ and I_{HD} are the experimentally measured intensities of the D_2 and HD RGA signals, respectively.

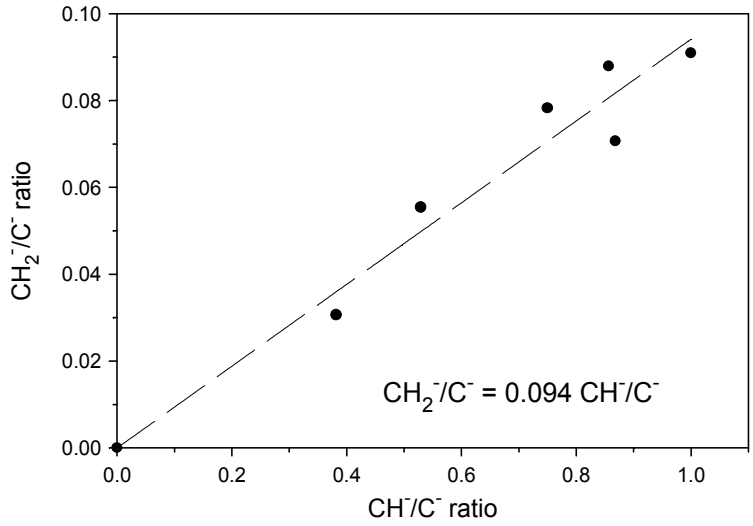

Figure 1. The relationship between CH_2^-/C^- and CH^-/C^- ratios obtained in SIMS analysis of highly ordered pyrolytic graphite containing protium alone.

Analyzing graphite implanted with D ions and D-containing carbon films, the intensity of the C^- line was used for standardization of the SIMS signals. The D atom concentration was determined by comparison of the integral SIMS CD^- signal (all over the implantation depth) with the total amount of deuterium in the sample implanted at 300 K to $\Phi = 5\times10^{19}$ D/m^2. For the above fluence graphite retains 100% of implanted atoms [43] and the value of I_{mol} is zero. The amount of D_2 molecules released under sputtering was estimated from a I_{mol} signal value taking into account the sensitivity of RGA QMS and a known pumping speed. The total error of RGA QMS calibration was about 40%.

When tungsten and tungsten carbide implanted with D ions and D-containing mixed tungsten-carbon films as well were analyzed, the calibration of D^- SIMS signal was carried out with the use of W crystal implanted with 10 keV D ions at 100 K to fluences below 3×10^{20} D/m^2 by comparison of the integral SIMS signal (all over the implantation depth) with the total amount of deuterium in this sample. Cooling down to 100 K was performed by the pumping of liquid nitrogen vapor through a tube inside the target holder. We believe that for the temperature of 100 K and fluences below 3×10^{20} D/m^2 tungsten retains 100% of implanted D atoms.

In the case of graphite, the SIMS and RGA measurements were carried out both after D ion implantation at 300 K and after heating of the implanted sample up to 970 K. The heating was performed by direct electron bombardment in a specially designed sample holder with a heating rate of about 5 K/s.

For W crystal implanted with D ions, deuterium profiling for a large depth (≥0.5 μm) has been made possible by removal of the surface layers on the irradiated side by electrochemical polishing in 2 wt% NaOH aqueous solution. In doing so, the opposite side and edges of the sample were protected by an adhesive tape. Before and after each polishing procedure the samples were weighed on an analytical balance and the depth of the etching was estimated from weight loss with an accuracy of ~40%. The uniformity of the electrochemical etching was controlled by optical and scanning electron microscopy.

3. RESULTS AND DISCUSSION

3.1. Deuterium retention in graphite implanted with D ions

The SIMS measurements have revealed that D^+, D^-, CD^+ and CD^- secondary ion yields are correlated with D ion fluence, Φ. Consequently, only these species are the fragments of configurations comprising chemical bonds between deuterium and carbon. The similarity of the depth variations of these signals with Φ both for implanted samples and for those heated after implantation up to 970 K has been established. This fact allows these four signals to be attributed to the same configuration. We will denote this configuration as [C-D] one.

The configuration which is responsible for direct release of D_2 molecules during sputtering will be denoted as [C-D_2].

Depth distributions of [C-D] and [C-D_2] configurations are shown in Fig. 2. At low ion fluences, the ratio of the depth where the maximum of the [C-D] profile is achieved, to its width (FWHM) is in a good agreement with that for deuterium implanted into other graphite materials [5,8,44]. When the fluence increases, the [C-D] profiles broaden towards the surface and form a plateau at Φ of about 5×10^{21} D/m^2. Meanwhile, the concentration of deuterium

related to [C-D] configurations rises to about 0.1 D/C (in units of atomic ratio) and does not change significantly with further fluence increase (Fig. 2a). The amount of deuterium in [C-D] configurations increases linearly with fluence in the Φ range 1×10^{19} to 5×10^{20} D/m^2 and reaches the saturation level equal to 0.9×10^{21} D/m^2 at $\Phi = 5\times10^{21}$ D/m^2 (Fig. 3). The subsequent heating of the irradiated sample up to 970 K leads to the decrease of D concentration in [C-D] configurations (Fig. 2a).

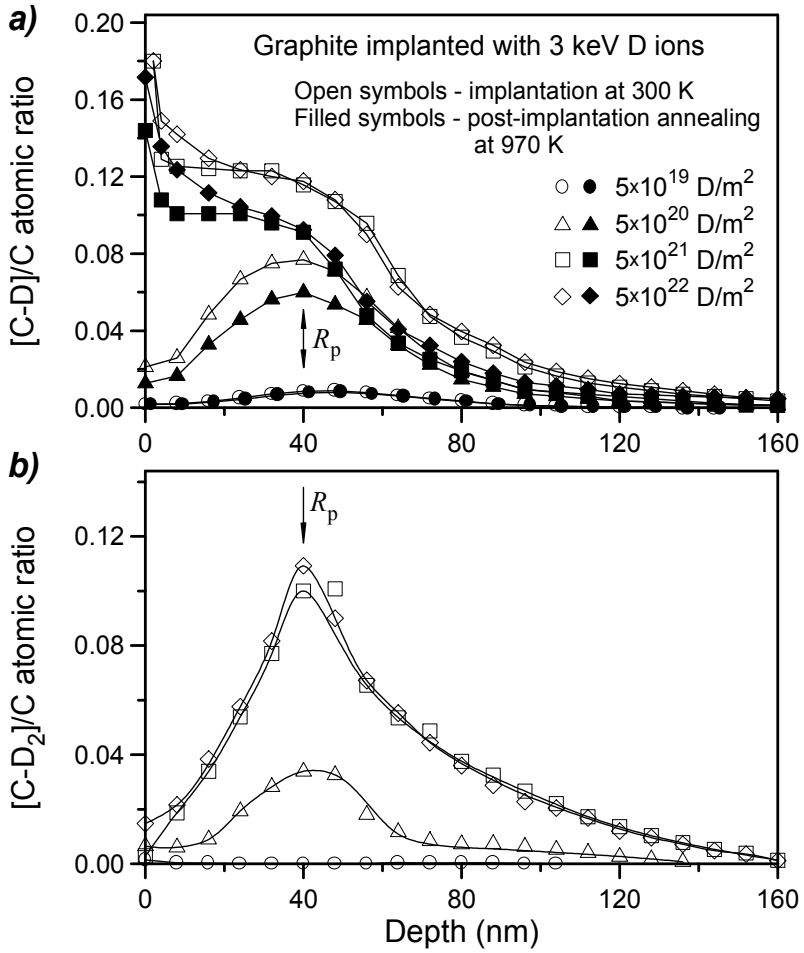

Figure 2. Depth profiles of [C-D] (a) and [C-D_2] (b) configurations formed in highly ordered pyrolytic graphite implanted with 3 keV D ions at 300 K and those after heating up to 970 K. After heating up to 970 K the [C-D_2] configurations disappear. The arrow indicates the mean projected range of D ions.

The [C-D_2] configurations start to form at Φ between 5×10^{19} and 5×10^{20} D/m^2, manifesting a nonlinear relationship of increasing D amounts with fluence (Fig. 3). The D/C ratio in the maximum of the [C-D_2] profile rises to about 0.2 (Fig. 2b). The maximum amount of deuterium related to [C-D_2] configurations is about 1.2×10^{21} D/m^2. After heating up to 970 K the [C-D_2] configurations disappear.

Thus, at low Φ the [C-D] configurations contain practically the majority of D atoms. As the amount of the [C-D] configurations approaches its maximum level, the [C-D_2] configurations appear. It appears that only the [C-D_2] configurations are responsible for the D_2 molecule formation during D ion implantation into D rich near-surface layers, i.e. for reemission of deuterium.

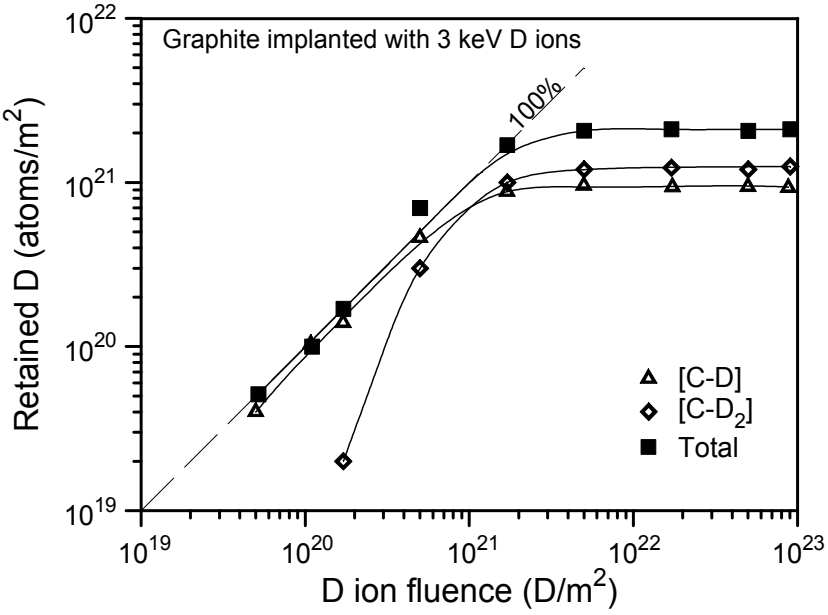

Figure 3. Quantities of deuterium trapped in the form of [C-D] and [C-D_2] configurations and the total amount of deuterium retained in highly ordered pyrolytic graphite implanted with 3 keV D ions at 300 K in their dependence upon the ion fluence.

As it follows from Refs [45-47], implanted D atoms are assumed to be trapped by single vacancies and vacancy clusters created by D ions [48]. Taking this supposition as a basis and considering that the [C-D] configurations are detected both at low and high fluences, we come to the conclusion that the bonding in the [C-D] configuration is based on the linkage between the s-electron of the D atom and one of sp^2 trigonal hybrid orbitals inherent in a vacancy or vacancy cluster [49].

The fact that (i) there are similar sharp fluence dependencies both for the appearance of the [C-D_2] configurations and for the release of CD_4 molecules during subsequent heating of deuterium implanted graphite [50]; (ii) the post-implantation heating up to 970 K leads to the disappearance of the [C-D_2] configurations as well as to the release of practically all CD_4 molecules from the implanted layers [51]; indicates a close relation between the formation of the [C-D_2] configurations and the creation of deuterium-carbon bonding structures which are responsible for the CD_4 release. It was suggested [52] that the CD_4 release is caused by the change of the binding structure of the hybridized carbon atoms, namely the formation of sp^3–carbon bonds [53-55]. Thus it can be speculated that the [C-D_2] configurations reflect the trapping of D atoms by the sp^3 orbitals of C atoms. In this case the D atoms are positioned in the interlayer position as it was determined in Ref. [55].

The percentage of D atom quantities in the two above mentioned configurations varying from [C-D] : [C-D_2] ≅ 40 : 60 at 300 K to 100 : 0 after heating up to 970 K, is likely to reflect the ratio of C-D bonds of sp^2 and sp^3 hybridized carbon atoms in the deuterium implanted layers. It should be noted that for a typical hard a-C:H film the proportion of hybridization is sp^2 : sp^3 = 30 : 68 for the as-grown sample at 330 K and 100 : 0 after annealing at 870 K [56].

3.2. *Deuterium retention in tungsten, CVD tungsten-carbon coating and tungsten-carbon mixed film implanted with D ions*

SIMS/RGA depth profiles of D atoms and D_2 molecules in W single crystal irradiated with 6 keV D ions at T_{irr} = 300 K are shown in Fig. 4. The profiles of D atoms and D_2 molecules concur with the damage distributions rather than the ion projected ranges. With the fluence Φ increase, the D atom concentration C_D in the implantation zone (i.e. within the near-surface layer of about 150 nm in thickness) reaches the value of about 1.2×10^{27} atoms/m^3 (~0.02 D/W) and practically does not change thereafter (Fig. 4a). Even at lower fluence of 3.2×10^{20} D/m^2, D atom profile shows a long tail extending 300 nm that is beyond the ion implantation zone. As the fluence increases, the depth of D atom capture is enlarged and reaches ~2 μm at $\Phi \approx 1\times10^{23}$ D/m^2 (see insert in Fig. 4a).

Analysis of D_2 depth profiles shows that (i) the formation of deuterium molecules in W crystal at T_{irr} = 300 K starts at $\Phi \geq 2\times10^{21}$ D/m^2 (Fig. 4b), that is at $C_D \geq 1.5$ at% (Fig. 4a) and (ii) D_2 molecules are localized in the ion implantation zone alone. While C_D at a depth of about 10 nm increases of about 50 percent when rising Φ from 2.5×10^{21} to 9.8×10^{22} D/m^2 (Fig. 4a), the concentration of D_2 molecules, C_{D_2}, increases more than an order of magnitude reaching value of ~2×10^{27} molecules/m^3 (~0.03 D_2/W) (Fig. 4b).

After implantation at 650 K, D_2 molecules were not detected in our experiments, and we draw the conclusion that deuterium is accumulated in the form of D atoms alone at the high temperature. D atoms are retained in the sub-surface layer of ~500 nm in thickness (note that at T_{irr} =300 K depth of D atom capture reaches ~2 μm) and the maximum concentration C_D in the ion stopping zone does not exceed 9×10^{26} atoms/m^3 (~0.015 D/W) (Fig. 5).

Figure 6 shows the fraction quantities of deuterium trapped in W crystal in different states. At T_{irr} =300 K, the total amount of atomic deuterium retained in the ion implantation zone Q_D(IZ) 24-26 h after ion beam switch-off increases with fluence and reaches the saturated value of about 1.5×10^{20} D/m^2 at $\Phi = 3\times10^{21}$ D/m^2. The amount of D atoms captured beyond the implantation zone Q_D(>IZ) increases linearly with the fluence at $\Phi \leq 2\times10^{21}$ D/m^2 and scales with the square root of the incident D ion fluence at $\Phi \geq 3\times10^{21}$ D/m^2. The amount of deuterium retained in the form of D_2 molecules Q_{D2}(IZ) increases nonlinearly with the fluence and reaches the value of about 1.5×10^{20} D/m^2 at $\Phi = 1\times10^{23}$ D/m^2. Thus, at this fluence the percentage of deuterium trapped in the different states is in the ratio Q_D(IZ):Q_{D2}(IZ):Q_D(>IZ) ≅ 20:20:60. Therefore, the majority of implanted deuterium is accumulated far beyond the ion stopping zone. The total amount of deuterium trapped in W crystal at 300 K increases with D ion fluence and does not demonstrate the saturation within the ion fluence range utilized in our work.

At T_{irr} = 650 K and $\Phi = 8\times10^{22}$ D/m^2, the quantities of D atoms accumulated in the ion implantation zone Q_D(IZ) and beyond that Q_D(>IZ) are in the ratio Q_D(IZ):Q_D(>IZ) ≅ 70:30, i.e. the majority of deuterium retained at 650 K is localized within the near-surface layer of 150 nm in thickness. At $\Phi > 1\times10^{22}$ D/m^2, the amount Q_D(IZ) reaches the saturation level whereas Q_D(>IZ) shows tendency to increase as the square root of D ion fluence. Consequently, D retention beyond the implantation zone is expected to be dominated at fluences above 1×10^{24} D/m^2 (Fig. 6).

The study of the damage structure produced in W crystals under D ion implantation [58] and measurements of D atom and D_2 molecule profiles have revealed that there are at least two types of ion-induced defects which can be responsible for trapping of deuterium which is Implanted at keV energies above the threshold for displacement: (i) D_2 filled voids localised in the implantation zone, and (ii) dislocations which are distributed from the surface to depths far beyond 1 μm and capture D atoms. Moreover, intrinsic (natural) defects like grain and block boundaries are thought to be responsible for the accumulation of D atoms.

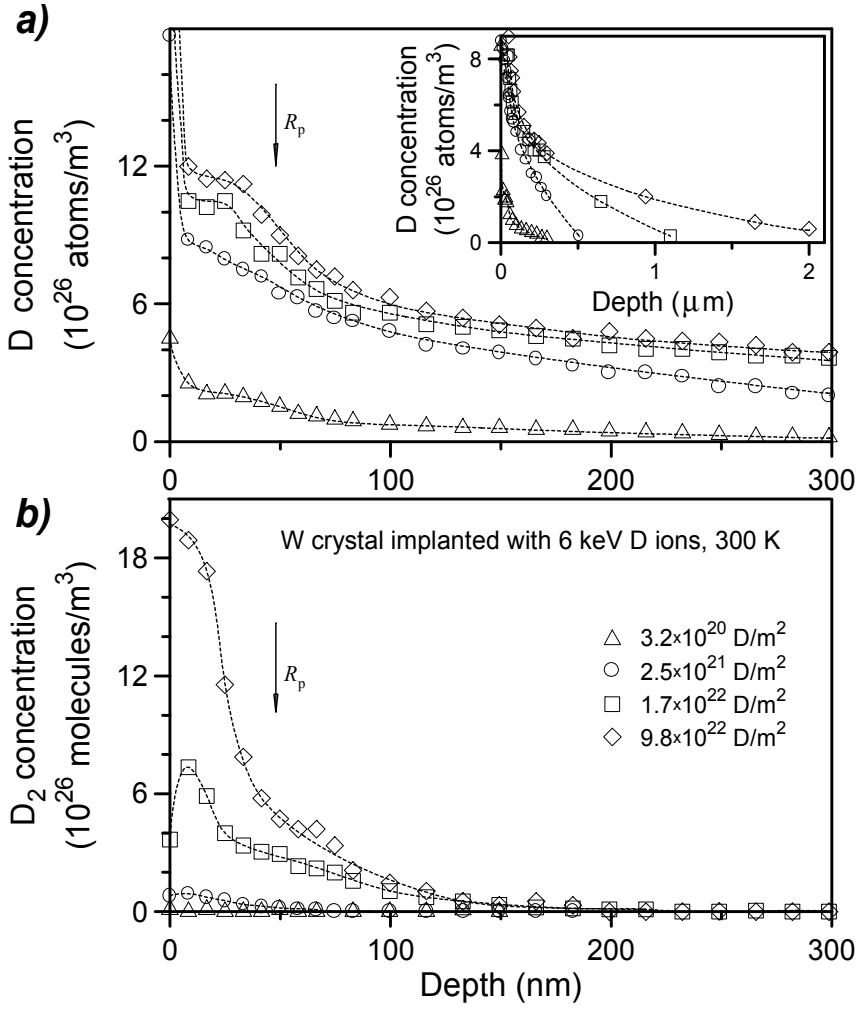

Figure 4. Depth profiles of deuterium trapped as D atoms (a) and in the form of D_2 molecules (b) in W single crystal implanted with 6 keV D ions at 300 K. The arrow indicates the mean projected range of D ions calculated by the TRIM.SP program [57]. The insert shows depth distributions of D atoms in the bulk of W crystal.

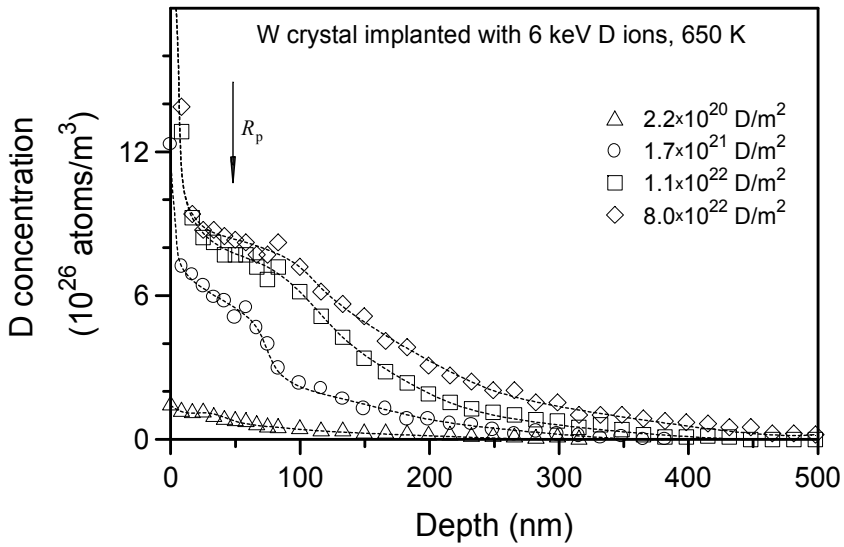

Figure 5. Concentration profiles of D atoms trapped in W single crystal implanted with 6 keV D ions at 650 K. The arrow indicates the mean projected range of D ions calculated by the TRIM.SP program [57].

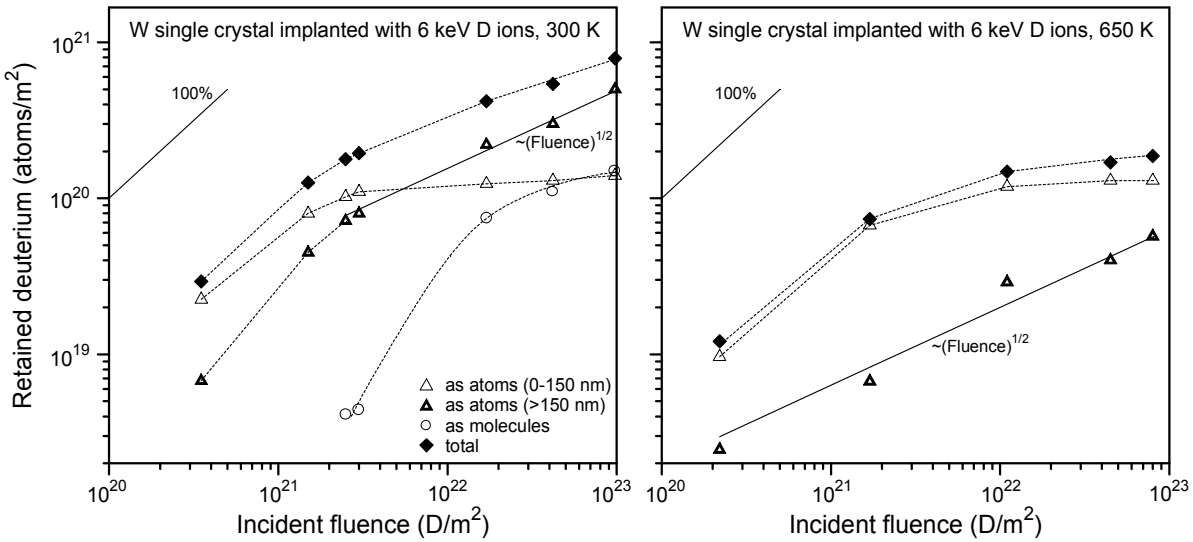

Figure 6. Quantities of deuterium trapped in W single crystal as D atoms in the ion implantation zone (0-150 nm), D atoms beyond the ion implantation zone (>150 nm) and D_2 molecules in the ion implantation zone, and the total amount of deuterium retained after implantation with 6 keV D ions at 300 and 650 K as a function of fluence.

According to SIMS/RGA measurements, the formation of D_2 molecules in the implantation zone at T_{irr} = 300 K starts at a fluence when the D atom concentration reaches ~1.5 at%. One would conclude that this value is a minimum D atom concentration necessary for bubble formation in tungsten at 300 K. It should be noted that in the implantation zone two important conditions necessary for gas bubble formation are fulfilled: a high level of vacancies and a high concentration of implanted deuterium playing the role of a stabilizer of bubble nucleation and growth. At T_{irr} = 650 K, the conditions necessary for the formation and growth of D_2 filled microvoids does not hold and W is free of deuterium molecules.

The high compressive stresses created in the near-surface layers due to the formation and growth of deuterium bubbles are the reason for generation of dislocations far beyond the ion implantation zone. Most of the D atoms implanted into tungsten at room temperature diffuse deep into the bulk and are captured by the dislocations and grain boundaries. Besides, in the ion stopping zone D atoms can be trapped by vacancies with binding energy of about 1.1 eV [59]. Another possible source of D atoms in the implantation zone is deuterium adsorbed on bubble walls [60].

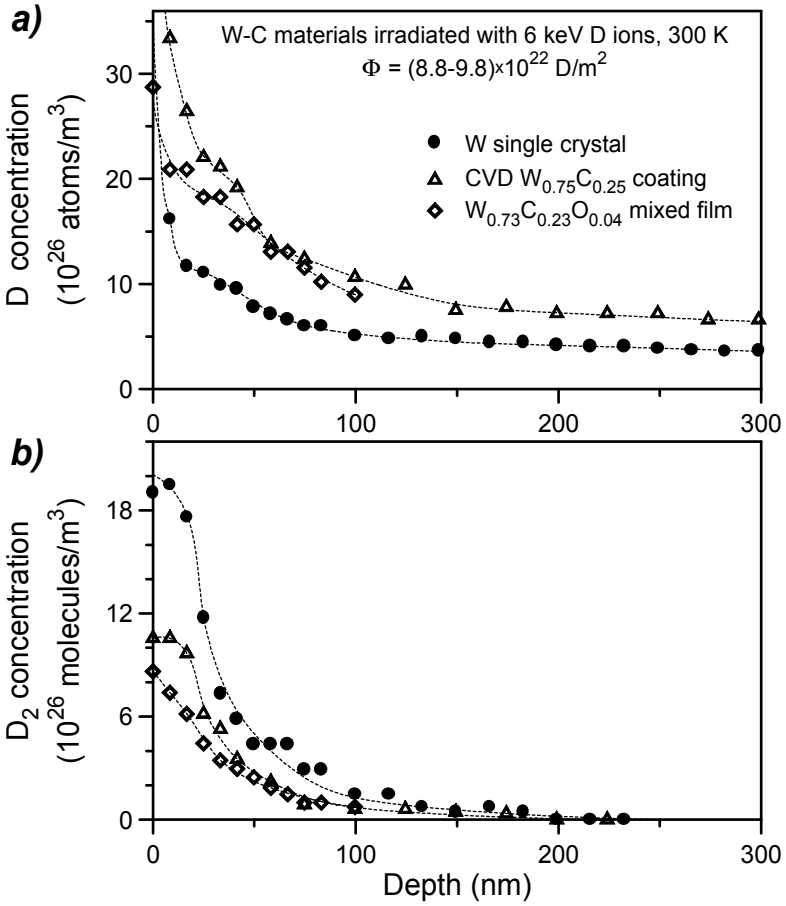

Figure 7. Concentration profiles of D atoms (a) and D_2 molecules (b) in W single crystal, CVD tungsten-carbon coating $W_{0.75}C_{0.25}$ and magnetron deposited tungsten-carbon (Ar) mixed film $W_{0.73}C_{0.23}O_{0.04}$ implanted with 6 keV D-ions at 300 K to fluences of (8.8-9.8)×10^{22} D/m^2. Note that a thickness of the W-C(Ar) mixed film is approximately 110 nm.

Steady-state distributions of D atoms and D_2 molecules in the W single crystal, the CVD tungsten-carbon coating $W_{0.75}C_{0.25}$ and the tungsten-carbon (Ar) mixed film $W_{0.73}C_{0.23}O_{0.04}$ irradiated with 6 keV D ions at T_{irr} = 300 K to high fluence of (4.2-4.3)×10^{22} D/m^2 are presented in Fig. 7. The maximum concentration of D atoms C_D^{max} trapped in the ion implantation zone for the materials investigated is in the range between ~1×10^{27} and ~2×10^{27} atoms/m^3 with observance of following inequality:

c_D^{max} (W single crystal) < c_D^{max} (CVD coating $W_{0.75}C_{0.25}$) ≅ c_D^{max} ($W_{0.73}C_{0.23}O_{0.04}$ mixed film).

It should be noted that in CVD-$W_{0.75}C_{0.25}$ the concentration C_D at depths beyond the implantation range is significantly higher than that for W single crystal. Probably, carbide inclusions play a role of additional traps for D atoms.

The differences in composition of the samples influence retention of deuterium in the form of D_2 molecules. At $\Phi \cong 1\times10^{23}$ D/m^2, the concentration of D_2 molecules in the ion stopping zone of these samples is higher for W crystal and lower for $W_{0.73}C_{0.23}O_{0.04}$ mixed film (Fig. 7).

After implantation of the tungsten-carbon (Ar) mixed film with D ions at 650 K, D_2 molecules were not detected in the bulk of the sample. The value of D atom concentration C_D^{max} is found to be approximately 1×10^{27} atoms/m^3, that is lower by a factor of about 2 than that for T_{irr} = 300 K. It should be noted that analogous tendency was observed for the W crystal implanted with D ions at room and elevated temperatures.

3.3. Deuterium retention in carbon and tungsten-carbon mixed films prepared by magnetron sputtering in D_2 atmosphere

EPMA analysis of samples prepared by magnetron sputtering of graphite cathode in a D_2 atmosphere has revealed that the carbon films are not significantly deposited in the temperature range 500 to 650 K. A negligible small value of carbon deposition rate around 600 K can be explained by temperature dependence of erosion of the growing hydrogenated C film due to exposure to D atoms formed in the magnetron plasma. It is well established that the erosion yield of hydrogenated carbon films exposed to thermal H atoms peaks just at 600 K with the erosion yield of ~0.1 C/H [61].

Concentration of deuterium in the hydrogenated C films prepared by magnetron sputtering of a graphite cathode in a D_2 atmosphere was determined by the combined SIMS/RGA method. As was proposed in Ref. [41], a deuterium atom bonded to the sp^2 trigonal hybrid orbital of C atom (monohydride D-(sp^2)C or [C-D] configuration) is detected by SIMS, whereas dihydride D^2-(sp^3)C (or [C-D_2] configuration) is detected by RGA only. The concentration of the [C-D] and [C-D_2] configurations formed in the hydrogenated C films and the concentration of all D atoms involving these configurations are presented in Fig. 8 as a function of substrate temperature (note that in the temperature range 500-650 K the deposition rate of C atoms was negligible small and the C films were not deposited). SIMS/RGA depth profiling has shown that the D-containing configurations are distributed of homogeneously throughout the whole thickness. With the temperature increase, the value of the D-(sp^2)C concentration is varied from ~0.03 [C-D]/C (in units of atomic ratio) at 400 K to ~0.02 [C-D]/C at 973 K (Fig. 8a). As this takes place, the D^2-(sp^3)C concentration value falls from ~0.20 [C-D_2]/C at 400 K to zero at 973 K (Fig. 8b). Therefore, the deuterium concentration is also varied from ~0.4 D/C at 400 K to ~0.02 D/C at 973 K (Fig. 8c). The results shown in Fig. 8c are in good agreement with the data of Doyle et al. for hydrogen concentration at saturation in graphite implanted with H ions [6].

According to RHEED analysis, tungsten carbide phase W_2C is present in the tungsten-carbon mixed films prepared by dc magnetron sputtering in D_2 atmosphere. Free carbon and tungsten atoms (not bound chemically) are also present in the films. The concentration of D atoms and D_2 molecules in the bulk of the hydrogenated tungsten-carbon mixed films are shown in Fig. 9 as a function of substrate temperature. As in the magnetron prepared hydrogenated C films, the D atoms and D_2 molecules in the W-C mixed films are distributed homogeneously throughout the whole thickness. As the deposition temperature is increased, the concentration of D atoms and D_2 molecules decreases (Fig. 9 a,b).

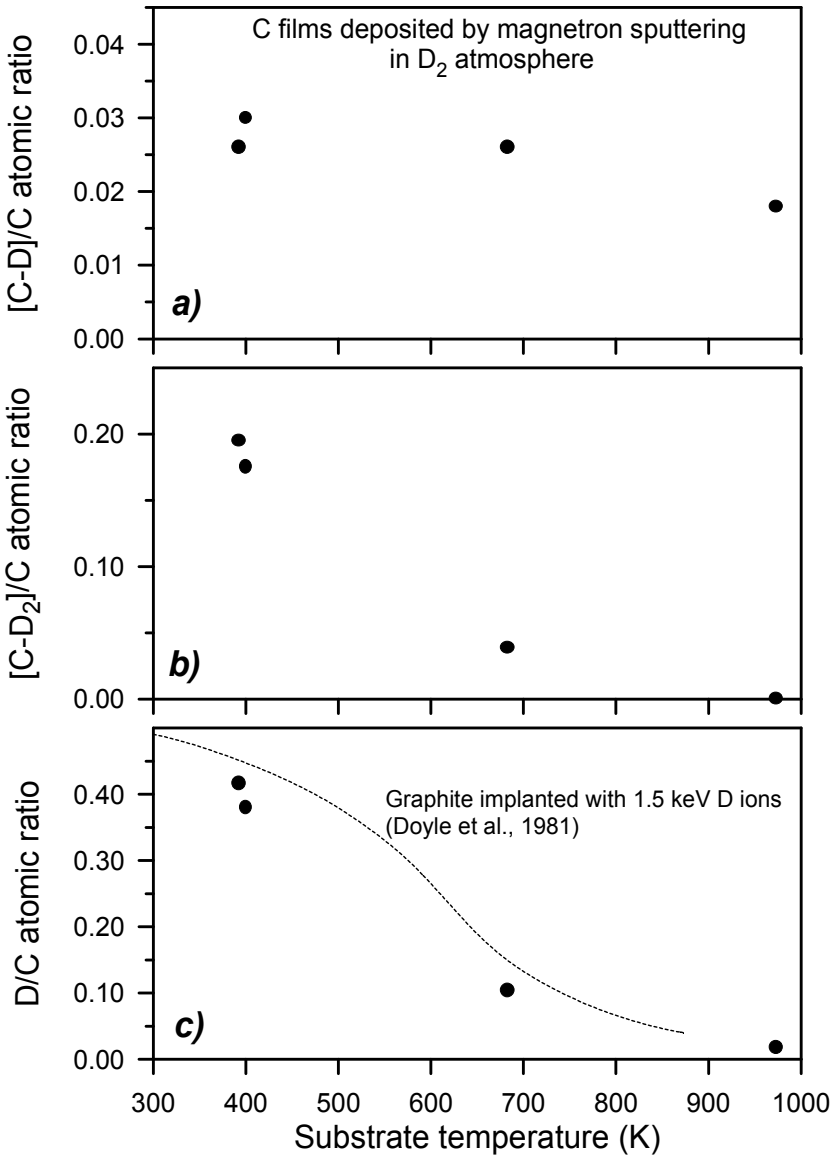

Figure 8. Concentration of [C-D] configurations (a) and [C-D_2] configurations (b), and concentration of total deuterium (c) in the bulk of carbon films prepared by dc magnetron sputtering in D_2 atmosphere as a function of substrate temperature. Solid line shows experimental results of Doyle et al. [6] for pyrolitic graphite implanted with 1.5 keV H ions.

At 400 K, the concentration of the D atoms and D_2 molecules (C_D and C_{D_2}, respectively) in the hydrogenated W-C mixed film is ~7×10^{26} D/m^3 (~0.007 D/host atoms) and ~8×10^{26} D_2/m^3 (~0.008 D_2/host atom), respectively (assuming that atomic density of the CVD tungsten-carbon coating $W_{0.75}C_{0.25}$ and the tungsten-carbon mixed films of analogous stoichiometry (see Table 1) is equal approximately to 1×10^{29} atoms/m^3 [62]). It should be noted that the values of C_D and C_{D_2} in the bulk of the hydrogenated C film deposited at 400 K are 0.03 D/C and 0.2 D_2/C (Fig. 8). Thus, in spite of the presence of carbon atoms in the hydrogenated W-C mixed films (up to 30%, see Table 1), the concentration of D_2 molecules in these films is much lower than it is expected from the assumption that the W-C mixed films consist of tungsten and graphite inclusions. Thus, it is felt that the amount of free carbon atoms is negligible small. In the opposite case, D concentration in the W-C films was expected to be much higher than is observed in reality.

The concentration of all deuterium (D atoms and D_2 molecules) in the samples investigated (namely, (i) the D concentration in the ion stopping zone at saturation for the sample implanted with D ions and (ii) the D concentration in the bulk of the magnetron-preparing films) is plotted in Fig. 10 as a function of implantation or deposition temperature. The results presented show that the value of the D concentration in the W-C mixed films is comparable with that for tungsten and tungsten carbide implanted with D ions, whereas the D concentration in the C films is more than one order of magnitude higher than that in the W-C mixed films (Fig. 10).

During magnetron sputtering in a D_2 atmosphere, the substrate surface facing the cathode is bombarded by the following particles:

(1) The physically sputtered particles (carbon or tungsten atoms depending on the cathode material) with energy of several eV. Additionally, hydrocarbon particles C_xD_y, which are formed due to sputtering of graphite cathode or carbon-contaminating walls by D ions, reach also the substrate surface.

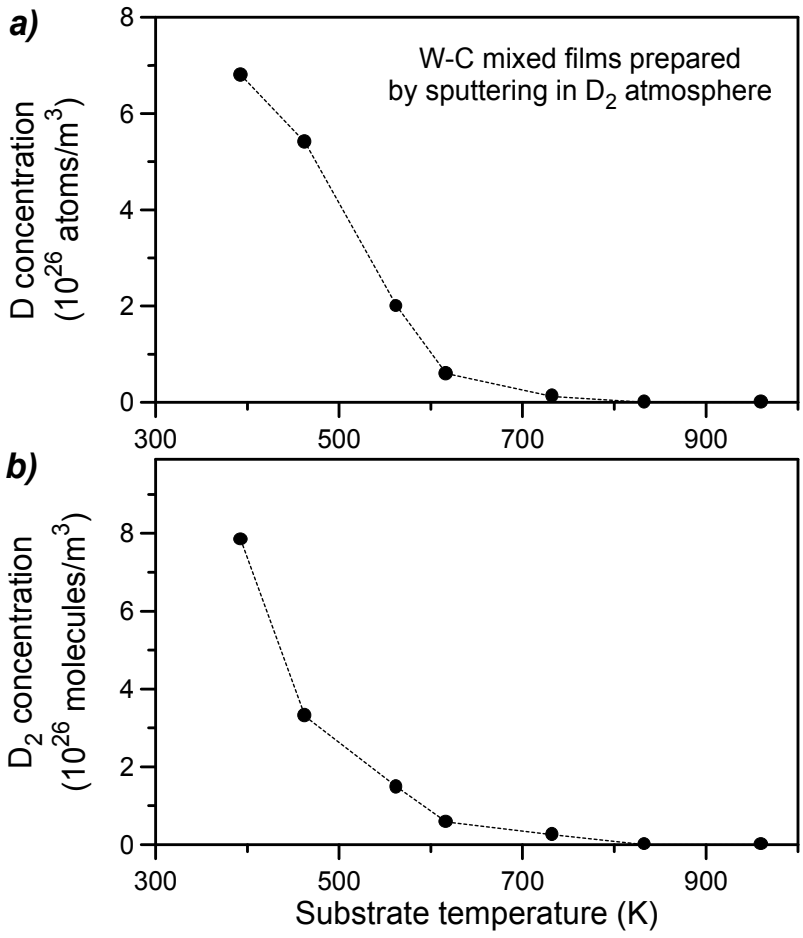

Figure 9. Concentration of D atoms (a) and D_2 molecules (b) in the bulk of tungsten-carbon mixed films prepared by dc magnetron sputtering in D_2 atmosphere as a function of substrate temperature.

2) The reflected D ions with energy in the range from 0 to a maximum value that depends on the atomic weights of the incident ion and the cathode material. Note that the maximum value of the discharge voltage in our experiments is 500 eV (see Table 1).
(3) The thermal deuterium atoms produced in the magnetron plasma.

When the hydrogenated W-C mixed film is prepared, the substrate surface is bombarded with a combination of tungsten, carbon, deuterium atoms and ions and C_xD_y particles as well. In doing so, precipitators of tungsten carbide phases are concluded to be formed in the bulk of growing film. EMPA analysis has shown that oxygen atoms are present in the films, and it is believed that the tungsten oxide precipitators are also formed in the growing film. Deuterium implanted as low energy ions and neutrals is captured by dissimilar defects formed during the film growth — carbide and oxide inclusion boundaries, microvoids, microcracks, etc. Probably, radiation induced defects are generated in the near-surface layer of the growing film and these defects are also responsible for D trapping.

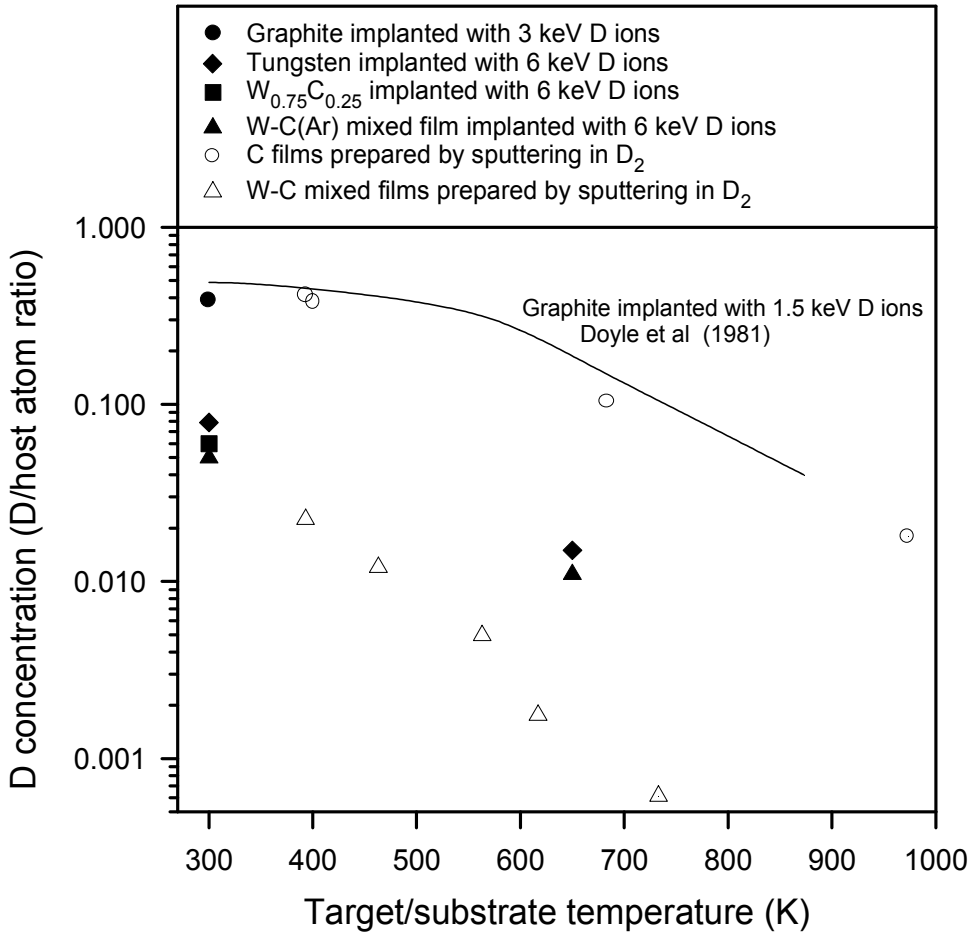

Figure 10. Maximum concentration of deuterium (i) in the ion stopping zone of graphite, W single crystal, CVD tungsten-carbon coating $W_{0.75}C_{0.25}$ and tungsten-carbon (Ar) mixed film implanted with D ions to a fluence $\Phi \cong 1\times10^{23}$ D/m^2 and (ii) D concentration in the bulk of carbon and tungsten-carbon mixed films prepared by magnetron sputtering in D_2 atmosphere as a function of target/substrate temperature in the process of ion implantation or film deposition. Solid line shows experimental results of Doyle et al. [6] for pyrolitic graphite implanted with 1.5 keV H ions.

Thus, it is believed that the co-deposition of carbon and tungsten atoms leads to the formation of chemical compounds, namely tungsten carbides, even at low temperature of 400 K. Deuterium incorporated into this process is accumulated in the growing film up to concentrations which are typical for tungsten carbides but not for graphite inclusions.

A thorough discussion of the mechanism of deuterium retention in and release from W-C materials would require additional experimental information, such as thermal desorption measurements and microscopy studies. A knowledge of hydrogen diffusivity and solubility in the tungsten carbides is also required.

4. CONCLUSIONS

Deuterium implanted into graphite at 300 K is retained in the form of at least two types of C-D configurations which are concluded to attribute to the monohydride D-(sp^2)C and dihydride D^2-(sp^3)C. The formation of these [C-D] and [C-D_2] configurations is caused by the bonds between D atoms and sp^2 or sp^3 hybridized C atoms. The maximum concentration of D accumulated in both states in the ion stopping zone reaches value of ~0.4 D/W at 300 K.

In the hydrogenated carbon films prepared by dc magnetron sputtering in a D_2 atmosphere, the C-D configurations are distributed homogeneously throughout the whole thickness. With an increase in the deposition temperature, the concentration of the D-(sp^2)C configurations is varied from ~0.03 [C-D]/C (in units of atomic ratio) at 400 K to ~0.02 [C-D]/C at 973 K. In its turn, the concentration of the D^2-(sp^3)C configurations falls from ~0.20 [C-D_2]/C at 400 K to zero at 973 K. Therefore, the deuterium concentration is varied from ~0.40 D/C at 400 K to ~0.02 D/C at 973 K.

Irradiation of W single crystal with 6 keV D ions at 300 K leads to the accumulation of D atoms both in the ion stopping zone and at depths up to several μm. Also, in the stopping zone deuterium is additionally accumulated in the form of D_2 molecules. The fraction of deuterium retained as D atoms beyond the implantation zone scales with the square root of the incident D ion fluence. After D ion implantation at 650 K, D_2 molecules are absent in the W samples and deuterium is accumulated in the form of D atoms alone at depths up to 500 nm. As this takes place, the majority of deuterium (approximately 70%) is localized within the implantation zone. The maximum concentration of D accumulated in both states in the ion stopping zone reaches value of ~0.08 D/W at 300 K. After irradiation at 650 K, this value is found to be ~0.015 D/W.

The maximum concentration of all deuterium (D atoms and D_2 molecules) trapped in the ion implantation zone of CVD coating $W_{0.75}C_{0.25}$ and tungsten-carbon (Ar) mixed film $W_{0.73}C_{0.23}O_{0.04}$ implanted with 6 keV D ions is ~0.06 D/host atom for T_{irr} = 300 K and ~0.01 D/host atom for T_{irr} = 650 K. In CVD-$W_{0.75}C_{0.25}$, the concentration of D atoms at depths beyond the implantation range is significantly higher than that for W single crystal. Probably, carbide inclusions play a role of additional traps for D atoms.

Tungsten-carbon mixed films prepared by dc magnetron sputtering in a D_2 atmosphere contain graphite-like, tungsten and tungsten carbide W_2C inclusions. At 400 K, the concentration of the D atoms and D_2 molecules in the hydrogenated W-C mixed film is ~7×10^{26} D/m^3 (~0.007 D/host atoms) and ~8×10^{26} D_2/m^3 (~0.008 D_2/host atom), respectively (assuming that atomic density of the tungsten-carbon mixed films is equal approximately to 1×10^{29} atoms/m^3). Thus, in spite of the presence of carbon atoms in the W-C mixed films (up

to 30%), the concentration of D_2 molecules in these films is much lower than it is expected from the assumption that the hydrogenated W-C mixed film consists of tungsten and graphite crystallites.

The co-deposition of carbon and tungsten atoms is speculated to lead to the formation of chemical compounds, namely tungsten carbides, even at low temperature of 400 K. Deuterium incorporated into this process is accumulated in the growing film up to concentrations which are typical for pure tungsten or tungsten carbides but not for graphite inclusions.

This work has been performed within an IAEA Co-ordinated Research Project (CRP) on "Plasma-Material Interaction Data for Mixed Plasma Facing Materials in Fusion Reactors" (1998-2000). The authors are grateful to Dr. A.E Gorodetsky for RHEED analyses.

REFERENCES

[1] WILSON, K.L., HSU, W.L., J. Nucl. Mater. **145-147** (1987) 121.
[2] MÖLLER, W., J. Nucl. Mater. **162-164** (1989) 138.
[3] CAUSEY, R.A., ELLEMAN, T.S., VERGHESE, K., Carbon **17** (1979) 323.
[4] SAEKI, M., J. Nucl. Mater. **131** (1985) 32.
[5] LANGLEY, R.A., BLEWER, R.S., ROTH, J., J. Nucl. Mater. **76&77** (1978) 313.
[6] DOYLE, B.L., WAMPLER, W.R., BRICE, D.K., J. Nucl. Mater. **103&104** (1981) 513.
[7] SCHERZER, B.M.U., BEHRISCH, R., ECKSTEIN, W., et al., J. Nucl. Mater. **63** (1976) 100.
[8] WAMPLER, W.R., BRICE, D.K., MAGEE, C.W., J. Nucl. Mater. **102** (1981) 304.
[9] WAMPLER, W.R., MAGEE, C.W., J. Nucl. Mater. **103&104** (1981) 509.
[10] MORITA, K., OHTSUKA, K., HASEBE, Y., J. Nucl. Mater. **162-164** (1989) 990.
[11] ASHIDA, K., ICHIMURA, K., MATSUYAMA, M., et al., J. Nucl. Mater. **111&112** (1982) 769.
[12] ASHIDA, K., ICHIMURA, K., WATANABE, K., J. Vac. Sci. Technol. A **1** (1983) 1465.
[13] GOTOH Y., OKADA, O., J. Nucl. Sci. Technol. **21** (1984) 205.
[14] MÖLLER, W., BORGESEN, P., SCHERZER, B.M.U., Nucl. Instr. and Meth. B **19** (1987) 826.
[15] MÖLLER W., SCHERZER, B.M.U., Appl. Phys. Lett. **50** (1987) 1870.
[16] WINTER, J., J. Vac. Sci. Technol. A **5** (1987) 2286.
[17] WINTER, J., J. Nucl. Mater. **145-147** (1987) 131.
[18] BESOCKE, K., FLENTJE, G., LITTMARK, U., et al., J. Nucl. Mater. **145-147** (1987) 651.
[19] JACOB, W., MÖLLER, W., Appl. Phys. Lett. **63** (1993) 1771.
[20] REINKE, P., JACOB, W., MÖLLER, W., J. Appl. Phys. **74** (1993) 1354.
[21] MÖLLER, W., FUKAREK, W., LANGE, K., et al., Jpn. J. Appl. Phys. **34** (1995) 2163.
[22] KEUDELL, A. von, JACOB, W., J. Vac. Sci. Technol. A **15** (1997) 402.
[23] JACOB, W., Thin Solid Films **326** (1998) 1.
[24] COAD, J.P., SKORODUMOV, B.G., ULANOV, V.G., WU, C.H., Vacuum **47** (1996) 985.
[25] DISCHLER, B., BUBENZER, A., KOIDL, P., Appl. Phys. Lett. **42** (1983) 636.
[26] NYAIESH, A.R., NOWAK, W.B., J. Vac. Sci. Technol. A **1** (1983) 308.
[27] ANGUS, J.C., STULTZ, J.E., SHILLER, P.J., et al., Thin Solid Films **118** (1984) 311.
[28] NADLER, M.P., DONOVAN, T.M., GREEN, A.K., Appl. Surf. Sci. **18** (1984) 10.

[29] GARCÍA-ROSALES, C., FRANZEN, P., PLANK, H., et al., J. Nucl. Mater. **233-237** (1996) 803.
[30] PISAREV, A.A., VARAVA, A.V., ZHDANOV, S.K., J. Nucl. Mater. **220-222** (1995) 926.
[31] SAKAMOTO, R., MUGORA T., YOSHIDA, N., J. Nucl. Mater. **233-237** (1996) 776.
[32] ALIMOV, V.KH, SCHERZER, B.M.U., J. Nucl. Mater. **240** (1996) 75.
[33] HAASZ, A.A., DAVIS, J.W., J. Nucl. Mater. **241-243** (1997) 1076.
[34] HAASZ, A.A., DAVIS, J.W., POON, M., MACAULAY-NEWCOMBE, R.G., J. Nucl. Mater. **258-263** (1998) 889.
[35] HAASZ, A.A., POON, M., DAVIS, J.W., J. Nucl. Mater. **266-269** (1999) 520.
[36] CAUSEY, R., WILSON, K., VENHAUS, T., WAMPLER, W.R., J. Nucl. Mater. **266-269** (1999) 467.
[37] WANG, W., ALIMOV, V.KH., SCHERZER, B.M.U., ROTH, J., J. Nucl. Mater. **241-243** (1997) 1087.
[38] NAGATA, S., TAKAHIRO, K., HORIIKE, S., YAMAGUCHI, S., J. Nucl. Mater. **266-269** (1999) 1151.
[39] HORIKAWA, T., TSUCHIYA, B., MORITA, K., J. Nucl. Mater. **258-263** (1998) 1087.
[40] ALIMOV, V.KH., ERTL, K., ROTH, J., SCHMID, K., J. Nucl. Mater. **282** (2000) 125.
[41] ALIMOV, V.KH., GORODETSKY, A.E., ZAKHAROV, A.P., J. Nucl. Mater. **186** (1991) 27.
[42] ALIMOV, V.KH., CHERNIKOV, V.N., ZAKHAROV, A.P., J. Nucl. Mater. **241-243** (1997) 1047.
[43] BRAUN, M., EMMOTH, B., J. Nucl. Mater. **128&129** (1984) 657.
[44] NIWASE, K., TANABE, T., SUGIMOTO, M., FUJITA, F.E., J. Nucl. Mater. **162-164** (1989) 856.
[45] SONE, K., MCCRACKEN, G.M., J. Nucl. Mater. **111&112** (1982) 606.
[46] SCHERZER, B.M.U., LANGLEY, R.A., MÖLLER, W., et al., Nucl. Instr. and Meth. **194** (1982) 497.
[47] KUZMINOV, D.B., KANASHENKO, S.L., GORODETSKY, A.E., ZAKHAROV, A.P., J. Nucl. Mater. **185** (1991) 123.
[48] KELLY, B.T., Physics of Graphite (Applied Science Publishers, Barking, 1981).
[49] COULSON, C.A., HERRAEZ, M.A., LEAL, M., et al., Proc. Roy. Soc. London A **274** (1963) 461.
[50] PHILIPPS, V., VIETZKE, E., ERDWEG, M., K. FLASKAMP, K., J. Nucl. Mater. **145-147** (1987) 292.
[51] ROTH, J., BOHDANSKY, J., Appl. Phys. Lett. **51** (1987) 964.
[52] VIETZKE, E., PHILIPPS, V., Nucl. Instr. and Meth. B **23** (1987) 449.
[53] BUBENZER, A., DISCHLER, D., BRANDT, G., KOIDL, P., J. Appl. Phys. **54** (1983) 4590.
[54] NIWASE, K., SUGIMOTO, M., TANABE, T., FUJITA, F.E., J. Nucl. Mater. **155-157** (1988) 303.
[55] GOTOH, Y., SHIMIZU, H., MURAKAMI, H., J. Nucl. Mater. **162-164** (1989) 851.
[56] DISCHLER, B., in: Amorphous Hydrogenated Carbon Films, Eds: P. Koidl and P. Oelhafen, E-MRS Symposia Proc. Vol. XVII (Les Editions de Physique, Paris) p. 189.
[57] ECKSTEIN, W., Computer Simulation of Ion-Solid Interaction, Springer Series in Materials Science, Vol. 10, Springer, Berlin, 1991.
[58] ALIMOV, V.KH., ERTL, K., ROTH, J., SCHMID, K., Deuterium Retention and Lattice Damage in Tungsten Irradiated with D Ions, Proc. 5th Intern Workshop on Hydrogen Isotopes in Solids, May 17-19, 2000, Stockholm, Sweden (to be published in Physica Scripta).

DEUTERIUM RETENTION STUDIES AT THE INEEL FOR C-Be AND C-W MIXED PLASMA-FACING MATERIALS

R.A. ANDERL, G.R. LONGHURST, R.J. PAWELKO
Idaho National Engineering and Environmental Laboratory,
Idaho Falls, Idaho, United States of America

Abstract

This paper presents a summary of the results of experiments to investigate hydrogen isotope retention in mixed plasma-facing component materials. The results are based on thermal desorption spectroscopy measurements of deuterium retained in ion implanted samples of C-Be and C-W mixed materials.

1. INTRODUCTION

Mixed-materials research at the Idaho National Engineering and Environmental Laboratory (INEEL) has focused on the C-Be and C-W systems. The primary purpose of this work was to investigate hydrogen isotope retention in these systems. For this purpose, we simulated plasma-mixed-material layers by using carbon-coated Be and carbon-coated W specimens that were heat-treated and tungsten carbide specimens prepared by chemical vapor deposition (CVD). Sample preparation and characterization activities are summarized in another contribution to this issue. This contribution summarizes the results of our hydrogen isotope retention studies based on thermal desorption spectroscopy (TDS) measurements for deuterium-implanted samples, with an emphasis on experiments for the C-W system. Detailed results of this work on C-Be were published in refs. [1-3]. References [4-6] document the results of our studies on the C-W system and compare deuterium retention data to results derived from previous permeation experiments for tungsten foil [7].

2. DEUTERIUM RETENTION STUDIES

2.1. C-Be samples

Deuterium retention studies were made by exposing pure Be and C-coated Be specimens to a fluence of ~2×10^{23} D/m^2 at a flux rate of 6×10^{19} D/m^2 for 1-keV D ions. Samples were heated to 400^{o}C during the implantation. Post-implantation TDS measurements (23 to 1000^{o}C, 30^{o}C/min) indicated that for comparable implantation conditions, the quantity of deuterium retained in the C-coated Be sample was about 40% more than that retained in the un-coated Be samples. Thermally-induced release of deuterium occurred predominately at lower temperatures for bare Be (principal D_2 desorption peak at ~250^{o}C) than that for C-coated Be (principal D_2 desorption peak at ~400^{o}C). These results suggest that, for the mixed C-Be layer, deuterium retention is affected by the presence of possible graphitic phases of C. Details of these studies have been published [1-3].

2.2. C-W samples

Many different sample types were prepared and characterized for our experiments on deuterium retention in W-C systems compared to pure W. All specimens were 16.5-mm in diameter with a thickness of 25 μm for W foil, 0.5-mm for W1%La and 0.75-mm for CVD-W and CVD-W_2C products. W foil samples were punched from high purity foil (99.95 % by

weight), a reduction-rolled, powder-metallurgy product. This material was from the same lot as that used for earlier permeation studies [7]. These foils were implanted "as-received" and after annealing at 1200°C. Samples of 0.5-mm W1%La discs were polished to a mirror finish and in some cases were annealed at 1000°C or coated with a carbon surface layer. Tungsten and tungsten carbide samples were made using proprietary CVD processes.

Test samples were implanted with a 1.5-keV D_3^+ ion beam (500 eV/D, flux density of ~3×10^{19} D/m^2-s) to fluences from 1 to 3×10^{23} D/m^2. Sample temperatures were set at values between 27°C and 400°C during implantation. Retained quantities of deuterium were measured using TDS (23 to 1000°C, 30°C/min). Figures 1-5 show representative TDS spectra for un-annealed W foil (Figure 1), annealed W foil (Figure 2), CVD-W disc (Figure 3), CVD-W_2C disc (Figure 4) and C-coated W1%La disc (Figure 5). Figure 6 shows a comparison of deuterium retention data that were derived from the various TDS experiments and from previous permeation experiments [7] for 25-μm W foil that was annealed at temperatures from 450 to 1400°C.

Principal findings of this work included the following:

(1) TDS retention data for the 25-μm W foil are consistent with retention values derived from the permeation experiments for material from the same batch.
(2) Annealing of 25-μm W foil to 1200°C results in a retention reduction by a factor of 4 for deuterium implanted at 200°C, with similar retention reductions observed for other W types that were annealed.
(3) Retention in CVD-W and W1%La is below that in W foil for implantation temperatures <200°C, indicating that different fabrication processes for disc and foil materials and the resulting intrinsic defect structures influence the retained quantities.
(4) Above 200°C, TDS results indicate the opposite trend, possibly due to higher bulk retention in thicker CVD-W and W1%La samples, resulting from diffusive transport into the bulk.
(5) Retention in CVD-W_2C was somewhat higher than that in CVD-W for temperatures below 300°C, most likely because of trapping at trace C impurities in the bulk, at impurities and porosities in micro-structural defects or at beam-induced damaged sites produced by recoil C.
(6) Desorption peaks (D_2 + HD) were observed at similar temperatures (130, 300, 400 and 530°C) for these W and W_2C materials, with the relative magnitudes varying from material to material.
(7) Implantation into C-coated tungsten specimens results in retention that is orders of magnitude greater than that in a pure tungsten surface. Implanted deuterium was released primarily as D_2 and CD_4 with TDS peaks at 750°C and 525°C, respectively. Annealing studies for C-coated W indicated little inter-diffusion of C and W for temperatures less than 800°C.

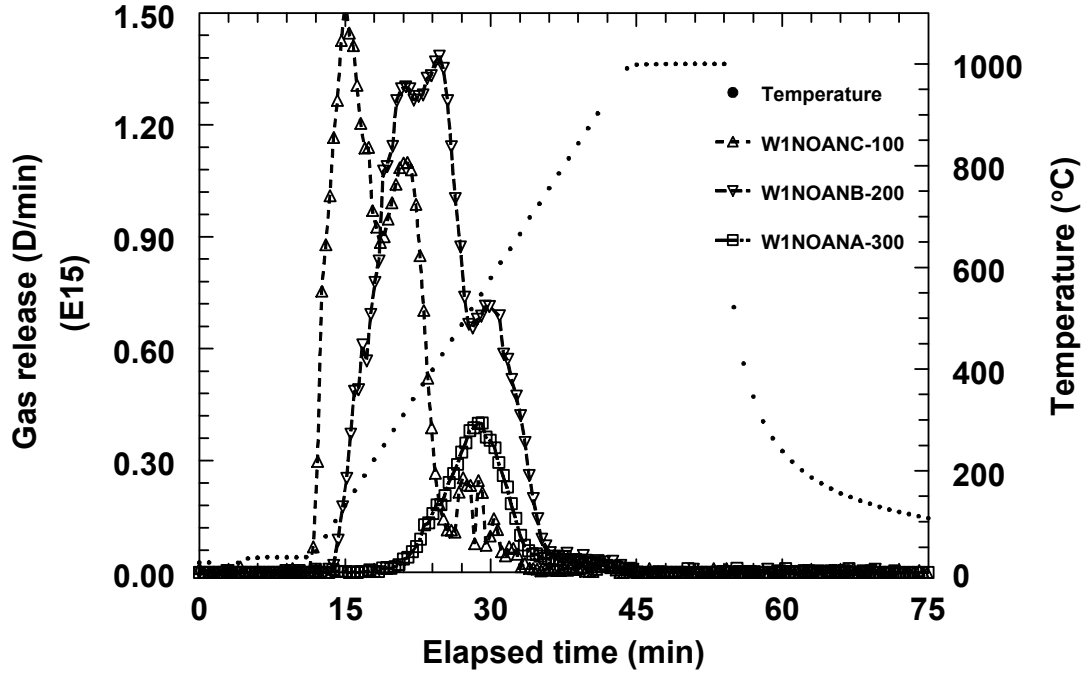

Figure 1. TDS spectra for un-annealed 25-μm W foils implanted at 100℃, 200℃ and 300℃.

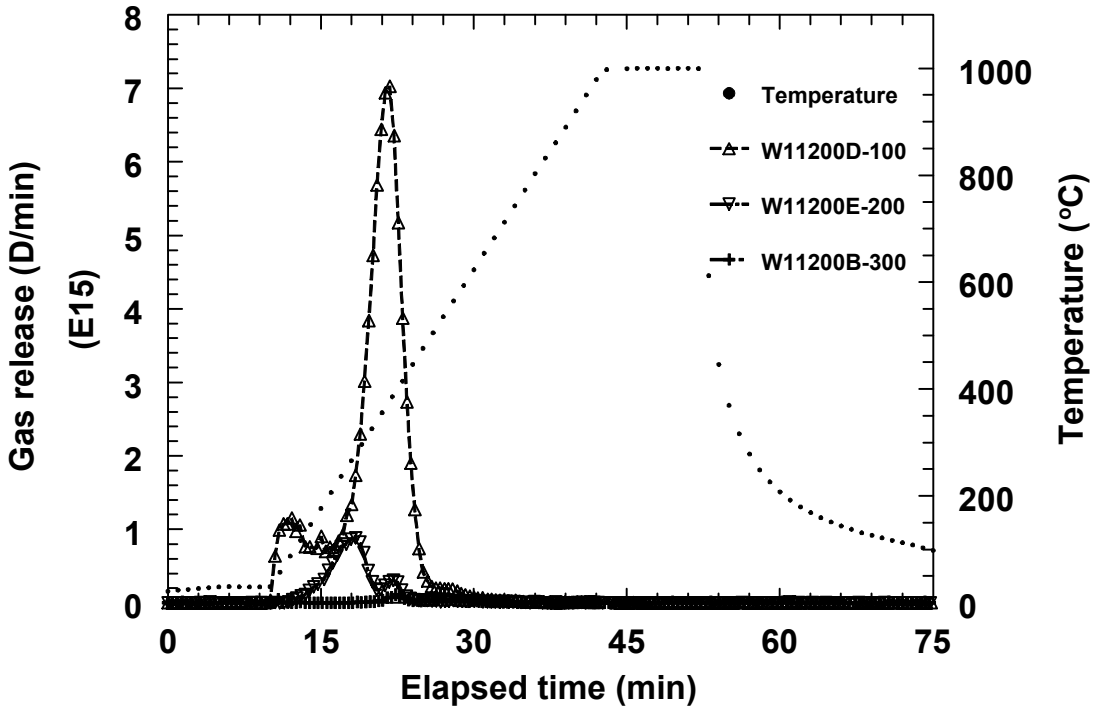

Figure 2. TDS spectra for 25-μm W foils annealed at 1200℃ and implanted at 100℃, 200℃ and 300℃.

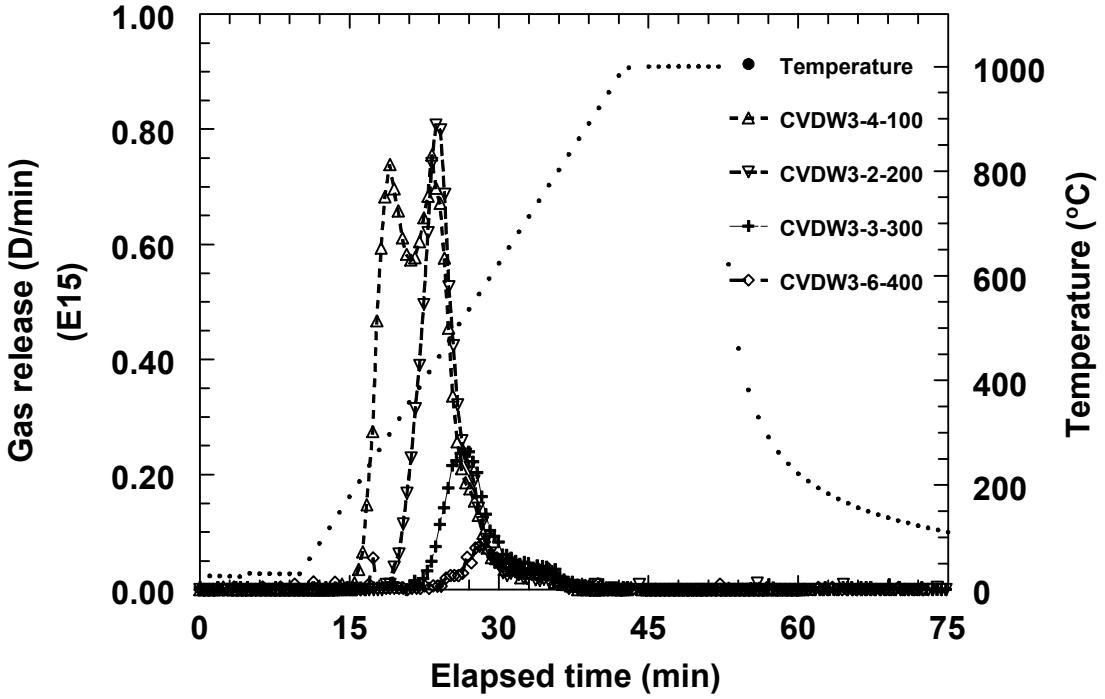

Figure 3. TDS spectra for CVD-W sample implanted at 100℃, 200℃, 300℃ and 400℃.

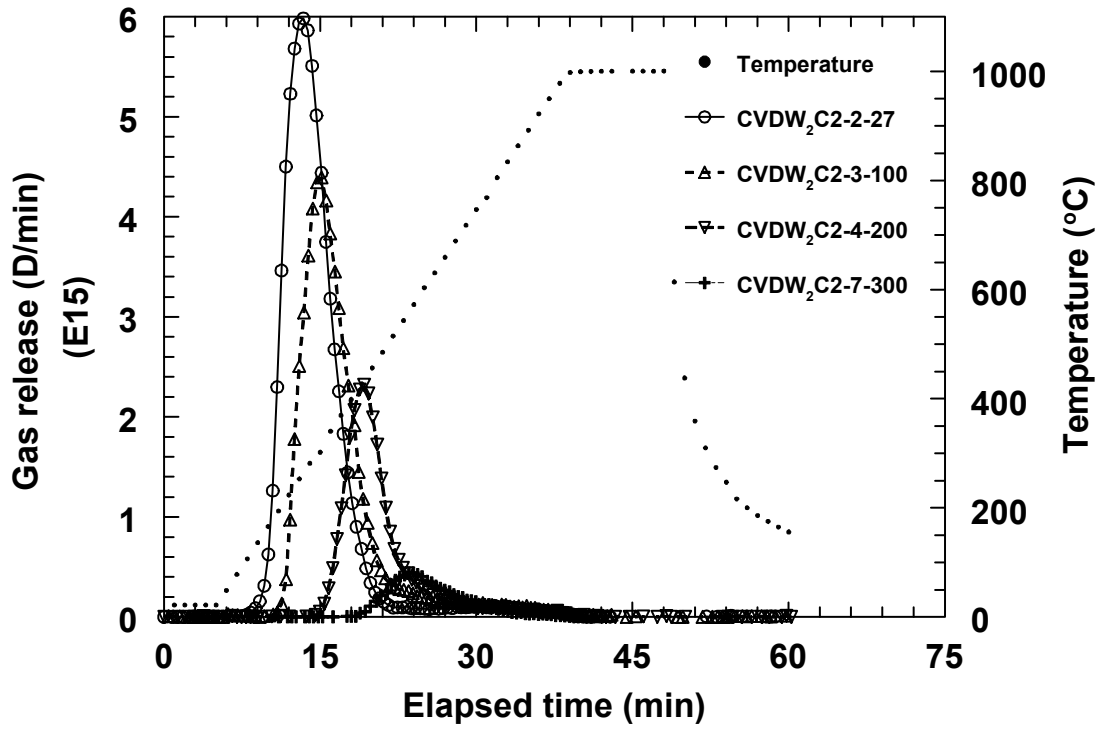

Figure 4. TDS spectra for CVD-W_2C sample implanted at 27℃, 100℃, 200℃, and 300℃.

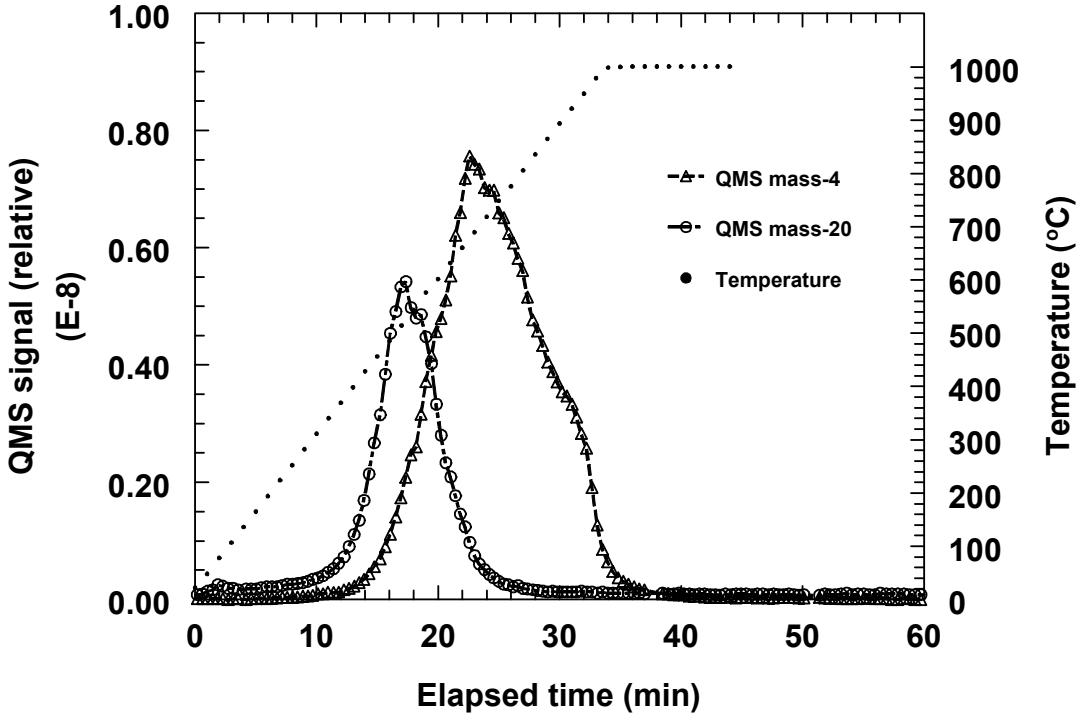

Figure 5. TDS spectra (Mass-4 is D_2 and Mass-20 is CD_4) for C-coated W1%La sample, implanted at 200°C with 500 eV/D ions to a fluence of $1.1x10^{23}$ D/m^2.

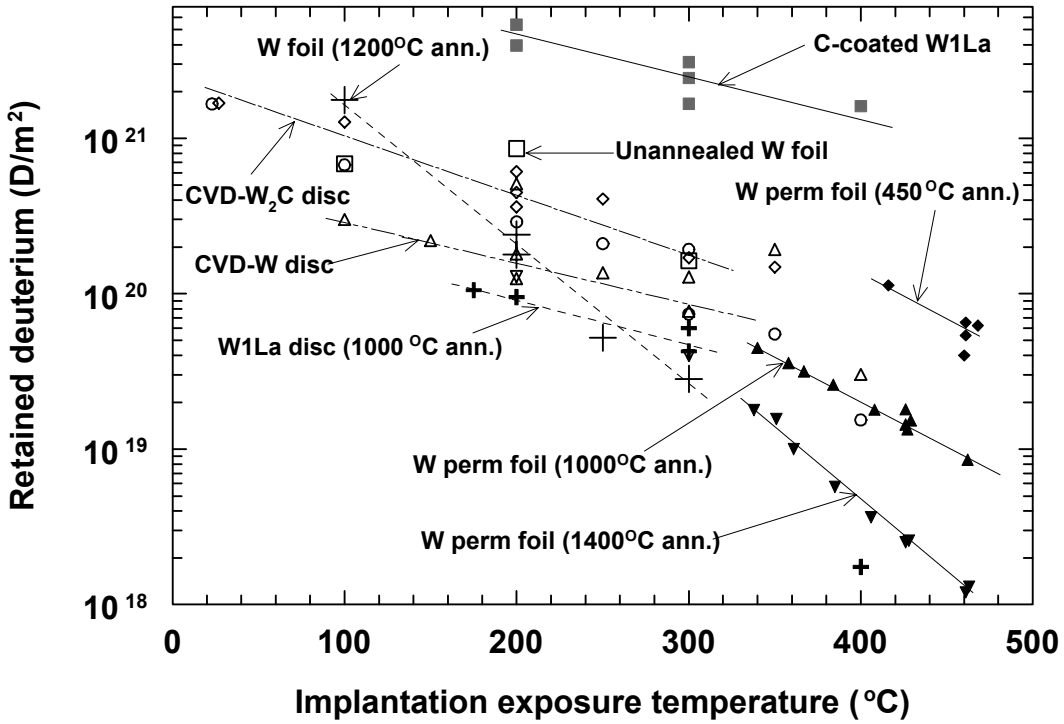

Figure 6. Deuterium retention data from implantation/TDS experiments for un-annealed and annealed W foil, W1%La discs, C-coated W1%La discs, CVD-W discs and CVD-W_2C discs.

Results of this work [4-6] demonstrated that retention of deuterium implanted into tungsten and tungsten carbide samples is highly dependent on the material type and structure, anneal condition and the presence of free carbon. Consequently, retention in W-C mixed material layers and carbon-covered tungsten PFC components may be dominated by uptake in the carbon.

This work was performed within an IAEA Co-ordinated Research Project (CRP) on "Plasma-Material Interaction (PMI) Data for Mixed Plasma Facing Materials in Fusion Reactors" and supported by the US Department of Energy, Office of Sciences, under DOE Idaho Operations Contract Number DE-AC07-99ID13727.

REFERENCES

[1] ANDERL, R. A., CAUSEY R. A., DAVIS, J. W., DOERNER, R. P., FEDERICI, G., HAASZ, A. A., LONGHURST, G. R., WAMPLER, W. R., WILSON, K. L., J. Nucl. Materials **273** (1999) 1–26.
[2] ANDERL, R. A., LONGHURST, G. R., PAWELKO, R. J., OATES, M. A., J. Fusion Energy **16** (1997) 95–100.
[3] ANDERL, R. A., "Initial Deuterium implantation thermal desorption experiments for Be and C-coated Be," Engineering Design File, EDF No: ITER/US/96/TE/SA-13, August 7, 1996, INEEL, Idaho Falls, ID.
[4] ANDERL, R. A., PAWELKO, R. J., SCHUETZ, S. T., J. Nucl. Materials **290-293** (2001) 38–41.
[5] ANDERL, R. A., PAWELKO, R. J., SCHUETZ, S. T., "Deuterium retention in W foil, CVD-W and CVD-W_2C," INEEL External Report INEEL/EXT-2000-00702, June, 2000.
[6] ANDERL, R. A., "Deuterium implantation and mobilization behavior in carbon-coated tungsten," Engineering Design File, EDF No: ITER/US/98/TE/SA-14, July 17, 1998, INEEL, Idaho Falls, ID.
[7] ANDERL, R. A., HOLLAND, D. F., LONGHURST, G. R., PAWELKO, R. J., TRYBUS, C. L., SELLERS, C. H., Fusion Technol. **21** (1992) 745–752.

MIXED-MATERIAL HYDROGEN INVENTORY AND REMOVAL TECHNIQUES IN PISCES

R.P. DOERNER and the PISCES Team
Center for Energy Research, University of California – San Diego,
La Jolla, California, United States of America

Abstract

The deuterium inventory in mixed-material surface layers formed during plasma bombardment of beryllium and tungsten samples has been investigated. The temperature of the sample during the formation of the layer plays a dominant role in determining the deuterium content of the layers. For carbon containing mixed-material films, the retention properties of the films are similar to that of pure graphite and can easily dominate the retention expected in the underlying substrate material. Cathodic transfer arc cleaning has been investigated as a mechanism to remove mixed-material films after they have formed on plasma-facing materials. The arc cleaning technique has been demonstrated to reduce the amount of deuterium in the coated samples to levels below our detection limit.

I. INTRODUCTION

The hydrogen isotope retention in a beryllium first wall has been shown to reach a saturated value and then to have only a small dependence on increasing fluence [1,2]. However, an impurity layer could easily be expected to form on the ITER first wall as was shown in a previous contribution to this issue. As the mixed-material layer forms it is possible that the retention in the surface layer may dominate the retention in the underlying, or bulk, beryllium.

II. DEUTERIUM RETENTION MEASUREMENTS

A series of measurements has been made in the PISCES-B facility at UCSD by injecting controlled amounts (≈2%) of CD_4 into a deuterium plasma column bombarding various beryllium samples. The exposure in each case lasted for 2 hours. After the conclusion of each exposure the sample was removed from vacuum and inserted in a separate vacuum chamber where TDS (thermal desorption spectrometry) was performed. The sample temperature was ramped up to a maximum of 900°C while recording the partial pressures of all the deuterium containing molecules (D_2, HD, D_20, HDO) which were released. The amount of deuterium released in the mass 19 and 20 peaks was measured to be negligible (<1%) compared to the mass 3 and 4 peaks. The results of the TDS measurements are compared in Figure 1 to the retention measured in uncoated ('clean') beryllium samples, both plasma-sprayed and press-sintered, exposed to plasma containing the 0.2% background carbon impurity concentration. Regardless of the substrate material the formation of a carbon-containing mixed-material layer is measured to increase the amount of deuterium retained.

At least an order of magnitude more deuterium is retained in the samples containing the mixed-material layers formed during room temperature exposures. As the temperature of the layer formation increases the amount of additional deuterium retained decreases until at 500°C there is no detectable difference in the retention between coated and clean samples. Although it is evident that the retention in mixed-material layers should be a concern for ITER, is also apparent that the proper design of the heat removal from the wall can minimize these concerns.

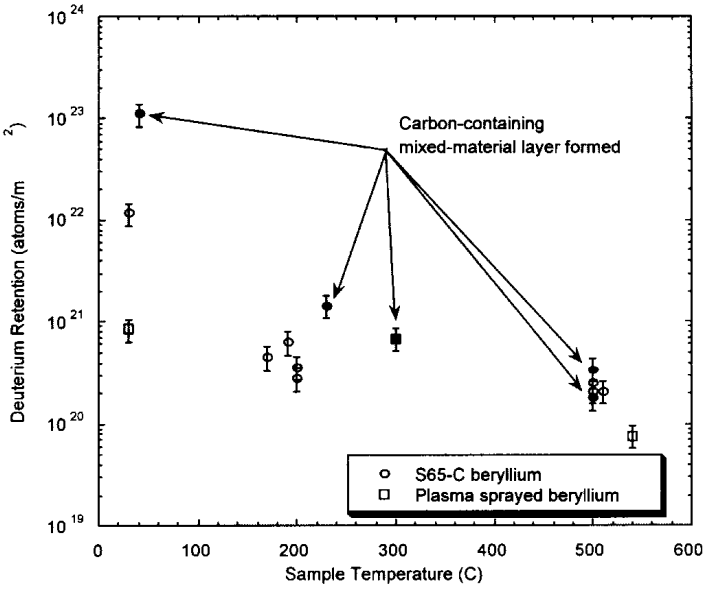

Figure 1. Deuterium retention in beryllium samples can increase when mixed-material layers form. The temperature dependence of the retention in the mixed-material layer is similar to that expected from a pure carbon sample.

There are two possible explanations for the reduced retention in the mixed-material layers at elevated temperatures. The first involves the temperature dependence of the retention in carbon films formed at different temperatures [3], as carbon films themselves form at higher temperature they tend to retain less hydrogen isotopes. It is also possible that at elevated temperatures there begins to be interdiffusion of the depositing carbon and the substrate beryllium. At temperatures above 490°C, beryllium carbide is expected to form and reduced retention is expected in beryllium carbide [4].

Similar experiments were performed in PISCES-B to investigate the interactions between the deuterium plasmas and the tungsten substrates with and without CD_4 puffing [5,6]. Three type of tungsten samples were used: (1) PLANSEE's W1%La_2O_3 tungsten disc, 2 mm thick; (2) AESAR's tungsten disc, 99%W, 2 mm thick, and (3) AESAR's tungsten foil, 99.95%W, 100 μm thick.

Figure 2 shows the total amount of deuterium atoms desorbed from carbon contaminated and non-contaminated tungsten samples. In general, results show that there is no significant difference in hydrogen retention between the three kinds of tungsten sample after plasma exposure. The dominant factors, which influence the hydrogen isotope retention in plasma exposed tungsten, are (i) the substrate temperature and (ii) whether carbon is deposited on the tungsten surface.

As is the case with the Be/C mixed-material system, the carbon films on W samples dominate the hydrogen isotope retention properties of the plasma-exposed materials. The quantity of retained gas is again seen to be dependent on the temperature at which the carbon films form on the surface, being less dramatic under higher temperature formation conditions.

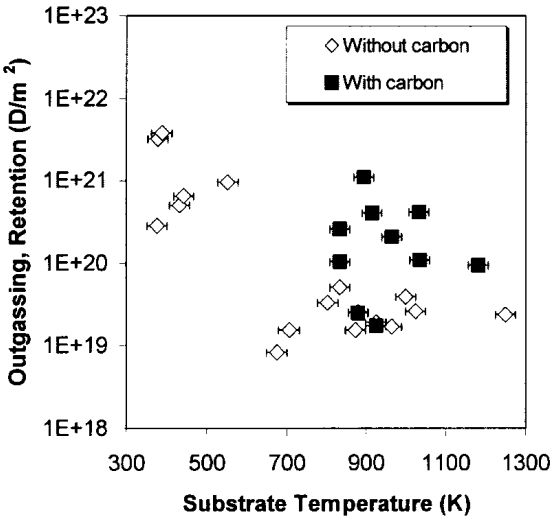

Figure 2. Total deuterium retention versus substrate temperatures and coating for the W/C system.

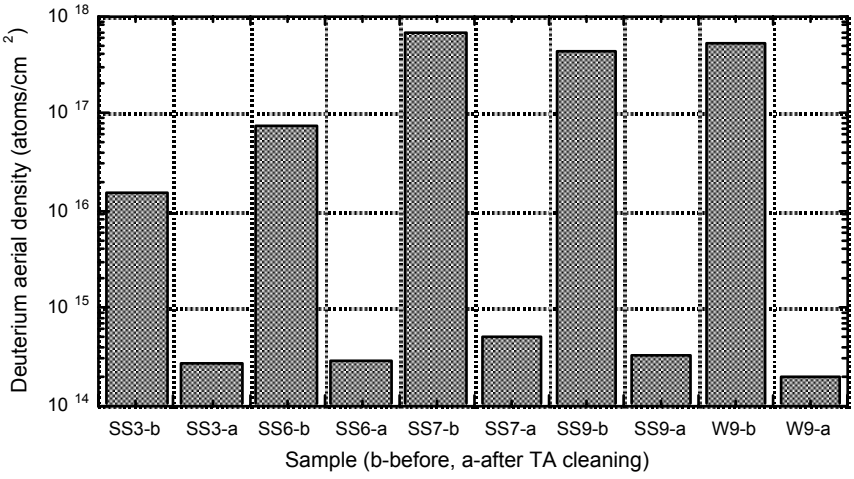

Figure 3. Aerial densities of deuterium before (b) and after (a) TA cleaning of stainless steel and tungsten samples. Measurements after cleaning are all below the accurately resolvable detection limit.

III. REMOVAL TECHNIQUES

In addition to examining the hydrogen isotope retention qualities of films formed on samples, techniques offering the possibility of removing these plasma-deposited layers have been investigated [7]. Deuterium and carbon were co-deposited onto tungsten and stainless steel samples using a deuterated methane plasma to simulate deposited layers in magnetic-confinement fusion devices. Cathodic arc, or transferred-arc (TA) cleaning was employed to remove the deposits from the samples. TA cleaning utilizes a direct current (DC) plasma torch and a secondary DC power supply attached between the torch and the part to be cleaned to establish arcing between the torch face (anode) and the part (cathode). The samples were characterized by ion beam analysis both before and after cleaning to determine deuterium and carbon concentrations present. The extent of TA cleaning was varied to determine the deuterium and carbon removal efficiency and sample erosion rate. The deuterium content

was greatly reduced by the cleaning thus demonstrating the possibility of using the TA cleaning technique for removing deuterium and/or tritium from components exposed to D-T fuels.

The aerial density of the deuterium was measured by elastic recoil ion beam analysis (measuring depth of $\leq$5 μm) and the results are shown in Figure 3. The minimum accurately resolvable measurement is 5×10^{14} atoms/cm^2. For reference, 1×10^{15} atoms/cm^2 corresponds to approximately one monolayer of atoms. All of the deuterium measurements after cleaning were near or below the threshold of 5×10^{14} atoms/cm^2.

Therefore, the values shown in Figure 3 for after cleaning represent maximum possible values rather than accurate measurements. Likewise, the measurement uncertainty of deuterium aerial density before cleaning is 5×10^{14} atoms/cm^2. Therefore, in the case of the co-deposited deuterium and carbon films studied here, the deuterium is removed at least to the level of the detection limit for the technique used.

The samples had carbon deposits of varying aerial density and distribution after plasma deposition. Some deposits were observed only on the surface of the sample (<5 nm depth into the sample) while others extended beyond the measurement depth (5 μm) of the ion beam technique. The carbon deposited below the surface layer will be referred to as "bulk carbon". The aerial densities are shown graphically in Figure 4. In all cases the surface carbon was removed from the tungsten samples. Similarly the surface carbon concentration on the stainless-steel samples was always reduced, as was the bulk carbon concentration found in some of the SS samples. Issues still remain before transfer-arc cleaning can be proposed as a cleaning technique for future devices, such as the creation of particulate residue, the release and recondensation mechanisms of hydrogen isotopes, etc., but these preliminary investigations have demonstrated the capabilities of the technique.

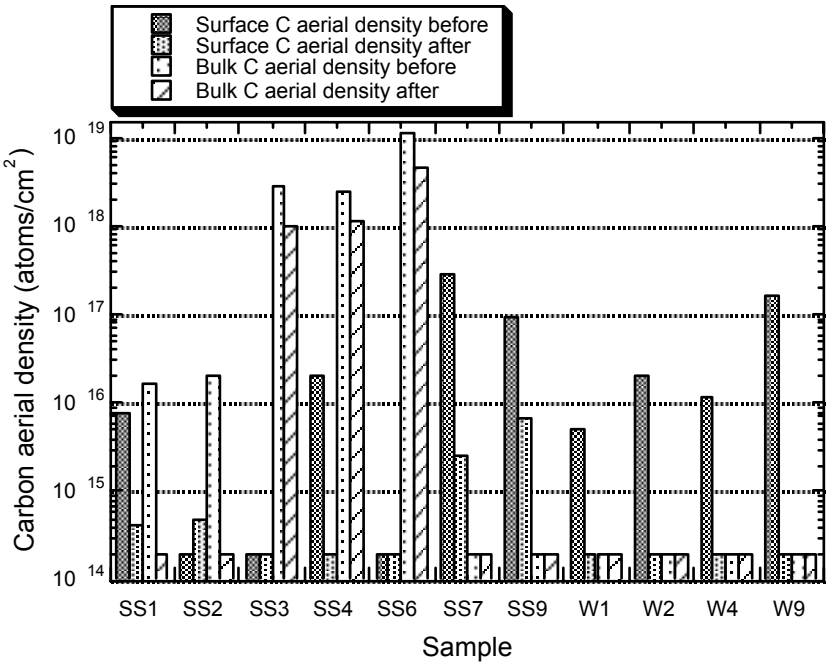

Figure 4. Surface and bulk carbon aerial densities before and after TA cleaning.

IV. SUMMARY

These investigations have examined the importance of carbon-containing mixed-material layer formation on plasma-facing components. Similarities in the hydrogen isotope retention qualities between the Be/C and W/C systems have been demonstrated. In addition, techniques both passive and active have been identified to minimize the role of these carbon-containing layers. Passive techniques could involve the design of plasma-facing components to maintain elevated surface temperatures where mixed-material layers may be expected to form. The capabilities of transfer-arc cleaning have been demonstrated as a possible active film control technique.

REFERENCES

[1] R. A. Anderl et al., J. Nucl. Mater. 273 (1999) 1.
[2] R. P. Doerner et al., Physica Scripta T81 (1999) 35.
[3] B.L. Doyle et al., J. Nucl. Mater. 103 &104 (1981) 513.
[4] J. Roth, W. R. Wampler and W. Jacob, J. Nucl. Mater. 250 (1997) 23.
[5] F.C. Sze, R.P. Doerner and S. Luckhardt, J. Nucl. Mater. 264 (1999) 89.
[6] F.C. Sze, L. Chousal, R.P. Doerner and S. Luckhardt, J. Nucl. Mater. 266-269 (1999) 1212.
[7] K.J. Hollis, R.G. Castro, R.P. Doerner, C.J. Maggiore, Fusion Engr. & Design, 55 (2001) 437.

THE METHOD OF H-ISOTOPES AND BORON DEPTH PROFILING USING NEUTRON FLUX AS A TOOL FOR PLASMA-FACING COMPONENTS INVESTIGATION

S.V. ARTEMOV, E.V. ZHUKOVSKAYA, G.A. RADYUK, V.G. ULANOV, V.P. JAKUSHEV
Institute of Nuclear Physics, Academy of Science RUz, Ulugbek, Tashkent, Uzbekistan

Abstract

The combination of elastic recoil detection technique with monochromatic 14 MeV neutrons and a procedure of energy spectra simulation for (n,^{1,2,3}H) recoil nuclei was applied for hydrogen isotope concentration depth profiles study in plasma-facing components of a thermonuclear reactor.

1. INTRODUCTION

Accumulation and recycling of different hydrogen isotopes in construction elements plays an important role in fusion devices. Therefore, the development of novel methods for reliable detection of H, D and T contents and their depth concentration profiles inside plasma-facing components of a thermonuclear reactor is now required. The recently developed direct method of study of hydrogen isotope behaviour in materials is based on using of fast quasi-monochromatic neutrons as analysing particles and the measurement of hydrogen recoils energy spectra [1,2,3]. This Neutron-induced Elastic Recoil Detection (NERD) method has advantages over other nuclear-physical tools. Besides, it allows one to probe hydrogen contents up to depth a few hundred microns and to measure concentrations of all hydrogen isotopes simultaneously.

2. EXPERIMENT

The scheme of the experimental set-up is shown in figure 1. Monochromatic 14 MeV neutrons emitted from a neutron generator are incident on the specimen under study. In the case of neutron elastic collision with a hydrogen atom in the specimen the recoiling nucleus is detected with a telescope of semiconducting detectors which is tuned to record protons, deuterons or tritons. Use of 3 detectors in the telescope is dictated by the need to decrease the background by the coincidence technique as well as to identify the type of recoils by the well-known ΔE-E method. Detector thickness has to be chosen according to the hydrogen isotope to be analysed and the analysable depth of interest The telescope output signals are displayed as two-dimensional spectra. The events corresponding to different recoil types on hyperbola-like locus are localised.

The detected energy E is connected with depth x so far as a recoil loses part of its energy on the way toward the specimen surface:

$$x = R(E_r) - R(E) \qquad (1)$$

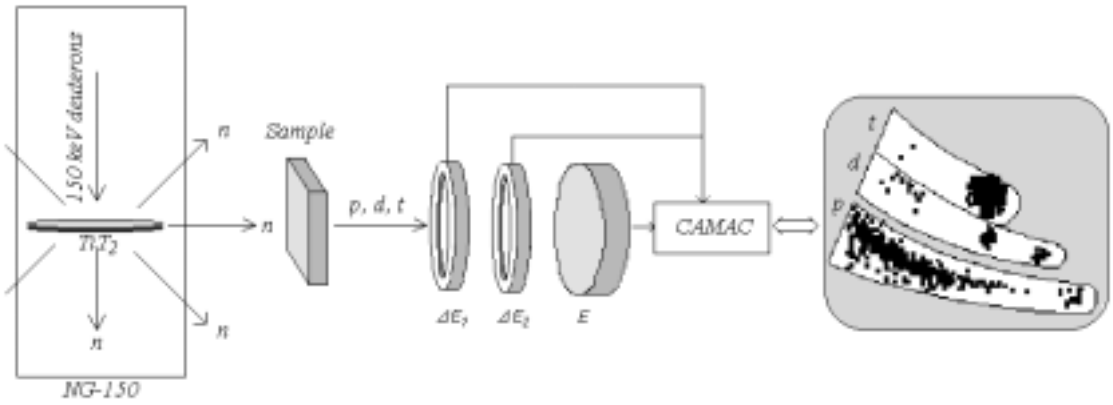

Figure 1. Scheme of experimental set-up.

where ***x*** is depth where collision has taken place. The recoil energy spectrum ***N(E)*** gives the possibility to obtain the distribution of hydrogen concentration along specimen depth ***c(x)*** (depth profile) by the equation

$$c(x) = A \cdot N(E) \cdot S^{-1}(E), \qquad (2)$$

where the constant ***A*** may be obtained by measurement with a standard specimen (with known depth profile); stopping power ***S(E)*** and range of a recoil ***R(E)*** for given specimen substance might be found by the well-known TRIM code [4]. However, this simple formula (2) doesn't work properly for thickness of specimens comparable with the method depth resolution (~ 5% of maximum analysis depth for each isotope). In these cases obtaining concentration profiles from experimental data is a difficult problem.

3. SIMULATION MODEL

For obtaining profiles from energy spectra when the specimen thickness is comparable with depth resolution a new computer simulation model has been designed. It is based on the Monte Carlo method and analytical geometry technique. This model allows calculation of the energy and angular distributions for neutrons and recoils in conditions of real experiment. With the assistance of the random events one can consider all stages from the moment of neutron generation up to the moment of corresponding recoil detection. A specimen has finite thickness and consists of one or several macrolayers with arbitrary chemical composition. A conjectured form of hydrogen isotope concentration profile ***c(z)*** in each layer is an analytically defined function. The certain weight is assigned to each event and than the array of events forms the energy distribution which may be compared with experimental spectra after necessary treatment. Criteria χ^2 was used for the comparison. The model has been developed as a computer code named Distribution Recoil Induced Neutron (DRIN). So by use of the DRIN code one has the possibility of extracting the deep depth concentration profiles for sufficiently thin structures**.**

4. RESULTS AND DISCUSSION

4.1 JET specimens

The NERD method was applied to the study of hydrogen isotopes concentration depth profiles in plasma-facing components of thermonuclear reactors [5]. The capability of the technique can be demonstrated on JET carbon specimens investigation. It was devoted to determination of hydrogen isotopes amount in the specimen. The experiments were performed assuming the homogenous distribution of hydrogen isotopes in the redeposited layer. The results are shown in Table 1.

TABLE I. HYDROGEN AND DEUTERIUM CONTENTS FOR **JET** SPECIMENS

Specimen	C_H, $10^{18}cm^{-2}$	C_D, $10^{18}cm^{-2}$
1	8.8 ± 0.5	1.5 ± 0.2
2	9.3 ± 0.4	1.1 ± 0.1
5	0.7 ± 0.1	0.17 ± 0.03
2 (2)	1.9 ± 0.3	0.62 ± 0.08
3 (2)	7.2 ± 0.5	0.80 ± 0.11
4 (2)	6.5 ± 0.3	0.85 ± 0.09
5 (2)	8.7 ± 0.4	0.53 ± 0.07
control (C_D=0.6×10^{18}cm)	-	0.75 ± 0.14
$TiD_{1.97}$ (C_D=26×$10^{18}cm^{-2}$)	-	23±2

However, these data do not correspond to the data obtained by using ion methods. Deuterium content in 100 mkm thick layer obtained with our technique only slightly exceeds one obtained by using of ion methods for the thickness of 1 mkm. This fact made us to refuse of our supposition of homogenous distribution and we had to resolve the problem of deep depth concentration profiling. We had tried to attain the deep depth distribution in these specimens by the use of computer simulation. A part of the calculations is shown in fig.2, hence it follows that neither uniform distribution of deuterium (fig.2a) nor its accumulation in 1 μm layer near surface (fig.2b) fits the experimental data. A linear slope of deuterium contents from maximum value in surface to 0 in 70 μm depth, fig 2c, is also unsatisfactory. The best description was achieved for the profile shape shown in fig. 2e.The sensitivity of DRIN is very well from the comparison of fig.2e with fig.2d: one can see that a small Assumption of the identity of deuterium and protium distributions, fig. 3a, or the uniform hydrogen distribution, fig.3b, does not lead to satisfactory description of experimental data. A good fitting is obtained here for a hypothesis that the most amount of protium is concentrated in 50 μm layer near surface while the total analysable thickness of specimen is 120 μm (fig. 3c). The availability of hydrogen may be explained by absorption of a water steam in specimens after removal it from reactor.

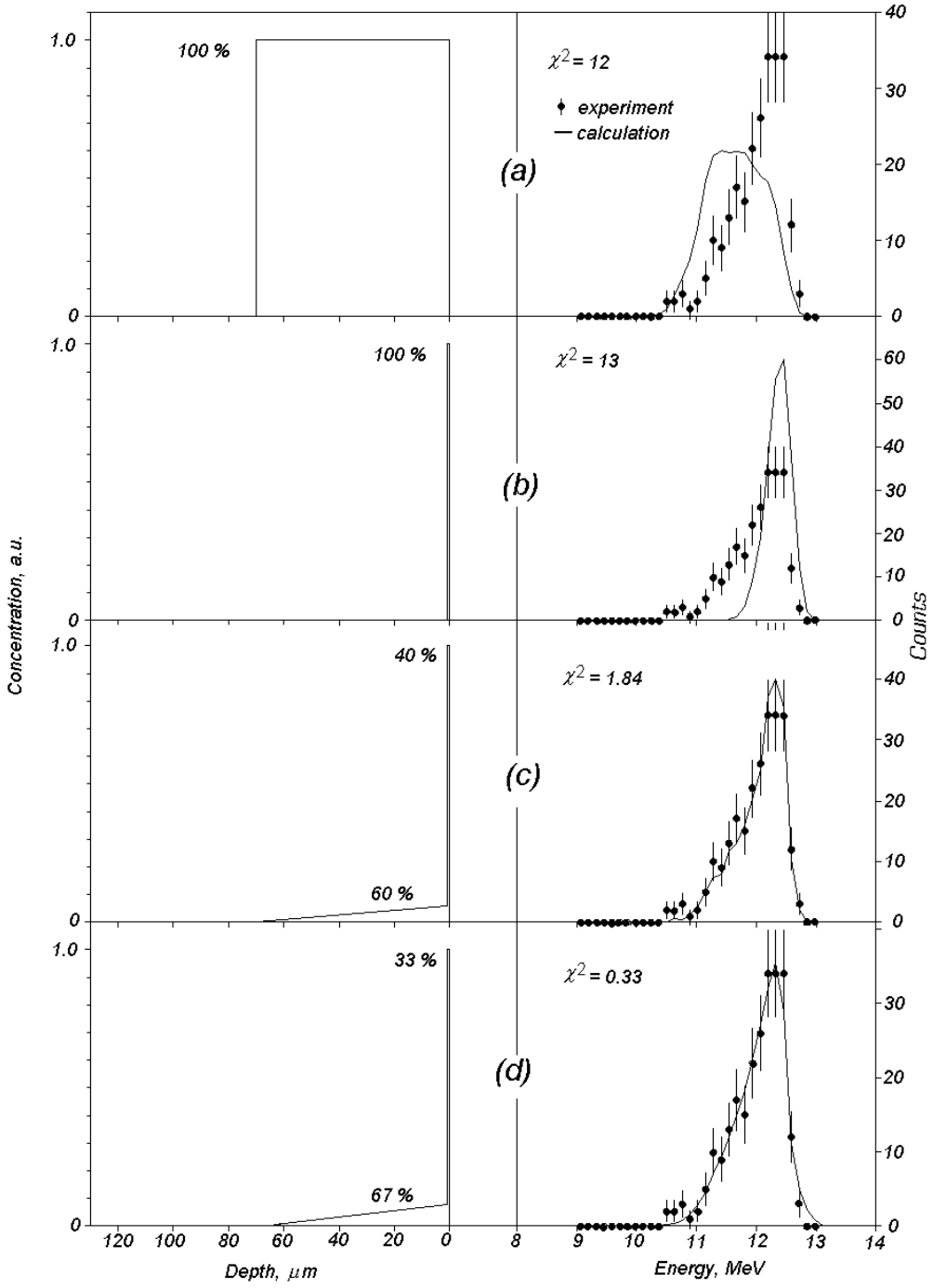

Figure 2. The comparison of experimental deuteron spectrum for the carbon JET sample with spectra simulated by the DRIN for different assumption on the depth profile of concentration shapes.

The supposed shape of the deuterium concentration profile can be defined more precisely by using 2.5 MeV dD neutrons. Such experiment have been carried out. It confirmed validity of profile choice in fig.2e. Variant of the NERD method on dD neutrons (total flux 10^8 n/s) allows to carry out the investigation of hydrogen distribution in thin (≤20 μm on carbon) hydrogen containing layers.

4.2 DIII-D specimens

Five different carbon specimens were investigated. Four of them had been previously exposed to plasma: 3 with boron coating and one carbon specimen without covering. The fifth boronized specimen had no contact with plasma. Two dimensional spectrum obtained for pure carbon specimen is shown at the right of figure 4. The left part of this figure shows the spectrum measured for boron coated graphite specimen taken from divertor of DIII-D tokamak. Visual analysis of these two spectra shows that the presence of boron atoms is displayed by the ^{10}B - neutron interaction with protons, deuterons and tritons production. The background is practically absent in region of deuteron localisation on the two dimensional energy spectra and the presence of boron atom does not affect the D isotope determinations.

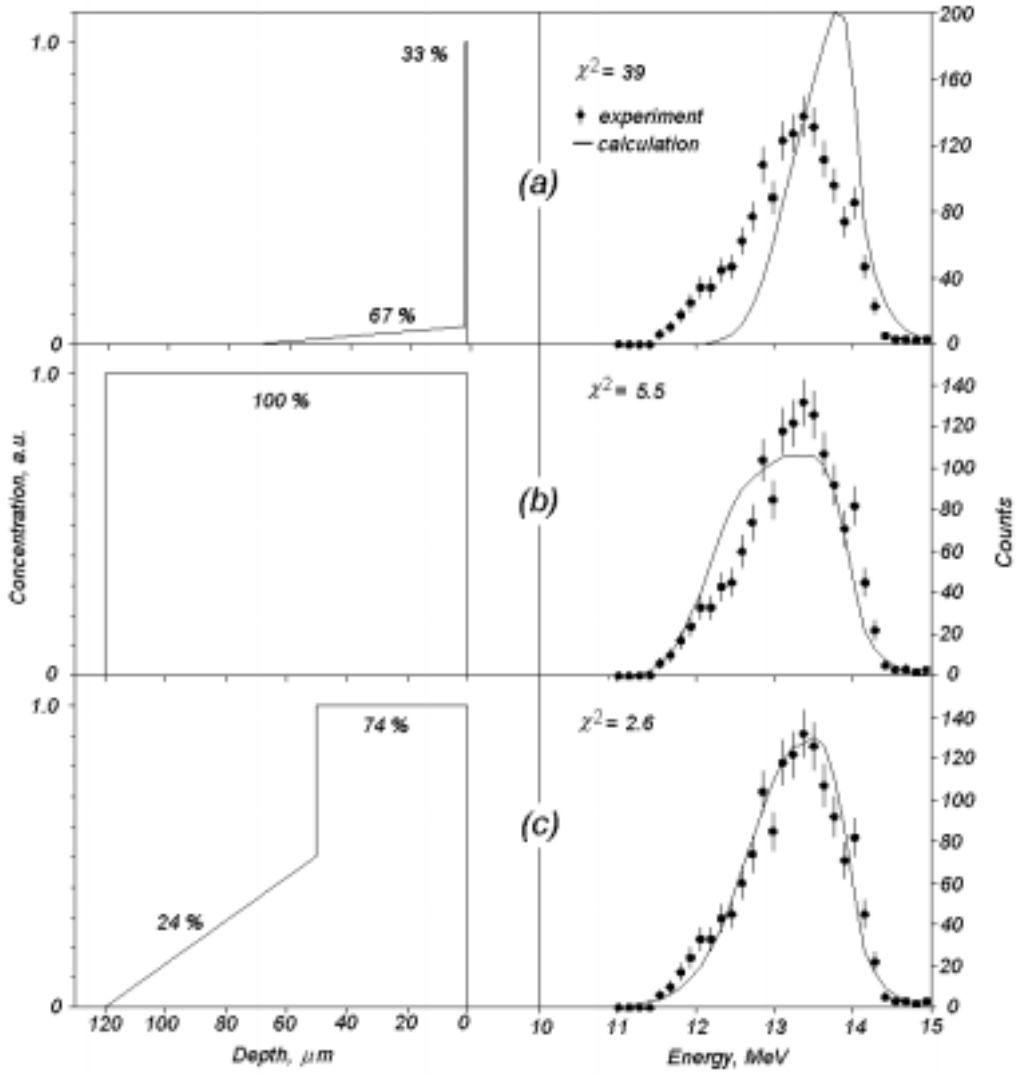

Figure 3. The comparison of experimental proton spectrum for the carbon JET sample with spectra simulated by the DRIN for different assumption on the depth profile of concentration.

Boron content is most simply determined from deuteron spectrum from reaction $n+^{10}B=d+^{9}Be$ which leads to excitation of two levels of final nucleus ^{9}Be: ground (right peak in fig. 5) and first excited with energy E*=2.43 MeV (left peak in fig. 5). The deuteron energy spectrum and boron concentration profile, which is restored by using of the right peak of this spectra, are shown in the figure. The "true" concentration profile of a boron restored by DRIN code is shown too. The concentration profile obtained by DRIN code for triton spectra is analogous (fig. 6). An agreement between the boron depth distributions restored from deuteron and triton energy spectra is shown in these figures.

After the boron concentration profile has been restored, we calculate the shape of proton energy spectrum for $n+^{10}B=p+^{10}Be$ reaction by DRIN code. The concentration profile of hydrogen in a specimen is obtained by subtraction of calculated spectrum from an experimental one. The triton concentration profile can be obtained by a similar way.

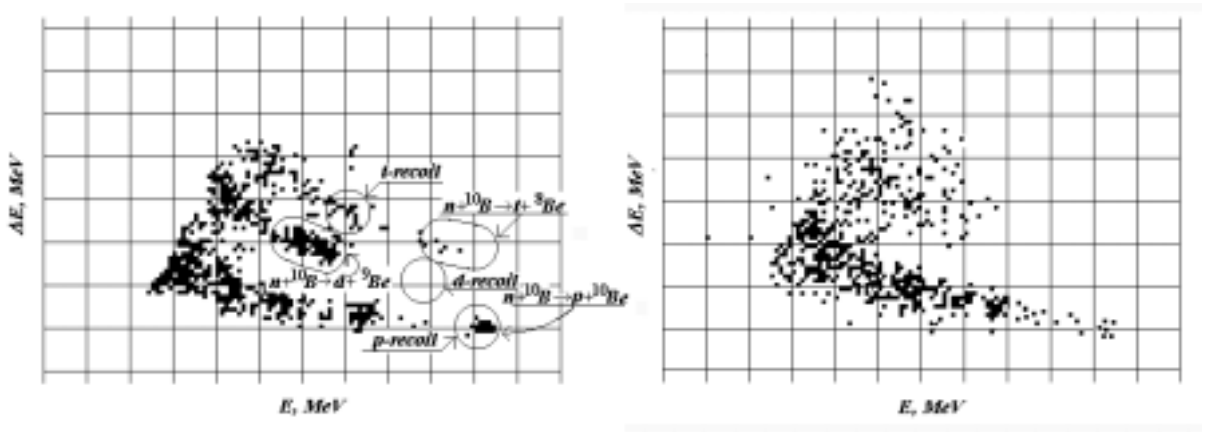

Figure 4. Two-dimensional ΔE-E spectra from carbon sample coated with B_4C layer (at the top) and from carbon (at the bottom)

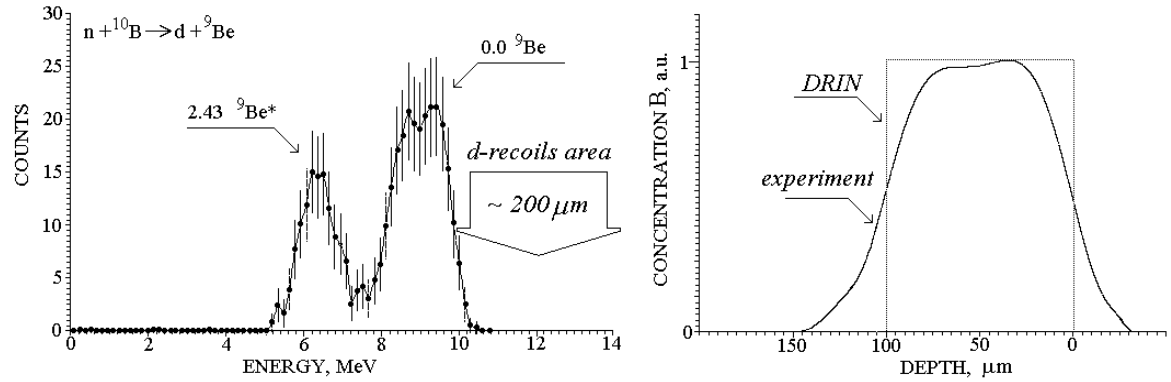

Figure 5. Deuteron energy spectra taken from a carbon specimen coated B_4C and its depth profiles both calculated by DRIN code and extracted from experiment.

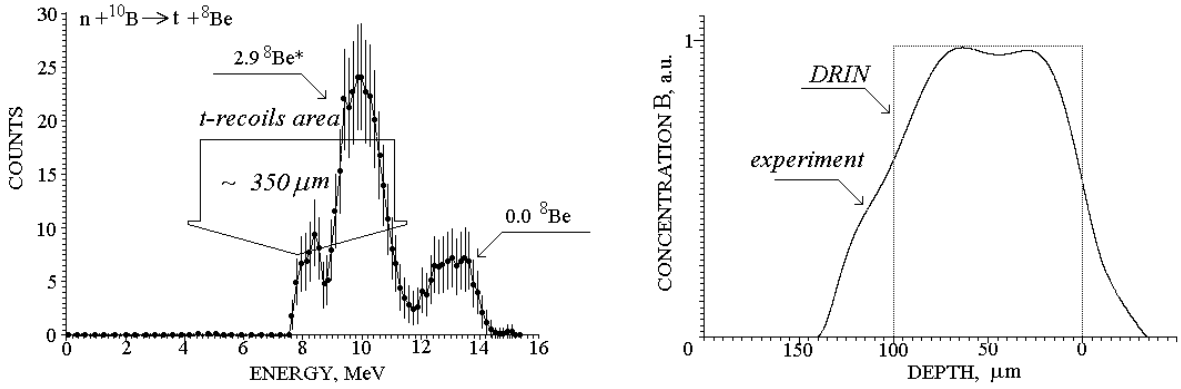

Figure 6. Triton energy spectra taken from a carbon specimen coated B_4C and its depth profiles both calculated by DRIN code and extracted from experiment.

TABLE II. HYDROGEN AND DEUTERIUM CONCENTRATION AND LAYER THICKNESS [6]

Specimen	**Concentration, $H\times10^{18}$ñm^{-2}**	**Relative concentration *B***	***B* thickness, μm**
Control	< 0.3	1	~ 80
6410	1.4 ± .4	1.5 ± 0.1	~ 115
6420	2.5 ± 0.3	0.15 ± 0.03	-
6440	< 0.3	1 ± 0.08	~ 80
6250	2.8 ± 0.3	0.79 ± 0.08	~ 80

4.3 RGT and tungsten specimens

We used the technique described above for the analysis of RGT specimens (from TRINITI) coated by boron carbide also. We expected a presence of hydrogen isotopes inside the specimen which was in touch with the plasma. The traces of plasma are clearly seen on the specimen surface. The front and back specimen sides were studied visually. The surface hydrogen only is found out for both sides of RGT-graphite specimen. However the hydrogen contents on the surface covered by B_4C is nearly twice as low as on the reverse. The layer of a B_4C coating has a thickness 115 ± 5 microns and the volume concentration of boron ~ 0.75 ± 0.05 relative to the control specimen. The probable reason of a change of boron concentration is the burn-out of a boron at some microplots on all area of plasma influence.

The tungsten specimens from RRC "Kurchatov Institute" irradiated by deuterium ions with the energy 200 eV. One of them (#02) has been irradiated by stationary plasma at the temperature 800 K. Another tungsten specimen (#4) has been additionally treated by the irradiation of pulsed plasma flux. The availability of hydrogen isotopes inside of material of tungsten specimens is not revealed. The surface content is a little bit higher for specimen which was subjected to pulse plasma processing then for another one (treated by stationary plasma flux). It may be explained by a change of adsorbing properties of a surface after pulse treating by plasma.

TABLE III. AMOUNT CONTENT OF HYDROGEN ISOTOPE AND BORON

Specimen		Hydrogen		Deuterium	Boron	
		C_H, atH/cm^2	Thickness, μm	C_D, atD/cm^2	C_B, cm^{-3}	Thickness, μm
Control (C coating B_4C)					1	95 ± 5
RGT-graphite	*front*	0.3×10^{20}	< 20	-	0.75 ± 0.05	115 ± 5
coating B4C	*back*	0.6×10^{20}	<20	-	-	
W(N02)	*front*	0.2×10^{20}		$< 1\cdot10^{17}$	-	
W (N4)	*front*	0.4×10^{20}		$< 1\cdot10^{17}$	-	
	back	0.5×10^{20}		-	-	

CONCLUSIONS

The NERD method combined with computer simulation model is fairly suitable for the simultaneous non-destructive determination of overall absolute content of hydrogen isotopes and boron as well as their deep depth concentration profile in plasma-facing components of tokamak. The detection limit values are ~10^{17} cm^{-2} for H and ~ 10^{16} cm^{-2} for other isotopes. The proposed method can be used for the definition of the coating thickness without specimen destruction. The presented results should be considered as preliminary demonstration of the NERD method possibility which may be substantially expanded, if higher neutron flux intensity be used.

REFERENCES

[1] B.G.SKORODUMOV, V.G.ULANOV, I.O.YATSEVICH, E.V.ZHUKOVSKA, O.A.ZHU-KOVSKY, Nucl. Instr. and Meth. in Phys. Res., **B85** (1994) 803–807.

[2] B.G.SKORODUMOV, V.N.SEREBRYAKOV, V.G.ULANOV, E.V.ZHUKOVSKA, O.A.ZHUKOVSKY, Int. J. Hydrogen Energy V. 21 No. **11/12** (1996) 961–968.

[3] B.G.SKORODUMOV, V.N.SEREBRJAKOV, V.G.ULANOV, E.V.ZHUKOVSKAJA AND O.A.ZHUKOVSKIJ. The Physics of Metals and Metallography, Vol.83, No.**1** (1997) 61–66.

[4] ZIEGLER, J.P.BIERSACK, U.LITTMARK. The stopping and range of ions in solids. Vol.1, N.Y., Pergamon Press, 1985, 321pp.

[5] J.P.COAD, B.G.SKORODUMOV, V.G.ULANOV, C.H.WU, Vacuum V.47 No.**6-8** (1996) 985–990.

[6] B.G.SKORODUMOV, O.I.BUZHINSKIJ, W.P.WEST AND V.G.ULANOV, Journal of Nuclear Materials **233–237** (1996) 1107–1112.

Contents of previous volumes of Atomic and Plasma–Material Interaction Data for Fusion

Volume 1 (1991)

Volume 2 (1992)

Volume 3 (1992)

Volume 4 (1993)

Volume 5 (1994)

Volume 6 (1995)

Volume 7/A (1998)

Volume 7/B (1998)

Volume 8 (2001)

Volume 9 (2001)

Volume 10 (2002)

Volume 11 (2003)